

Doctorate School in Physics,
Astrophysics and Applied Physics
Università degli Studi di Milano

Ecole Doctorale de
Particules, Noyaux et Cosmologie
Université Paris Diderot (Paris 7)



The ${}^8\text{B}$ Solar Neutrino Analysis in Borexino and Simulations of Muon Interaction Products in Borexino and Double Chooz

s.s.d. FIS/04

Ph.D. Thesis of:
Margherita BUIZZA AVANZINI
XXIV Cycle

Thesis Director: Prof. Gianpaolo BELLINI

Directeur de Thèse: Prof. Alessandra TONAZZO

Director of the Doctoral School: Prof. Marco BERSANELLI

Directeur de l'Ecole Doctorale: Prof. Philippe SCHWEMLING

A.A. 2010/2011

Abstract

The present work deals with both ^8B solar neutrino analysis in Borexino, and Monte Carlo (MC) simulation of cosmic muon interaction products in Borexino and Double Chooz. In Borexino, the ^8B solar neutrino analysis was performed at the lowest energy thresholds ever reached: 3 and 2 MeV. Setting the energy threshold at 3 MeV required the study and development of removal techniques for cosmogenic isotopes. Decreasing the energy threshold down to 2 MeV required a deep study of the external backgrounds affecting the Borexino core, and the development of precise MC tools to reproduce their radial and energy distributions. The measured rates, $(0.22 \pm 0.04_{\text{stat}} \pm 0.01_{\text{syst}})$ cpd/100 t above 3 MeV and $(0.31 \pm 0.04_{\text{stat}} \pm 0.01_{\text{syst}})$ cpd/100 t above 2 MeV, are compatible with the expectation based on the Standard Solar Model plus MSW-LMA oscillation solution.

Borexino and Double Chooz experiments use liquid scintillator detectors, affected by cosmogenic contaminations from underground surviving muons. Many MC codes have been developed to describe muon interactions and subsequent hadronic cascades and neutron or isotope productions. Simulations through Geant4 and FLUKA were performed. The comparison with the Borexino data showed two important results concerning muon beam with mean energy around 270 GeV. First, the neutron interactions are well reproduced by Geant4 and FLUKA. On the contrary, the hadronic shower development is underestimated, as proven by the disagreement with the cosmogenic isotope and neutron rates. Double Chooz data on cosmogenics rates will soon be available. They will allow MC/data comparison for a muon beam energy range of about 64 GeV.

Résumé

Une analyse des neutrinos solaires du ${}^8\text{B}$ de Borexino et la simulation Monte Carlo (MC) des produits de l'interaction des muons cosmiques en Borexino et Double Chooz sont présentées dans ce mémoire.

L'analyse des neutrinos solaires du ${}^8\text{B}$ de Borexino a été réalisée aux plus faibles seuils d'énergie jamais atteints: 3 MeV et 2 MeV. Le seuil 3 MeV a demandé l'étude et la mise en oeuvre de nouvelles techniques de rejection des isotopes cosmogéniques. Le seuil 2 MeV a demandé une étude approfondie du bruit de fond extérieur affectant le noyau de Borexino et la réalisation d'outils MC pour reproduire sa distribution spatiale et énergétique. Les fréquences mesurés, $(0.22 \pm 0.04_{\text{stat}} \pm 0.01_{\text{syst}}) \text{ cpd}/100 \text{ t}$ à 3 MeV et $(0.31 \pm 0.04_{\text{stat}} \pm 0.01_{\text{syst}}) \text{ cpd}/100 \text{ t}$ à 2 MeV, sont compatibles avec les prévisions du modèle solaire standard intégré par la solution des oscillations MSW-LMA.

Borexino et Double Chooz utilisent des scintillateurs liquides, sensibles à la contamination des muons survivant en sous-sol. Plusieurs codes MC ont été développés pour décrire les interactions des muons et les conséquentes cascades hadroniques et production de neutrons ou d'isotopes. La comparaison des simulations par Geant4 et FLUKA avec les résultats de Borexino pour des faisceaux de muons d'énergie autour de 270 GeV a montré que: (a) l'interaction des neutrons est bien reproduite, mais (b) la cascade d'hadrons est sous estimée comme le montrent les données concernant les fréquences des isotopes et des neutrons. La validation des simulations MC dans la bande d'énergie autour de 64 GeV sera possible dès que les données concernant les fréquences cosmogéniques en Double Chooz seront disponibles.

Contents

Abstract	3
Résumé	5
Introduction	11
1 The Neutrino Physics	15
1.1 The Standard Model in brief	15
1.1.1 The mass sector	17
1.1.2 Dirac Particles and Majorana Particles	18
1.2 Massive neutrinos beyond the Standard Model	19
1.2.1 Massive Dirac Neutrinos	19
1.2.2 Massive Majorana Neutrinos	20
1.2.3 The See-Saw mechanism	21
1.3 The neutrino sources	22
1.3.1 Relic neutrinos	22
1.3.2 Solar neutrinos	22
1.3.3 Geoneutrinos	23
1.3.4 Reactor neutrinos	24
1.3.5 Supernova neutrinos	24
1.3.6 Atmospheric neutrinos	25
1.3.7 Accelerator neutrinos	26
1.3.8 Galactic and extragalactic high energy neutrinos	27
1.4 Neutrino Oscillations	27
1.4.1 Neutrino oscillations in vacuum	27
1.4.2 Neutrino oscillations in matter	33
1.5 The experimental status	37
1.6 The open questions in the solar neutrino sector	39
1.6.1 Solar Neutrinos	39
1.6.2 Standard Solar Models	40
1.6.3 The pp chain	41
1.6.4 The CNO cycle	43
1.6.5 The Solar Abundance Problem	44
1.6.6 The mapping of the solar neutrino survival probability	46
1.6.7 Future solar neutrino experiments	50
1.7 Reactor neutrino experiments for θ_{13}	51
1.7.1 Double Chooz	55

1.7.2	Daya Bay	56
1.7.3	Reno	56
2	The Borexino Experiment	57
2.1	The Borexino force points	57
2.1.1	The location: I Laboratori Nazionali del Gran Sasso	58
2.1.2	Detection principle in Borexino	58
2.1.3	The extreme scintillator radiopurity	59
2.2	The Borexino detector	63
2.2.1	The Water Tank	63
2.2.2	The Stainless Steel Sphere	64
2.2.3	The Photomultipliers	65
2.2.4	The nylon vessels	67
2.2.5	The scintillator	68
2.2.6	Purification Plants	71
2.3	Background sources	73
2.3.1	The internal backgorunds	73
2.3.2	Muons and cosmogenics	73
2.3.3	The surface background	73
2.3.4	The buffer backgrounds	74
2.3.5	The external backgrounds	74
2.4	The electronics chain	74
2.4.1	Inner Detector DAQ system	74
2.4.2	Outer Detector DAQ system	76
2.4.3	Trigger formation	77
2.5	The data taking	77
2.6	Detector calibrations	78
2.6.1	The internal calibration campaigns	79
2.6.2	The external calibration campaign	81
3	Borexino Reconstruction and Simulation Codes	83
3.1	The Borexino data reconstruction code	83
3.1.1	Precalibration	83
3.1.2	The energy reconstruction	84
3.1.3	The position reconstruction	85
3.2	The Borexino simulation code	86
3.2.1	Detector description	87
3.2.2	Particle Generators	88
3.2.3	Tracking and Stepping	89
3.2.4	Simulation of the Optical Processes	90
3.3	Simulation of the Electronics	91
4	^8B Solar Neutrino Measurement above 3 MeV	93
4.1	Physical motivation	93
4.2	The energy and the radial cuts	94
4.2.1	Energy threshold determination	95
4.2.2	Fiducial volume definition	96

4.3	Background removal	97
4.3.1	Muon rejection	98
4.3.2	Cosmogenic background study and rejection	99
4.3.3	External background rejection	103
4.3.4	Internal intrinsic contamination rejection	103
4.4	^8B solar neutrino rate above 3 MeV	104
4.4.1	Evaluation of systematic errors	105
4.4.2	Results on ^8B solar neutrino rates	105
4.5	The ^8B solar neutrino flux and the P_{ee}	105
4.6	Conclusions	107
5	Study of External Background Sources above 2 MeV	109
5.1	Approaching the analysis	109
5.1.1	The energy threshold	110
5.1.2	The radial analysis technique	112
5.1.3	The external background simulator	115
5.2	Radial analysis above 5 MeV in the whole IV	117
5.2.1	Study of high energy contaminants from the buffer	118
5.2.2	Monte Carlo predictions of ^{208}Tl emanated by the vessel	119
5.2.3	Monte Carlo simulation of bulk components	120
5.2.4	Results for the energy region above 5 MeV	120
5.3	Radial analysis between 2 and 5 MeV in the whole IV	121
5.3.1	Monte Carlo predictions of γ 's rate from (α, n) reactions in the buffer	122
5.3.2	Monte Carlo predictions of buffer ^{208}Tl rate	123
5.3.3	Monte Carlo predictions of surface ^{208}Tl rate	123
5.3.4	Monte Carlo simulation of bulk components	123
5.3.5	Monte Carlo study of external ^{208}Tl and ^{214}Bi	124
5.4	Conclusions	128
6	^8B Solar Neutrino Measurement above 2 MeV	129
6.1	The expected backgrounds above 2 MeV in the Borexino Fiducial Volume	129
6.1.1	The energy threshold	130
6.1.2	The expected contaminants	130
6.2	The binned likelihood spectral fit above 2 MeV in the Fiducial Volume	132
6.2.1	Systematic errors for the spectral fit	133
6.2.2	Final result	136
6.3	The binned likelihood radial fit above 2 MeV in the Fiducial Volume	136
6.3.1	The external and surface component in the FV	136
6.3.2	The bulk component in the FV	137
6.3.3	Radial fit in the energy region above 780 nhits in the FV	137
6.4	The multivariate binned likelihood fit above 2 MeV in the Fiducial Volume	143
6.4.1	Systematic errors for the multivariate fit	145
6.5	What about NSI?	147
6.6	The flux and the survival probability above 2 MeV	149
6.7	Conclusions	149

7 Simulations of Muon Interaction Products in Borexino and Double Chooz	153
7.1 Cosmic muons	153
7.2 Neutron and isotope production by muon spallation	155
7.3 Muon and neutron detection in Borexino	156
7.4 The simulation codes: Geant4 and FLUKA	158
7.4.1 Something about Geant4	159
7.4.2 Something about FLUKA	161
7.4.3 Choice of the Hadronic Physics Lists	161
7.5 Cosmogenic neutron and isotope simulations in Borexino	165
7.5.1 The muon spectrum underground at LNGS	166
7.5.2 Simulation procedure	167
7.5.3 Geant4 and FLUKA simulation results and comparison with data .	170
7.6 Simulations of the CNGS muon beam in Borexino	177
7.7 Cosmogenic neutron and isotope simulations in Double Chooz	180
7.7.1 The muon spectrum underground at DC-Far site	182
7.7.2 Simulation procedure	182
7.7.3 Geant4 and FLUKA simulation results	183
7.8 Conclusions	188
Conclusions	191
Appendix A	195
Bibliography	207
Acknowledges	217

Introduction

Several important discoveries have been made in the field of Neutrino Physics in the past decades. However several important questions are still without answer. Some of them concern the nature of neutrinos (Are neutrinos Majorana or Dirac particles? Do sterile neutrinos exist?), some others the oscillation parameters (the value of θ_{13} , the possible CP violation in the lepton sector), some others neutrino interactions (Is neutrino propagation affected by Non Standard Interactions (NSI)?) and others on neutrino properties (absolute mass value). In addition the oscillation model MSW-LMA, the adopted at the moment, needs confirmations in several aspects.

During my Ph.D. I had the opportunity of studying neutrinos from the Sun (Borexino experiment) and of approaching another neutrino source: the nuclear reactor (Double Chooz experiment).

The evidence of neutrino flavor oscillations comes from several experiments on solar, atmospheric, reactor and accelerator neutrinos. This phenomenon describes the possibility that a neutrino born as ν_α ($\alpha=e, \mu, \tau$) could change its flavor during traveling. The importance of matter interaction effects in the phenomenon of the oscillations plays a crucial role in the case of solar neutrinos. Matter interaction effects can dramatically influence the pattern of neutrino oscillations in the Sun because the neutrino matter interaction cross-sections are flavor dependent and the matter distribution in the Sun contains only first generation particles. The Standard Solar Model (SSM) allows to describe the evolution of the Sun and to predict the produced neutrino fluxes. The oscillation theory in the SSM+(MSW-LMA) scenario, the widely accepted at the moment, predicts a peculiar behavior of electron neutrino survival probability as a function of neutrino energy. The high energy region ($>4\text{-}5$ MeV), so called *matter region*, has been explored by the solar neutrino experiment SNO and SuperKamiokande. The Borexino experiment has been designed to perform a real time measurement of the low energy component of the solar neutrino flux with few percent precision: through the measurement of ${}^7\text{Be}$ neutrino flux (0.86 MeV), Borexino first investigated the low energy oscillation region (so called *vacuum region*). The ${}^7\text{Be}$ neutrinos detection also represents a confirmation of the SSM: before Borexino only 10^{-4} of the total solar neutrino flux had been measured in real time.

This was the Status of the Art in 2009, when I started my Ph.D.. In particular, the energy region between 1 and 4 MeV represented an unexplored ground where the ultimate validation of MSW-LMA solution or the evidence for NSI can be present. In this Thesis, I will show the relevance of my work in improving our knowledge of the solar neutrino survival probability.

The T2K experiment has recently claimed (June 15th 2011) that "the probability of the existence of electron neutrino appearance is estimated to be 99.3%, suggesting the appearance of electron neutrinos for the first time"; this means that the neutrino mixing angle θ_{13} is not zero, at 99.3% of confidence level. Long (appearance) and short (disap-

pearance) baseline experiments are being dedicated to the fundamental measurement of the non vanishing value of θ_{13} . The Double Chooz experiment was born with this aim. Double Chooz is a reactor anti-neutrino disappearance experiment. The measurement will be based on the comparison of neutrino rate and spectrum in two identical detectors at different distances from the reactor cores, allowing for a reduction of the systematic error below one percent. The far detector has recently started taking data (April 2011) and just showed the first results (November 2011); the near one is already under construction.

During my Ph.D. activity I have had the chance of working for the two challenging experiments, Borexino, measuring solar neutrinos and Double Chooz, measuring reactor antineutrinos. This has been possible thanks to the IDAPP (International Doctorate in AstroParticle Physics) program: as IDAPP student I performed my thesis work in co-tutorship between the Universitá di Milano and the Université Paris Diderot (Paris 7). For the Borexino side, I deeply participated to (and in some cases, I performed alone) the measurement of the ^8B solar neutrino flux, to the development of the Monte Carlo (MC) simulation program (Geant4) for the study of the background components and to the simulation of muon interaction products, through FLUKA and Geant4. For Double Chooz I performed a simulation study of the cosmogenics production, again comparing results from FLUKA and Geant4.

The first part of my work was devoted to the ^8B neutrino analysis. The expected rate in the Borexino Fiducial Volume (FV, a sphere of 3 m radius) is about 0.5 counts per day (cpd), based on the Standard Solar Model and the oscillation solution MSW-LMA. At that time, we decided to set the energy threshold at 3 MeV, in order to reject the external background contamination, consisting basically in the 2.61 MeV gammas from ^{208}Tl coming from the Stainless Steel Sphere (SSS, sphere of 6.5 m radius supporting the photomultipliers). The main contaminants surviving above 3 MeV are cosmogenic isotopes. They are produced via cosmic muon spallation on the ^{12}C nuclei composing the scintillator. We developed different analysis techniques based on the coincidence with the parent muon, allowing to individuate and reject with high efficiency all the cosmogenic background. The Borexino measurement of ^8B neutrino above 3 MeV has been published in ???. It is in agreement with the prediction based on the SSM+(MSW-LMA), rejecting the non-oscillation hypothesis at 4σ level. We performed another analysis above 5 MeV to be compared with results of other real time experiments (SuperKamiokande and SNO): results are in agreement within the errors. Considering the already published ^7Be neutrino measurement performer by Borexino, we demonstrated that Borexino is the only real time solar neutrino experiment able to simultaneously detect solar neutrinos in two different oscillation regimes.

It is clear that the oscillation energy region between 1 and 3 MeV is still unexplored. With the aim of decreasing the energy threshold down to 2 MeV, I started a deep study of all the background sources above 2 MeV, in particular between 2 and 3 MeV, an energy region not yet investigated for the Borexino analyses. The main background contribution comes from the PMTs, contaminated by ^{238}U and ^{232}Th . In particular the 2.61 MeV γ 's from ^{208}Tl decay can reach the Borexino FV. The knowledge of the radial and energy distribution is needed not only for ^8B neutrino analysis, but also for the ^7Be and the recent pep ones. Two ways have been taken for this goal: the calibration campaign with external source and the Monte Carlo simulations of external contaminants. I have been designed for this

second task. Considering the attenuation length of about 23 cm and the required amount of simulated events in the FV of about 200 cpd, I had to simulate about 10^{12} events. I developed some methods allowing to speed up the simulations, taking into account the changing of the detector configuration in time (number of dead PMTs, Inner Vessel deformation,...). Results are very satisfactory: the comparison between the reconstructed simulation events and the external calibration data are in excellent agreement, showing a discrepancy in the distributions less than 0.6%.

The deep MC study of the external background surviving within 3 m made possible the measurement of ^8B solar neutrino above 2 MeV. This challenge is particularly stimulating because it allows approaching the unexplored oscillation region between 1 and 3 MeV. My curiosity on this task has been immediately activated and I have been pursuing this aim almost alone.

Given the presence of the unavoidable external background, a new analysis approach is necessary. The penetrating external background can be distinguished from the internal events through an energy or a radial analysis. Combining the informations, I performed a two-dimensional fit: the rate result from the multivariate fit is accurate at level of 15% and is in agreement with the prediction based on the SSM+(MSW-LMA). In particular, a new point, involving the transition region, has been added in the mapping of the Pee. The ^8B measurement above 2 MeV from Borexino, added to the recent pep one, shows the feasibility of precise measurements, with liquid scintillator detector, of solar neutrino sources in the transition oscillation region.

During the five months of co-tutorship at APC Laboratories (Paris), I had the opportunity of being involved in another neutrino experiment: Double Chooz. Like Borexino, Double Chooz is an underground liquid scintillator detector. Liquid scintillators are affected by the cosmogenic contaminations: muons surviving underground can interact with ^{12}C nuclei, producing neutrons and unstable isotopes. This kind of background is particularly dangerous for experiments looking for rare events. Many Monte Carlo codes have been developed to describe muon interactions and subsequent hadronic cascades and neutron or isotope productions. The simulation must be accompanied by validation of the codes through experimental data and by comparison between different packages. This has been my task. I performed the simulations through Geant4 and FLUKA for Borexino and Double Chooz. In Borexino, the cosmogenic isotope rates have been measured for the ^8B analysis; recently we also quoted the neutron capture rates. So, I could compare the simulation results with data, stressing the imprecisions of the Monte Carlo codes. In Double Chooz, the measurement of the neutron capture rate will be soon available for a comparison. For the moment I could provide the expected rates to the DC collaboration. From the conclusions of this study it is clear that the neutron interactions are well reproduced by Geant4 and FLUKA; on the contrary, done the discrepancy Monte Carlo/data on the rate values, a problem is present at level of the muon interactions, or in other words, of the description of the hadronic shower development.

In the present Thesis, I report the results of my work. Starting with the status of Neutrino Physics (Chapter 1) and continuing with a deep description of the Borexino Experiment (Chapters 2 and 3) I will enter in the core of the Thesis. I will first report the measurement of ^8B solar neutrino above 3 MeV (Chapter 4). Then I will describe the effort for the study of the external background falling in the energy region between 2 and

3 MeV (Chapter 5), making thus possible the measurement of ^8B solar neutrino above 2 MeV (Chapter 6). Last Chapter is dedicated to the work I did in parallel for Borexino and Double Chooz: the validation of Geant4 and FLUKA codes for the muon interaction products.

Chapter 1

The Neutrino Physics

When in 2008 I chose solar neutrinos as subject for my Ph.D. Thesis, I was pull on by the curiosity of the "mystery to solve". And Neutrinos Physics presents many interesting points in this sense: it is opening many questions, which answers can belong to very different Physics Scenarios. Neutrino experiments recently discovered something new, as the possibility of sterile neutrinos or non standard interaction, maybe related to New Physics. It is clear that the scientific investigation on this field is a "hot matter" at the moment, also because understanding neutrino propagation could provide informations to astrophysics, cosmology and geology studies.

In this first Chapter I will show the actual status of Neutrino Research and I will focus on the main open questions about Low Energy Neutrino Physics.

1.1 The Standard Model in brief

Before starting the description of neutrinos it is necessary to remind the Physics framework in which we are working: the Standard Model (SM). The SM is a quantum field theory describing the strong and the electroweak interactions of elementary particles. It is founded on a set of quantum fields that correspond to the elementary particles, which number and properties are determined by experiments.

The quantum fields are requested to respect a well defined set of local gauge symmetries, described by the local symmetry group at the basis of the Standard Model, $SU(3)_C \times SU(2)_L \times U(1)_Y$, where:

- $SU(3)_C$ is the group underlying the Quantum Chromodynamics (QCD), namely the theory of strong interactions;
- $SU(2)_L \times U(1)_Y$ is the group Quantum Electrodynamics (QED), the theory of electroweak interactions.

As $SU(3)_C$ and $SU(2)_L \times U(1)_Y$ do not mix with each other, the strong and electroweak interactions can be treated separately.

In Table 1.1 the list of fermions entering the Standard Model is reported. These fermions have been selected heuristically on the basis of the experimental observations. Since the SM is a chiral theory, the right-handed and left-handed fields are distinguished from one another, as shown in the Table. The most general Lagrangian of the Standard Model

Quantum Field	SU(3) _C	SU(2) _L	U(1) _Y
$Q_L^i = \begin{pmatrix} u_L \\ d_L \end{pmatrix}, \begin{pmatrix} c_L \\ s_L \end{pmatrix}, \begin{pmatrix} t_L \\ b_L \end{pmatrix}$	3	2	1/6
$u_R^i = u_R, c_R, t_R$	3	1	2/3
$d_R^i = d_R, s_R, b_R$	3	1	-1/3
$L_L^i = \begin{pmatrix} \nu_{eL} \\ e_L \end{pmatrix}, \begin{pmatrix} \nu_{\mu L} \\ \mu_L \end{pmatrix}, \begin{pmatrix} \nu_{\tau L} \\ \tau_L \end{pmatrix}$	1	2	-1/2
$e_R^i = e_R, \mu_R, \tau_R$	3	1	-1
$\phi = \begin{pmatrix} \nu_{eL} \\ e_L \end{pmatrix}$	1	2	1/2

Table 1.1: List of quantum fields of the Standard Model. Quantum numbers relative to the gauge symmetries are indicated.

based on the fields listed in Table 1.1 and on the local symmetry groups is:

$$\begin{aligned} \mathcal{L} = & -\frac{1}{4}F^{\mu\nu}F_{\mu\nu} - \frac{1}{4}G^{A\mu\nu}G^A_{\mu\nu} - \frac{1}{4}W^A{}^{\mu\nu}W^A_{\mu\nu} \\ & + i\bar{Q}_L^i D Q_L^i + i\bar{u}_R^i D u_R^i + i\bar{d}_R^i D d_R^i + i\bar{L}_L^i D L_L^i + i\bar{e}_R^i D e_R^i \\ & - \Gamma_u^{ij}\bar{Q}_L^i \epsilon \phi^* u_R^j - \Gamma_d^{ij}\bar{Q}_L^i \phi d_R^j - \Gamma_e^{ij}\bar{L}_L^i \phi e_R^j + h.c. \\ & + (D^\mu \phi)^\dagger D_\mu \phi + \mu^2 \phi^\dagger \phi - \lambda (\phi^\dagger \phi)^2 \end{aligned} \quad (1.1)$$

This is the Lagrangian of the Standard Model. In the definition of the Lagrangian, an important constraint is about dimension. Since the action S , related to the Lagrangian by

$$S = \int d^4x \mathcal{L}, \quad (1.2)$$

must be dimensionless, the \mathcal{L} must have dimension 4. If dimension $d > 4$ terms are added in the Lagrangian, they have to be proportional to the factor $\frac{1}{M^{d-4}}$, where M is a parameter with the dimension of a mass (dimension 1).¹ Among the terms with dimension higher than 4, the dimension 5 term plays a central role in the so called *see-saw* mechanism, which is an extension of the Standard Model that aims at introducing in the Lagrangian a mass term for neutrinos (see Section 1.2).

Coming back to the Eq. 1.1, the different lines represent:

1. the first line contains the kinetic terms of the gauge bosons;
2. the second line shows the kinetic terms of the fermionic fields;
3. the third describes the Yukawa interactions;
4. the last line refers to the Higgs field.

¹Actually, dimension > 4 terms are not renormalizable, but this is not considered a valid argument not to add them to the Standard Model Lagrangian. The reason why they are not included in the Lagrangian is that they are negligible, suppressed by the very small multiplicative factor $\frac{1}{M^{d-4}}$.

It is noteworthy that the Lagrangian of the Standard Model fulfills a relevant conservation law: the barion number B and the lepton number L are conserved. This conservation is not imposed, but it comes out as a natural consequence. According to the Noether's theorem, this conservation law is related to a symmetry of the Lagrangian: it is an *accidental* global symmetry corresponding to the invariance under rotation of the quark and lepton fields.

1.1.1 The mass sector

The mass sector of the SM Lagrangian is:

$$\begin{aligned}\mathcal{L}_M &= -M_u^{ij} \bar{u}_L^i u_R^j - M_d^{ij} \bar{d}_L^i d_R^j - M_e^{ij} \bar{e}_L^i e_R^j + \text{h.c.} \\ &+ M_W W_\mu^\dagger W^\mu + \frac{1}{2} M_Z Z_\mu Z^\mu - \frac{1}{2} m_h^2 h^2 \dots\end{aligned}\quad (1.3)$$

where the fermion terms appear in the first line, while the terms referring to the gauge bosons and to the Higgs field appear in the second line.

All the fermion masses in the first line are given by:

$$M_{\text{fermion}}^{ij} = \frac{v}{\sqrt{2}} \Gamma^{ij} \quad (1.4)$$

where Γ^{ij} is the Yukawa coupling of the fermion fields with the Higgs field, while:

$$\langle \phi^0 \rangle = \frac{v}{\sqrt{2}} = 246 \text{ GeV} \quad (1.5)$$

is the Vacuum Expectation Value of the Higgs field. Since the Yukawa couplings are unpredicted by the Standard Model, the fermion masses must be determined by experiments. The proportionality between the fermion masses and the vacuum expectation value is a crucial point as it fixes the order of magnitude of the masses and represents the explanation of the smallness of the fermion masses with respect to M_{Planck} and M_{GUT} .

In general, the matrix Γ in Eq. 1.4 is non-diagonal. This means that the fermion fields in the mass sector of the Lagrangian don't have a definite mass. In order to find the mass eigenstates, the mass matrix diagonalization is necessary. It must be carried out separately for quarks and leptons, as they are independent of each other. The procedure is exactly the same in the two cases, nevertheless for quarks it is straightforward while, for the lepton sector, neutrino masses must be introduced first.

The quark masses

Concerning quarks, the diagonal mass matrix is obtained through a redefinition of the fermion fields:

$$\Psi_{L/R}^i \rightarrow (A_\Psi)_j^i \Psi_{L/R}^j \quad (1.6)$$

Here, Ψ stands for both $u^i = \{u, c, t\}$ and $d^i = \{d, s, b\}$, while the matrix A is a 3×3 unitary matrix. The new fields resulting from the transformation in Eq. 1.6 describe the definite quark masses. Because of the field redefinition, the mass matrix becomes:

$$M_\Psi^{\text{diag}} = A_{\Psi_L}^\dagger M_\Psi A_{\Psi_R} i \quad (1.7)$$

The redefinition of the quark fields leads to the introduction of a new charged current interaction term, that is:

$$\mathcal{L}_{CC} = -i \frac{g}{2\sqrt{2}} \bar{u}^i V_{ij} \gamma^\mu (1 - \gamma_5) d^j W_\mu. \quad (1.8)$$

It depends on the matrix V , given by the product:

$$V_{ij} = A_{u_L}^\dagger A_{d_L}. \quad (1.9)$$

The matrix V is the famous Cabibbo-Kobayashi-Maskawa (CKM) matrix, which completely describes the effects of quark mixing.

$$V = \begin{pmatrix} c_{12}c_{13} & s_{12}c_{13} & s_{13}e^{-i\delta} \\ -s_{12}c_{23} - c_{12}c_{23}s_{13}e^{i\delta} & c_{12}c_{23} - s_{12}s_{23}s_{13}e^{i\delta} & s_{23}c_{13} \\ s_{12}s_{23} - c_{12}c_{23}s_{13}e^{i\delta} & -c_{12}s_{23} - s_{12}c_{23}s_{13}e^{i\delta} & c_{23}c_{13} \end{pmatrix} \quad (1.10)$$

where $s_{ij} = \sin \theta_{ij}$ and $c_{ij} = \cos \theta_{ij}$. From Eq. 1.10 it is clear that the CKM matrix is parametrized by three angles (θ_{12} , θ_{23} and θ_{13}), which describe the quark mixing, and a phase (δ), that accounts for a possible CP violation.

Massless Neutrinos in the SM

Positive helicity neutrinos, related to right-handed fields, have never been experimentally observed. For this reason they are not included in the SM; in other words, the right-handed neutrinos *do not exist* in the Standard Model, that has been developed under this assumption.

Considering the Eq. 1.3, it is evident that the mass term for a Dirac particle has the form:

$$\mathcal{L}_{M_\Psi} = m_D \bar{\Psi}_L \Psi_R + h.c. \quad (1.11)$$

Since in the original SM ν_R don't exist, neutrinos are massless. To introduce a Dirac mass term for neutrinos, the introduction of ν_R is required. In addition, as mentioned in Section 1.5, the observation of solar, atmospheric and reactor neutrinos indicates that the phenomenon of the neutrino flavor oscillation occurs (see Section 1.4). This means that neutrinos have a non-zero mass.

The subject of neutrino mass is tightly bound to the nature of neutrinos, in particular if they are Majorana or Dirac particles; this is one of the still open questions about neutrinos.

1.1.2 Dirac Particles and Majorana Particles

As already mentioned, the experimental results of the last decades impose that neutrino have a nonzero mass. For this reason, the absence of positive helicity neutrinos must vanish. In fact, massless particles move at speed of light, contrarily to massive particles. Then, a massless neutrino has the same helicity in every frame of reference, while for a massive neutrino a frame of reference in which the helicity has the opposite sign can be found. So, the helicity of a massive neutrino depends on the frame of reference².

²It can be shown that production of positive helicity neutrinos is physically allowed indeed, but it is suppressed by a factor $\frac{m_i}{E}$.

Done to the nature of neutrinos, an other aspect must be taken into account: the difference between Majorana and Dirac particles. In the case of Dirac particles, particle and antiparticle differ from each other, while in the case of Majorana particle they coincide. In the Dirac particle scenario, four states are possible: a negative helicity neutrino, a positive helicity neutrino, a negative helicity antineutrino and a positive helicity antineutrino. Instead, in the Majorana particle scenario, only two states are possible as neutrino coincides with its own antiparticle: positive helicity and negative helicity neutrinos. Since neutrino is a neutral particle, the two scenarios are possible: it could be a Dirac or a Majorana particle. And, as already mentioned, this represents one of the still open questions about neutrinos.

1.2 Massive neutrinos beyond the Standard Model

The problem of introducing a mass term for neutrinos in the Lagrangian of the Standard Model can be solved in different ways. Even if it is possible to develop solutions that introduce either a Dirac or a Majorana mass term separately, the most satisfactory model available, called the **see-saw** model, plans to include both terms, as described in Sec. 1.2.3.

1.2.1 Massive Dirac Neutrinos

The simplest solution consists in introducing the fields $\nu_R^i = \nu_R^e, \nu_R^\mu, \nu_R^\tau$, allowing the addition of a Dirac mass term in the Lagrangian. The properties of the right-handed neutrino fields are determined on the basis of the experimental observations. As they have never been detected, they have to be insensitive to the electro-weak interactions; that means they must be singlets under all the Standard Model symmetries: they must be sterile neutrinos.

In this framework, neutrino masses are described by a term like the one in Eq. 1.11:

$$L_{m_\nu} = -M_\nu \bar{\nu}_L \nu_R + \text{h.c.} \quad (1.12)$$

Also in this case, the mass is proportional to the Higgs vacuum expectation value. The introduction of the neutrino mass term allows to diagonalize also the mass matrix in the leptonic sector. The procedure is exactly the same as in the quark sector. First, a redefinition of the lepton fields:

$$e_{L/R}^i \rightarrow \left(A_{e_{L/R}} \right)_j^i e_{L/R}^j, \quad (1.13)$$

$$\nu_{L/R}^i \rightarrow \left(A_{\nu_{L/R}} \right)_j^i \nu_{L/R}^j. \quad (1.14)$$

Second, the re-writing of the mass term $-M_{D_\nu} \bar{\nu}_L \nu_R$, with $M_{D_\nu} = A_\nu^\dagger M_\nu A_\nu$. The only difference is that the CKM matrix is replaced with the Pontecorvo-Maki-Nakagawa-Sakata (PMNS) matrix. However, the two matrices have exactly the same form (Eq. 1.10) and the same parametrization, consisting in three mixing angles, θ_{12}, θ_{23} and θ_{13} , and a Dirac phase, δ , that accounts for a possible CP violation. Different are, instead, the parameter values.

Also in this case, the diagonalization of the mass terms leads to the introduction of a new

charged current interaction term, that is:

$$\mathcal{L}_{CC} = -i \frac{g}{2\sqrt{2}} \bar{\nu}^i U_{\alpha i}^* \gamma^\mu (1 - \gamma_5) l^\alpha W_\mu \quad (1.15)$$

where $i = 1, 2, 3$, $\alpha = e, \mu, \tau$ and the matrix $U = A^\dagger A$ is the PMNS matrix.

As for the quark sector, the fields ν_α ($\alpha = e, \mu, \tau$), namely the ones that appear in the interaction terms, do not have a definite mass as the corresponding mass matrix is non-diagonal. The definite mass fields are the fields ν_i ($i = 1, 2, 3$), linked to ν_α by the field redefinition in Eq. 1.14.

This approach leads to add a Dirac mass term for neutrinos at the Lagrangian of the Standard Model in a very straightforward way. The new terms that arise from the introduction of the right-handed neutrino fields still preserve the conservation of the lepton number. On the other hand, the flavor lepton number is not conserved and this leads to neutrino oscillations (see Section 1.4). Nevertheless, this is an unsatisfactory approach as the neutrino masses have exactly the same features of the other lepton masses and there is no explanation of why the neutrino masses are so much smaller than the other lepton masses.

1.2.2 Massive Majorana Neutrinos

A deeply different approach consists in the introduction of a dimension 5 operator in the Lagrangian of the Standard Model:

$$\mathcal{L}_{SM+d5} = \mathcal{L}_{SM} + \frac{c^{ij}}{M} (L_L^{iT} \epsilon \phi) C (\phi^T \epsilon L_L^j) + h.c. \quad (1.16)$$

As explained in Section 1.1, the dimension 5 operator must be proportional to a $\frac{1}{M}$ factor in order to be homogeneous with \mathcal{L}_{SM} .

The neutrino mass term resulting from the dimension 5 term is:

$$\mathcal{L}_{M_\nu} = \frac{1}{2} M_\nu^{ij} \nu_L^{iT} C \nu_L^j \quad (1.17)$$

representing a Majorana mass term.

The Majorana mass is related to the Higgs vacuum expectation value by the relation:

$$M_\nu^{ij} = \frac{v^2}{M} c^{ij} \quad (1.18)$$

i.e. it is proportional to v^2 instead of v , and it is inversely proportional to the parameter M . Therefore, if $v \ll M$, M_ν is very tiny with respect to the other lepton masses. In particular, the neutrino mass is the tinier the higher the parameter M is. This can be a good explanation of the difference between the neutrino masses and the lepton masses. It must be noted that the Majorana mass term in Eq. 1.17 violates the conservation of the lepton number. This is not a compromising effect, as the conservation of lepton number is not requested *a priori* in the Standard Model, but is an accidental consequence.

The mass sector of the Lagrangian of the Standard Model plus the dimension 5 operator is:

$$\mathcal{L}_{\text{SM+d5 mass}} = \mathcal{L}_M + \frac{1}{2} M^{ij} \nu_L^{iT} C \nu_L^j \quad (1.19)$$

where \mathcal{L}_M is given by Eq. 1.3. As done for the Dirac neutrino case, the diagonalization of the mass matrix is performed through a redefinition of the lepton fields. Also in this case, a charged current interaction term equal to the one in Eq. 1.15 is introduced.

The only difference with respect to the Dirac case resides in the parametrization of the PMNS matrix. While in the Dirac neutrino case the PMNS matrix contains 4 parameters, in the Majorana neutrino case there are two more CP violating phases, α_1 and α_2 , called **Majorana phases**. They originate from the fact that a Majorana neutrino field is not invariant under phase redefinition, due to the constraint $\nu_i = \nu_i^C$. Nevertheless, the phases can be factorized and the PMSN matrix assumes the following aspect:

$$U = U_D \times \text{diag}(e^{i\alpha_1/2}, e^{i\alpha_2/2}, 1) \quad (1.20)$$

where U_D is the PMNS matrix of the Dirac scenario (Eq. 1.10). Summarizing, the parametrization of the PMNS matrix in the Majorana case consists six parameters instead of four: three mixing angles, the Dirac phase and the two Majorana phases.

1.2.3 The See-Saw mechanism

The most appreciated model allowing the introduction of neutrino masses into the Standard Model is the *see-saw* mechanism [1]. In particular, it provides an exhaustive explanation of why neutrino masses are orders of magnitude lighter with respect to the ones of the other leptons.

The model is developed in accordance to the principle that every operation that is not strictly forbidden is done. Therefore, the right-handed neutrino field, ν_R , is introduced provided with a Majorana mass. As the introduction of ν_R entails to add a new Yukawa interaction term, the Lagrangian becomes:

$$\mathcal{L} = \mathcal{L}_{\text{SM}} - \Gamma_v^{ij} \bar{L}_L^i \epsilon \phi^* \nu_R^j - \frac{1}{2} M_R^{ij} \nu_R^{iT} C \nu_R^j + \text{h.c.} \quad (1.21)$$

where M_R is the Majorana mass of the right handed neutrino, a non-zero parameter whose value is undetermined. The Yukawa term describes the interaction between a left-handed lepton field, L_L , and the Higgs field, mediated by a right-handed neutrino, with the interaction radius being inversely proportional to the neutrino mass, M_R . In the assumption of a super-heavy right-handed neutrino ($M_R \gg v$), the Yukawa interaction can be approximated with a point-like interaction, whose description is given by a dimension 5 operator (Eq. 1.16):

$$\Gamma_v^{ij} \bar{L}_L^i \epsilon \phi^* \nu_R^j \xrightarrow{M_R \gg v} \frac{c^{ij}}{M} (L_L^{iT} \epsilon \phi) C (\phi^T \epsilon L_L^j) \quad (1.22)$$

where:

$$\frac{c^{ij}}{M} = \frac{(\Gamma^{ij})^2}{M_R}. \quad (1.23)$$

As described in the previous section, the dimension 5 term gives a Majorana mass term for the left-handed neutrino. In accordance with Eq. 1.18 and Eq. 1.23, the resulting left-handed neutrino mass is:

$$M_L^{ij} = \frac{v}{M_R} (\Gamma^{ij})^2. \quad (1.24)$$

This means that M_L is inversely proportional to M_R .

This is the fundamental aspect of the see-saw mechanism, as the left-handed field mass is the lighter the heavier the right-hand field is. Then, a super-heavy right-handed field can explain why the neutrino masses are in the sub-eV range.

With this example I can conclude the description of neutrinos in and beyond the Standard Model and start a new section about an other aspect of Neutrino Physics: the neutrino flavor oscillation. Before this it is interesting to know the origin of neutrinos.

1.3 The neutrino sources

An overview of the neutrino (and antineutrino) sources is following. For all the sources, the production mechanism is based on the same physics, namely the weak interactions mediated by the exchange of the W and Z bosons. The only difference in the several cases is the energy available in the process. It follows that the different sources produce neutrinos distributed over a wide energy range. In order of growing energy, there are: relic neutrinos (meV), solar neutrinos (hundreds keV - MeV), geoneutrinos (MeV), reactor neutrinos (MeV), Supernova neutrinos (MeV), atmospheric neutrinos (GeV), accelerator neutrinos (GeV), neutrinos from extra-galactic sources (\gg TeV).

1.3.1 Relic neutrinos

The existence of the Cosmic Microwave Background radiation and Primordial Nucleosynthesis lead to infer about the existence of a primordial background of neutrinos. The Cosmic Neutrino Background originated in the same way as the CMB, less than 1 s after the Big Bang: as the Universe expanded and cooled down, neutrinos passed from being in thermal equilibrium with electrons to decoupling from them. Decoupling happened when the expansion rate of the Universe and the annihilation rate were equivalent, namely at a temperature of about 2.4 MeV for ν_e and about 3.7 MeV for $\nu_{\mu/\tau}$.

Temperature and density of relic neutrinos are calculated from the CMB properties: CMB temperature is 1.9 K, corresponding to an energy of about 0.17 meV, while density is about 110 v's/cm^3 . Detection of relic neutrinos has not yet been accomplished: even if cosmological neutrinos are by far the most abundant in the Universe, their observation is hard due to their extremely low energy. Actually, the detection hypothesis has not yet been validated by experimental measurements.

1.3.2 Solar neutrinos

Another important source of neutrinos are the stars. The series of nuclear reactions that take place in the stellar core, determining the luminosity of the star and balancing gravity, involve beta decays and weak reactions that produces several neutrinos. The best known star is the Sun, playing a crucial role in the development of stellar models.

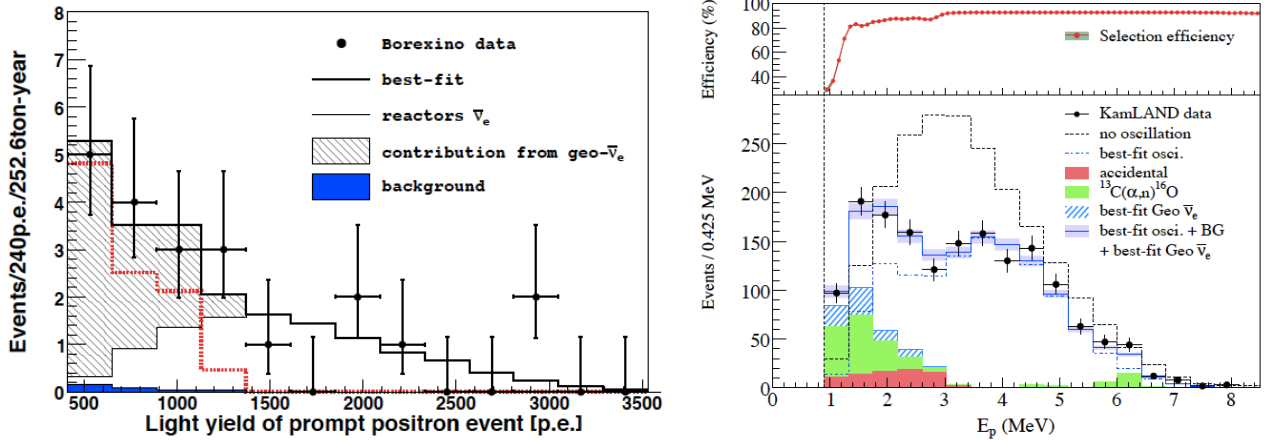


Figure 1.1: *Left:* Light yield spectrum for the positron prompt events of the 21 $\bar{\nu}_e$ candidates in Borexino [14] and the best-fit (solid thick line). The horizontal axis shows the number of p.e. detected by the PMTs. The small filled area on the lower left part of the spectrum is the background. Thin solid line: reactor- $\bar{\nu}_e$ signal from the fit. Dotted line (red): geo- $\bar{\nu}_e$ signal resulting from the fit. The darker area isolates the contribution of the geo- $\bar{\nu}_e$ in the total signal. *Right:* Prompt event energy spectrum of $\bar{\nu}_e$ candidate events in KamLAND [15]. All histograms corresponding to reactor spectra and expected backgrounds incorporate the energy-dependent selection efficiency (top panel). The shaded background and geo-neutrino histograms are cumulative. Statistical uncertainties are shown for the data; the band on the blue histogram indicates the event rate systematic uncertainty.

Done the relevance of solar neutrinos for the present thesis work, I will dedicate a deep description to them in Section 1.6.

1.3.3 Geoneutrinos

A fraction of the Earth's heat is expected to be due to radioactivity. Radioactive isotopes undergoing beta decay are sources of electron antineutrinos. Unstable isotopes naturally present in the Earth's interior are responsible for the production of the so called geo-neutrinos. The study of this neutrino source is fundamental to develop the Earth's model³. Geoneutrino stem from the beta decay of ^{40}K and of isotopes of the ^{238}U and ^{232}Th decay chains. Measurement of the geo-neutrino flux can contribute to define the Earth's model, as nuclear reactions are expected to be responsible for an unknown fraction, at least 40%, of the terrestrial heat. Measurements of the ^{238}U and ^{232}Th abundances could help in fixing this fraction.

Antineutrinos are detected in liquid scintillator through the inverse beta decay $\bar{\nu}_e + p \rightarrow n + e^+$, reaction that put a lower threshold on the neutrino energy at 1.806 MeV. The geoneutrino spectrum ranges up to ~ 2.6 MeV, but the ^{40}K component cannot be detected because it falls under the 1.806 MeV threshold of the inverse beta decay. Observation of geo-neutrinos has been realized by KamLAND (at 2.5σ C.L. [12]⁴) and by Borexino

³ Current uncertainty on the measurement of geoneutrino flux restrains from any conclusions on the Earth's model.

⁴ An update of the result is done in [13].

(at 4.2σ C.L. [14]). In particular, the observation in Borexino has been done with a signal to background ratio of 50:1 due to the extreme radiopurity of the detector (see left panel of Figure 1.1). The number of observed geo-neutrino events, $N_{\text{geo}} = 9.9^{+4.1}_{-3.4} ({}^{+14.6}_{-8.2})$ at 68.3% C.L. (99.73% C.L.), allows to exclude the hypothesis of $N_{\text{geo}} = 0$ at 99.997% C.L. Measurement has been compared with expectation from different models, but the current uncertainty does not allow to draw conclusions. With a 5 year exposure, Borexino will provide a measurement of the total geoneutrino flux with an accuracy of 20%.

Only future very large mass experiments, as SNO+ (see Section 1.6.7) or the proposed 50 kton LENA (see Section 1.6.7), could measure the ${}^{238}\text{U}/{}^{232}\text{Th}$ ratio with an uncertainty of the order of few percent.

1.3.4 Reactor neutrinos

Beta decay of unstable isotopes is massively exploited in nuclear reactors. This antineutrino source is detected to measure the last unmeasured mixing angle, θ_{13} (see Section 1.7). In nuclear reactors, the main used fuels are ${}^{235}\text{U}$, ${}^{238}\text{U}$, ${}^{239}\text{Pu}$ and ${}^{241}\text{Pu}$. The produced neutrino flux covers the energy range between 1 MeV and 10 MeV, the largest part ($\sim 75\%$) being under the 1.8 MeV threshold. An estimation of the antineutrino flux can be done considering that, on average, every fission cycle produces about 200 MeV and 6 neutrinos. Hence, 1 GW thermal power corresponds to $\sim 2 \times 10^{20} \bar{\nu}_e/\text{s}$.⁵ Nevertheless, the flux is isotropic and it rapidly decreases with the distance from the reactor. A partial compensation comes from the fact that the low neutrino energy implies a short oscillation length, of the order of few kilometers. On the other hand, such a low energy allows to perform only disappearance experiments, as muons or taus cannot be generated at the detector (see right panel of Figure 1.1).

A precise calculation of the expected flux is complicated. Therefore, the upcoming reactor experiments (see Section 1.7) will adopt the two detectors configuration, that is the simultaneous use of a near detector (hundreds of meters far from the reactor), which measures the unoscillated flux, and a far detector (about 1 km far), to perform the real oscillation measure. This configuration reduces the systematics tied to the flux and to the detector response.

1.3.5 Supernova neutrinos

Supernovae are stellar collapses that happen when nuclear reactions become insufficient to balance gravity. They are very unique processes in the Universe, as extremely particular conditions are realized: the core collapse proceeds until the matter density becomes of the order of $10^{11}\text{-}10^{15} \text{ g/cm}^3$, that is the density of nuclear matter, and temperature reaches values between 1 and 50 MeV. Explosion occur in a very narrow time window: in about 10 seconds, an energy of the order of 10^{53} erg is released, 99% of which is emitted as 10-20 MeV neutrinos and the remaining 1% is emitted as photons.

Observation of Supernova neutrinos is fundamental to shed light on the process of stellar explosion. Moreover, it would be very significant to test what is the impact of such high matter density on neutrino flavor oscillation. Neutrinos emitted by the Supernova

⁵The huge neutrino flux has been exploited by the pioneers Cowan and Reines to perform the very first observation of neutrinos at the Savannah River power plant.

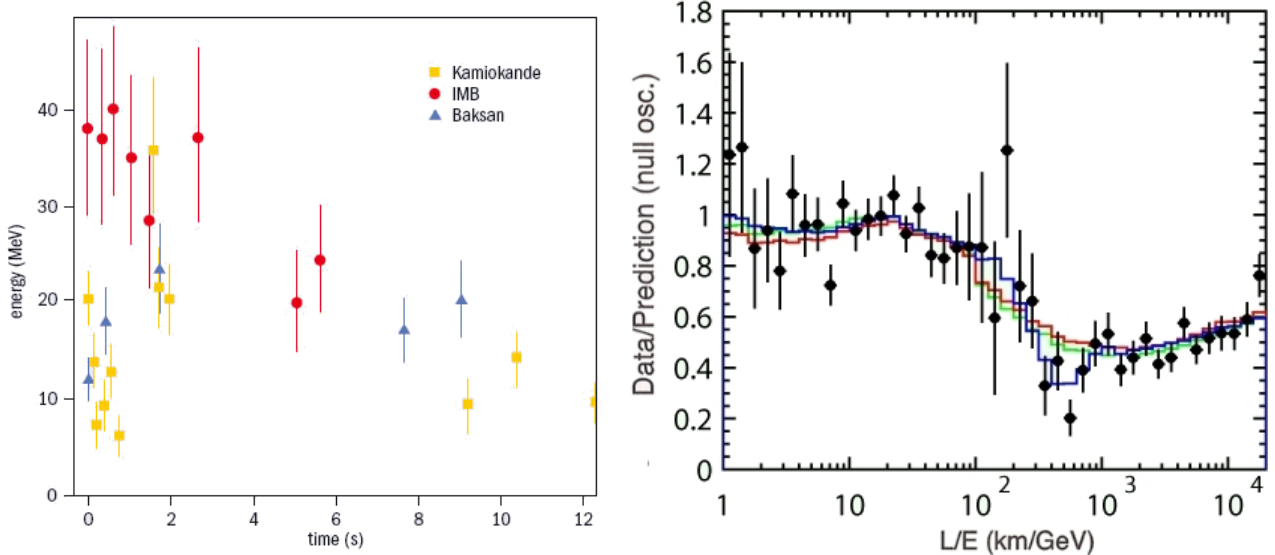


Figure 1.2: *Left:* Spectrum of the events produced by neutrinos from the Supernova SN1987A, as observed by Super Kamiokande, IMB and Baksan. *Right:* Ratio of data and Monte Carlo prediction in the no-oscillation hypothesis for μ -like events, as a function of L/E in SuperKamiokande. The solid histogram shows the best fit for $\nu_\mu \rightarrow \nu_\tau$ oscillation. The dip around $L/E \sim 500\text{km/GeV}$ corresponds to the first maximum of the oscillation probability.

SN1987A have been observed by three experiments: Kamiokande, IMB and Baksan. The spectrum of the events is shown in right panel of Figure 1.2. Nevertheless, because of the low statistics and because of some technical hitches affecting the experiments, the relevance of this observation uniquely resides in the fact that it was the first observation of Supernova neutrinos: no other information can be extracted about the Supernova explosion process.

1.3.6 Atmospheric neutrinos

The atmospheric neutrinos have been almost the first source of neutrino studied in last century: from their observation the oscillation phenomenon has been discovered [17] (see Section 1.4).

Cosmic rays entering the atmosphere produce a hadron shower in which pions and kaons are generated. The dominant neutrino production mechanism is:

$$\pi^+ \rightarrow \nu_\mu + \mu^+ \quad (1.25)$$

$$\mu^+ \rightarrow \bar{\nu}_\mu + e^+ + \nu_e. \quad (1.26)$$

The contribution of kaons is important only at energies higher than 10 GeV. Atmospheric neutrinos are observed at large detectors, like Super-Kamiokande, that are located underground in order to reduce the cosmic rays background.

Calculation of the expected neutrino flux is not trivial, since it requires a precise knowledge of many aspects, such as the primary cosmic rays flux and the hadronization processes taking place in the atmosphere. Moreover, the measured neutrino flux is affected by a very large uncertainty, of the order of 20%.

Many observables related to atmospheric neutrinos are studied, as the $(\nu_\mu + \bar{\nu}_\mu) / (\nu_e + \bar{\nu}_e)$ ratio and the zenith variation. The ratio is constrained by the production process to be ~ 2 for energies up to 1 GeV. At higher energies, the ratio grows because the number of muons decaying before reaching the ground decreases. Uncertainty affecting the ratio is less than 5% under 5 GeV; it becomes of the order of 10% at 100 GeV mainly because of the kaon contribution to the neutrino production⁶. The zenith variation allows to probe neutrinos at very different production distances and hence to look for oscillation signatures. For energies above a few GeV, neutrino production is isotropic and uniform all around the Earth. Hence, neutrino flux can be studied as a function of the L/E ratio looking at the flux coming from all zenith angles.

One of the most relevant studied quantity is the upcoming-downcoming asymmetry; the presence of this asymmetry in the atmospheric neutrino flux of a fixed flavor would be a signal of neutrino oscillation. For this reason, atmospheric neutrinos have been the first probe of the oscillation mechanism. As already mentioned, results from Super-Kamiokande (1998) show a nonzero muon neutrino up-down asymmetry ($A_\mu^{\text{up-down}} = -0.296 \pm 0.048 \pm 0.01$), while the electron neutrino up-down asymmetry is compatible with zero ($A_e^{\text{up-down}} = -0.036 \pm 0.067 \pm 0.02$). The muon asymmetry is given by oscillation, as confirmed by the dependence on L/E of the ratio between measured and expected fluxes shown in left panel of Figure 1.2. The oscillation channel favored by SK data is $\nu_\mu \rightarrow \nu_\tau$, oscillation to ν_e being disfavored by the absence of any electron asymmetry and the oscillation to ν_s being excluded by the absence of matter effects.

1.3.7 Accelerator neutrinos

Accelerator neutrino experiments are fundamental in the measurement of the oscillation parameters, as the already unknown value of θ_{13} , and in the investigation of the existence of sterile neutrinos. The source-detector distance can be fixed in order to get a suitable value of the ratio L/E.

Neutrino beams can be produced in three ways. In conventional beams, neutrinos are produced using the same process as for atmospheric neutrinos: protons are accelerated on a target, where pions and kaons are produced. Particles of correct charge are selected (positive charge for producing neutrinos and negative charge for antineutrinos) and focused, then they enter the decay pipe where they decay into muons and muon neutrinos. After the decay pipe, an absorber removes the residual charged particles and neutrons, while neutrinos proceed towards the detector. Conventional beams provide a high flavor purity and high intensity. In addition, neutrino energies can be selected in order to maximize the oscillation at the detector.

In beta beams, beta decaying atoms are ionized and accelerated; neutrinos are produced in the boosted decay. Examples of accelerated atoms are:



The resulting beam is an extremely pure electron neutrino or antineutrino beam, whose spectrum is very well known as it is a boosted beta spectrum. Ion production is the most problematic aspect of this new technology, but solutions are under development.

⁶Kaons have many decay channels, which lead to neutrino productions in different flavor percentages.

The last neutrino beam type is the one produced in neutrino factories. Muons are accelerated and kept in a storage ring the longer the more muons are accelerated. An extremely pure beam is produced, but both neutrinos and antineutrinos are present at the same time. Moreover, storage times are still short.

According to the source-detector distance, accelerator experiments are classified as short-baseline (km), long-baseline (hundreds km), very long baseline (thousands km).

All short baseline experiments couldn't find any evidence of neutrino oscillation in the channels $\nu_\mu \rightarrow \nu_e$ and $\nu_\mu \rightarrow \nu_\tau$. The only exception is represented by LSND, which found a signal in the channel $\bar{\nu}_\mu \rightarrow \bar{\nu}_e$ and $\nu_\mu \rightarrow \nu_e$. The MiniBooNE experiment didn't exclude the LNSD results and the problem is still open. A possible solution could require the introduction of a fourth sterile neutrino, corresponding to a new $\Delta m^2 \simeq 1$ eV.

Long baseline experiments are intended to check the results of atmospheric neutrino oscillation and to investigate the $\nu_\mu \leftrightarrow \nu_e$ transition (K2K, T2K, NOvA); they are also involved in the measurement of θ_{13} , in the observation of CP violation and in the determination of the mass hierarchy. Some long baseline experiments will adopt the off-axis configuration, in which a monochromatic neutrino flux is obtained, at the expense of beam intensity, by shifting the detector by 1-2 degrees from the beam. New projects, involving a longer base line and a non monochromatic neutrino beam, are already under study: T2KK and LBNE.

1.3.8 Galactic and extragalactic high energy neutrinos

A series of processes, taking place both inside and outside the galaxy, produces neutrinos in the energy range above 1 TeV. Such energetic neutrinos can originate from the decay of heavy particles, from annihilation processes, such as the annihilation of dark matter particles, or from the interaction of high energy protons with other particles: in this last case, the particle shower originated in the interaction contains a large amount of mesons, whose decay produces neutrinos. High energy neutrinos are a probe to study several processes, such as the interaction of protons with the interstellar medium. They are a fundamental probe also to study Supernova remnants and binary systems, where accelerated protons interact with other particles.

1.4 Neutrino Oscillations

Neutrino oscillations are actually flavor oscillations; they characterize the neutrino propagation both in vacuum and in matter. In brief, what happens is that neutrinos created with a particular flavor (for example, ν_e in case of solar neutrino) change their flavor during their propagation. The fundamental property allowing this phenomenon is that the propagation eigenstates are the mass ones and not the flavor ones.

1.4.1 Neutrino oscillations in vacuum

There are some fundamental conditions to be respected in order to allow the oscillation conversion:

1. neutrino must be massive;
2. neutrino masses must be non degenerate;
3. leptons must mix in the same way as quarks.

This last condition means that flavor eigenstates ν_α do not coincide with mass eigenstates ν_i : they must be a linear combination of mass eigenstates:

$$|\nu_\alpha\rangle = \sum_i U_{\alpha i}^* |\nu_i\rangle, \quad (1.29)$$

where U is the PMNS mixing matrix. As $|\nu_\alpha\rangle$ are orthogonal vectors, there must be at least three mass eigenstates.

The survival probability

Since it is not possible to determine which mass eigenstate has propagated, the amplitude for this process to occur is the coherent sum of the all the mass eigenstate contributes, namely:

$$\text{Amp} [\nu_\alpha \rightarrow \nu_\beta] = \sum_i U_{\alpha i}^* \text{Prop}(\nu_i) U_{\beta i} \quad (1.30)$$

From calculation in the rest frame of the neutrino and then with a Lorentz transformation to the laboratory frame, the propagator $\text{Prop}(\nu_i)$ comes out to be:

$$\text{Prop}(\nu_i) = e^{-i(E_i t - p_i L)} \quad (1.31)$$

where t and L are the neutrino time of flight and the source-detector distance respectively. Remembering that only neutrinos with different mass eigenstates and the same energy oscillate:

$$\begin{aligned} \text{Prop}(\nu_i) &= e^{-i(E_i t - p_i L)} \\ &\approx e^{-i[E(t-L) + m_i^2 \frac{L}{2E}]} \end{aligned} \quad (1.32)$$

The factor $e^{-iE(t-L)}$ on the right hand side of the last line is a nonessential overall phase. It does not depend on the mass eigenstate propagating and it is omitted as it gives no contribution to the oscillation probability.

Then, the amplitude in Eq. 1.30 becomes:

$$\text{Amp} [\nu_\alpha \rightarrow \nu_\beta] = \sum_i U_{\alpha i}^* e^{-im_i^2 \frac{L}{2E}} U_{\beta i} \quad (1.33)$$

The probability of the transition $\nu_\alpha \rightarrow \nu_\beta$ is:

$$\begin{aligned} P(\nu_\alpha \rightarrow \nu_\beta) &= |\text{Amp}(\nu_\alpha \rightarrow \nu_\beta)|^2 \\ &= \delta_{\alpha\beta} - 4 \sum_{i>j} \mathcal{R}(U_{\alpha i}^* U_{\beta i} U_{\alpha j} U_{\beta j}^*) \sin^2 \left(\Delta m_{ij}^2 \frac{L}{4E} \right) \\ &\quad + 2 \sum_{i>j} \mathcal{I}(U_{\alpha i}^* U_{\beta i} U_{\alpha j} U_{\beta j}^*) \sin \left(\Delta m_{ij}^2 \frac{L}{4E} \right) \end{aligned} \quad (1.34)$$

Source	E	L	Δm^2 (eV ²)
Sun	0.1–10 MeV	1.5–10 ¹¹ m	10 ⁻¹² –10 ⁻¹⁰
Reactors	1–10 MeV	10 m–100 km	10 ⁻³ –1
Accelerators	0.1–10 GeV	10 m–10 km	10 ⁻² –10 ³
Atmosphere	1–10 GeV	10–10 ⁴ km	10 ⁻⁵ –1

Table 1.2: Δm^2 sensitivity for different kind of experiments, or in other words, for different kind of neutrino sources.

where $\Delta m_{ij}^2 = m_i^2 - m_j^2$. This equation represents the most general expression of the *oscillation/conversion probability*. As the probability oscillates with the ratio L/E , the process is called *flavor oscillation*.

The oscillatory terms in Eq. 1.34 result from the interference of the different mass eigenstates. Then, the probability oscillates only if the superposition of the mass eigenstates is coherent. If the superposition is incoherent, or when the coherence between the mass eigenstates is lost, probability does not oscillate anymore with L/E and reduces to the constant value:

$$P(\nu_\alpha \rightarrow \nu_\beta) = \sum_k |U_{\alpha k}|^2 |U_{\beta k}|^2 \quad (1.35)$$

Converting formulae into numbers, a useful way of expressing the argument of the sine in Eq. 1.34 is:

$$\Delta m^2 \frac{L}{4E} = 1.27 \Delta m^2 [\text{eV}^2] \frac{L [\text{km}]}{E [\text{GeV}]} \quad (1.36)$$

in which the values of \hbar and c are included.

Oscillation is appreciable when the argument is $\mathcal{O}(1)$, then oscillation experiments are sensitive to a mass splitting:

$$\Delta m^2 \geq \frac{E (\text{GeV})}{L (\text{km})}. \quad (1.37)$$

For example, an experiment aiming at observing neutrino oscillations on atmospheric neutrinos is sensible to a mass splitting of the order of 10^{-4} eV². Then, oscillation experiments are extremely sensitive in measuring the mass splittings. On the other hand, such experiments are not capable of measuring the absolute values of the masses. In Table 1.2 the mass splitting sensitivity for different kind of neutrino experiments is resumed. From Eq. 1.34 it is evident that if neutrinos are massless or if lepton mixing does not occur, oscillation probability becomes $P(\nu_\alpha \rightarrow \nu_\beta) = \delta_{\alpha\beta}$.

Oscillation probability for antineutrinos

The oscillation probability for antineutrinos can be obtained assuming CPT invariance. Since:

$$P(\bar{\nu}_\alpha \rightarrow \bar{\nu}_\beta) = P(\nu_\beta \rightarrow \nu_\alpha) = P(\nu_\alpha \rightarrow \nu_\beta; U \rightarrow U^*) \quad (1.38)$$

the oscillation probability can be directly obtained from Eq. 1.34, resulting in:

$$\begin{aligned} P(\bar{\nu}_\alpha \rightarrow \bar{\nu}_\beta) &= \delta_{\alpha\beta} - 4 \sum_{i>j} \mathcal{R}(U_{\alpha i}^* U_{\beta i} U_{\alpha j} U_{\beta j}^*) \sin^2 \left(\Delta m_{ij}^2 \frac{L}{4E} \right) \\ &\quad - 2 \sum_{i>j} \mathcal{I}(U_{\alpha i}^* U_{\beta i} U_{\alpha j} U_{\beta j}^*) \sin \left(\Delta m_{ij}^2 \frac{L}{4E} \right) \end{aligned} \quad (1.39)$$

The comparison between Eq. 1.34 and Eq. 1.39 shows that the only difference between the oscillation probability for neutrinos and antineutrinos is the sign of the imaginary part. Then, if the U matrix is complex, the two probabilities differ from one another, the difference representing a CP violation. The parametrization of the U matrix given in Eq. 1.10 shows that CP violation is due to the Dirac phase and is independent on the Majorana phases. In fact, the Majorana phases can be factorized in a diagonal matrix (Eq. 1.20) and can be removed with a proper re-phasing, since the oscillation probability depends on the quartic product $U_{\alpha k}^* U_{\beta k} U_{\alpha j} U_{\beta j}^*$, which is invariant under the redefinition of the mixing matrix $U_{\alpha k} \rightarrow e^{i\phi_\alpha} U_{\alpha k} e^{i\phi_k}$. As a consequence, Majorana phases do not affect neutrino oscillation and then they cannot be measured in oscillation experiments. So, oscillation experiments cannot determine if neutrino has a Dirac or a Majorana nature.

A fundamental approximation: 2 flavors and 2 mass eigenstates

In many oscillation experiments, one of the three mass eigenstates can be neglected because it is slightly coupled to the flavor neutrino produced at the source, due to the mixing angle value. Then, only two massive neutrinos and two flavor eigenstates can be considered, well describing the real phenomenon. This is a useful approximation, as a smaller number of parameters enter the formulas, which become very simple.

Let's call the two flavor neutrinos ν_α and ν_β . The last one can coincide with one of the two remaining flavors ($\neq \alpha$) or it can be a linear combination of them. A practical example is: considering solar neutrinos (see Section 1.6.1) ν_α is the ν_e produced in the Sun and ν_β is a combination of $\nu_\mu - \nu_\tau$, dominated by ν_μ .

The two flavor neutrinos are superposition of two mass eigenstates and the mixing matrix in Eq. 1.20 reduces to:

$$U = \begin{pmatrix} \cos \theta & \sin \theta \\ -\sin \theta & \cos \theta \end{pmatrix} \begin{pmatrix} e^{i\alpha_1/2} & 0 \\ 0 & 1 \end{pmatrix} \quad (1.40)$$

where θ is the mixing angle and α_1 is the (unique) Majorana phase. There is only one mass splitting $\Delta m^2 = m_2^2 - m_1^2$, where m_1 is defined to be the lightest one, so that Δm^2 is positive. Then, the oscillation probability in Eq. 1.34 reduces to:

$$P(\nu_\alpha \rightarrow \nu_\beta) = \frac{1}{2} \sin^2 2\theta \left[1 - \cos \left(\frac{\Delta m^2 L}{2E} \right) \right] \quad (1.41)$$

$$= \sin^2 2\theta \sin^2 \left(\frac{\Delta m^2 L}{4E} \right) \quad (1.42)$$

Conversely, the survival probability is:

$$P(\nu_\alpha \rightarrow \nu_\alpha) = 1 - \sin^2 2\theta \sin^2 \left(\frac{\Delta m^2 L}{4E} \right) \quad (1.43)$$

according with Eq. 1.34 in the case $\alpha = \beta$.

The average probability, that coincides with the incoherent transition probability, given by Eq. 1.35, reduces to:

$$\langle P(\nu_\alpha \rightarrow \nu_\beta) \rangle = \frac{1}{2} \sin^2 2\theta. \quad (1.44)$$

Previous equations show that the oscillation probability depends on the mixing angle through $\sin^2 2\theta$, that is symmetric under the change $\theta \leftrightarrow \pi/2 - \theta$. However, these are two physically different situations: for $\theta < \pi/4$, ν_e is composed more by ν_1 than by ν_2 ; viceversa, for $\theta > \pi/4$, the ν_2 component in the electron neutrino is the largest one. The symmetry on θ is broken by the oscillation in matter (see Section 1.4.2).

It must be underlined that, in the two generations approximation, the Dirac phase does not compare in the mixing matrix. Therefore, no CP violations can be observed: in fact, neutrino and antineutrino transition probabilities coincide.

Averaged probability

In all experiments, the source-detector distance L and the neutrino energy E are known with some uncertainty. Besides the finite spatial resolution, uncertainty on L is due to the source size; similarly, uncertainty on energy originates from the detector energy resolution and from the fact that neutrinos could have a continuous spectrum. Hence, the oscillation probability must be always averaged over the distributions of L and E . If $\phi(L/E)$ is the distribution of L/E , Eq. 1.42 becomes:

$$\langle P(\nu_\alpha \rightarrow \nu_\beta) \rangle = \frac{1}{2} \sin^2 2\theta \left[1 - \left\langle \cos \left(\frac{\Delta m^2 L}{2E} \right) \right\rangle \right] \quad (\alpha \neq \beta) \quad (1.45)$$

where:

$$\left\langle \cos \left(\frac{\Delta m^2 L}{2E} \right) \right\rangle = \int \cos \left(\frac{\Delta m^2 L}{2E} \right) \phi \left(\frac{L}{E} \right) d\frac{L}{E}. \quad (1.46)$$

Eq. 1.45 describes the probability that is measured in all the experiments.

The oscillation probability as a function of the factor $\Delta m^2 \langle L/E \rangle$ is shown in Figure 1.3. In the plot, it is assumed that $\sin^2 2\theta = 1$ and that $\langle L/E \rangle$ has a gaussian distribution with $\sigma = 0.2 \langle L/E \rangle$. Dashed line represents the unaveraged probability (Eq. 1.42), while the solid line represents the averaged probability (Eq. 1.45). If Δm^2 and the average energy $\langle E \rangle$ are fixed, the plot represents the dependence of the oscillation probability on the average distance. The maximal probability is reached at $\Delta m^2 \langle L/E \rangle \approx 1.24$, while the first minimum is in correspondence of an average distance equal to the oscillation length, that is at $\Delta m^2 \langle L/E \rangle \approx 2.47$.

Important to note is that at a distance smaller than the oscillation length, unaveraged and averaged probability follow the same pattern, with the amplitude of the second one being reduced the more the larger the sigma of the $\langle L/E \rangle$ gaussian distribution. At distances larger than the oscillation length, the oscillatory pattern of the averaged probability rapidly vanishes and for $\langle L \rangle \gg L^{osc}$ only the average transition probability (or incoherent transition probability) of Eq. 1.44 can be observed.

On the basis of the measurement of $\langle P(\nu_\alpha \rightarrow \nu_\beta) \rangle$ performed by an experiment, the allowed couples of θ and Δm^2 can be discriminated from the forbidden ones. The result is

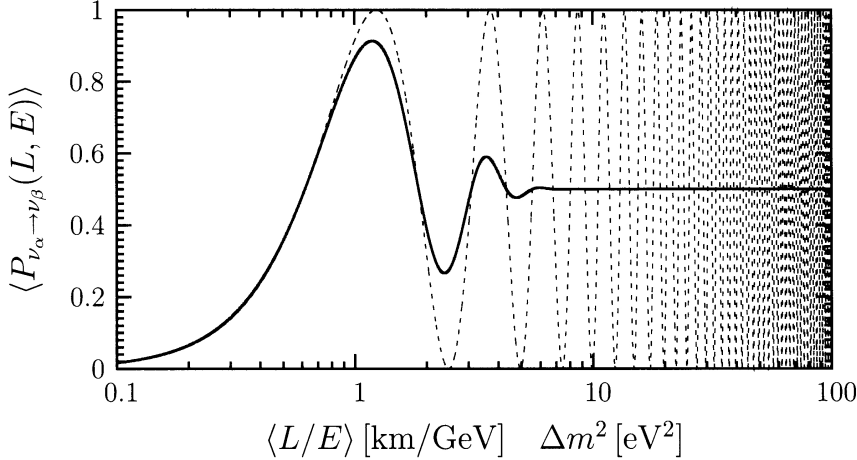


Figure 1.3: Oscillation probability as a function of $\Delta m^2 \langle L/E \rangle$. For fixed Δm^2 and E , it represents the oscillation pattern as a function of the source-detector distance. Dashed line represents the unaveraged probability of Eq. 1.42, while solid line the averaged probability of Eq. 1.45.

represented through the exclusion plot, consisting in the plane $(\Delta m^2, \sin^2 2\theta)$, where the allowed regions are distinguished from the forbidden ones. In particular, if an oscillation experiment does not observe any oscillation, an upper limit on the averaged probability is set:

$$\langle P_{\nu_\alpha \rightarrow \nu_\beta} \rangle \leq P_{\nu_\alpha \rightarrow \nu_\beta}^{\max} \quad (1.47)$$

Hence, the upper limit on $\sin^2 2\theta$ as a function of Δm^2 is

$$\sin^2 2\theta \leq \frac{2P_{\nu_\alpha \rightarrow \nu_\beta}^{\max}}{1 - \left\langle \cos \left(\frac{\Delta m^2 L}{2E} \right) \right\rangle} \quad (1.48)$$

In left panel of Figure 1.4 an exclusion plot representing such a situation, considering an upper limit of $P_{\nu_\alpha \rightarrow \nu_\beta}^{\max} = 0.1$, is shown. Solid line refers to the averaged oscillation probability, $\langle L/E \rangle$ having gaussian distribution with $\sigma = 0.2 \langle L/E \rangle$, while dashed line refers to the unaveraged probability.

Instead, if an experiment observes the oscillation, then the oscillation probability corresponds to a band in the plane $(\Delta m^2, \sin^2 2\theta)$, the larger the higher the probability uncertainty is (see right panel of Figure 1.4).

In most experiments, position and energy of the events are measured (even if with some uncertainty) and the data distributions are binned. Then, there is not just one global L/E distribution, but each bin has its own L/E distribution. Every bin determines a different band on the $(\Delta m^2, \sin^2 2\theta)$ plane. The regions in which the different bands overlap are compatible with all the measurements of the oscillation probability. Taking into account the measured $P_{\nu_\alpha \rightarrow \nu_\beta}$ and their uncertainties, a global fit yields to the definition of one or more overlap regions, that correspond to the allowed regions of parameters. Obviously, the final goal is to determine one unique region, as narrow as possible, in order to precisely identify the values of the oscillation parameters.

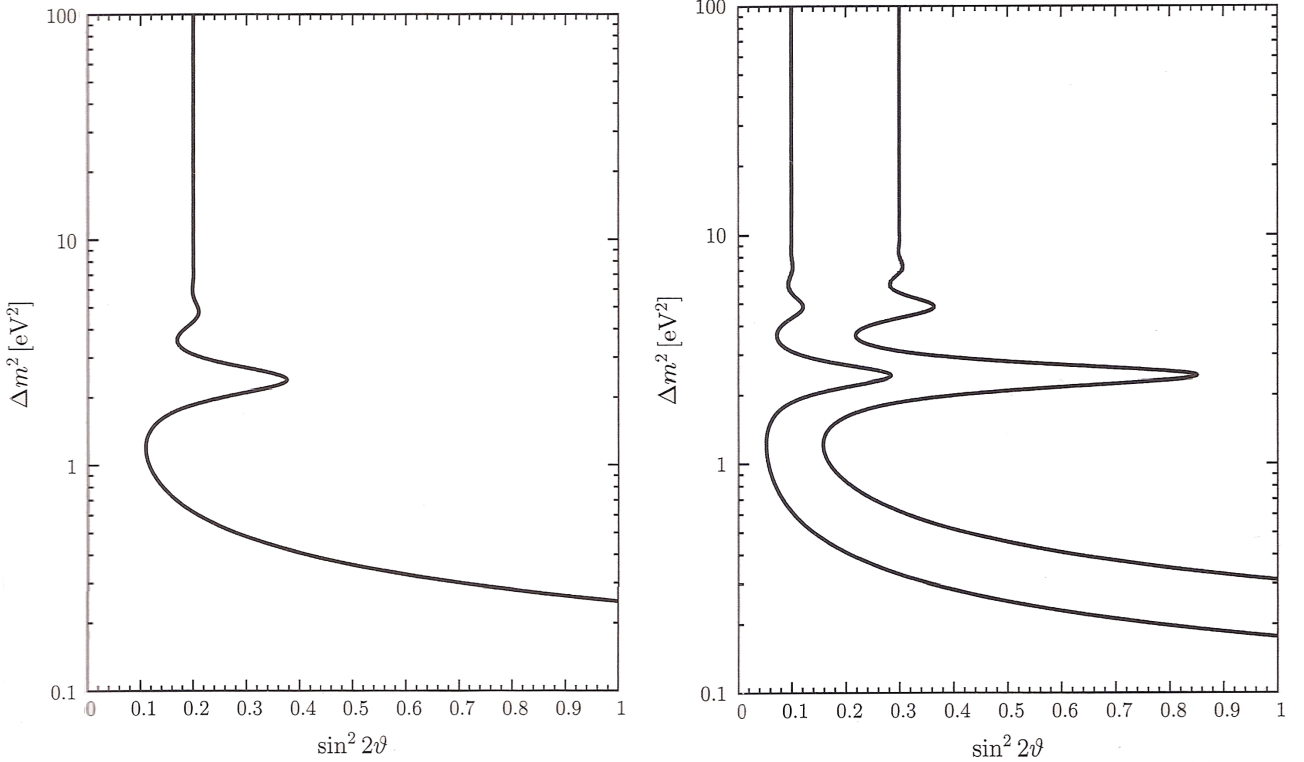


Figure 1.4: *Left:* Exclusion plane of the oscillation parameters in case of upper limit to the oscillation probability. The allowed region is *below* the exclusion line. *Right:* Exclusion plane in case of measurement of the oscillation probability.

1.4.2 Neutrino oscillations in matter

Considering once again the Table 1.1 it is easy to observe that ν_e is coupled with e^- , ν_μ is coupled with μ^- and ν_τ is coupled with τ^- . Moreover, considering that in ordinary matter only electrons are present, it is also easy to imagine that interactions of neutrinos in matter depend on the flavor.

The first physicist to study this phenomenon was L. Wolfenstein, who published in 1978 a work [2] showing that the neutrino flavor oscillation is modified when neutrinos propagate in a medium. Interaction of neutrinos with electrons through coherent forward elastic scattering⁷ give rise to a potential that alters the flavor mixing. The oscillation parameters are replaced by effective parameters depending on the medium properties: the effective mixing angle can become large even if the mixing angle in vacuum is small.

In 1985, S.P. Mikheev and A.Yu. Smirnov [3, 4] found out the most relevant property of oscillation in matter. They discovered that the matter effect can lead to a resonant flavor transition: under particular conditions, the effective mixing angle becomes maximal. This effect, known as MSW mechanism, is the key point to explain the solar neutrinos flavor oscillation (see Section 1.6.6): in fact, the mixing angle in vacuum relevant for solar neutrinos is large but not maximal; the flavor conversion takes place because of the MSW effect in the interior of the Sun. But not only, matter effects are fundamental also for

⁷In principle, neutrinos undergo also forward inelastic scattering, but it can be shown that this effect is negligible in most situations. It is relevant only in neutron stars and Supernova cores or for extremely high energetic neutrinos ($E_\nu < 10^5 \text{ GeV}$), otherwise the mean free path is of the order of light years.

the Long Base Line experiments aiming to measure θ_{13} , the mass hierarchy and the CP violation in lepton sector.

For simplicity, the oscillation in matter is described here in the two-generations approximation.

Neutrino interaction with matter

When neutrinos propagate in a medium, they interact with the electrons through the coherent forward elastic weak CC and NC scatterings. The CC interaction involves only electron neutrinos (and antineutrinos) and the electrons of the medium. The effective potential of this interaction is:

$$V_{CC} = \pm \sqrt{2} G_F N_e \quad (1.49)$$

where G_F is the Fermi coupling constant and N_e is the electron numerical density (cm^{-3}). The sign is positive for neutrinos and negative for antineutrinos.

On the other side, neutrinos of every flavor can interact with the protons, the neutrons and the electrons of the medium through NC interaction. The effective potential for the process involving the fermion f ($f = e^-, n, p$) of the medium is:

$$V_{NC}^f = \sqrt{2} G_F N_f g_V^f \quad (1.50)$$

Since:

$$\begin{aligned} g_V^e &= -g_V^p = -\frac{1}{2} + 2 \sin^2 \theta_W \\ g_V^n &= -\frac{1}{2}, \end{aligned}$$

the electron and the proton contributions cancel out and, then, the effective potential coincides with the neutron contribution:

$$V_{NC} = \mp \frac{1}{2} \sqrt{2} G_F N_n. \quad (1.51)$$

The negative sign stands for neutrinos and the positive one for antineutrinos. The effective potentials presented here represent the potential energy of neutrinos and antineutrinos propagating through matter.

Oscillation comes from the interference of the different terms, then only relative phase, namely relative energy, is important. Since only relative energy matter, every multiple of the identity in the Hamiltonian can be neglected as it gives just a shift in energy common to all the mass eigenstates and doesn't change the relative phase. If all the multiples of the identity are neglected, the Hamiltonian is:

$$H_M = H_{vac} + \frac{V_{CC}}{2} \begin{bmatrix} 1 & 0 \\ 0 & -1 \end{bmatrix} = \frac{\Delta m^2}{4E} \begin{bmatrix} -(\cos 2\theta - A_{CC}) & \sin 2\theta \\ \sin 2\theta & \cos 2\theta - A_{CC} \end{bmatrix} \quad (1.52)$$

where the mass splitting Δm^2 is defined positive, assuming ν_2 as the eigenstate with the heaviest mass. The parameter A_{CC} in the diagonal terms represents the intensity of the matter effect. It is given by:

$$A_{CC} = \frac{V_{CC}/2}{\Delta m^2/4E} = \frac{2\sqrt{2}G_F N_e E}{\Delta m^2}, \quad (1.53)$$

then the matter effect grows linearly with energy and, since it is proportional to V_{CC} , it has a different sign for neutrinos and antineutrinos.

If effective parameters are defined, the Hamiltonian in Eq. 1.52 assumes the same structure of the Hamiltonian of the propagation in vacuum. The effective parameters that must be defined are the mass splitting in matter:

$$\Delta m_M^2 = \sqrt{\sin^2 2\theta + (\cos 2\theta - A_{CC})^2} \quad (1.54)$$

and the mixing angle in matter:

$$\tan 2\theta_M = \frac{\tan 2\theta}{1 - \frac{A_{CC}}{\Delta m^2 \cos 2\theta}}. \quad (1.55)$$

With the introduction of these parameters, the Hamiltonian in Eq. 1.52 becomes:

$$H_M = \frac{\Delta m_M^2}{4E} \begin{bmatrix} -\cos 2\theta_M & \sin 2\theta_M \\ \sin 2\theta_M & \cos 2\theta_M \end{bmatrix} \quad (1.56)$$

that is the same formula as the Hamiltonian in vacuum. It is important to notice that Δm_M^2 and $\tan 2\theta_M$ have different values for neutrinos and antineutrinos, as the parameter A_{CC} has opposite sign in the two cases.

The matter effects introduce an asymmetry between neutrinos and antineutrinos, called *fake CP violation*: it is simply due to the different interactions of ν and $\bar{\nu}$ with matter, that is composed by particles and not by antiparticles. Disentangling the two sources of asymmetry, real and fake CP violation, is an important challenge for next experiments.

An important feature of oscillation in matter is that it allows to determine if the mixing angle in vacuum is smaller or bigger than $\pi/4$. In fact, a direct comparison of Δm^2 with Δm_M^2 leads to the determination of the sign of $\cos 2\theta$ in Eq. 1.54.

However, the most interesting feature of the oscillation in matter, discovered by Mikheev and Smirnov in 1985, is that the mixing angle is maximal under some conditions, independently from the mixing angle in vacuum. In particular, from Eq. 1.55 it comes out that when the electron density matches the value:

$$N_e = \frac{\Delta m^2 \cos 2\theta}{2\sqrt{2}EG_F} \quad (1.57)$$

the effective mixing angle reaches the value $\pi/4$. Then, it is possible to have a total flavor transition. In correspondence of the resonance, the mass splitting reaches the lowest value $\Delta m_M^2 = \Delta m^2 \sin 2\theta$. Since the parameter A_{CC} is positive for neutrinos, from Eq. 1.55 it follows that there can be a resonance only for $\theta < \pi/4$; viceversa, for antineutrinos there can be a resonance only for $\theta > \pi/4$.

Depending on how intense is the variation of the electron density along the neutrino trajectory, three scenarios are possible for the oscillation in matter: constant electron density, adiabatic density variation, non adiabatic variation.

- **The constant density case.** This is the simplest case: the electron density is constant along the neutrino trajectory. This is the case of the neutrino beams. H_M is position

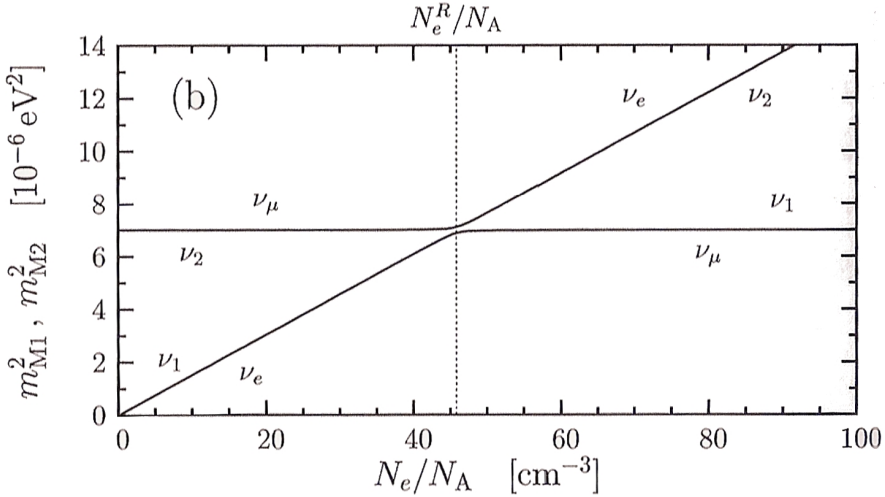


Figure 1.5: In the core of the Sun ($N_e \sim 100 N_A \text{ cm}^{-3}$), ν_e are produced essentially as ν_2 . While they propagate outwards, the electron density decreases. If the resonance (dotted line) is crossed adiabatically, neutrinos exit the Sun as ν_2 , hence as ν_μ .

independent, like H_{vac} , and the transition probability is specular to the oscillation probability in vacuum:

$$P_M(\nu_e \rightarrow \nu_\mu) = \sin^2 2\theta_M \sin^2 \left(\frac{\Delta m_M^2 L}{4E} \right) \quad (1.58)$$

- **The adiabatic case.** If the electron density along the neutrino trajectory is not constant, then the effect of oscillation in matter can have a bigger impact. In this case the resonant electron density in Eq. 1.57 can be crossed and lead to a maximal mixing. For example, if the electron density in the core of the Sun is larger than the resonant electron density, neutrinos are produced mainly as ν_2 . If the density variation around the resonance is smooth, then neutrinos exit the Sun as ν_2 and will interact mainly as ν_μ . This effect is shown in Figure 1.5. This is the most striking effect of the MSW mechanism. In the case of varying electron density, transitions between ν_1^M and ν_2^M can happen. If the variation of the electron density is smooth (adiabatic variation), then the transition probability is negligible. In case of a non adiabatic variation, the transition probability has an effect on the overall flavor oscillation probability. In order to discriminate the two cases, the adiabaticity parameter γ is evaluated:

$$\gamma = \frac{(\Delta m_M^2)^2}{2E \sin 2\theta_M |dA_{CC}/dx|} \quad (1.59)$$

The adiabatic transition occurs for $\gamma \gg 1$. In this case, transitions between ν_1^M and ν_2^M are negligible and the survival probability is given by:

$$\begin{aligned} P_{\nu_e \rightarrow \nu_e}^{\text{adiab}}(x) &= \frac{1}{2} + \frac{1}{2} \cos 2\theta_M^i \cos 2\theta_M^f \\ &\quad + \frac{1}{2} \sin 2\theta_M^i \sin 2\theta_M^f \cos \left(\int_0^x \frac{\Delta m_M^2(x')}{2E} dx' \right) \end{aligned} \quad (1.60)$$

where θ_M^i and θ_M^f are the mixing angle at the source and at the detector respectively. This is the case of solar neutrinos or Supernova neutrinos. In this case, θ_M^f coincides with the mixing angle in vacuum and the cosine averages to zero because the fluctuations on energy of its phase are larger than 2π . Then the probability reduces to:

$$\langle P_{\nu_e \rightarrow \nu_e}^{\text{adiab}} \rangle = \frac{1}{2} + \frac{1}{2} \cos 2\theta_M^i \cos 2\theta \quad (1.61)$$

and does not depend any more on the source-detector distance.

- **The non adiabatic case.** In the case of non adiabatic evolution, transitions between ν_1^M and ν_2^M are important and are maximal at the point in which γ reaches its minimum. In good approximation, this point coincides with the resonance point. For the case of neutrinos produced in the core of the Sun, at a density larger than the resonant one, and crossing the resonance in a non adiabatic way, the averaged survival probability is given by the Parke formula [5]:

$$\langle P_{\nu_e \rightarrow \nu_e} \rangle = \frac{1}{2} + \left(\frac{1}{2} - P_c \right) \cos 2\theta_M^i \cos 2\theta. \quad (1.62)$$

P_c is the $\nu_1^M \leftrightarrow \nu_2^M$ crossing probability. The expression giving the crossing probability depends upon the electron density profile and on the adiabatic parameter at the resonance [6, 7]. For a linear density profile, with a large adiabatic parameter at the resonance, it can be shown that $P_c \ll 1$. In this case, the Parke formula reduces to the adiabatic survival probability of Eq. 1.61. On the other hand, in the so called *extreme nonadiabatic limit*, P_c results to be about 1. Under this condition, the Parke formula reduces to the average survival probability in vacuum. Then, the strongest effect of the MSW mechanism is get for the adiabatic crossing of the resonance.

1.5 The experimental status

In this section I just want to give a summary of most important results found by Neutrino Experiments in last forty-fifty years. The fundamental results can be resumed in the following points:

- * The SuperKamiokande (SK) experiment observed disappearance of ν_μ and $\bar{\nu}_\mu$ atmospheric neutrinos, with "infinite" statistical significance ($\sim 17\sigma$) [17]. The anomaly is also seen by the MACRO experiment [18] and other atmospheric experiments. If interpreted as oscillations, it necessary to assume $\nu_\mu \rightarrow \nu_\tau$ with quasi-maximal mixing angle. The SK discovery is confirmed by ν_μ beam experiments, as K2K [19].
- * Various solar experiments [20, 21, 22, 23] see a 8σ evidence for a $\sim 50\%$ deficit of solar ν_e . The SNO experiment sees a 5σ evidence for $\nu_e \rightarrow \nu_{\mu,\tau}$ appearance. The KamLAND experiment [24] sees a 6σ evidence for disappearance of $\bar{\nu}_e$ produced by nuclear reactors. To interpret it as oscillations, it is necessary to assume a large but not maximal mixing angle.
- * Globally, atmospheric and solar data directly show that lepton flavor is not conserved. Theoretical simplicity suggests that oscillations of massive neutrinos are

responsible of these anomalies. But the observed flavor conversions could be produced by other mechanisms. Future experiments should confirm and complete this picture.

Next to these almost clear results, other experiments found some so called "anomalies", adding some puzzle to the description of Neutrino Physics. In particular, I am talking about:

- The LSND [25] claimed a 3.8σ $\bar{\nu}_\mu \rightarrow \bar{\nu}_e$ anomaly.
- Preliminary data from MiniBoone [26] show a $\sim 3\sigma$ $\nu_\mu \rightarrow \nu_e$ anomaly: it cannot be fitted by vacuum oscillations since the anomaly is concentrated in the lower part of the energy spectrum probed by MiniBoone. If the LSND and MiniBoone anomalies are caused by new physics, something exotic is needed.
- The NuTeV experiment [27] claims a 3σ anomaly in neutrino *couplings*: the measured ratio between the ν_μ/iron NC and CC couplings is about 1% lower than some SM prediction. Specific QCD effects that cannot be computed in a reliable way could be the origin of the NuTeV anomaly.
- A reanalysis [28] of the Heidelberg-Moscow data [29] performed by a sub-set of the collaboration claims a hint for violation of lepton number. The simplest interpretation would be in terms of Majorana neutrino masses, implying approximatively degenerate neutrinos with mass $m_{\beta\beta} \sim 0.4\text{ eV}$.
- Very recently a news from the OPERA experiment [30] has just shocked the scientific community: the OPERA Collaboration claimed "An early arrival time of CNGS muon neutrinos with respect to the one computed assuming the speed of light in vacuum of $(60.7 \pm 6.9_{\text{stat}} \pm 7.4_{\text{sys}})\text{ ns}$ was measured. This anomaly corresponds to a relative difference of the muon neutrino velocity with respect to the speed of light $\frac{v-c}{c} = (2.48 \pm 0.28_{\text{stat}} \pm 0.30_{\text{sys}}) \times 10^{-5}$.

At the light of these results, an exhaustive paint of "the status of the art", including open issues, can be done by the following "hot points" [16]:

1. Oscillations can be directly seen by precise reactor and long-baseline beam experiments, that are nowadays respectively testing the solar and atmospheric anomalies. The "hot subject" at the moment is the value of the neutrino mixing angle θ_{13} .
2. Another question concerns the mass hierarchy; new long base line experiments, as T2K or NOVA, and maybe double beta experiments could give an answer.
3. Thanks to involved matter effects, long base line experiments also aim at the measurement of the CP violation phase in the lepton sector.
4. A precise description of the solar neutrino survival probability is not yet available; this can hide some New Physics effects as explained in Section 1.6.6.
5. Future non-oscillation experiments should detect neutrino masses and test if neutrinos violate lepton number, in other words if neutrinos are Majorana or Dirac particles.

Done the contents of the present Thesis, I am particularly interested in focusing on some of the listed open questions; in particular, those related to solar and reactor neutrinos.

1.6 The open questions in the solar neutrino sector

Even if solar neutrinos have been studied since many years, there are still some doubts needing an answer. Some of them are related to the Sun description (see Section 1.6.5), some others are related to neutrino oscillations (see Section 1.6.6). After the description of the Sun and of solar neutrinos, I will focus on the open questions on this subject.

1.6.1 Solar Neutrinos

The fusion process occurring in the core of the Sun proceeds by fusing four protons to yield: one helium atom, two positrons, and two electron neutrinos. The reaction has a total energy release given by the mass difference between the initial and final state particles of 26.7 MeV:



For stars with masses less than $1.3M_\odot$, the elemental burning proceeds via the pp (proton-proton) cycle, and for larger stars, the core temperature is high enough to burn heavier elements and proceeds via the CNO (Carbon-Nitrogen-Oxygen) cycle. The method by which the burning proceeds determines the energy spectrum of the neutrinos observed in the detectors.

Since the same reactions producing the neutrinos also produce the energy emitted as the light that we see (even if it is delayed by 10^5 years, due to the photon diffusion within the Sun), it is possible to obtain a constraint on the total neutrino flux by measuring the light output of the Sun. This constraint, known as the luminosity constraint [8], assumes that:

1. the reactions producing neutrinos are all known;
2. the fusion rate of the Sun is stable over the time; it takes for the energy produced in the core to be emitted as photons at the surface of the Sun.

The neutrino flux is given by:

$$\Phi_\nu = \frac{2L_\odot}{26.7 \text{ MeV} 4\pi r^2} \quad (1.64)$$

The factor of 2 in the numerator in Eq. 1.64 is due to the fact that two neutrinos are emitted for each reaction which releases the 26.7 MeV. As the distance from the Sun to the Earth, r , is not a constant due to the elliptical orbit, it is necessary to average the Earth-Sun distance, obtaining an average neutrino flux of $6.6 \times 10^{10} \text{ cm}^{-2}\text{s}^{-1}$. This means that on the Earth almost 70 billion neutrinos per second pass through a square centimeter every second.

The actual luminosity constraint is given by the simple relation:

$$\frac{L_\odot^\gamma}{4\pi r^2} = \sum_i \alpha_i^\gamma \Phi_i^\gamma \quad (1.65)$$

where:

- L_\odot is the solar luminosity;
- r is the Earth-Sun distance;

- the factors α_i is the average energy released by the neutrino producing reaction i ;
- Φ_i is the neutrino flux from the reaction i .

A precise test of whether or not $L_\gamma/L_\odot = 1$ is of paramount importance for the neutrino community in order to vet our current understanding of solar energy production. Since the pp neutrinos comprise the vast majority of the flux, a truly rigorous test of the luminosity constraint requires a precise measurement of the pp neutrino flux.

Combining the Borexino ^7Be measurement with the Gallium and Chlorine results allows to obtain a value for f_{pp} which is the ratio of the model prediction to the measured value of $f_{\text{pp}} = 0.97 \pm 0.09$ [9].

1.6.2 Standard Solar Models

Standard Solar Models (SSMs) are models of the Sun-like stars constructed with "the best available physics and input data" (Bahcall), in the sense that they are continuously updated to take into account the latest experimental results regarding the several sectors of physics involved in the modelization. SSMs purpose is to describe the structure of stars, their functioning, starting from energy production mechanisms and finishing with energy transport, and their evolution. They are developed on the basis of the observations from our Sun, because it is a unique source of informations due to its nearness. Many models have been constructed in the last decades by several groups, but the ones that played a major role in neutrino physics are the ones by Bahcall and collaborators [11].

The Sun is modeled through a set of equations of state, on the basis of four equilibrium principles:

1. it is assumed that in any layer of the star, gravity is balanced by the thermal pressure gradient (hydrostatic equilibrium);
2. the energy escaping the star is imposed to equal the energy produced by nuclear reactions in the star core (thermal equilibrium);
3. the energy from nuclear reactions, which entirely determines the luminosity of the star, is assumed to propagate through the star by radiative transport (radiative equilibrium);
4. in case of radiative transport inadequacy in a certain layer, convective motions can take place to mix the material and soften the thermal gradient (convective equilibrium).

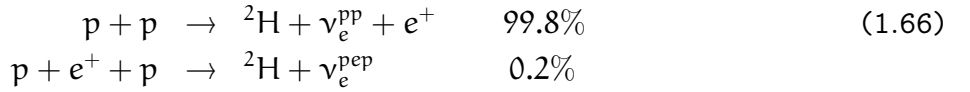
The usual development of a solar model consists in numerically evolving the solar model for a $1M_\odot$ star from the protostellar stage, when the chemical composition is uniform, to the present solar age (4.57 Gyr). A set of boundary conditions, experimentally measured, are imposed: the solar radius ($6.9598 \times 10^{10} \text{ cm}$), luminosity ($3.8418 \times 10^{33} \text{ erg/s}$) and metal-to-hydrogen fraction $(Z/H)_{\text{ph}}$ in the photosphere. Three parameters are let free in the construction of the SSM: the mass fractions of helium and metals and the so called mixing length parameter, which is a parameter used in the modelization of the convective motions in the Mixing Length Theory approximation. What comes out is the following structure: a central core, where nuclear reactions take place, then a radiative zone, enveloped in the external region where the high temperature gradient induces convective motions, the

boundary between the two regions being at $\sim 0.7R_\odot$.

Sun-like stars are powered by two groups of nuclear reactions: the so called *pp* chain and CNO cycle. By far the largest part of solar energy is produced by the *pp* chain, while the small contribution of the CNO cycle to the energy balance is not well known and could be determined experimentally by measuring the flux of neutrinos produced in the cycle.

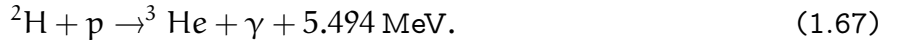
1.6.3 The pp chain

The *pp* chain, shown in left panel of Figure 1.6, provides four possible terminations for the fusion of four protons [10]. However, lepton number conservation dictates that two neutrinos must be produced by the end of whichever reactions occur to produce the helium nuclei. The first step of the chain is one of the two following reactions with the relative branching ratios indicated:



The Q value for both the reactions is 1.44 MeV. This first step of the chain is the slowest step in the process because it is governed by the weak interaction. The second of the two interactions which produces the so-called pep neutrinos is an even slower process because it requires three initiating particles as opposed to two. The ratio of initiating reactions which produce *pp* neutrinos to those which produce *pep* neutrinos is approximately 400:1. In Figure 1.7, we can see that the energy spectrum for the *pp* neutrinos is a continuum with an endpoint at about 420 keV, however the direct measurement of such a low energy neutrino is very complicated due to the presence of naturally occurring background in the energy region of interest. By contrast, the *pep* neutrinos are mono-energetic at 1.44 MeV, and therefore lie above the vast majority of naturally occurring background, and a direct measurement is a slightly easier task. For the moment only Borexino succeeded in measuring it [31]. Since the two reactions are effectively identical (they are transformed into each other by adding an electron to both sides), their matrix elements are identical and they describe effectively the same physics. Therefore, the easier measurement of the *pep* neutrinos can constrain the *pp* interaction.

Regardless of the method by which the deuterium nucleus is formed, it will quickly capture a free proton via:



From this point, there are three possible reactions that are collectively known as the *ppII* branch:

1. In approximately 85% of the cases, two such ${}^3\text{He}$ nuclei will undergo:



The chain is complete if it reaches this point, which it usually does.

2. Another possibility which occurs 15% of the time is for a ${}^3\text{He}$ to find a ${}^4\text{He}$ produced by reactions 1.68 or 1.70 and undergo:



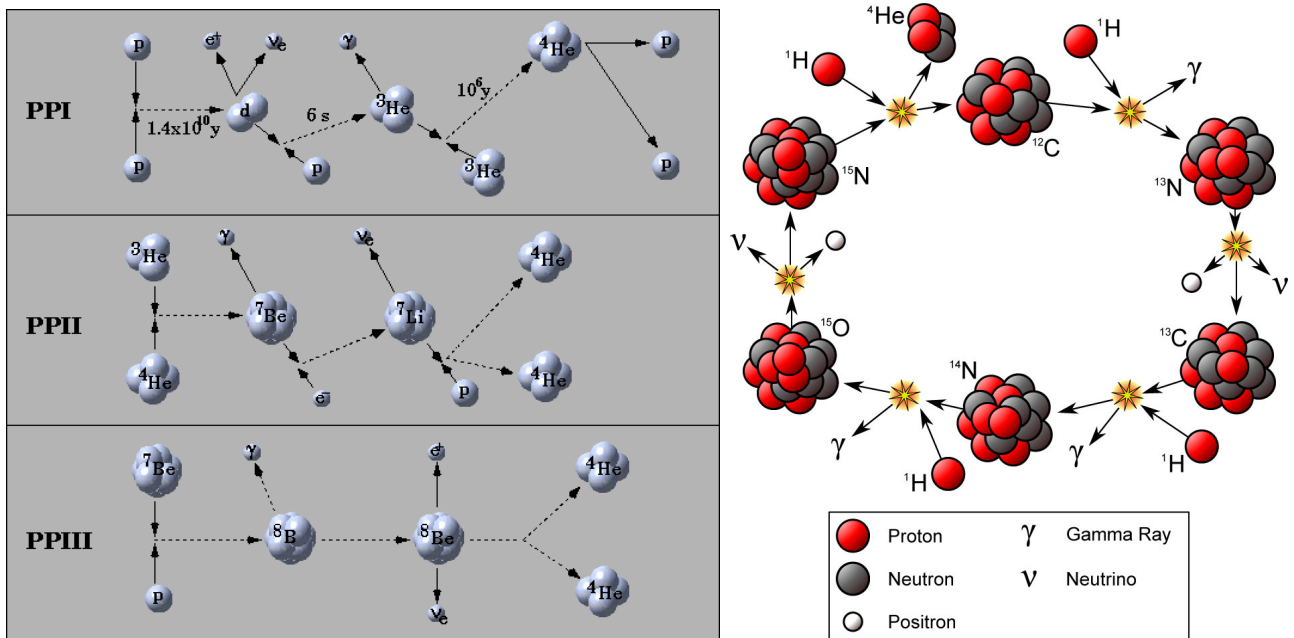


Figure 1.6: Representation of the pp-chain (left) and the CNO cycle (right), happening in the Sun.

3. The final possible variation is for a single ^3He to undergo proton capture:



productions in different flavor percentages. However, this interaction requires a flavor change and is thus weak and very slow compared to the other two possible interactions: the branching ratio is about 10^{-8} . The chain would also conclude at this point since a helium nucleus is produced.

After the conclusion of the ppII branch, only one possible reaction 1.69 has not led to a termination. If a ppI branch results in ^7Be , then the chain continues with the ppIII branch with two possible interactions to burn the ^7Be :

1. The vast majority of the time that the reaction gets to this point in the chain (roughly 15% of all the reactions), the ^7Be encounters an electron and captures it in the reaction:



The electron capture can occur to the ground state as well as the first excited state of ^7Li , the former gives the full energy 0.862 MeV to the neutrino, and the latter gives only 0.383 MeV to the neutrino. The branching ratio to the excited state of ^7Li is roughly 10%. Once the Li has been produced it quickly captures a free proton in the reaction:



2. The remaining 0.016% of the time, the ^7Be captures a proton in the reaction:



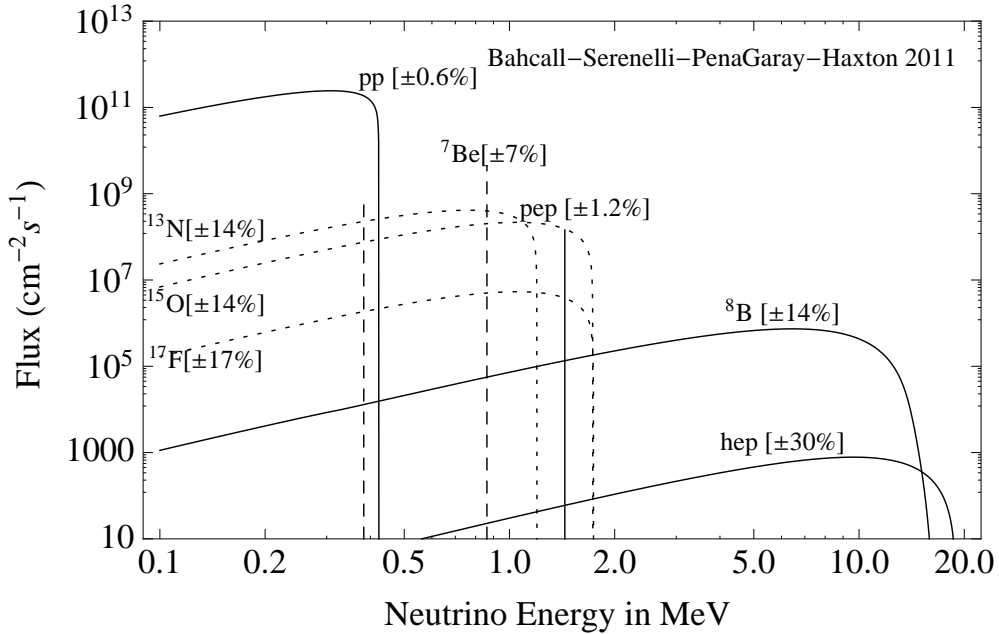


Figure 1.7: Plot of neutrino flux versus energy for the pp chain (black) neutrinos as well as the CNO cycle (blue) neutrinos. Model uncertainties in the fluxes are indicated for each component of the pp chain and CNO cycle. The data used to draw the picture are from [34].

The ${}^8\text{B}$ produced is unstable and splits into two helium nuclei via:



A plot of the neutrino fluxes versus energy is given in Figure 1.7. One might wonder why the production of He does not proceed immediately after the first step in the chain by merging two deuterium nuclei via: ${}^2\text{H} + {}^2\text{H} \rightarrow {}^4\text{He}$. While in theory this is possible, the production of ${}^3\text{He}$ via the reaction depicted in Eq. 1.67 occurs so rapidly, and the first step is so slow, that the local abundance of deuterium is never (statistically speaking) high enough for the fusion of two deuterium nuclei into helium to occur.

1.6.4 The CNO cycle

The Sun produces its energy primarily through the pp chain reactions. Approximately 98.5% of its luminosity is from the pp chain, and the remaining 1.5% is generated by the reactions in the CNO cycle. In terms of the solar neutrino flux, the CNO neutrinos contribute about 0.76% of the total solar neutrino flux with the pp chain taking up the rest. The basic process of fusing four protons into a helium nucleus, two positrons, and two neutrinos is still the same, however, in this case, nuclei of carbon, nitrogen, and oxygen participate as spectators which catalyze the reactions. In stars significantly larger than the Sun, the core temperature is high enough for the participating particles to overcome the Coulomb barrier and thus for the CNO cycle to become the dominant energy production scheme. This high degree of correlation to the core temperature introduces significant uncertainty in the CNO fluxes.

The chain of reactions is shown in right panel of Figure 1.6. The cycle begins with a ^{12}C nucleus capturing a free proton to form radioactive ^{13}N which in turn produces a neutrino:



The neutrino produced in reaction 1.76 has a continuous spectrum up to $2.221 - 2.0511 = 1.199$ MeV. The reaction continues with the decay of ^{13}C until it reaches a branching point after the production of ^{15}N :



Again, the neutrino produced in reaction 1.79 has a continuous energy with an endpoint given by the Q value minus the energy of the annihilation gammas: 1.732 MeV. At this point, the ^{15}N can decay by one of two channels; the most probable one has a branching ratio of 99.9% and proceeds via:



The ^{12}C produced in reaction 1.80 is now available to begin the chain again at reaction 1.75. The other possible method of burning the ^{15}N proceeds at much lower rate because the temperature in the core is not sufficient to appreciably burn it.



Only in 0.01% of the cases the CNO chain produces a neutrino from the decay of ^{17}F , thus the flux is much lower. In Figure 1.7 also the fluxes of neutrinos from CNO cycle are shown.

1.6.5 The Solar Abundance Problem

Currently, the scenario of the solar models is affected by a controversy about the solar chemical composition. The solar metallicity, that is the abundance of the elements heavier than He, is inferred in two complementary ways: from meteorites (in particular from the so-called chondrites) and from the solar photospheric spectrum. As the extraction of informations about the chemical composition from the solar spectrum requires first a modelization of the solar atmosphere, the solar abundances obtained in this way are strongly model-dependent. Until about 2005, the solar atmosphere was described by a 1D time-independent model that has some problems in the reproduction of the spectral lines and doesn't reproduce the surface granulation. Then, a new generation of atmospheric models has been introduced, namely 3D hydrostatic and time-dependent models that very well reproduce the spectral lines with their characteristics, as shifts and asymmetries. The two kind of models give noticeably different chemical compositions: 3D models lead to a

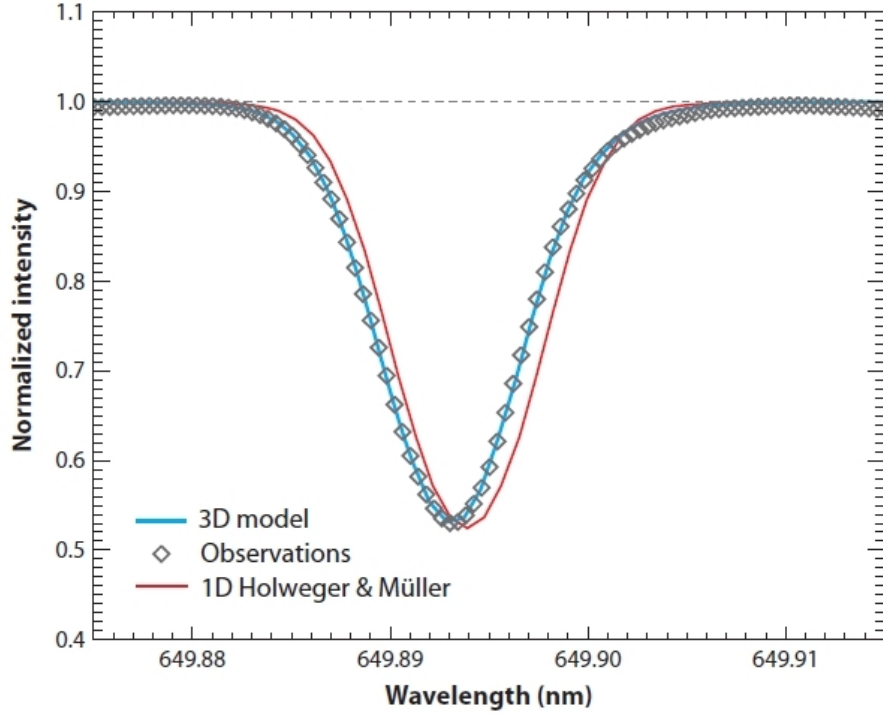


Figure 1.8: Reproduction of a spectral line, according to the 3D model (light blue line) and to the 1D model (red line). Comparison with data (rhombes) highlights the accuracy of the 3D model.

noticeable reduction of the solar metallicity, especially for the elements C, N and O. Then, solar models assuming the metallicity from 1D models (GS98) are named *high metallicity* models, while the other based on abundances from 3D atmospheric models (AGS05, AGSS09) are named *low metallicity* models.

The internal structure of the Sun predicted by the standard models can be tested against helioseismological observations on some characteristics, namely: the depth of the convective envelope $R_{\text{CZ}}/R_{\text{Sun}}$, the profiles of density and sound speed and the surface helium mass fraction. Moreover, the study of the low-degree modes, which penetrate the inner solar region, allows to investigate the functioning of the two models also in the solar core. The internal structure predicted by high metallicity models is in exceptional agreement with helioseismology for all the mentioned characteristics; conversely, the low metallicity models are in disagreement with helioseismology. In particular, the GS98 model predicts a depth of the convective envelope in agreement with observation at 1.8σ , while the AGS05 model gives a discrepancy at 15σ . The discrepancy in the sound speed for the GS98 model is 0.3%, while for the AGS05 model it is 1.2%; analogous results for the density profile.

In conclusion, the solar abundance problem consists in the incompatibility between the best solar atmosphere model and the best solar interior model. The difference in metallicities rebounds on the amplitude of the neutrino flux predicted by the models. Table 1.3 shows the amplitude of the neutrino flux components predicted by the high and low metallicity models in the last version [34]. As the last column highlights, the drop in metallicity causes a 9% reduction in the ${}^7\text{Be}$ neutrino flux; the decrease is even larger for ${}^8\text{B}$ neutrinos and for neutrinos produced in the CNO cycle. Unlikely, due to the uncertainty of the models, even a very precise measurement of ${}^7\text{Be}$ or ${}^8\text{B}$ neutrinos is not enough

Component	SFII-GS98	SFII-AGS09	Difference (%)
pp	5.98(1 ± 0.006)	6.03(1 ± 0.006)	0.8
pep	1.44(1 ± 0.011)	1.47(1 ± 0.012)	2.0
hep	8.04(1 ± 0.15)	8.31(1 ± 0.30)	3.4
^7Be	5.00(1 ± 0.06)	4.56(1 ± 0.07)	-8.8
^8B	5.58(1 ± 0.11)	4.59(1 ± 0.14)	-17.7
^{13}N	2.96(1 ± 0.15)	2.17(1 ± 0.14)	-26.7
^{15}O	2.23(1 ± 0.15)	1.56(1 ± 0.15)	-30.0
^{17}F	5.52(1 ± 0.17)	3.40(1 ± 0.16)	-38.4

Table 1.3: Amplitudes of the solar neutrino flux components predicted by the SFII-GS98 model (high metallicity) and by the SFII-AGS09 model (low metallicity) [34]. Components are expressed in unit of 10^{10} (pp), 10^8 (pep, ^{13}N , ^{15}O), 10^3 (hep), 10^9 (^7Be), 10^6 (^8B , ^{17}F) $\text{cm}^{-2} \text{s}^{-1}$. The difference is quoted with respect to the SFII-GS98 values.

to discriminate between the two models. The hope is related to the CNO measurement: independently from the model uncertainty, the difference between the central values could be enough for a disentanglement. In addition, a measure of the CNO component would be extremely important: it could lead to determine the solar core composition since the CNO neutrinos are the most sensitive to the differences in metallicity. In [31], Borexino has just published an upper limit for the CNO rate.

1.6.6 The mapping of the solar neutrino survival probability

As already described, matter interaction effects can dramatically influence the pattern of neutrino oscillations in the Sun, since the neutrino matter interaction cross sections are flavor dependent and the matter distribution in the Sun contains only first generation particles (electrons). The oscillation theory in the MSW-LMA scenario predicts a peculiar behavior of survival probability (P_{ee}) as a function of neutrino energy (see Figure 4.1):

- at low energies ($E < 1 \text{ MeV}$) the oscillation mechanism is the same as in the *vacuum* and P_{ee} is about 60%;
- at high energies ($E > 5 \text{ MeV}$) the oscillations are dominated by *matter* effects during the travel through the Sun, and P_{ee} decreases down to 30%.

The real time experiments based on Čerenkov technique have a high energy threshold and could observe only the final part of ^8B neutrino spectrum. In 2008 the Borexino Collaboration published the measurement of ^7Be solar neutrino, investigating for the first time in real time the vacuum region and giving a strong constraint on the pp value [35]. Thus, in 2008 the situation for the P_{ee} mapping was the one showed in Figure 1.9. It is evident that the energy region between 1 and 4 MeV was totally unexplored⁸. As well explained in Chapter 4 and 6, new experimental dots have been added thanks to the ^8B solar neutrino measurements performed by Borexino [36] and SNO [37] experiments. In

⁸After the present ^8B analysis in Borexino, the lowest energy threshold in Čerenkov experiments, corresponding to 3.5 MeV, has been reached by the SNO experiment [37].

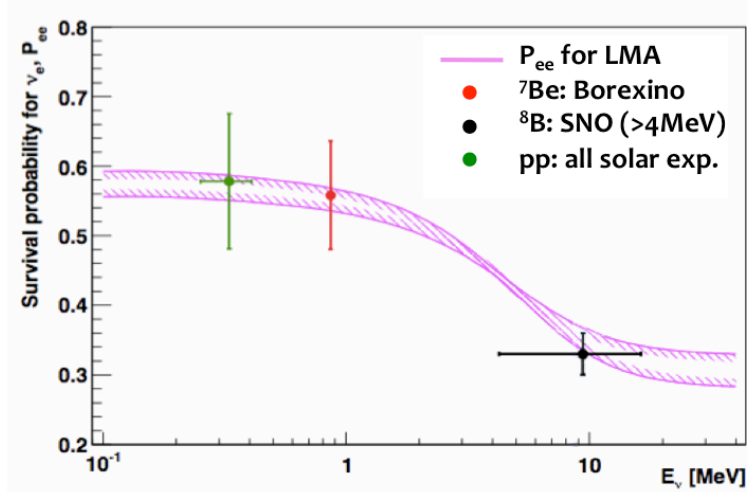


Figure 1.9: Electron neutrino survival probability as function of the neutrino energy, evaluated for the ^8B neutrino source assuming the BPS09(GS98) Standard Solar Model [38, 39] and the oscillation parameters from the MSW-LMA solution $\Delta m^2 = 7.69 \times 10^{-5} \text{ eV}^2$ and $\tan^2 \theta = 0.45$ [40]. Dots represent the experimental results: ^7Be by Borexino (red), ^8B from SNO (black) and pp from all the solar neutrino experiments (green).

addition, the error on the P_{ee} measured by Borexino for ^7Be neutrinos have been reduced. Extremely recently a new dot from Borexino appeared on the P_{ee} map, thanks to the pep solar neutrino measurement [31]. The present situation is shown in Figure 1.10. Nevertheless, it is evident that the so called *intermediate region* still needs some further investigations: the complete validation (or not) of the MSW-LMA solution needs new and more accurate measurement of low energy solar neutrinos.

Non Standard Interactions?

Non Standard Interaction (NSI) can play a crucial role in defining the neutrino interaction with matter [41, 42, 43]. In particular, such new interactions may produce appreciable deviations only in the intermediate energy region [44] describing the transition between vacuum-like and matter-dominated conversions, without affecting the well established behaviors observed at low and high energies. Therefore, the accurate observation of this energy region is of crucial importance for pinning down potential new physics beyond the Standard Model.

NSI are described by low-energy four-fermion operators $\mathcal{O}_{\alpha\beta} \sim \bar{\nu}_\alpha \nu_\beta \bar{f} f$ of sub-weak strength $\epsilon_{\alpha\beta} G_F$, especially of the flavor-changing type ($\alpha \neq \beta$). As already mentioned, in the presence of ordinary matter, the standard electroweak theory predicts $H_{\text{dyn}}^{\text{std}} = \text{diag}(V, 0)$, where $V(x) = \sqrt{2}G_F N_e(x)$ is the effective potential induced by the charged current ν_e interaction with the electrons having number density $N_e(x)$. For interactions with a background fermion f with number density $N_f(x)$, the new term can be expressed as:

$$H_{\text{dyn}}^{\text{NSI}} = \sqrt{2}G_F N_f(x) \begin{pmatrix} 0 & \epsilon \\ \epsilon & \epsilon' \end{pmatrix}, \quad (1.85)$$

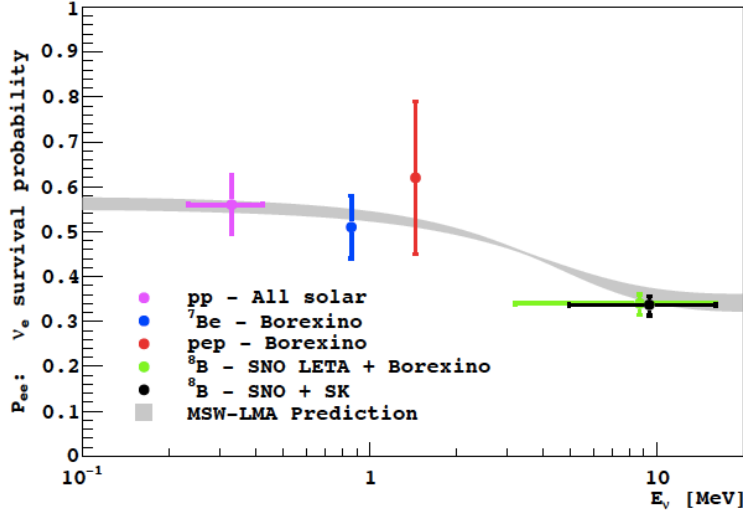


Figure 1.10: Electron neutrino survival probability as a function of energy. The experimental points are also shown, corresponding to different measurements: pep neutrinos (red), pp neutrinos (pink), ${}^7\text{Be}$ neutrinos (blue) and ${}^8\text{B}$ neutrinos (green and black). See [31] for details.

where ϵ and ϵ' are two effective parameters which, restricting to the case of flavor-changing interactions with d-quarks, are related to the fundamental vectorial couplings $\epsilon_{\alpha\beta}^{dV}$ as:

$$\epsilon = \epsilon_{e\mu}^{dV} \cos \theta_{23} - \epsilon_{e\tau}^{dV} \sin \theta_{23}, \quad \epsilon' = -\epsilon_{\mu\tau}^{dV} \sin 2\theta_{23} \quad (1.86)$$

where θ_{23} is the atmospheric mixing angle. The diagonal effective coupling ϵ' can be neglected. Therefore, the conversion of solar neutrinos is described by the mass-squared splitting $\Delta m^2 = m_2^2 - m_1^2$, the mixing angle θ_{12} , and the effective parameter ϵ .

Neglecting the effect due to the terrestrial matter, the P_{ee} can be written as usual:

$$P_{ee} = \frac{1}{2} + \frac{1}{2} \cos 2\theta_{12} \cos 2\theta_{\text{NSI}} \quad (1.87)$$

where θ_{NSI} is:

$$\theta_{\text{NSI}} = \frac{2\theta_{12} - \nu}{\sqrt{(\cos 2\theta_{12} - \nu)^2 + (\sin 2\theta_{12} + 2\epsilon\nu)^2}}. \quad (1.88)$$

The ν parameter depends on x_\odot , the solar radius unity:

$$\nu(x) = 1.53 \times 10^{-7} \left(\frac{\Delta m_{12}^2}{E} \frac{\text{MeV}}{\text{eV}^2} \right)^{-1} \left(\frac{N_e(x)}{\text{mol/cm}^3} \right), \quad (1.89)$$

where $N_e(x)$ is the electron density in the Sun. For ${}^8\text{B}$ neutrinos, $x=0.04$, so:

$$\nu(x=0.04) = 0.18 \frac{E}{\text{MeV}}. \quad (1.90)$$

In Figure 1.11 the effect on the survival probability for $\epsilon=-0.16$ is shown [45]. As pointed out in [45], latest solar neutrino data from SNO and Borexino (in combination with the other solar experiments and KamLAND) favor the presence of non-standard dynamical terms in the MSW Hamiltonian at a non negligible statistical level; this hints at

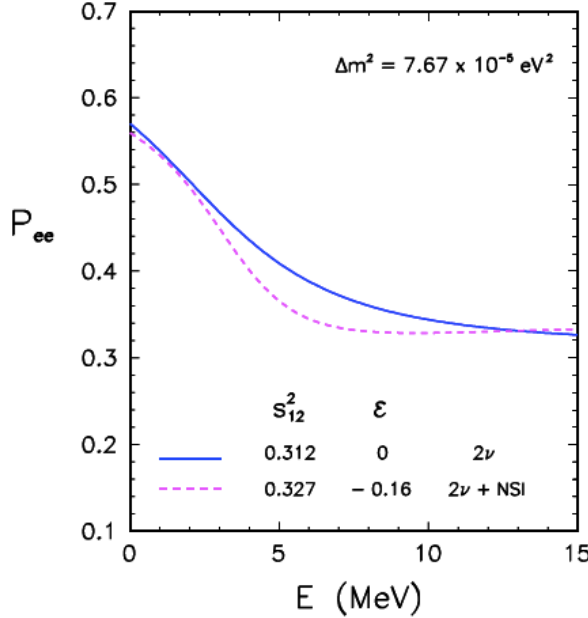


Figure 1.11: Solar ν_e survival probability (averaged over the ${}^8\text{B}$ production region) for the best-fit points obtained with (dashed line) and without (solid line) NSI effects.

new neutrino interactions, such new sterile neutrino states or Non Standard Interactions. The identification of the correct sub-leading effect needs further corroboration from new indispensable low-energy solar neutrino measurements. This has been the attempt during my Thesis, pushing me in working on the measurement of low energy ${}^8\text{B}$ neutrinos (see Chapter 6) and collaborating on the pep neutrino analysis [31].

Sterile neutrinos?

In [46], the consequences of the hypothesis of new sterile neutrino species at the eV scale are explored in the solar sector phenomenology. The interest around the possible manifestation of novel neutrino properties in very short baseline (VSBL) setups has been recently reawakened by the emergence of new inconsistencies (see Section 1.5) that may represent a manifestation of new physics. From this perspective, they seem to point towards a phenomenon of (dis-)appearance of the electron neutrinos, possibly mediated by oscillations into new sterile species [47, 48]. An independent hint in the same direction arises from the latest cosmological data analyses [49], which favor a significant extra relativistic energy content, although pointing towards masses of the new presumptive light particles [49], which are at the borderline of those (larger) suggested for the sterile neutrinos by the oscillation data.

The putative sterile neutrinos must be introduced without spoiling the basic success of the standard 3-flavor paradigm. This can be achieved in the so-called $3+s$ schemes, where the s new mass eigenstates are assumed to be separated from the three standard ones by large splittings, giving rise to the hierachal pattern:

$$|m_2^2 - m_1^2| \ll |m_3^2 - m_1^2| \ll |m_k^2 - m_1^2| \quad (k = 4, \dots, 3+s).$$

This ensures that the fast oscillations induced by the new mass eigenstates are completely averaged in all settings sensitive to the Δm_{12}^2 -driven (solar) and Δm_{13}^2 -driven (atmospheric) transitions, leaving unmodified the two well-established oscillation frequencies. With the additional assumption of a small admixture of the active flavors with the new mass eigenstates, the 3+s schemes leave basically unaltered also the standard oscillation amplitudes, thus realizing a genuine perturbation of the leading 3-flavor scenario, whose size must respect the constraints imposed by all the existing phenomenology.

The solar sector data (Solar and KamLAND) have had a pivotal role in establishing and shaping the 3-flavor framework. These data are the only ones sensitive to the admixture of the electron neutrino with the first two mass eigenstates (ν_1, ν_2), also possessing a subleading sensitivity to the (averaged) ν_3 -driven oscillations. It is of certain interest to explore how such a sector “responds” to the perturbations generated by a non-zero mixing of the electron neutrino with new sterile species.

In [46] the perturbations induced by a non-negligible mixing of the electron neutrino with a fourth sterile neutrino specie, in a CPT-conserving 3+1 scheme, has been studied. The quantitative analysis shows that the present data posses a sensitivity to the amplitude of the lepton mixing matrix element U_{e4} , which is comparable to that achieved on the standard matrix element U_{e3} . In addition, this analysis evidences that, in a 4-flavor framework, the current preference for $|U_{e3}| \neq 0$ is indistinguishable from that for $|U_{e4}| \neq 0$, having both a similar statistical significance (which is $\sim 1.3\sigma$ adopting the old reactor fluxes determinations, and $\sim 1.8\sigma$ using their new estimates.) Such a degeneracy extends to the more general 3+s schemes, implying that in these frameworks, the present hint for non-zero θ_{13} must be reinterpreted as a preference for a non-zero mixing of the electron neutrino with mass eigenstates distant from the (ν_1, ν_2) “doublet”. Different kinds of probes are needed in order to discriminate whether such an admixture is realized with the third standard mass eigenstate ν_3 or with new neutrino specie(s).

Done the curiosity around the sterile neutrino mystery, many projects are currently under study in order to investigate the $\Delta m^2 \simeq 1\text{ eV}^2$ sector. In particular, a proposal involves the measure of $\nu_\mu \rightarrow \nu_e$ oscillations with liquid Argon detector [50], and others involve the use of ν_e or $\bar{\nu}_e$ sources with liquid scintillator detectors [51, 52].

1.6.7 Future solar neutrino experiments

The answers for the open issues just exposed will arrive from new Borexino data and next solar neutrino experiments.

About Borexino, a re-purification campaign has just been taken, allowing the reduction of ^{210}Bi contaminant. This could allow in the future a reduction on the errors of the ^7Be and pep measurements.

About new experiments, they will take advantage of the experience of old experiments, improving the known techniques. The main projects at the moment are SNO+ and Laguna.

- **The SNO+ experiment.** The excellent conditions of depth and cleanliness of the Sudbury Neutrino Observatory (SNO) have allowed it to perform very accurate spectral and flavor composition measurements of the ^8B solar neutrino flux [23, 37, 53]. After the removal to the heavy water, the SNO+ experiment [54, 55] aims at adapting the SNO detector to address further fundamental questions in Neutrino Physics:

the Dirac/Majorana nature of the neutrino fields and the nature of neutrino oscillations, as well as to use neutrinos to probe the Sun, the Earth and Supernovae. For oscillation experiments, solar neutrinos remain a convenient source due to their high flux and flavor purity. The pep solar neutrino component is especially favorable due to having a single energy (1.442 MeV) and a very well predicted flux (1.5% uncertainty), basically determined (as the pp neutrinos) by the Sun's luminosity constraint (see Section 1.6). Accurate measurements of neutrino survival probabilities in this energy range can improve the precision on the oscillation parameters and provide sensitivity to alternative models of neutrino mixing (as NSI or sterile neutrinos). In high-radiopurity experiments, decays of the cosmogenically produced ^{11}C isotope are the main background for this signal. Coincidence event can be used to partially tag this background (see Chapter 7 and [32]). However, a deep location is of course much more effective. The SNO detector is located at a depth of 6000 m w.e. (meters of water equivalent), where the cosmic muon flux is low enough to minimize the cosmogenic ^{11}C and ^{10}C backgrounds, making the pep solar neutrino flux measurement (through $\nu_e - e^-$ elastic scattering) possible at SNO+ with a good accuracy. In addition, in this energy range, a measurement of the CNO solar neutrino component should also be possible, providing important information for Solar models (see Section 1.6).

- **The Laguna project.** The FP7 Design Study LAGUNA (Large Apparatus studying Grand Unification and Neutrino Astrophysics) is a collaborative scientific project [56] addressing the feasibility of a new European research infrastructure hosting a deep and large underground neutrino detector for fundamental research in particle and astroparticle physics. It is an EC-funded project carrying on underground sites studies and developments in view detectors observatories with a mass in the range of $10^5 - 10^6$ tons in a low background environment. The detector will perform studies of neutrino properties, detect terrestrial, solar or galactic sources of neutrinos and look for the radioactive decays of proton. The detector is envisioned as a very large target made of either water (MEMPHYS), liquid argon (GLACIER) or liquid scintillator (LENA). The study is evaluating possible extensions of the existing deep underground laboratories, and on top of it, the creation of new laboratories in the following regions: Umbria Region (Italy), Pyhäsalmi (Finland), Sieroszowice (Poland) and Slanic (Romania).

The combination of the large mass with the background shield will allow improved measurements of low energy solar neutrinos.

1.7 Reactor neutrino experiments for θ_{13}

As already described in Section 1.4, the amplitudes and frequencies of flavor oscillation phenomena are governed, respectively, by the θ_{ij} angles and by two squared mass differences, namely, Δm_{12}^2 and Δm_{23}^2 . Typically, a single experiment is mainly sensitive to only one of the above mass gaps and to one mixing parameter, although subleading effects driven by the remaining parameters may become relevant in precision oscillation searches.

Solar and long-baseline reactor neutrino experiments have measured the mass-mixing parameters ($\Delta m_{12}^2, \theta_{12}$) in the $\nu_e \rightarrow \nu_e$ channel, while atmospheric and long-baseline accel-

erator (LBL) experiments have measured $(\Delta m_{23}^2, \theta_{23})$ in the $\nu_\mu \rightarrow \nu_\mu$ channel. Conversely, short-baseline reactor experiments, mainly sensitive to $(\Delta m_{23}^2, \theta_{13})$, have set upper-bounds on the mixing angle θ_{13} . As shown in [57, 58], the two data sets mainly sensitive to Δm_{12}^2 and to Δm_{23}^2 provided two separate hints in favor of $\theta_{13} > 0$ which, in combination, disfavored the null hypothesis $\theta_{13} = 0$ at 90% C.L. [58].

Within the standard 3ν framework, the overall statistical significance of $\theta_{13} > 0$ has, so far, not exceeded the level of $\sim 2\sigma$, with a corresponding estimated range $\sin^2 \theta_{13} \simeq 0.02 \pm 0.01$ [59].

Very recently (June 2011), new relevant results have been announced by two long-baseline accelerator experiments probing the $\nu_\mu \rightarrow \nu_e$ appearance channel, which is governed by the $(\Delta m_{23}^2, \theta_{13})$ parameters. In particular, the Tokai-to-Kamioka (T2K) experiment has observed 6 electron-like events with an estimated background of 1.5 events, rejecting $\theta_{13} = 0$ at the level of 2.5σ [60].

Shortly after, the Main Injector Neutrino Oscillation Search (MINOS) experiment has reported the observation of 62 electron-like events with an estimated background of 49 events, disfavoring $\theta_{13} = 0$ at 1.5σ [61, 62]. Taken together, these data suggest $\sin^2 \theta_{13} \simeq \text{few}\%$.

Including the latest T2K and MINOS results, as well as other data which have been published in the last few years, the result is [63]:

- $\sin^2 \theta_{13} = 0.021 \pm 0.007$, for old reactor fluxes;
- $\sin^2 \theta_{13} = 0.025 \pm 0.007$, for new reactor fluxes⁹:

corresponding to a $>3\sigma$ evidence in favor of nonzero θ_{13} (while previous hints did not exceed the $\sim 2\sigma$ level).

Reactor experiments see a large signal of $\bar{\nu}_e$ events (see Section 1.3.4), and search for a small deviation from the non-oscillation prediction due to θ_{13} -induced $\bar{\nu}_e$ disappearance. The signal of a reactor anti-neutrino is provided by the reaction:



a process with an energy threshold of 1.8 MeV where the positron provides a prompt signal (boosted by the two 511 keV annihilation gamma rays) and the neutron a delayed signal (in liquid scintillator this delay is about 170 μs). The coincidence of the two signals is powerful enough to make possible the running of the experiment with a tolerable level of backgrounds.

Liquid scintillator can be loaded with 0.1% natural gadolinium, an element with high thermal neutron capture cross-section. In this way the neutron capture time is reduced from $\sim 170\ \mu\text{s}$ to $\sim 27\ \mu\text{s}$, allowing for the reduction of the uncorrelated background. Furthermore, Gd de-excitation after capture releases an 8 MeV γ cascade (it would be ~ 2 MeV in pure liquid scintillator), producing an integrated signal well above the natural radioactivity.

The CHOOZ experiment [66] concluded its data taking with a 2.8% statistical and a 2.7% systematical error. The goals of a follow-up experiment are to improve CHOOZ sensitivity

⁹For details about the new evaluations of reactor fluxes see [64].

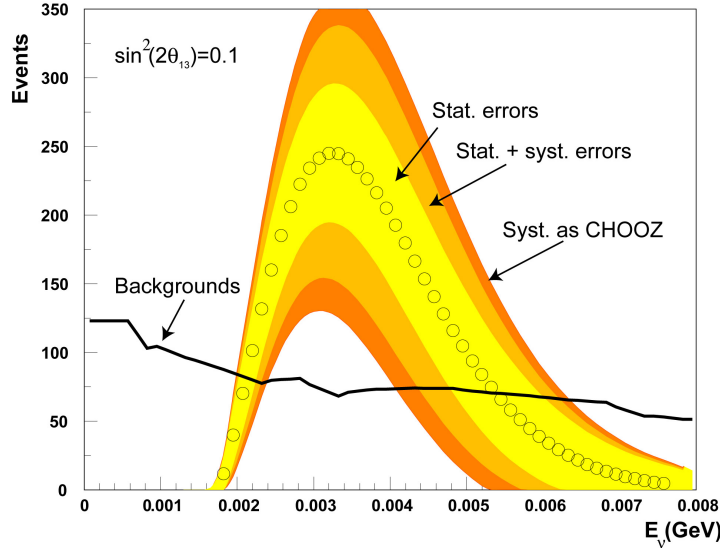


Figure 1.12: Expectation for number of disappeared events in Double Chooz for $\sin^2 2\theta_{13} = 0.1$, i.e., the difference between no-oscillation and oscillation spectra in the far detector. Also shown are statistic and expected systematic errors, together with systematic errors as big as the former Chooz experiment. The signal is compared to the expected background rate. Based on data from [72].

by a factor 5 at least. This roughly reflects on a factor five improvement both in statistics and in systematics:

- **Improving the statistics.** The CHOOZ detector was a 5 ton detector exposed to two reactors of 8.6 MW thermal power at a distance of 1.05 km. The experiment integrated a total run of 8761.7 h, only 1543.1 of which with the two reactors on and 3245.8 h with one of the two reactors on. To gain a factor 25 in the number of neutrinos a detector twice as big running 3 years with an improved efficiency is needed. The main limiting factor in this direction is the stability of a gadolinium doped liquid scintillation detector. Important progress has been made in this field in recent years [67] such that a running time of 5 or more years seems feasible.
- **Improving the systematics.** More difficult is the reduction of systematics. This task is particularly challenging because CHOOZ had the very rare opportunity of directly measuring the backgrounds with the nuclear reactors off. The first important action is to introduce a close detector as similar as possible to the far detector [68], in order to measure the neutrino interaction rate before oscillations. In this way uncertainties on the neutrino rates (around 2%) almost cancel out. This approach has some intrinsic limitations. The neutrino rates can't be the same in the two detectors (even in absence of oscillation) because of the different coverage and of the different distance from the source. The calibration and live-time of the detectors must be kept as similar as possible. In a configuration where more than one reactors are present, the close detector doesn't measure the identical flux of the far one. This is because the neutrino flux of a reactor varies in time according to the core composition which differs from reactor to reactor following their fuel refurbishment.

In Figure 1.12 the size of the disappearance signal in Double Chooz, compared to statistical and systematical errors as well as the expected background, is shown.

Setup	P_{Th} [GW]	L [m]	m_{Det} [t]	Events/year	Backgrounds/day
Double Chooz [72]	8.6	1050	8.3	$1.5 \cdot 10^4$	3.6
Daya Bay [73]	17.4	1700	80	$10 \cdot 10^4$	0.4
RENO [70]	16.4	1400	15.4	$3 \cdot 10^4$	2.6

Table 1.4: Summary of experimental key parameters of upcoming reactor neutrino experiments: the thermal reactor power, the approximate distance between reactors and far detector, and detector mass, neutrino events per year, and background events per day, all for the far detector. RENO backgrounds are the sum of correlated backgrounds as computed in [70] and uncorrelated backgrounds as estimated in [71].

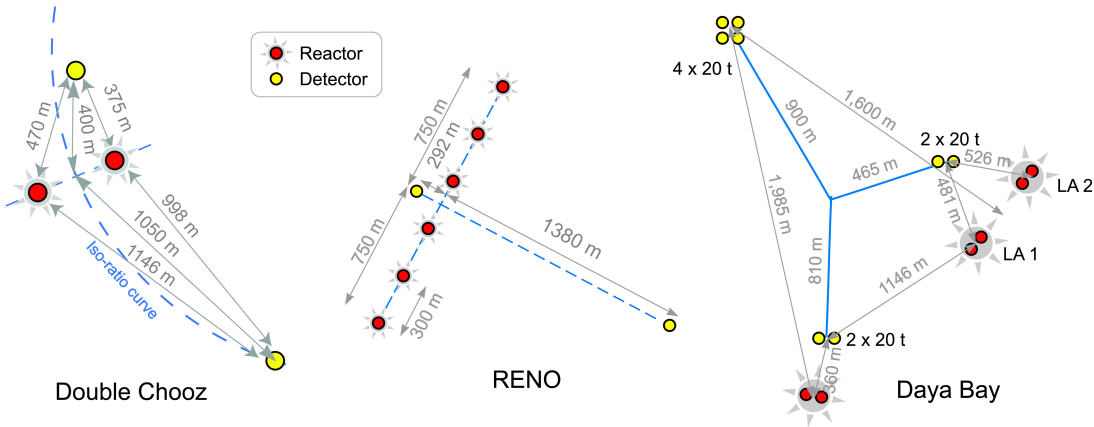


Figure 1.13: Configuration of the experimental layout of Double Chooz, RENO, and Daya Bay. The dashed curve in the Double Chooz configuration is the far flux iso-ratio curve. Updated from [71].

The backgrounds of reactor neutrino experiments are of two types: uncorrelated signals from cosmic rays and natural radioactivity and correlated signals from neutrons generated by cosmic muons. Uncorrelated signals can be separately measured and normalized. Their random coincidences can generate background events that can be kept at a negligible level with a careful choice of low activity materials and design of the detector.

More problematic are neutrons induced by cosmic muons (see Chapter 7). A cosmic muon not crossing the detector can induce spallation or be captured on the materials outside the detector. These can produce neutrons that escape the vetoes and produce correlated signals inside the detector that can mimic the anti-neutrino signals. Among the cosmogenically produced isotopes there are some long lived, as ${}^8\text{He}$ and ${}^9\text{Li}$, with decay times of 119 ms and 174 ms respectively [69], that make hardware active vetoes impractical. As an example, the close detector of RENO is expected to have a 25% dead time for a 0.5 ms veto after any detected muon in the outer veto. This is the main reason that forces detectors to run at shallow depth, complicating very much the choice of the possible sites.

In next Sections I will describe briefly the three next generation reactor experiments. Table 1.4 summarises a few key parameters and Figure 1.13 illustrates the reactor/detector configurations.

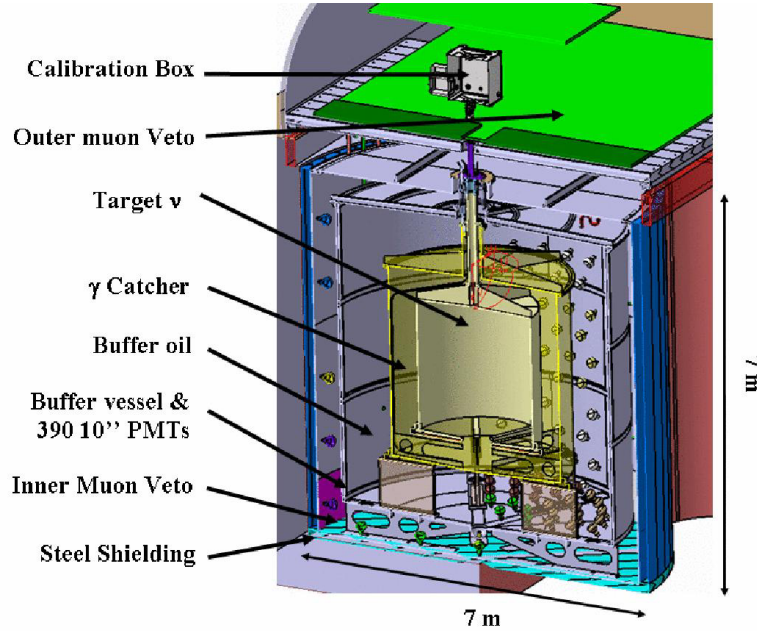


Figure 1.14: Sketch of the Double Chooz detector design [72].

1.7.1 Double Chooz

The Double Chooz experiment [72] is being installed near the Chooz two-core (4.27 + 4.27 GW) nuclear power plant. The far detector, already taking data, is at 1.05 km from the two reactor cores, in the same site as the original CHOOZ experiment, at a depth of about 300 m w.e. (meters of water equivalent). The close detector is designed to be identical to the far detector, it is placed 400 m from the two reactors, at a depth of 115 m w.e., see Fig. 1.13. Let us mention that for $\Delta m_{13}^2 \simeq 2.5 \times 10^{-3} \text{ eV}^2$ the far detector distance of 1 km is somewhat too short, shifting the oscillation signal to the lower part of the spectrum, whereas the near detector distance of 400 m is somewhat too far, with some effect of oscillations already present, see e.g. [68] for far and near detector baseline optimisation studies.

Even if clearly inspired by the CHOOZ design, next generation reactor neutrino detectors have introduced improvements in the design in order to reduce the primary sources of systematics: knowledge of the fiducial volume and backgrounds. The detector of the Double Chooz experiment is shown in Figure 1.14. The inner detector is made of 10.3 m^3 (8.3 metric tons, with a diameter of 2.3 m) of Gd-loaded (0.1%) liquid scintillator in an acrylic vessel. It is immersed in a gamma catcher of 22 m^3 (3.4 m of diameter) of undoped scintillator, aimed to detect the gammas emitted in both the neutron-capture process and positron annihilation in the target. In this way gammas emitted from signal neutrino events in the outer volume of the target are detected, providing a well-defined target volume. A third shield of non-scintillating paraffin oil, 5.5 m diameter, separates the active target and the gamma catcher from the photo-multipliers, greatly reducing the intrinsic radioactivity of the 390 10-inch photo-multipliers, the most radioactive component of the detector (this third shield was not installed inside the CHOOZ detector). The outer detector volume is steel walled, 6.6 m diameter, filled with scintillator and lined with 70 8-inch photo-multipliers, equipping the Inner Veto, having the purpose of detecting and tracking muons and fast neutrons. An Outer Veto is placed on top of the detector, made

of strips of plastic scintillator and wavelength-shifting fibres. Its task is to tag muons interacting around the detector producing cosmogenic isotopes, some of which produce correlated backgrounds in the inner detector, the most dangerous source of backgrounds for the experiment.

The number of neutrinos detected in the far detector assuming 3 years running time will be $\simeq 45000$ compared to 2700 in the CHOOZ experiment, reducing the statistical error from 2.8% to 0.47%. The goal about systematic errors is to reach a level of 0.6%. Without the near detector the systematic error would be about 2.5%.

1.7.2 Daya Bay

The Daya Bay experiment [73] will receive neutrinos from three nuclear plants, each consisting of two cores: Daya Bay, Ling Ao I and Ling Ao II (scheduled to be commissioned by the end of 2010) located in the south of China, 55 km to the northeast of Hong Kong. The thermal power of each core is 2.9 GW, hence the existing total thermal power is 11.6 GW, and will be 17.4 GW after 2010.

The basic experimental layout of Daya Bay consists of three underground experimental halls, one far and two close, linked by horizontal tunnels under construction. The geometry of the reactor cores, the two near detector stations and the far detector station is illustrated in Figure 1.13. It is evident from this configuration that the flux measured by the near detectors will not be identical to the one seen by the far detector. Each close detector hall, at a depth of about 100 m w.e., will host two 20 ton Gadolinium doped (0.1%) liquid scintillator detectors, while the far hall, 350 m w.e., will host four such detectors. The detectors are designed to be movable so that the close detectors and the far ones can be swapped. This swapping is not necessary to reach the designed systematics (0.38%), but could be performed to cross check the sensitivity and possibly further reduce the systematic errors (down to 0.18%).

The design of the detectors is very similar to the Double Chooz one, with the notable difference that the three stations will be submerged in a water pool of 2.5 m depth to shield the detectors from ambient radiation and spallation neutrons. Above the pool a muon tracking detector made of 4 layers of resistive-plate chambers (RPCs) will be installed.

1.7.3 Reno

The RENO [70] experiment is located on the site of the Yonggwang nuclear power plant in the southwestern part of Korea. The plant consists of six reactors lined up in roughly equal distances and spans about 1.3 km. With a total thermal power of 16.4 GW it is at present the second largest nuclear reactor plant in the world.

RENO will use two identical detectors, a close detector at about 290 m from the reactor array (at a depth of about 110 m w.e.) and a far detector at 1380 m (at a depth of about 450 m w.e.), see fig. 1.13. The design of the RENO detectors is very similar to Double Chooz, the active target will be 15.5 ton of Gd loaded (0.1%) liquid scintillator. The outer veto system is a layer of water, 1.5 m thick, contained in a 30 cm thick concrete vessel. PMTs are mounted on the inner surface of the veto container for detecting Čerenkov light from cosmic muons.

Goal of the experiment is to reach a <0.5% systematic error.

Chapter 2

The Borexino Experiment

The Borexino proposal dates back to 1991 [74], in connection with the so called *solar neutrino problems*, whose envisaged solutions were then either an experimental problem, or difficulties in the solar modeling or in the neutrino propagation description.

The main goal of the experiment is the measurement of sub-MeV solar neutrinos. The necessity to develop experiments able to measure the total flux and the flavor content of the ${}^7\text{Be}$ neutrinos (0.86 MeV) had been pointed out by John Bachall [75], the father of the Standard Solar Model (SSM). In particular, in [75] we read "Magic things can be done with neutrino lines, like the 0.86 MeV ${}^7\text{Be}$ line. To make the magic work, one has to measure the neutrino-electron scattering rate (as will be done for the ${}^7\text{Be}$ line with the Borexino experiment)". In addition, Bachall underlines "I think a 1σ measurement of the total rate, for ${}^7\text{Be}$ and for pp neutrinos, that is at least as accurate as $\pm 10\%$ is necessary in order to make real progress". Well, Borexino has recently reached this goal, with the measurement of the ${}^7\text{Be}$ solar neutrino flux with an accuracy better than 5% [9]. And not only: the Borexino publication list involves also the best limit on neutrino magnetic moment [35], the first evidence of geo-neutrinos [14], the measurement ${}^8\text{B}$ solar neutrinos with the lowest energy threshold ever reached in real time (see Chapter 4), the absence of the Day/Night Asymmetry (ADN) [76] and the first observation of pep neutrinos [31]. In this Chapter I will describe how the "magic work" on ${}^7\text{Be}-\nu$ (and all the other Borexino works) has been accurately and patiently driven to the success.

2.1 The Borexino force points

Borexino is a real time solar neutrino experiment, having as a main goal the measurement of low energy solar neutrino flux. The Borexino force lies in three principle features:

- the location, expressly chosen to protect the detector from cosmic rays;
- the use of liquid scintillator as active part of the detector;
- the extreme radiopurity of materials, precisely reached with challenging techniques.

The background problems are particularly hard when the detection energy threshold falls within the energy range of natural radioactivity. The difficulty is not only to reach the required radiopurity levels, but also to have a detector able to measure the counting rate at that level. And Borexino succeeded in getting over these difficulties.



Figure 2.1: *Left:* map of Italy central part; the red A indicates the position of Assergi where LNGS are located. *Right:* the Gran Sasso mountain, protecting all the underground experiments with its 1400 m of rock thickness.

2.1.1 The location: I Laboratori Nazionali del Gran Sasso

The Borexino detector is situated in Hall C of the Laboratori Nazionali del Gran Sasso (LNGS) in Assergi, Italy (see Figures 2.1 and 2.2). The underground portion of the laboratory is located adjacent to the A24 highway tunnel linking Rome with the eastern shoreline of Italy. This location is particularly desired for underground experiment thanks to the low rock radioactivity [78] and excellent protection against cosmic rays: 3.8 km w.e. (km of water equivalent) reduce the cosmic muon flux of a factor 10^6 with respect to the value at sea level. The surviving cosmic muon rate is just $(1.16 \pm 0.03) \text{ m}^{-2}\text{hr}^{-1}$ [77].

2.1.2 Detection principle in Borexino

As pointed out by Bachall, the "magic work" for sub-MeV solar neutrino detection lies in the observation of neutrino-electron scattering rate. In fact, in Borexino solar neutrinos interact with liquid scintillator electrons through elastic scattering:

$$\nu_x + e^- \rightarrow \nu_x + e^- . \quad (2.1)$$

Neutrinos of all flavors can interact through elastic scattering, even if cross sections are different between electron neutrinos and non-electron neutrinos, as the former can undergo CC and NC interactions, while the latter only NC interaction. Energy loss of the recoiling electron kinetic energy produces scintillation light, which is detected by an array of PMTs. The force point is the high scintillator light-yield (about 10000 photons per deposited MeV), allowing to set the energy threshold to a very low value of some tens of keV; because of the presence of ^{14}C , an unavoidable background in organic liquid scintillators ($Q=156 \text{ keV}$), the actual solar neutrino detection threshold is around 200 keV. This does not avoid the clear signature of ^7Be neutrinos and other low energy solar neutrinos.

However, since the emission of scintillation light is isotropic, the employment of scintillator implies the loss of information about neutrino direction.

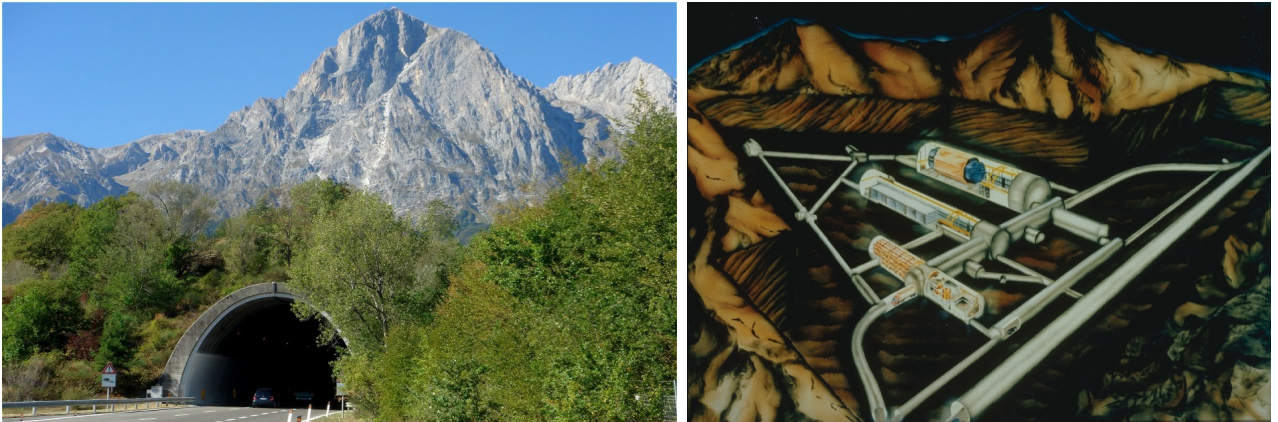


Figure 2.2: *Left:* entrance of the Gran Sasso Tunnel from the highway; underground laboratories are located in tunnels on the right side of the highway. *Right:* scheme of underground laboratories halls; Borexino is located in the Hall C, the first from the top.

In addition, electrons recoiled by neutrinos are indistinguishable from electrons and gammas produced in radioactive decays. Hence, the materials constituting the detector, starting from the scintillator, must fulfill exceptional requirements of radiopurity. In order to allow the measurement feasibility, the background rate must be at maximum of the same order of magnitude of the signal rate. The ^{7}Be neutrino event rate is about 0.5 events per day per ton of scintillator, corresponding to an activity of about $5 \cdot 10^{-9}$ Bq/kg. This value has to be compared with the ordinary radioactivity of water and air, which is about 10 Bq/kg, and with radioactivity of rock, which is about 100-1000 Bq/kg. This means that the materials inside the detector must be characterized by a radioactivity 10 orders of magnitude lower than usual radioactivity on the Earth surface and that radioactivity from the rock must be shielded.

2.1.3 The extreme scintillator radiopurity

The realization of an ultra-low background detector is the key feature of the Borexino experiment. In order to fulfill the severe requirements of radiopurity, several solutions have been adopted and specifically developed.

The radiopurity requirements

First of all, each material constituting the detector has been accurately screened and chosen to be as low radioactive as possible. Suitable purification techniques have been expressly developed to clean the metal surfaces. Moreover, the detector has been designed exploiting the principle of graded shielding: an onion-like structure allows to protect the detector core from external radiation and from radiation produced in the external shielding layers. The requirements on material radiopurity increase when going to the innermost region of the detector.

Long debates concerning the choice of the scintillator have been taken within the Collaboration. As the liquid scintillator (LS) represents the detector active volume, this represents a crucial point. The LS has been accurately selected and purified, in order to

Isotope	Source	Typical abundance	Requirements	Achievements
$^{14}\text{C}/^{12}\text{C}$	radiogenic (oilfields)	$1.2 \cdot 10^{-12} \text{ g/g}$ (organic materials)	$3 \cdot 10^{-18} \text{ g/g}$	$(1.94 \pm 0.09) \cdot 10^{-18} \text{ g/g}$
^{222}Rn	air, emanation, detector materials	150 Bq/m^3 (air)	$< 10^{-16} \text{ g/g}$	$\sim 10^{-17} \text{ g/g}$
^{232}Th	dusts	$2 \cdot 10^{-5} \text{ g/g}$ (dusts)	$< 10^{-16} \text{ g/g}$	$(6.8 \pm 1.5) \cdot 10^{-18} \text{ g/g}$
^{238}U	dusts	$2 \cdot 10^{-5} \text{ g/g}$ (dusts)	$< 10^{-16} \text{ g/g}$	$(1.6 \pm 0.1) \cdot 10^{-17} \text{ g/g}$
^{210}Po	surface contamination		$\sim 1 \text{ cpd/t}$	$\sim 70 \text{ cpd/t}$
^{40}K	dusts, materials, fluor	$2 \cdot 10^{-6} \text{ g/g}$ (dusts)	$< 10^{-14} \text{ g/g}$	$< 3 \cdot 10^{-18} \text{ g/g}$ (90%)
^{85}Kr	air	1 Bq/m^3 (air)	$\sim 1 \text{ cpd/100 t}$	$\sim 30 \text{ cpd/100 t}$
^{39}Ar	air	17 mBq/m^3 (air)	$0.1 \mu\text{Bq/m}^3$	$<< ^{85}\text{Kr}$

Table 2.1: Radiopurity requirements and achievements for the Borexino scintillator.

have a contamination by ^{238}U and ^{232}Th of the order of 10^{-16} g/g , which corresponds to a signal to background ratio of about 1. In addition, since the ^{14}C abundance in the organic scintillator determines the energy threshold of the ^7Be neutrino window, the requirement for the ratio $^{14}\text{C}/^{12}\text{C}$ is 10^{-18} g/g . This allows to set the detection threshold at 250 keV.¹ For five years, the collaboration have been developing appropriate techniques to purify the scintillator at such levels of radiopurity.

Also water and Nitrogen are needed at exceptionally high levels of radiopurity. The Nitrogen purity requirement is such that the expected background from ^{222}Rn , ^{39}Ar and ^{85}Kr in 100 t of target scintillator must be less than 1 count/day. This corresponds to 0.36 ppm for Ar and 0.16 ppt for Kr. Nitrogen is needed to profusely sparge the scintillator, in order to remove Oxygen, which alters its optical properties, and radioactive isotopes carried by air, such as ^{222}Rn , ^{39}Ar and ^{85}Kr . Water is employed as the most external shield.

Also the construction techniques have been finalized to avoid any contaminations: each detector part was treated in class 10-100 clean room; during the assembling, the detector was treated as a class 1000-100000 clean room; each plant was cleaned through pickling, passivation and final rinsing with high purity water and kept in ultra-pure Ar protection.

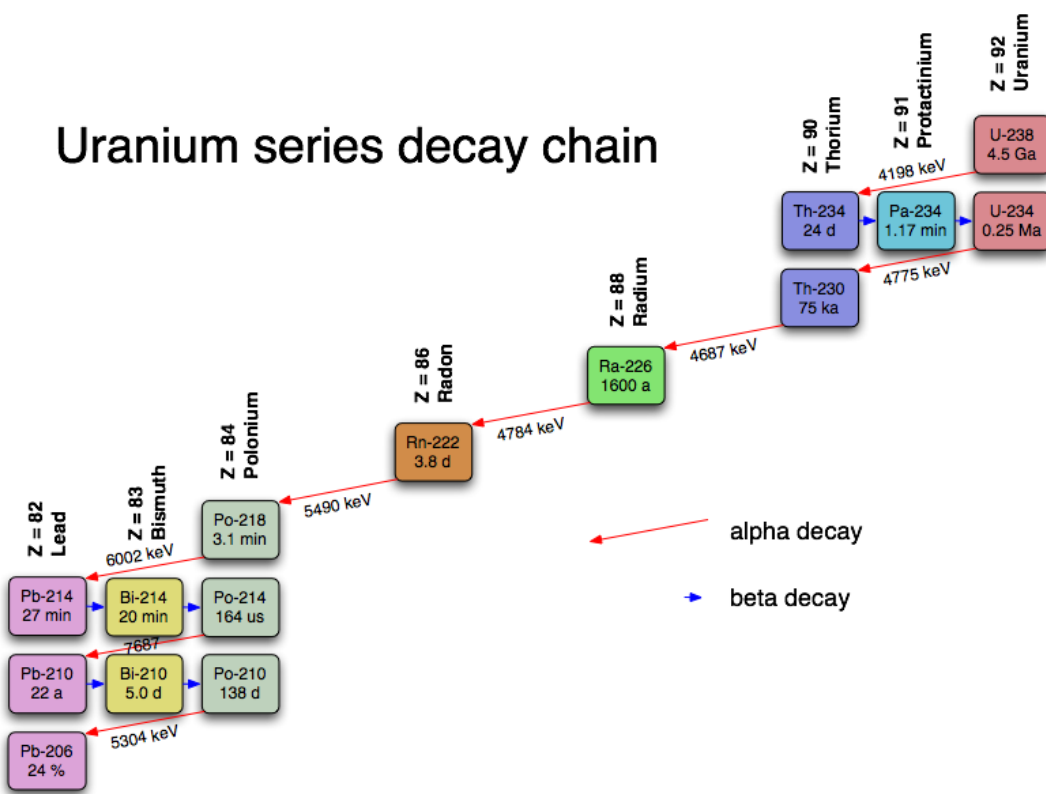
The achieved radiopurity

The applied solutions to bring radioactivity down has given results that are even better than the project requirements (see Table 2.1). Such remarkable results have been obtained also thanks to CTF, the Borexino prototype. It is a simplified version of the Borexino detector, built in the underground laboratories near the main detector. It has been built before the main detector and it has been the fundamental device in the R&D phase, in the development of the new purification techniques and in the measurement of radiopurity levels never reached before. CTF is the only existing device, together with Borexino, able to measure backgrounds at such ultra-low level.

The contamination from ^{238}U and ^{232}Th (see Figures 2.3) has been measured from the

¹This is due to the fact that the energy resolution and the pile-up lengthen the tail above the ^{14}C endpoint at 156 keV.

Uranium series decay chain



Thorium series decay chain

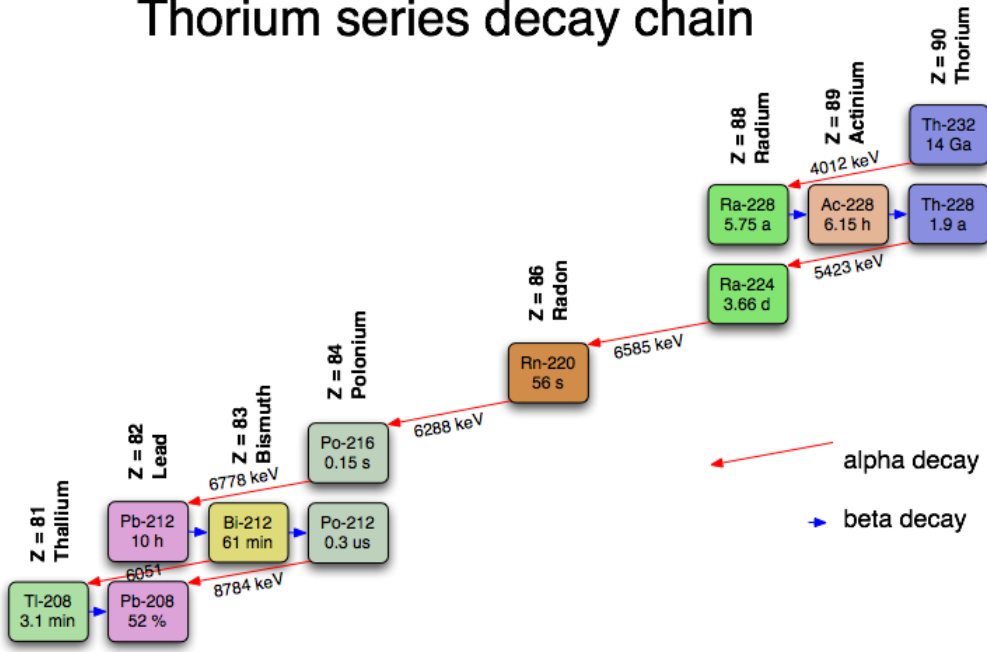


Figure 2.3: ^{238}U (top) and ^{232}Th (bottom) decay chains.

identification of the fast coincidences of ^{214}Bi - ^{214}Po and ^{212}Bi - ^{212}Po , respectively. It results to be $(1.6 \pm 0.1) \times 10^{-17} \text{ g/g}$ and $(6.8 \pm 1.5) \times 10^{-18} \text{ g/g}$ respectively. As evident from Table 2.1 these values are more than one order of magnitude lower than required. In agreement with the requirements, the accurate scintillator choice allowed a concentration $^{14}\text{C}/^{12}\text{C} = (1.94 \pm 0.09) \times 10^{-18}$.

A deep treatment of the Borexino radiopurity study can be found in [79].

The residual contamination is managed through the knowledge of the energy spectra of the various components. The most relevant backgrounds in the solar neutrino energy window are ^{14}C , ^{210}Po , ^{214}Pb , ^{210}Bi and ^{85}Kr .

- As already pointed out, ^{14}C determines the lower threshold of the neutrino window. The energy spectrum of electrons produced in the ^{14}C β decay has an end-point at 156 keV, but energy resolution and pile-up raises the threshold to 200 keV. At the abundance level achieved in Borexino, its presence allows the detection of low energy solar neutrinos, as ^7Be and pep. It is not excluded the possibility to measure pp neutrinos too.
- ^{214}Pb and ^{210}Bi are radioactive isotopes produced in the ^{238}U decay chain and belong to the ^{222}Rn sub-chain (see Figure 2.3). The former undergoes a $\beta + \gamma$ decay, with a $Q=1.024 \text{ MeV}$; the latter undergoes a β decay with endpoint at 1.162 MeV . ^{210}Po belongs to the ^{222}Rn sub-chain as well; it produces 5.407 MeV α 's resulting in a peak falling in the neutrino window, due to the quenching. Since ^{222}Rn is a gas diffused in air, it is strictly necessary to avoid any contact of scintillator with air: the presence of ^{222}Rn in the scintillator is mainly due to minor air contaminations occurred during the detector filling. In addition, each operation involving the scintillator (as calibration campaign, water loop, water extraction, refilling...) can easily cause Rn introduction. Also ^{210}Po , present on the internal surface of tubes can be introduced; for this reason, a great accuracy and an on-line check on data is necessary during this kind of operations.
Done these considerations, the isotopes of the sub-chain are not in equilibrium with the ^{238}U chain.
- The most problematic spectral background is due to ^{85}Kr . It is not a naturally occurring isotope, but it is produced in copious amounts in the fission of ^{238}U and has been dispersed through atmospheric weapons testing and venting of radioactive gases produced in spent nuclear fuel rod assemblies. At present, ^{85}Kr exists in air at a concentration of 1 Bq/m^3 . A small amount of air was introduced by mistake in Borexino during the refilling in June 2007 because of a pump failure, causing ^{85}Kr insertion. It is particularly dangerous as its beta spectrum, with end-point at 687 keV, is similar to the neutrino induced Compton-like spectrum: disentangling the signal to the background is the most critical operation in the spectral analysis. Since ^{85}Kr is often linked to Rn, it is noticed that operations on the detector may cause an increasing of ^{85}Kr .

The ^{210}Po alpha background can be removed exploiting the particle identification, as scintillator light response is different for alpha and beta events (see Section 2.2.5).

All the others backgrounds produce β -events that cannot be distinguished by the neutrino

induced beta events. The only way to disentangle signal from background is through a spectral analysis or by looking for coincidence.

2.2 The Borexino detector

The Borexino detector design is shown in Figure 2.4. In order to protect the detector core, where the scintillator is contained, the adopted design is a series of concentric volumes, each with increasingly higher purity requirements. As evident from the bottom panel in Figure 2.4, the most external shield consists in a Water Tank (WT), containing ultra-pure water. A Stainless Steel Sphere (SSS), located at the center of the Water Tank, contains a liquid buffer and supports on the inside PMTs detecting the scintillation light. The liquid buffer is constituted by the same solvent (PC) as the scintillator (for buoyancy reason) and doped with a light quencher, in order to avoid the scintillations close to the PMTs. The buoyancy force acting on the SSS is balanced by 20 steel legs that anchor the SSS to the WT floor. Two concentric nylon vessels divide the scintillator solvent PC into three regions; in particular, the Inner Vessel (IV) represents the active part of the detector, containing PC doped with a light enhancer. Usually, a 3 m radius software cut, selecting the innermost part of the detector (the so called Fiducial Volume), is applied for the neutrino analysis; this allows to avoid the penetration of γ contaminations coming from the IV and from PMTs, basically Rn daughters.

On the outside part of the SSS PMTs, detecting the Čerenkov light of cosmic muons crossing the WT, are mounted. The Borexino detectors are actually two: the Outer Detector (OD), consisting in the Water Tank, is used as Muon Veto; the Inner Detector (ID), consisting in the part of the detector inside the SSS, is the neutrino detector. ID and OD are effectively independent detectors.

In the following, I give a deeper description of the various components.

2.2.1 The Water Tank

The outermost layer of shielding is the Water Tank (WT, diameter of 18 meters) which holds over 2100 cubic meters of deionized water (see left panel of Figure 2.5). The overall height of the WT is limited by the height of Hall C, and as such, it was not possible to have the same quantity of shielding water below and above the SSS. To compensate for the reduced shielding at the south pole of the SSS, there are two large steel plates underneath the WT to balance the shielding capability.

The WT has actually a double function:

1. shield against gammas and neutrons from the rock;
2. Čerenkov detector for cosmic muons surviving underground.

Cosmic muons crossing the WT produce Čerenkov radiation, detected by the 208 photomultiplier tubes (PMTs) placed on the outer surface of the SSS (see left panel of Figure 2.6) and on the WT floor. In order to enhance light collection, the area between the Water Tank inner wall and the outside of the Stainless Steel Sphere is covered with highly reflective Tyvek sheets.

A detailed description of the Borexino Outer Detector is available in [80].

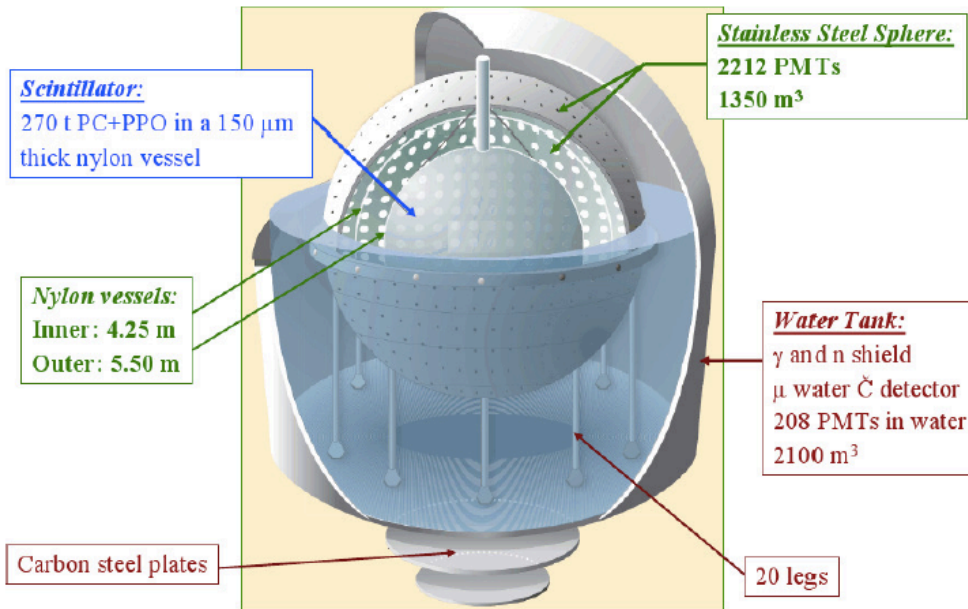


Figure 2.4: Top: model of the Borexino detector and the Wild West Building, where the Borexino Electronic Room and Counting Room are located, in Hall C at LNGS. Bottom: a partial section view of the Borexino detector. Not depicted is a small tunnel underneath the Water Tank where one could place an intense neutrino source for sterile neutrino and calibration studies.

2.2.2 The Stainless Steel Sphere

Inside of the Water Tank is the 6.85 m radius Stainless Steel Sphere which acts as the support structure for the 2212 inner PMTs (see right panel of Figure 2.5) and as container for the buffer liquid. The SSS is constructed from 8 mm thick sheets of stainless steel in the northern hemisphere, and 10 mm thick sheets in the bottom hemisphere, and is supported

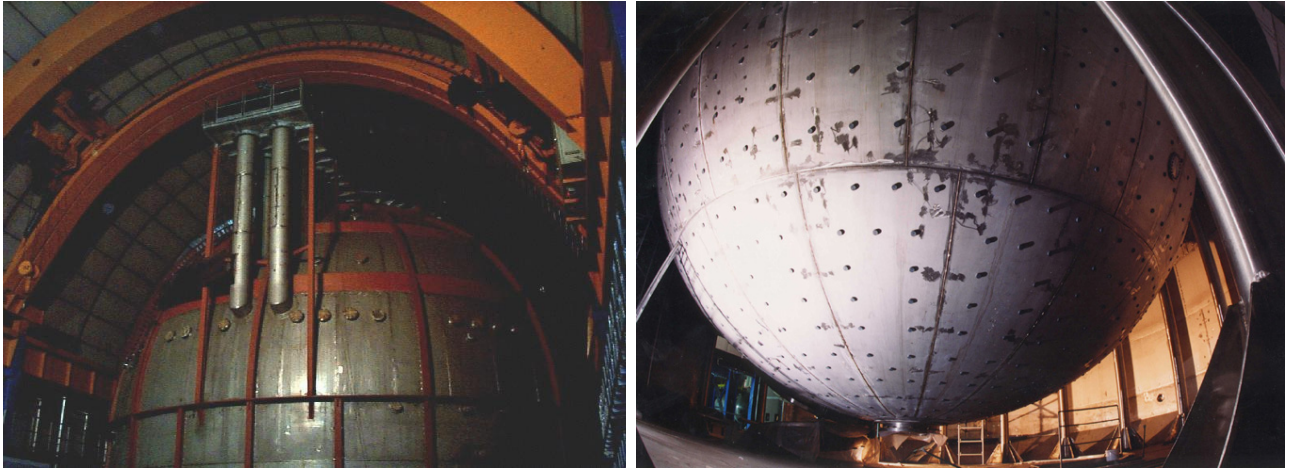


Figure 2.5: *Left:* The top of the Borexino Water Tank with its "Organ Pipes" (before construction of BBW) in Hall C at LNGS. *Right:* View of the Borexino Stainless Steel Sphere (SSS) from the Water Tank, before cables and PMTs installation.

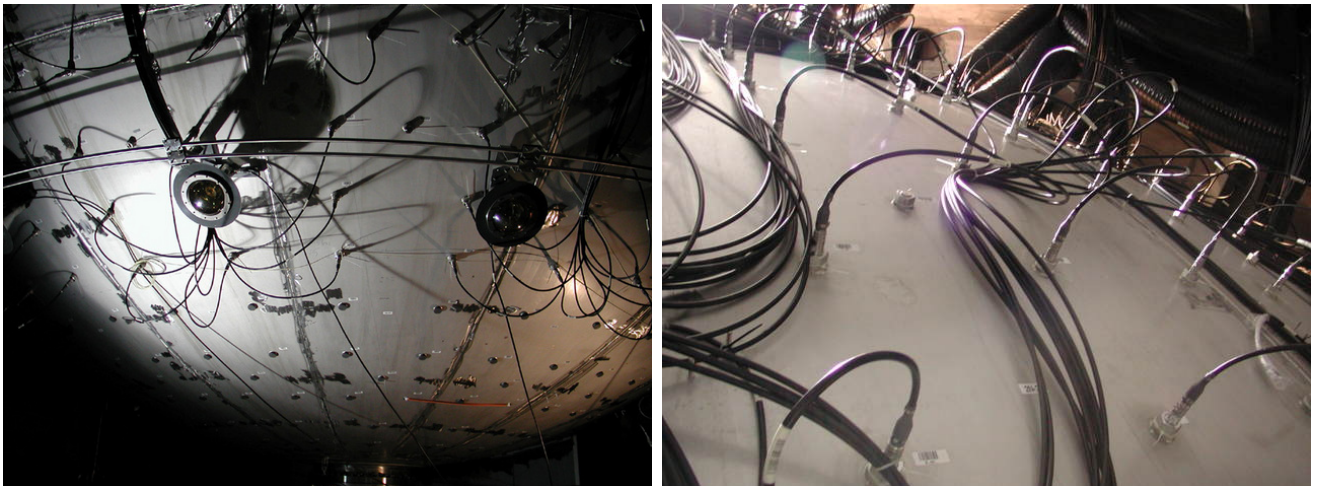


Figure 2.6: *Left:* PMTs for the outer muon veto in the Water Tank (Tyvek not yet installed). *Right:* The cables on the SSS, with connectors screwed in on the PMTs.

by 20 massive legs.

2.2.3 The Photomultipliers

The determination of the event energy and position strongly depends on the PMT resolution in the single photoelectron charge and in the photon arrival time. For this reason, the PMT model has been chosen in order to have a good single photoelectron performance. The selected model is the 8 in. ETL 9351 with special low activity glass (see Table 2.2). In addition, the PMTs feature a special pseudocumene-resistant sealing and coupling mechanism.

The Borexino PMTs have an hemispherical cathode with a section area equal to 366 cm^2 and with a curvature radius 11 cm long. The glass of the photocathode has been selected

Gain	10^7
Voltage for gain 10^7	1650 V
Quantum Efficiency at 420 nm	26.5%
SPE peak-to-valley ratio	2.5
Transit time spread FWHM	2.8 ns
Rise Time	4-6 ns
FWHM	7-10 s
Fall Time	8-12 ns
Linearity on peak current (gain 10^7)	10 mA
Linearity on charge (gain 10^7)	100-150 pC
After-pulsing (0.05-12.4 μ s)	2.5
Dark counts at gain 10^7	3000

Table 2.2: Specifications for the 8 in. ETL 9351 phototube. The gain used in Borexino is specified.

to be low radioactive, as much as the other materials constituting the structure surrounding the PMT. The result is that the overall radioactive background coming from the PMT and from the surrounding structure is of the order of 1 Bq/kg, mainly due to ^{232}Th , ^{238}U and ^{40}K . The resulting total activity from the 2200 PMTs is about 1.6×10^4 Bq. The attenuation factor in the standard Borexino Fiducial Volume (FV) is about 10^7 . Nevertheless, as deeply explained in Chapter 5, γ 's coming from PMTs represent the main background in the energy region above 2 MeV.

The multiplication structure, consisting in 12 dynodes, gives a gain of 10^7 at 1650 V. The PMTs are positioned in appropriate holes in the SSS (see left panel in Figure 2.7): they lie in the internal part of the sphere, immersed in the scintillator, while the cable connections remain outside the sphere, immersed in the water of the outer detector (see right panel of Figure 2.6). For this reason, the connectors and the cables have been developed for submarine applications. The connection cables are about 57 m long, corresponding to an electrical length of (282.10 ± 0.25) ns. Both the high voltage and the signal are carried by the same cable; hence, every PMT is connected to just one cable. The signal and the high voltage are disentangled by the front-end boards, the first stage of the electronics chain (see Section 2.4).

The PMT mechanical structure is shown in right panel of Figure 2.7. It has been designed to fasten the PMT to the SSS and to guarantee its correct functioning in such a complex environment. The structure consists in a stainless steel housing, which completely envelop the neck of the phototube and whose endcap is fixed to the hole in the SSS. The housing, filled with mineral oil, insulates the PMT from the external environment and prevents any contact with PC and water.

A 0.5 mm thick μ -metal cone fixed to the steel housing protects the photocathode and the dynodes against the Earth's magnetic field.

In order to improve the photon collection, 1800 PMTs are provided with Aluminium light concentrators; their shape has been expressly designed to reflect on the photocathode the photons emitted within the nylon Inner Vessel. The remaining 412 PMTs are left without light concentrators in order to make them efficient in collecting light from the buffer.

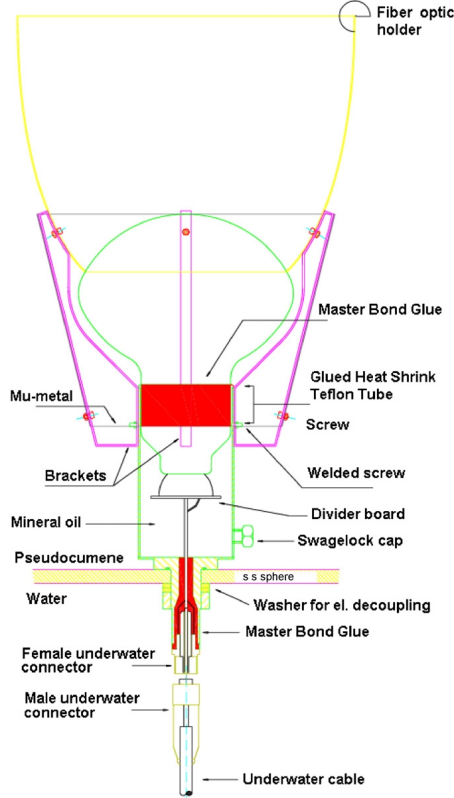


Figure 2.7: *Left:* Closer view of the PMTs on the Borexino SSS during the PMT installation. *Right:* Design of the Borexino photomultiplier tubes.

Finally, each PMT is equipped with a light guide positioned towards the photocathode, used for the detector calibration and channels alignment by means of a laser pulse distributed to all the PMTs.

2.2.4 The nylon vessels

After the SSS, following concentric spheres constituting the detector are the inner and outer scintillator containment vessels (see left panel of Figure 2.8).

In order to avoid to overwhelm the data acquisition system, the liquid in the region closest to the detector materials must be non-scintillating. Thus, it is necessary the presence of a physical barrier to separate the scintillating and non-scintillating volumes: this barrier is provided by the Inner Vessel (IV). A second concentric vessel, the Outer Vessel (OV), has been added in the outer region in order to reduce the radon diffusion towards the IV. Due to the corrosive nature of the scintillator mixture used for Borexino, material compatibility requirements made a rigid vessel impossible. By the way, since the scintillator used in the three volumes separated by these two vessels have almost the same density, the vessels need only to be able to support their own weight (under the assumption of isotropic temperature), and thus could be made very thin. Since Borexino performs its position reconstruction based on the arrival time of photons at the PMTs, the vessel material also needs to have a nearly identical index of refraction as that of the scintillator itself. To prevent radon daughters and dust from collecting on the surfaces of the nylon vessels, they were constructed inside a radon-filtered Class 100 clean room located in Jadwin Hall, Princeton University. Finally, the Inner Vessel in particular, must be very leak tight to avoid the mixing of the non-scintillating buffer and the active scintillator. The measured leak rate of the IV is $<5 \times 10^{-3} \text{ cm}^3 \text{s}^{-1} \text{mbar}^{-1}$; the OV one is $<0.1 \text{ cm}^3 \text{s}^{-1} \text{mbar}^{-1}$ [81].

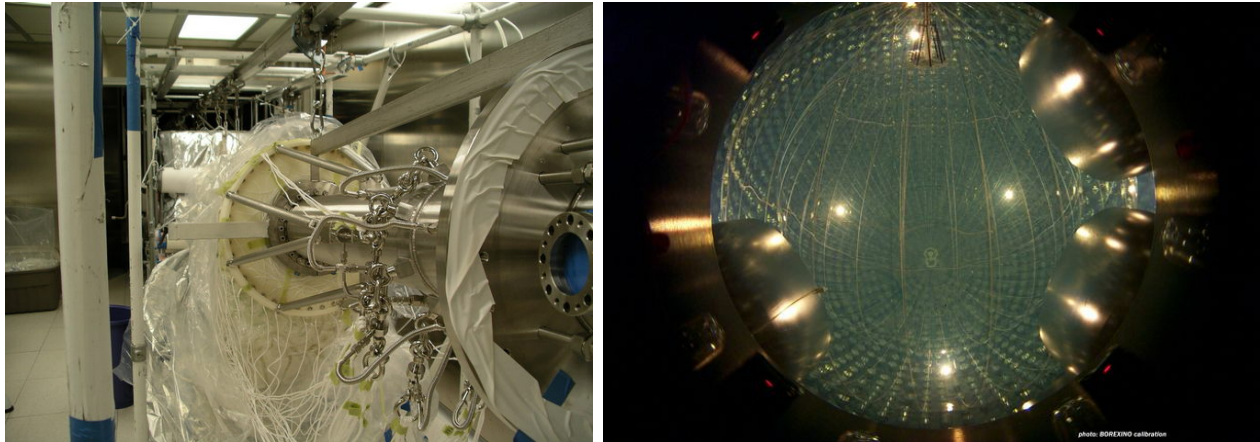


Figure 2.8: *Left:* The vessels in the clean room being prepared for installation. *Right:* May 15th 2007, inside view of the Borexino detector: scintillator filling completed, start of data taking!

Supporting the two vessels and maintaining their location inside of the detector was accomplished via a series of Tensylon ropes and belts. Each vessel has a series of ropes running from the top to the bottom, exactly half of which are used to hold the vessel "up" and "down" if it were trying to sink or float. Another set of ropes encircle the vessel in the ϕ direction and are primarily used to keep the vertical ropes equally spaced. The vertical ropes are connected to load cells at either end of the vessel so the strain can be monitored at all times.

The vessel position can be monitored visually by mean of the CCD calibration cameras. The taking picture procedure requires illuminating the entire detector with very high levels of light; for this reason it is necessary to turn off the high voltage to the PMTs. Since the operation of cycling the PMT voltage is thought to be a catalyst for various problems with PMTs, pictures are taken only few times during the year (basically less than once per month).

The Outer Vessel was fabricated from Capron B737ZP nylon (a homopolymer of nylon 6) extruded into a film 125 μm thick. The Inner Vessel, however, is fabricated from a mixture of 83% Sniamid ADS40T and 17% Ultramid B4 pellets, also 125 μm thick [81].

2.2.5 The scintillator

As already mentioned, the selection of the scintillator was done on the basis of the following scintillation properties:

- a high light yield and a low photon auto-absorption, in order to have a good energy resolution;
- the fast light response for a precise position reconstruction;
- a good alpha-beta discrimination, in order to distinguish particles;
- an emission spectrum matching as much as possible the wavelength region where PMTs have the highest quantum efficiency.

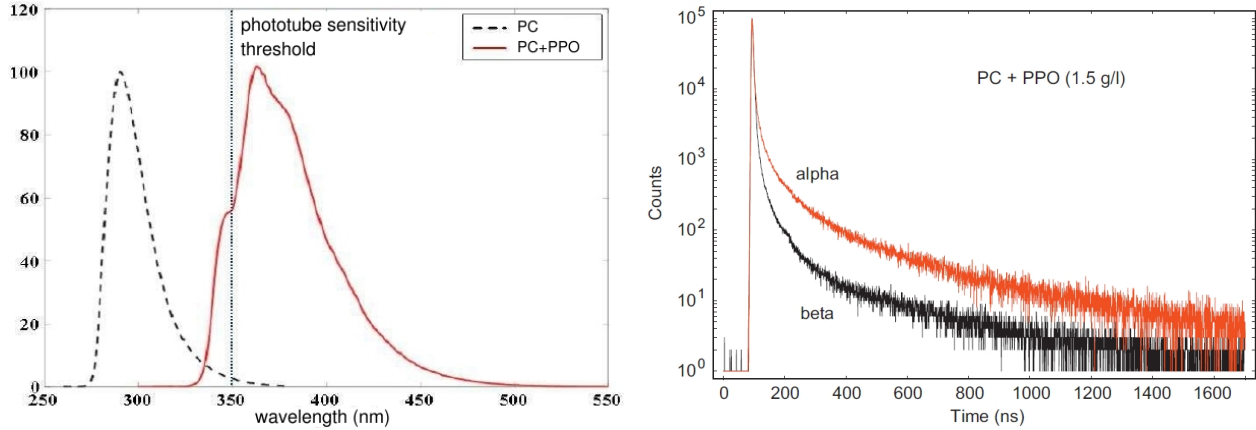


Figure 2.9: *Left:* Emission spectrum of PC (black dotted line) and of PC+PPO (1.5 g/l) mixture (red line). *Right:* Time profile of light emission for alpha (red line) and beta (black line) particles.

The study of different scintillators, both in laboratory and in the CTF prototype, led to the choice of the mixture PC+PPO (1.5 g/l) for the active volume. Both the solvent, the Pseudocumene (PC, 1,2,4-trimethylbenzene), and the solute, the PPO (2,5-diphenyloxazole), have scintillating molecules based on a benzene ring.

The addition of PPO to the scintillator has a double function:

1. PPO enhances the light emission: at the concentration of 1.5 g/l, it increases the light response of about a factor 20. In this way, the overall light yield is 10000 photons per MeV, that, considering the PMT quantum efficiency, corresponds to 500 collected photo electrons per MeV. Thus, the energy resolution is 5% at 1 MeV.
2. PPO works as wavelength shifter, namely it shifts the emission spectrum towards the region of sensitivity of the PMTs (see left panel of Figure 2.9).

A complete characterization of the Borexino scintillator is given in [82].

The liquid used for the buffer region is PC+DMP (5 g/l). DMP has the effect of quenching the light emission, in order to reduce the number of scintillation events due to external background.

In the following Sections the scintillation process, with particular attention to the Borexino scintillator, is described.

Light emission processes

In PC and PPO molecules, the valence electrons are tied to the Carbon atoms in σ and π bonds. When a particle dissipates its energy in the scintillator, both σ and π can switch to an excited state. However, the two electron types differently return to the ground state:

- π electrons de-excite in a radiative way;
- σ electrons de-excite in a thermal way.

Therefore, scintillation is strictly due to π electron de-excitations.

Electron excitations can lead to singlet or to triplet states. Singlet states (S_0, S_1, S_2, \dots) are further divided into vibrational sub-states. While the separation between the singlet states is of the order of 1 eV, the separation of the vibrational sub-states is of the order of 0.15 eV. Thus, at thermal energies most molecules are in the state S_0 . Transition from the S_{10} state to one of the S_0 sub-states causes photon emission on the time scale of 1-10 ns, a process known as **fluorescence** which is the main part of scintillation.

Excitations to triplet states are responsible for the so called **phosphorescence**, namely photon emission with a decay time of 1-10 ms, due to the longer mean life of triplet states. Moreover, light is emitted at longer wavelengths as $E(S_1) > E(T_1)$: for these reasons, phosphorescence is not relevant in the scintillation process. However, a pair of triplet states can recombine into two singlet states, leading to a de-excitation with the fluorescence spectrum but at longer times: this is the so called **delayed fluorescence**.

In the case of the mixture used in Borexino, the energy level structure is similar for PC and PPO molecules, even if the PPO levels are at slightly lower energies. Particles dissipating their energy in the scintillator mainly cause the excitation of PC molecules, which get excited to the levels S_1 or T_1 . Then, energy is directly transferred to the PPO molecules, which radiatively de-excite with a higher scintillation efficiency.

Light emission by the PC+PPO mixture has a time distribution that is suitable both for event's position reconstruction and for particle identification. The time profile of the light pulse is usually described as the superposition of different exponentials. The one describing the fastest component accounts for 90% of the emitted light and has a proper decay time of 3.5 ns, fast enough for a good position reconstruction. The other exponentials describe the delayed fluorescence and are the basis for particle identification: in fact, alpha particles are characterized by a high energy loss and produce more frequently excitations to triplet states. Therefore, alpha particles cause light pulses with a higher light emission at longer times, as it is shown in right panel of Figure 2.9. This feature makes it possible to recognize alpha like events via the pulse-shape discrimination technique.

The Quenching effect

The kinetic energy dissipated in the scintillator by the crossing particles is not completely converted in light. Processes like excitation of σ electrons, which lead to non radiative de-excitation, reduce the conversion efficiency and are known as quenching effects.

The non-linear process of conversion in light of the deposited energy is described by different models. The one used in Borexino is the Birks parametrization, in which the light emission per unit length depends on the energy loss by means of two parameters, according to the semi-empirical relation:

$$\frac{dL}{dx} = \frac{LY \cdot \frac{dE}{dx}}{1 + kB \cdot \frac{dE}{dx}}. \quad (2.2)$$

Here, LY is the light yield, namely the number of photons emitted per unit energy, $B \cdot dE/dx$ is the density of ionized molecules along the track and k is the fraction of these that undergo quenching effects. The product kB is treated as a unique parameter, known as the **Birks factor**, which expresses the intensity of the quenching effect. It is determined by the

experimental conditions and it could vary with the scintillator temperature and could be altered by the presence of electric fields. However, in a fixed experimental environment, it is expected to be the same for all the particle types [83].

In Borexino, the scintillator light yield is of the order of 10000 photons/MeV, while the Birks factor is 0.012 cm/MeV.

For particles with a low energy loss, such as electrons above 100 keV, the Eq. 2.2 reduces to the linear case:

$$\frac{dL}{dx} = LY \cdot \frac{dE}{dx}. \quad (2.3)$$

On the other hand, for highly ionizing particles saturation occurs:

$$\frac{dL}{dx} = \frac{LY}{kB}. \quad (2.4)$$

This is the case of alpha particles.

Another useful parameter is introduced to quantify the quenching effect, namely the quenching factor $Q_i(E)$, which is the ratio between the light emitted for an electron of energy E and the light emitted for an ion i of the same energy. If $L_i(E)$ is the total light emitted for the particle i , the quenching factor is:

$$Q_i(E) = \frac{L_e(E)}{L_i(E)}. \quad (2.5)$$

For alpha particles, the quenching factor is given by the relation:

$$Q(E) = 20.3 - 1.3 \cdot E[\text{MeV}] \quad (2.6)$$

which implies that the alpha particles emitted in the ^{238}U and ^{232}Th chains, whose energy is between 5 and 8 MeV, are shifted in the ^7Be neutrino energy window.

2.2.6 Purification Plants

The reduction in the level of intrinsic background radiation down to the requirements necessitates a very intense purification effort. A schematic of the overall fluid handling and filling system is shown in Figure 2.10.

Pseudocumene Purification

After being delivered in specially designed tanker trucks, the pseudocumene is pumped into one of four storage tanks (each holding approximately 100 tons). From here, the Pseudocumene first undergoes vacuum distillation and water extraction to remove compounds which adversely affect the light yield and attenuation length. Following water extraction, it is possible that the Pseudocumene still contains some dissolved gases such as Radon and Krypton, both troublesome for Borexino. Therefore, the scintillator is sent through a Nitrogen stripping stage to remove these contaminants. The Pseudocumene is introduced at the top of a very tall packed column and allowed to flow downwards against a stream of special Low Argon and Krypton Nitrogen (LAKN) which is introduced at the bottom of the column. After leaving the Nitrogen stripping column, the now purified PC is sent to a storage tank to await its mixing with either PPO or DMP. Due to its very high

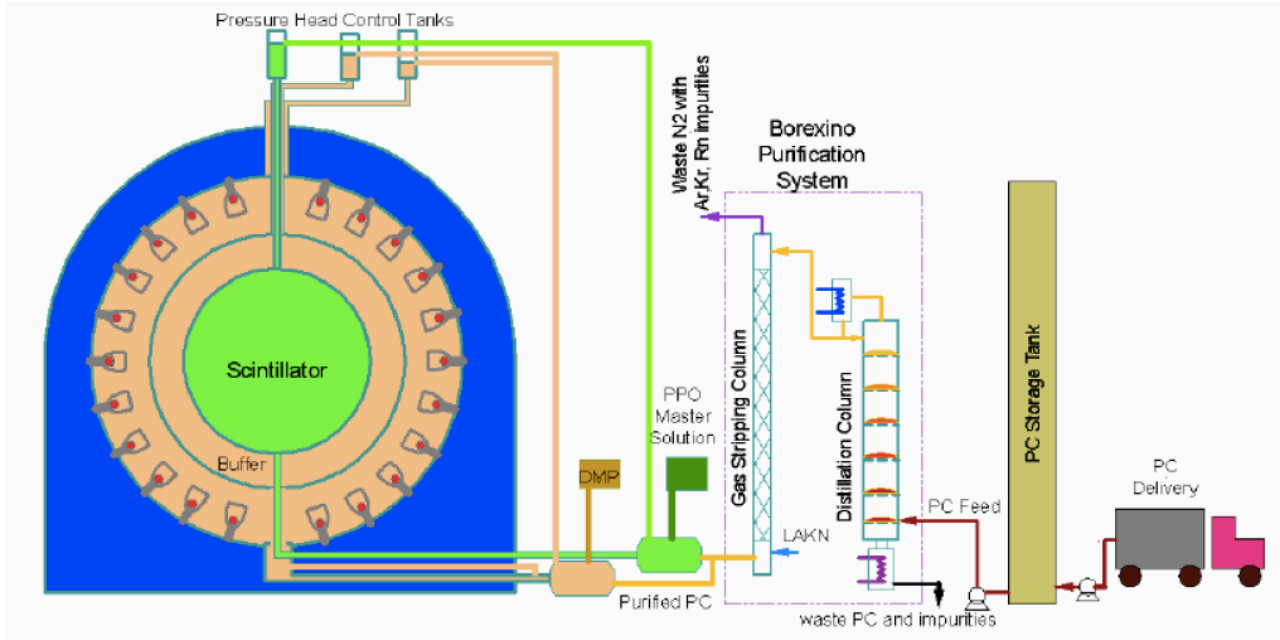


Figure 2.10: Overall view of the purification and filling procedure for Borexino [84]. After being delivered in special tanker trucks, the PC is unloaded into storage tanks and then undergoes distillation, Nitrogen stripping, and then mixing with either a flash-distilled concentrated master solution with PPO, or a master solution of the quencher DMP.

melting point (70°C), PPO cannot be purified directly without extensive measures being taken to avoid solidification. The method adopted is to prepare a highly concentrated "master solution" of PC with 140 g/l of PPO which can be purified by flash distillation. This solution is then metered into the pure PC when filling the inner vessel. To guard against possible re-contamination of the scintillator during and after the purification process, all critical valves, fittings and pumps are out fitted with sealed, Nitrogen-blanketed, secondary enclosures. During the commissioning phases, all components were individually leak checked to provide further assurance against air leaks.

Water Plant and Cleaning Module

The purification and filling operations of Borexino require large amounts of ultrapure water (2000 tons for filling the Water Tank; and large volumes required for rinsing components after cleaning) and Nitrogen (Nitrogen blanketing of pumps, fittings, valves, and vessels; Nitrogen stripping; drying). Water from the underground labs is sent through the water plant where it and passes through filters, and then undergoes nitrogen-stripping, deionization, and reverse osmosis purification stages. The resulting water has a resistance of $18\text{ m}\Omega$ and a reduction by approximately four orders of magnitude in the activity of Uranium and its daughters. The plant is currently used in a loop mode, drawing water from the bottom of the Water Tank, heating it and reintroducing it to the top of the Water Tank to maintain a constant temperature gradient inside of the Water Tank, and therefore the Stainless Steel Sphere.

The commissioning of Borexino and its associated plants required extensive cleaning of all surfaces, pipes, and vessels. To facilitate this process, a dedicated cleaning module

was constructed with the ability to circulate hot detergent, chelating agents, rinse water, and subsequent nitrogen drying. The usual cleaning procedure consists of several hours of circulating with a critical cleaning detergent, then rinsing with ultra high purity water until resistivity measurements ceased to indicate the presence of residual detergent. In an effort to remove surface metal impurities (lead, polonium, etc.), a solution of EDTA is then circulated for several hours, followed by a water rinse until particulate counting indicates the desired cleanliness level and a final drying with LAKN.

2.3 Background sources

As just described, the purification techniques developed for Borexino allowed to reach an excellent radiopurity level, the best so far. Nevertheless, some background components can affect the neutrino detection efficiency.

2.3.1 The internal backgrounds

The internal background sources have already been treated in Section 2.1.3. In the following I will describe the other possible background sources.

2.3.2 Muons and cosmogenics

As already mentioned, the surviving cosmic muon rate at Gran Sasso depth is just $(1.16 \pm 0.03) \text{ m}^{-2} \text{ hr}^{-1}$ [77]. It significantly contributes to the total experimental rate. Muons crossing the scintillator are easily rejected, due to the huge energy amount of these events, compared to the neutrino ones, and to the OD veto. Nevertheless, muon interactions can mimic neutrinos. As well described in Chapter 7, muon interactions with the scintillator nuclei result in unstable isotopes and neutrons. In particular, the most abundant component ($\sim 240 \text{ cpd}/278 \text{ t}$) is represented by neutrons that can be captured on ^1H or ^{12}C , with consequent emission of a 2.22 MeV or 4.94 MeV gamma, respectively. The second most abundant ($\sim 30 \text{ cpd}/100 \text{ t}$) cosmogenic products is ^{11}C that undergoes β^+ decay with end-point at 1.98 MeV. It represents the main background for pep solar neutrinos ($E_\nu = 1.44 \text{ MeV}$), having an energy spectrum similar to the ^7Be one with an end point at around 1.4 MeV.

All the other cosmogenic isotopes (see Chapters 4 and 7) have higher end points (up to 18 MeV) and represent the main background sources for the $^8\text{B}-\nu$ analysis above 3 MeV (see Chapter 4).

2.3.3 The surface background

Possible contaminants coming from the Inner Vessel materials are classified as Surface Background. As already mentioned, the nylon film used in Inner Vessel construction meets the most stringent cleanliness requirements, since it is the only material in direct contact with the liquid scintillator. Radon exposure during production and installation was kept under a strict control in order to avoid the build up of Radon daughters. Furthermore, several different materials have been measured before the choice of the adopted film; nevertheless, as explained in [86], the vessel contains a little amount of ^{238}U and ^{232}Th ,

that emit the Rn gas. The Rn daughters (in particular ^{208}Tl and ^{214}Bi) can represent a contamination in the energy range above 2 MeV (see Chapter 5).

2.3.4 The buffer backgrounds

As well described in Chapter 5, the Borexino buffer is more contaminated than the scintillator in the Inner Vessel. The main contaminants are ^{210}Po , ^{238}U and ^{232}Th , being roughly estimated as 100 times the ones in the scintillator. The presence of these contaminants can imply the production of high energy γ 's in the buffer, propagating within the vessel. In particular, from ^{210}Po we expect (α, n) reactions on ^{13}C producing both deexcitation γ 's and γ 's from neutron capture, basically on ^1H (2.223 MeV); from ^{232}Th we expect a contamination of ^{208}Tl ($\beta + \gamma$, $Q=5.001$ MeV).

2.3.5 The external backgrounds

The γ -rays emitted outside the Inner Vessel and the buffer compose the so called External Background. The suppression of this flux played a major role in the detector construction: a systematic measurement and selection of the materials were realized in order to reduce this contamination. The main sources of such a background are: photomultipliers and light concentrators, rock walls of the experimental hall, environmental materials composing the detector. As deeply described in Chapter 5, the external 2.61 MeV γ 's coming from the PMTs represent the main background source for the ^8B neutrino analysis above 2 MeV.

2.4 The electronics chain

Event informations necessary for the Borexino physics are basically two: the deposited energy and the position. In order to determine these two quantities, the Borexino electronics is conceived to measure both the charge and the time of flight of the photons. In the following, I will briefly show the acquisition system for the Inner and Outer Detectors.

2.4.1 Inner Detector DAQ system

The Borexino Electronic Room contains 14 identical electronics racks dedicated to the ID data acquisition. The goal is the extraction of the charge and time informations from all of the ID PMTs. Each rack contains different items (see Figure 2.11) described in the following [85].

Patch Panel

The 55 m submarine cables attached to the PMTs arrive at the top of each electronics rack where they are routed to the front-end board to which it belongs. The patch panel simply functions as a common termination point for all 158 of the submarine cables processed by one rack.

Front-End Boards (FEB)

The 14 front-end boards comprise the first half of the pulse processing for the inner-detector electronics. The input to a given channel on a front-end board contains both the DC high voltage for that channel and the AC signal riding on top of it; the first stage of the front-end board decouples these two components. Each PMT signal is split into two copies:

- the first one is amplified and shaped to be used in a subsequent stage for the timing pickoff;
- the second one is integrated in preparation for digitization.

Moreover, the front-end board produces an analog sum of all 12 channels on the board, sent to the scaler module on each rack.

Laben Boards

They are VME digitizer boards produced by the Laben S.P.A. electronics company (no more existing) in Milan, based on a project developed by the Borexino Collaboration. Each VME crate contains 20 boards, each one processing 8 channels. These boards accept the timing and integrated charge outputs produced by the front-end boards and subsequently perform the time pick-off to an accuracy of 200 ps. For trigger evaluation, each board contains a coincidence unit with a coincidence time of 50 ns and sends its output to the trigger processing logic. Each channel also contains its own memory registers where the data are stored for a duration of 6 μ s. If a trigger is received, these data are copied to on-board RAM in preparation for event-building. Each VME crate possesses one PowerPC module, having three consequent tasks:

- retrieving the data from all the channels in all the boards in its crate;
- building this data into part of one event;
- sending the event over an internal network to the main event-building computer, called BxBuild.

Scaler

The analog sum output of all the channels in each FEB are sent to one scaler, an adder module, in each crate. This module performs an analog sum of all of the board-level sums, that is the analog sum of all PMTs in that particular crate. The crate analog sum is then used in the flash ADC based supernova monitoring system, the Princeton neutron DAQ, as well as the Genova neutron DAQ. The module also has an internal discriminator and scaler for each FEB connected to it; they are routed to a web interface, very useful for detector monitoring and diagnostic purposes.

High Voltage

Finally, each crate houses a high voltage unit for all of the PMTs in its crate. Each HV crate holds 7 modules, each one powering two front-end boards. The entire high voltage system is interlocked and can only be operated when a key is inserted into a special module



Figure 2.11: View of Borexino electronics racks. From top to bottom: PMT cables entering from the SSS, patch panel, FE power supply, adder/scaler module, FE crate and boards, Laben crate and boards, HV crate.

in the counting room. In order to operate the high-powered lights used to illuminate the SSS when taking a photo this key must be removed and placed in a similar box for the camera system.

2.4.2 Outer Detector DAQ system

The ID electronics are designed primarily for the detection of rather small amounts of light (in principle, they are operating in single photoelectron regime). For the detection of the large amount of light produced by muons, a separate electronics chain is used [80]. The PMTs are decoupled in special decoupling units, and then sent directly to charge-to-time converters (QTC) and then forwarded to TDCs. Here they are integrated to determine the total charge registered by that channel (the width of the output from the QTC), and

the time of the hit (start of the pulse). There is also a dedicated trigger system for the outer-detector which provides a muon veto signal to the main Borexino trigger.

2.4.3 Trigger formation

During normal data taking, the Borexino Trigger Board (BTB) is constantly fed with the number of channels that have crossed preset detection thresholds in both the inner and outer detector. For the ID, the coincidence counting begins at board level and is then fed to special coincidence adders attached to each crate, forwarding the information to another set of adders in the trigger crate. The result is then analyzed by the BTB. Usually ID trigger formation occurs when 25 channels (corresponding to approximately 50 keV) register hits in a time window of 60 ns. This threshold is configurable at DAQ run time and is sometimes varied to reduce the trigger rate (i.e. during a calibration with a high activity source).

The OD produces its muon trigger when 6 channels are hit within a time window of 150 ns.

The trigger board can also produce triggers when:

- one of the calibration lasers is fired;
- a calibration signal is fed to all of the front-end boards in lieu of a PMT signal;
- at random intervals so as to measure the PMT dark noise.

Regardless of the source of the trigger, when it occurs, all of the data in both the inner and outer detector is recorded and sent to disk. The window during which data is recorded lasts a total of 16 μ s, appropriately delayed such that the recording of the data starts before the hits causing the trigger.

As already mentioned, there are several sets of radioactive isotopes which decay in rapid succession, quickly enough that the two events will often occur inside of the same 16 μ s trigger window². The tagging of these isotopes requires their identification as two separate event: a software reconstruction stage is actually focused on deconvolving the entire trigger window into as many physical events as appropriate.

The huge amount of visible energy deposited by a muon crossing the ID can saturate the Borexino electronics³. The result is that these channels report a value of zero for their measured charge, biasing the event energy towards lower values. To fix this problem, when both the ID and OD triggers occur at the same time, the normal trigger is issued and immediately after it expires, a new 1.6 ms trigger gate is opened. In this way the ADCs are cleared and cosmogenic neutrons and isotopes can be detected.

2.5 The data taking

In Borexino data are taken 24 h a day. Runs are usually 6 h long; this run duration is long enough to have a good efficiency in the long coincidence search⁴ and short enough to

²The mean life for the ^{212}Bi - ^{212}Po coincidence, from of the ^{232}Th decay chain is 431 ns.

³Immediately following a muon, a large number of channels see so much light that their ADCs are saturated.

⁴For example, the removal of the cosmogenic ^{11}C ($\tau=29.4$ min), particularly dangerous for the pep analysis, requires the search of coincidences between the parent muon and the ^{11}C daughters in a time

allow the fast data reconstruction and the continue detector monitoring. Once per week a calibration run is taken, in order to check the channel alignment.

Shifters change each week; they are usually two and can be three when the third is in training. Their main duty is the presence underground and the run monitoring. Runs must be supervised at least 16 hours per day, usually from 8 a.m. to midnight. At least one shifter is required to be present in Control Room everyday. When a run ends, shifters must start the data processing sequence as soon as possible in order to monitor the effects of scintillator operations in real time. When the data reconstruction is done, shifters must check the runs through a specific tool and if everything is fine validate the data. In addition, in case of flasher or tripping PMTs, shifters must individuate the bad PMT and in case disconnect it.

Shifters are always helped during their work by the Run Coordinator (RC). This person is in charge for a full month at LNGS. The RC must be the contact between the Operational Group, the experts and the shifters and ensure the weekly exchange of informations between shifters. He/she must be an expert shifter, able to help shifters in case of any problems/doubts; he/she must also check their responsibilities in order to guarantee the efficient data taking. The monthly duty cycle is RC responsibility. During my Run Coordination, duty cycle has been 97%.

2.6 Detector calibrations

The completion of the Borexino scientific program, in particular the solar neutrino program, needs an accurate calibration of the detector, for the energy and position reconstructions.

In particular, the goals of the calibration campaign are the following:

- the better understanding of the detector response, with particular focus to its dependence on the energy scale, on the particle type and on the event position;
- the precise knowledge of the energy scales of gamma, beta and alpha particles;
- the optimization of the particle identification ($\alpha - \beta$ discrimination);
- the improvement of the position reconstruction, aiming a 2 cm accuracy in the definition of the Fiducial Volume radius;
- the study of the energy and position distribution of external 2.61 MeV γ 's coming from the PMTs.

The last point has been realized through a specific calibration campaign performed with an external source, positioned at two positions on the SSS. The other goals have been reached through a calibration campaign involving internal sources.

Detector calibrations are extremely delicate operations, as it is absolutely necessary to avoid any detector contamination.

The calibration data were also fundamental in the development and optimization of the Borexino simulation program, that I widely used and developed during my thesis work.

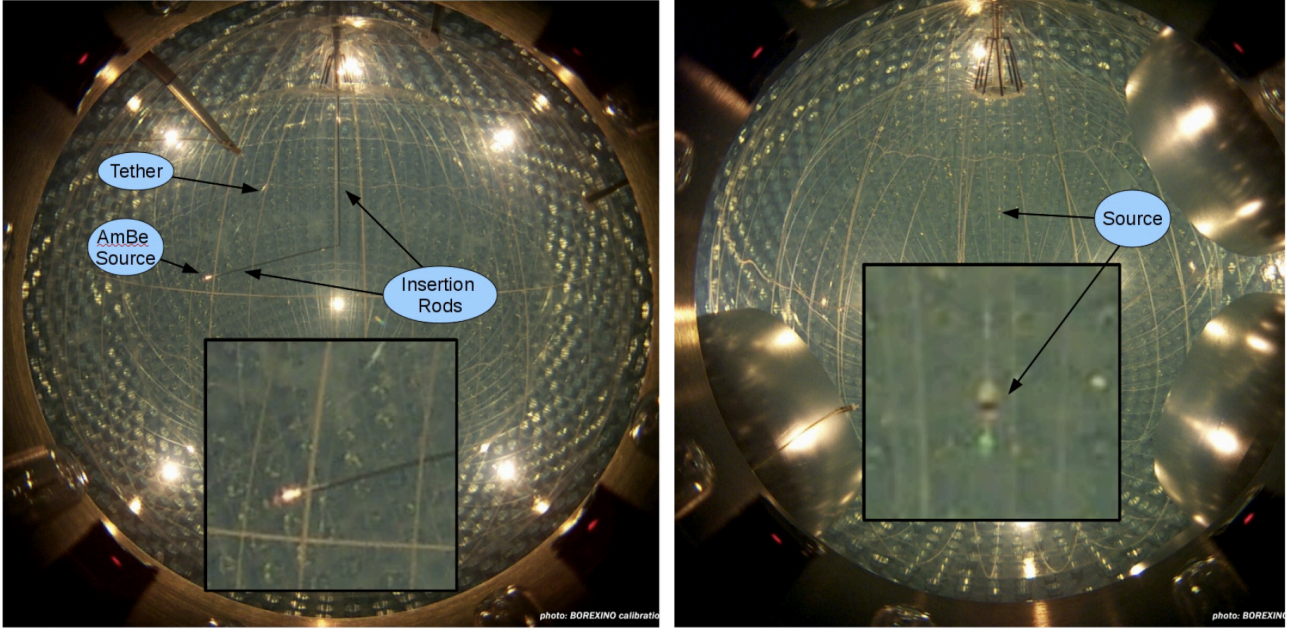


Figure 2.12: *Left:* AmBe neutron source deployed at the conclusion of the calibration in June 2009. The insertion rods are clearly visible entering the detector through the Inner Vessel fill pipe. The inset is zoomed-in to better show the source. *Right:* Photo of a source deployed with the on-axis system taken on October 10, 2008. The bright spot just above the source in the full image is a reflection of the house lights from the tether tube. The zoomed photo shows the cone, counterweight, and diffuser illuminated with the green laser light.

2.6.1 The internal calibration campaigns

The detector calibrations were organized in four campaigns [87]. Global results have been extremely satisfactory:

- the reduction of the uncertainty on the Fiducial Volume from 6% to 1.2%;
- the energy scale is determined with a 1.5% uncertainty.

Avoiding any contamination of the detector core, α , β , γ and neutron sources have been deployed in 295 positions inside the Inner Vessel.

Calibration System

The calibration system is designed to deploy the calibration source in any position within the IV. Insertion within the detector is done through a glove box, located in a class 10 clean room located above the detector. The glove box is kept under Low Argon and Krypton Nitrogen (LAKN) atmosphere, in order to avoid any contact between the scintillator and Radon. Moreover, every component of the insertion system coming into contact with the scintillator has been accurately treated to reach a radioactive contamination of about 2×10^{-16} g/g both in ^{232}Th and ^{238}U , in order to reduce to a minimum the risk of contamination of the detector core.

The insertion system consists in a series of 1 m long stainless steel rods, at the edge of which the source is fixed. The arm can contain a hinged section that allows a rotation

Source	Energy [MeV]	Type	Vial Content	x [cm]	y [cm]	z [cm]
^{57}Co	0.122	γ	Water	7.5	-3.3	292.5
^{139}Ce	0.165	γ	Water	0.3	-6.2	142.8
^{203}Hg	0.279	γ	Water	6.6	-7.1	-6.4
^{85}Sr	0.514	γ	Water	2.2	-13.1	-156.6
^{54}Mn	0.834	γ	Water	293.7	12.5	-11.4
^{65}Zn	1.1	γ	Water	260.1	13.4	-137.7
^{60}Co	1.1+1.3	γ	Water	5.3	-9.0	-301.2
^{40}K	1.4	γ	Water	145.7	3.8	-346.0
^{14}C	0.156	β	Scintillator	310.0	20.6	-200.0
^{222}Rn	-	β, α	Scintillator	271.1	-8.7	216.1
AmBe	2.2, 4.9, 7.5	n	-	130.0	-66.0	-14.0
				267.2	-27.3	116.4
				8.5	-6.1	1.9
				11.1	300	-13.1
				-286.0	-32.9	-22.6
				55.2	-288.7	-20.0
				133.5	-334.4	-7.4
				-332.3	-117.5	-10.9
				-8.4	358.8	-6.8
				362.6	-3.5	-5.6
				189.6	179.8	-261.3
				-242.2	16.7	-264.2
				73.6	-245.2	-263.3
				-2.2	5.6	-401.1
				1.9	2.3	400.8
				182.5	199.1	278.3
				-257.7	60.0	274.3
				107.2	-245.9	276.4

Table 2.3: *Left:* List of radioactive sources used for calibration. For every source, the type of the emitted particle and its energy are indicated. The last column indicates in which solute the source is dissolved inside the vial. For the Radon source, no energy is indicated because the source contains all the isotopes of the sub-chain. Concerning the AmBe source, the reported values correspond to the energies released for neutron absorption on H, C and Fe; the source is not dissolved in a solute, so the last column is empty. *Right:* List of positions reached for the AmBe source, during the Borexino calibration campaign in June-July 2009.

up to 90° on the vertical plane. Rotation is performed by pulling on a teflon tether tube attached to the edge of the arm, near the source. The arm can also be rotated on the horizontal plane, so that every position inside the IV can be reached.

The source fixed to the arm can be radioactive sources or fiber optics sources. In the first case, the source consists in a quartz sphere, 2.5 cm in radius, containing the radioactive source dissolved in either water or scintillator. On the other hand, the fiber optics sources are cylindrical quartz vials that contain the fiber optics terminations.

Both the sources are provided of a light source for an accurate position determination. Indeed, the insertion system does not allow to determine the source position with sufficient precision, which is then evaluated by means of a location system consisting in seven CCD cameras, mounted on the SSS and looking inward, having a 2 cm in the precision in the position reconstruction. Once the source is positioned in the needed location, pictures are taken with the cameras and analyzed by an *ad hoc* program. In Figure 2.12, two Borexino pictures taken during the calibration campaign are shown.

Radioactive Sources

A detailed description of the source construction is given in [87].

The radioactive isotopes used as calibration sources have been selected according to the following criteria:

- As the gamma rays are the only particles that succeed in escaping the source and

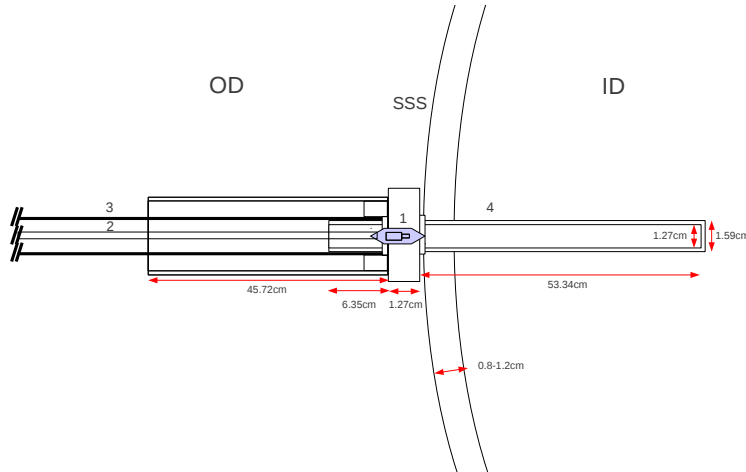


Figure 2.13: Drawing of the reentrant tubes where the external source was placed.

release their energy in the scintillator, a series of gamma sources have been chosen to study the energy scale. The different sources have been selected in order to cover the whole ^{7}Be neutrino energy window. In particular, the region below 1 MeV is sampled because the non-linear quenching effect is more important there. Five gamma sources, namely ^{85}Sr , ^{54}Mn , ^{65}Zn , ^{60}Co and ^{40}K , were arranged in two sources, avoiding any spectral overlapping.

- The ^{57}Co has been selected also to study the trigger efficiency, which is tested at low energy (122 keV), in order to check the trigger threshold effect and because the low energy range is the most delicate region, where the trigger could have the worst behaviour.
- The ^{222}Rn source comprises all the isotopes of the sub-chain, emitting both alpha and beta particles at different energies. Since alpha and beta particles would not succeed in escaping the vial, the source is dissolved in a sample of IV scintillator, accurately treated in order to avoid contact with air.
- A neutron source, the AmBe source, has been employed in order to perform studies important to calibrate the detector at higher energies (above 1 MeV). In fact, the neutron captures can happen on protons, ^{12}C or Fe with a consequent γ emission with energy of 2.2 MeV, 4.9 MeV and 7.5 MeV, respectively. The list of positions for the AmBe source is reported in right part of Table 2.3.

A list of the sources used for the internal calibration campaign is reported in left part of Table 2.3.

2.6.2 The external calibration campaign

The external calibration was performed using a custom-made ^{228}Th [88]. ^{228}Th was selected since it is long-lived ($\tau_{1/2}=1.9\text{ y}$) and one of its daughter nuclides, ^{208}Tl , emits the characteristic 2.61 MeV γ -rays dominating the external background observed in Borexino. The used ^{228}Th source had to fulfill several requirements:

1. the source had an activity of $\sim 5\text{ mBq}$ which allows to collect high statistics in the innermost part of the detector in short time;
2. the unwanted indirect neutron source strength from the ^{228}Th source is suppressed to approximately 7 neutrons/sec.

Neutrons are namely emitted via (α, n) reactions, when alpha particles from the ^{228}Th decay chain interact with low-Z material contained in ceramic, which is often used as matrix in the construction of commercial ^{228}Th sources.

During the first external calibration campaign, the ^{228}Th source was deployed in two positions close to the SSS, one in the upper and one in the lower hemisphere of the detector. This was possible thanks to the presence of steel reentrant tubes crossing the SSS and reaching the buffer liquid (see Figure 2.13). The connection between the tubes and the outside is realized through polyethylene tubes. The source was placed at the SSS level.

Collected data have been fundamental as a check for the external background simulations, as well explained in Chapter 5.

Based on the success and the utility of the first one, a second external calibration campaign will be performed soon (within the end of 2011).

Chapter 3

Borexino Reconstruction and Simulation Codes

Time and charge informations from each Borexino electronic channel need to be converted in usable variables for the physics analyses. The transformation process is performed by the software reconstruction program.

An other fundamental instrument in phase of analysis is the Borexino Monte Carlo simulation code. It has been developed to reproduce all the processes taking place between the energy deposition in the scintillator and the data acquisition. The simulation code consists in a series of numerical codes, named Geneb, G4bx and bx-elec, each one aiming at simulating a particular set of processes. While the core of the Monte Carlo chain, G4bx, is a program based on Geant4 [91], a toolkit for the simulation of the passage of particles through matter, the other two codes are implemented *ad hoc* for the Borexino experiment.

In this Chapter I will explain the features of both these official Borexino codes.

3.1 The Borexino data reconstruction code

The Borexino reconstruction codes have been written entirely in C++ and produces as its output a flat ROOT ntuple [92] for each run. The code is open to all collaboration members via CVS access, and the data are stored on RAID disk arrays in Italy, Princeton, Virginia Tech, and UMass Amherst. The code follows a typical development cycle of modifications, testing, freezing, and culminates with a batch reprocessing of all of the data with the new code cycle. The original and oldest part of the code is called *Echidna*. Recently, some other variables have been constructed and added by the USA collaborators, through a new part of the code called *Mach4*. Since for the thesis work I used only Echidna variables, they will be presented in more details.

3.1.1 Precalibration

The reconstruction code starts with the precalibration: a special set of routines runs over the raw data file and calculates:

- Timing offset values are calculated on a channel-by-channel basis to equalize the timing of all channels. This information is obtained from the pulser triggers at the

beginning of each run (these are the "fake" PMT signals fed to the calibration inputs of the FE boards), and the calibration laser triggers at the start of each run. The pulser events are used to align the timing of the FE and Laben boards, and the laser events are used to account for any cable length differences between the FE boards and the PMTs themselves.

- Charge calibration is performed with the pulses from the calibration laser fibers pointed at each PMT. In particular, the charge histogram for each channel is fit to a function and the position of the single photoelectron peak is recorded and used later in calculating the number of photoelectrons seen by that channel in an event.
- Calculation of the dark rate for each channel is performed with the dedicated random triggers. These triggers occur both at the beginning of each run and also throughout the entire run. This dark rate is used during calculation of the number of photoelectrons or hits occurring during a cluster: the number of expected dark hits for each channel is computed and subtracted to yield the "true" number of hits.

During this process of precalibration, individual channels may be marked as dead for not possessing any events in laser and/or random triggers, having a too high dark rate, having an abnormally wide or offset single photoelectron response, or requiring a timing correction too far out of specifications. Despite careful installation procedures, there are some channels whose calibration fiber is broken or damaged. In the former case, it is simply not used for calculating the energy of an event. A distinction is made between broken and damaged fibers; the latter typically do channel some light, but the laser statistics in a normal run are insufficient to allow the determination of its energy calibration variables. Therefore, at least once per week, a special laser calibration run is performed where the laser is fired at 100 Hz for a total of 250000 triggers. This is usually sufficient to extract the energy calibration data with high accuracy from all channels, including those with damaged fibers.

Since energy variables used in the analyses are calibrated to 2000 PMTs by scaling to the number of live PMTs, the reconstruction code monitors the number of channels responding to pulser triggers during the run. The pulser signal is injected in place of the PMT signal, thus, any failures in the electronics chain will cause that channel not to report the fake hit issued by the pulser. The Echidna code actually adjusts the scaling of the energy variables to 2000 PMTs on an event-by-event basis.

3.1.2 The energy reconstruction

As described in Section 2.4, when the trigger signal is delivered a $16\ \mu\text{s}$ gate is open around the scintillation event. The data acquisitions involves both noise hits and signal hits. Even if the noise hits are on average $1\ \mu\text{s}$ apart while the signal consists in hundreds hits within a few hundred ns, an algorithm is applied to precisely identify the edges of the scintillation event. The collection of the hits that are identified as belonging to the scintillation event is called *cluster*. In 0.1% of cases, the gate contains more than 1 clusters; moreover, every cluster is analyzed to determine if it is due to a single scintillation event or to multiple events. The array of clustered hits is exploited to extract the physical informations about the scintillation event. The hit time distribution is the basis for the position reconstruction and the particle identification, while the number of hits and the

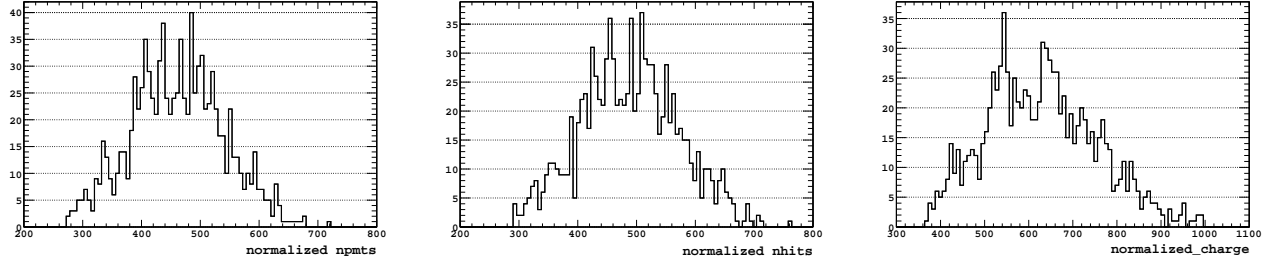


Figure 3.1: Variables npmt (left), nhits (center) and charge (right) for a pure sample of ^{11}C events, having a spectrum between 1.022 MeV and 1.982 MeV; each variable is normalized to 2000 PMTs; events are selected within 4 m.

features of every single hit are exploited to measure the energy.

Several variables are defined to evaluate the energy of the event. The most used in the analysis are:

1. **npmts**: it consists in the number of firing pmts. Below 1 MeV (~ 500 npmts) the number of firing PMTs is much less than the total number of working PMTs (~ 2200); in this energy region the npmts variable is in linear proportionality with event energy. Above 1 MeV, deviations from linearity are the more important the higher the energy and, eventually, saturation occurs.
2. **nhits**: it estimates the energy on the basis of the number of produced hits. Multiple hits on the same channel are taken into account, but also in this case deviations from linearity occurs at high energy.
3. **charge**: it is the sum of the PMT integrated signals corresponding to the scintillation event, normalized to the mean value of the single photoelectron charge. Multiple hits within 80 ns are taken into account, hence it is the most linear variable.

In Figure 3.1 the distributions of the energy spectrum of ^{11}C candidate are shown in the different variables.

It is possible to convert the energy variables to MeV, taking into account that the Borexino Light Yield is about 500 photoelectrons (p.e.) per MeV. The charge variable already represents the number of p.e.. For the other two variables it is necessary to use a decompression formula, allowing to pass from the number of hits or PMTs to the number of p.e. [89]:

$$\text{p.e.} = -2000 \times \log \left(1 - \frac{\text{npmts or nhits}}{\text{num. of live PMTs}} \right) \quad (3.1)$$

3.1.3 The position reconstruction

The time distribution of the clustered hits (see left panel of Figure 3.2) is used by Echidna to determine the position of the scintillation event inside the ID. The positions are reconstructed, as usual in scintillator detector, with a photon time-of-flight method. A probability density function (PDF) for the time of transit of photons from their emission point to their detection as photoelectron signals in the electronics chain has been computed with G4Bx (see below). After the Borexino internal calibration campaign (Section

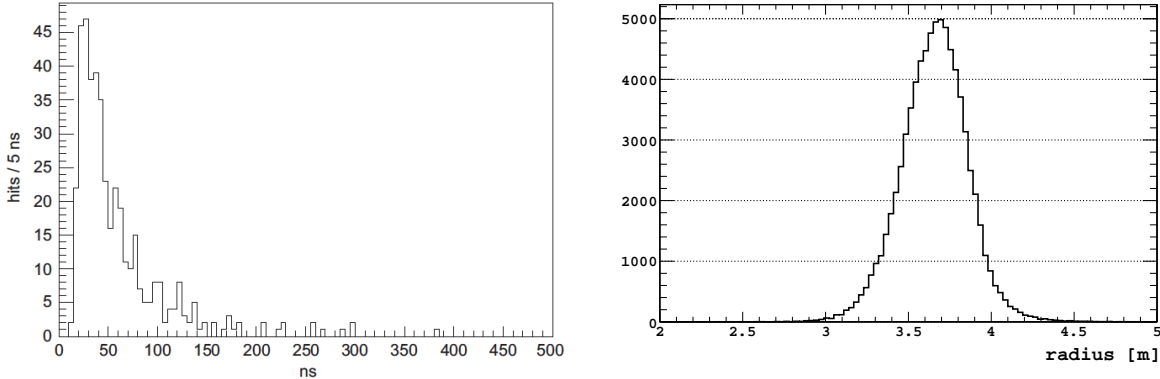


Figure 3.2: *Left:* Time distribution of the PMT hits in a single cluster event [85]. *Right:* Radial distribution of γ events from the AmBe source positioned at a radial distance of 3.7 m.

2.6.1), the PDF has been redefined. Event coordinates (x_0 , y_0 , z_0) and time (t_0) are obtained by minimizing:

$$\mathcal{L}(x_0, y_0, z_0, t_0) = \prod_i \text{PDF} \left(t_i - t_0 - \frac{d_{0,i} \cdot n_{\text{eff}}}{c} \right) \quad (3.2)$$

where the index i runs over the triggered PMTs, t_i is the time of arrival of the photoelectron on the i^{th} electronic channel, and $d_{0,i}$ is the distance from the event position and the i^{th} PMT. $n_{\text{eff}}=1.68$ is an empirically-determined effective index of refraction to account for any other effect that is not accounted for in the reconstruction algorithm but impacts the distribution of PMT hit times, both in the optics (e.g. Rayleigh scattering) and the electronics (e.g. multiple photoelectron occupancy)¹ [90].

Since the Borexino electronics records the time of each detected photoelectron introducing a dead time of 145 ns after each hit for each individual channel, the timing distribution is biased at high energy, where multiple photoelectrons are detected by each channel. This implies that position reconstruction is energy dependent. In addition, the non-homogeneous distribution of live PMTs, in particular the large deficit of live PMTs in the bottom hemisphere [85], is responsible for the different spatial response at mirrored positions about the x - y plane. These effects are perfectly reproduced in the Borexino Monte Carlo, thus they do not represent a real problem when analyses are performed using simulated event distributions.

In right panel of Figure 3.2 a radial distribution of events from the AmBe source (see Section 2.6.1) is shown.

3.2 The Borexino simulation code

As it will be evident in reading the present thesis, the Borexino simulation code G4Bx is a crucial instrument for most of the physical analysis. During my work I insistently used and modified the official code in order to reproduce and fit the data energy and position distributions.

The Monte Carlo chain takes care of the following processes:

¹The nominal refraction index of the Borexino scintillator is 1.53.

- reproduce the detector, including the properties of the materials (G4Bx);
- simulate the energy loss of different particles in the different regions of the detector (Geneb and G4Bx);
- simulate the scintillation and Čerenkov light emission (G4Bx);
- simulate the propagation of every single photon until it is absorbed on the photo-cathode or on other materials (G4Bx);
- reproduce the behavior of the electronics and the data collection (bx-elec).

The three Monte Carlo programs work in sequence. Actually, the Geneb features have been successfully replaced by G4Bx; thus Geneb is almost no more used by the Collaboration. The output of the simulation chain is a set of data that has precisely the same format as the real raw data file. At the end of the simulation, data are processed by the decoding and reconstruction code Echidna. The final informations are then stored into a ROOT file, identical to the data ones and containing in addition all the informations about the original simulations (for ex.: original position and energy, the number of deposits and daughters,...).

3.2.1 Detector description

The detector structure (see Section 2.2) is faithfully reproduced in the Monte Carlo code by means of the tools provided by Geant4. Water Tank, SSS, PMTs with their surrounding structure and the vessels are brought into simulation with the exact dimensions and properties. However, in order to speed up the simulation, it is possible to reproduce only the parts of the detector relevant for the considered process. This possibility has been widely used for simulations I will describe in Chapter 7.

The geometrical volumes are filled with the proper materials, namely water, buffer and scintillator. Different ID configurations are implemented to reproduce the various phases of the detector filling: ID filled with water, or partly with water and partly with scintillator or completely filled with scintillator. The properties of the materials are passed to the code as resulting from direct measurements.

Obviously, modelization of the ID has a particular importance.

The Stainless Steel Sphere

The SSS is described as a steel sphere 13.7 m radius. The definition of the SSS internal surface is fundamental for a correct simulation of interactions at boundary affecting the optical photons propagation. It is described as a polished surface and defined as a dielectric-metal interface by means of the standard models available in Geant4. The SSS reflectivity has been measured and it is introduced with a parameter. Mirror and diffusive reflections are taken into account separately.

The photomultipliers

The complex structure of the PMT and its encapsulation is included in the code in several versions, at different levels of detail. Even if the whole structure is implemented in detail, it is seldom used as it critically slows down the simulation due to its complexity.

Usually, approximations of the real structure are used: a simple disc with a re-corrected acceptance to take into account light concentrators; a disc provided of a steel light concentrator; a bi-alkali spherical photocathode provided of a steel light concentrator. The latter approximation is the best compromise between the real PMT configuration and a reasonable simulation speed and hence is by far the most used.

When PMTs are generated, three effects are included: the transit time spread, the after-pulse and the dark noise. For every firing PMT, the transit time spread is mimicked by adding an offset, distributed according to a Gaussian distribution with 1 ns RMS, to the photon detection time determined by G4Bx. With a certain probability, tuned on calibration data, the emitted photoelectron produces an after-pulse. In this case, a second pulse is generated according to a time distribution extracted from data. Finally, the dark noise pulses are generated with the rate defined by the user. The typical dark noise rate of each PMT is about 1 kHz.

The charge of the PMT pulse is randomly generated according to the single photoelectron spectrum, which is the sum of an exponential distribution describing the dark noise and of a gaussian referring to the single photoelectron pulse. Once that the charge is generated, the PMT pulse is simulated with a trapezoidal waveform having that charge.

The Inner Vessel

While the original detector design contains a spherical IV, the buoyancy forces due to the different density between active scintillator and buffer deform the IV real shape. The IV shape is periodically monitored by means of the CCD camera system, so that the history of the IV shape evolution is registered. The Monte Carlo code allows to reproduce the IV according either to the design shape or to the measured shape. In the first case, the IV is modeled as a spherical balloon, with the nominal 4.25 m radius and 0.125 mm thickness, concentric with the SSS. The second option allows to choose which shape must be used among the measured ones. In this case, the vessel is modeled according to the loaded profile, which automatically takes into account the shift upward in z. The simulation of the right IV shape is particularly important for the simulation of the external background, since the different properties of the active scintillator and the buffer are taken into account. As explained in Chapter 5, during my thesis work I also introduced the possibility of generate events on deformed vessel surface and in deformed buffer shapes, in order to simulate the surface and the buffer backgrounds, respectively.

3.2.2 Particle Generators

The starting point in the simulation of scintillation events is the calculation of the energy deposits. The Monte Carlo program allows to simulate the energy deposits produced by all the particles of interest for Borexino, namely neutrinos, electrons, positrons, gammas, neutrons and alpha particles. These particles can be generated in every region of the detector, using the particle generators implemented in G4Bx. Depending on the purpose, different Geant4 generators are available. The G4Bx main generators are listed in the following.

- **G4Gun** is by far the most versatile generator. In fact, it allows to generate a single particle type (electrons, positrons, alpha particles and so on) or more complicated

vertices (by means of the Multi generator) in which several particle types are produced at one time. Particles can be generated with an arbitrary spatial distribution: (isotropic or direction defined) point-like sources, spherical distributions or spherical surfaces. Particles can also be generated inside the IV, in the buffer or in the whole volume inside the SSS. As described in Chapter 5, a specific G4Gun configuration has been written to produce the first step of the external background simulations. With the G4Gun generator, the energy distribution can be arbitrarily set; particles can be produced with monochromatic energy or with a continuous spectrum, which can be chosen among a list of available candidates. It is also easy to introduce a specific energy spectrum for primary particles; for example, as described in Chapter 7, I introduced the possibility of generate cosmic muons with the expected energy spectrum at underground LNGS.

- SNU generates solar neutrinos, in accordance with the spectra predicted by the SSM and with the neutrino flavor oscillation. Informations on the flavor of the interacting neutrino is conserved. Also in this case, events spatial distribution can be set arbitrarily.
- RDM is the generator of radioactive isotopes, according to the ENDSF tables. Single isotopes or decay chains can be simulated with a spatial distribution selected among the ones mentioned above.

Besides the generators listed here, several generators have been developed to reproduce specific processes. In particular:

- * as described in Chapter 5, a specific generator has been written to produce the second step of external background simulations. It reads an input binary file, containing informations about deposit energy, position and direction and generates an electron for each deposit.
- * a specific Orto-Positronium (oPs) generator has been written, in order to allow the precise simulation of ^{11}C cosmogenic isotope, fundamental for the pep- ν analysis [31]. In this context, I introduced the possibility of generate oPs with the β^+ energy spectrum from the ^{11}C decay.
- * other *ad hoc* generators concern for example: neutrons from the rock, processes described by special cross sections (as ^{14}C), anti-neutrino absorption on protons, the AmBe calibration source and the laser pulses used for timing purposes.

3.2.3 Tracking and Stepping

In Geant4, it is possible to follow a generated event and all the subsequent produced daughters from their birth to their death. In particular, each primary particle is tagged with an *event number*. The deposits and the daughters from a specific primary particle belong to the same event and are such tagged with the same *event number* as their parent. So, the *event* includes the primary particle and all its daughters. Each particle belonging to an event is individuated as *track*: the track describes the particle until its *death*, that can be represented by a decay or the particle exit out of the World Volume. The origin of the track is called *vertex*. Each track describes only one particle and is subdivided in

steps, allowing to follow the particle during its travel.

The simulation of the energy deposits consists in the computation of the visible energy² released along the particle trajectory. The visible energy depends on two processes: the quenching effect and the particle energy loss. The first process is modeled according to the Birks parametrization, described in Sec. 2.2.5. Even if the Birks parameter is expected to be the same for α and β particles, in the code it is kept distinct for the two particles. The particle energy loss is computed in several ways, depending on the particle type. The visible energy deposited along every particle step is computed on the basis of the particle energy. If the visible energy released in the step is E , the quenching factor is Q and the light yield is LY , then the number of photons emitter in the step is $N_{ph} = LY \cdot Q \cdot E$ for a particle crossing the active scintillator. In the case of a particle crossing the buffer, N_{ph} is further multiplied by a factor 0.048 that reproduces the DMP quenching effect.

3.2.4 Simulation of the Optical Processes

Optical processes comprise two categories of phenomena: light emission and interactions of optical photons with the scintillator molecules [93].

Light Emission

The mechanism that leads to the light emission by the scintillator after excitation from a crossing charged particle has been discussed in Section 2.2.5. The Monte Carlo reproduction of light emission does not take into account the details of the process. In fact, it is implemented according to a simplified model. Light is emitted according to the spectra of the PC+PPO and PC+DMP mixtures, while the emission time profile is modeled by the superposition of four exponential. Every exponential is characterized by a proper decay time constant and by a weight. Their values have been measured in laboratory and are passed to the code as parameters, as well as the Birks parameter and the other scintillator properties. Light pulses of alpha and beta particles are described by two different sets of decay times and weights, as the light pulse of alpha particles has a longer tail.

The Čerenkov light is also generated along the particle track in accordance with the *Frank-Tamm law*. The implementation of the refraction index as a function of the photon wavelength is a fundamental aspect for the right simulation of the Čerenkov effect. The PC+PPO mixture refraction index has been measured at different wavelengths in the range relevant for the scintillation physics. The measured refraction index refers to the phase velocity and is used in the Čerenkov light generation. Instead, the refraction index relevant for group velocity, computed on the basis of the measured values, is used for the optical photon propagation.

Photon Tracking

Due to the low energy (sub-MeV) of most the events relevant in the solar neutrino analysis, the number of emitted optical photons is low enough to track them one by one. Thus, every photon can experience the interaction with the scintillator molecules and

²The visible energy is the fraction of the dissipated energy that is converted in light.

with the surrounding materials. This is a crucial feature that makes the Monte Carlo program able to reproduce data with very high accuracy. Moreover, it permits to reproduce in detail the shape of the distributions of the variables characterizing the scintillation event. While an optical photon propagates through the active scintillator, it can undergo two types of interactions with the scintillator molecules: either it can be absorbed by PPO molecules and then be reemitted with a high probability, or it can scatter on a PC molecule (Rayleigh Scattering). The probability of the two events to occur depends on the photon wavelength: at short wavelength, optical photons interact most likely with PPO molecules a few mm near the scintillation point, while at long wavelength it undergoes Rayleigh scattering on PC molecules. Moreover, when crossing the buffer, photons can be absorbed by the DMP molecules.

Interaction of photons at boundaries depends on the properties of the materials facing the interface and on the properties of the surface. As discussed above, the properties of the materials are introduced into the code as resulting from measurements in laboratory, while the properties of the surfaces are defined both through the models provided by Geant4 and through measured parameters. The main interactions at boundaries consist in reflection on the SSS and on the PMT components; interaction with the vessels has a low probability to occur, because the vessel index of refraction matches the scintillator's one. Mainly, they undergo reflection on the SSS and on the PMT components. All these interactions are implemented in the simulation [93].

Photon tracking goes on until the photon is absorbed on a photocathode or on another material, in which case it is lost. For photons absorbed by a photocathode, the process of emission of a photoelectron is reproduced taking into account the wavelength dependence of the PMT quantum efficiency.

3.3 Simulation of the Electronics

The G4Bx output consists in a binary file containing event informations, depending on the purpose. In most of cases, it is necessary to reproduce the real data. For this reason the bx-elec code, simulating the effect of the Borexino electronics chain, has been written. The electronics behavior discussed in Section 2.4 is accurately reproduced. The charge collected within 80 ns from the rising edge of the signal is summed up. The electronics simulation includes also the 140 ns dead time.

The trigger system is emulated, with the trigger condition being fulfilled if 25 PMTs fire within 60 ns. The 16 μ s gate is reproduced and the physical scintillation event is saved together with the dark noise background, so that the time structure of simulated data is exactly equal to the one of raw data. Moreover, additional informations characterizing the event, such as the gps time, are generated by the code.

bx-elec can reproduce the detector configuration of every run: the code loads from database the array of working channels. Thus, the detector configuration can be taken into account in the simulation, with the exclusion of the disabled channels from the simulation. This features, together with the change of the vessel shape, has been widely applied in the production of all the energy and radial spectra I produced for neutrino analyses (see Chapters 5 and 6).

The bx-elec output has exactly the same format as the acquired raw data. Thus, it can easily be reconstructed through the Echidna+Mach4 code.

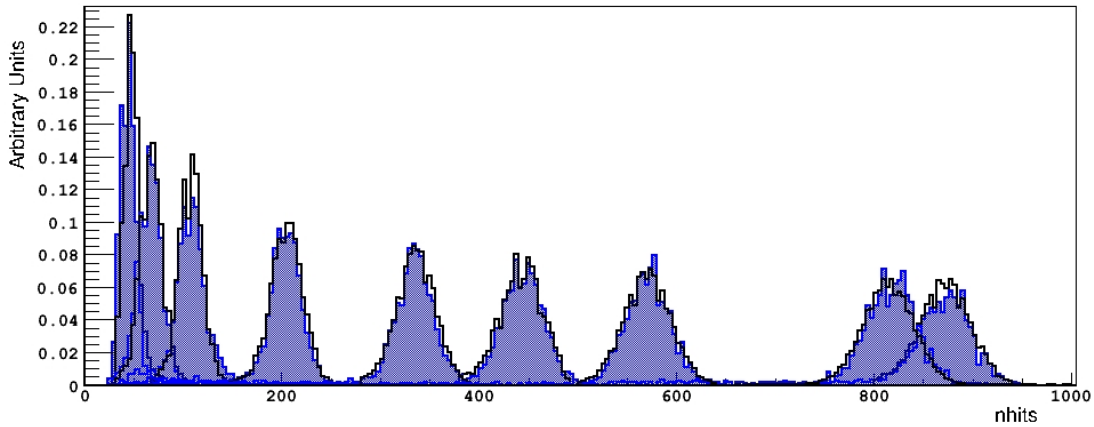


Figure 3.3: Energy comparison between G4Bx simulations reproducing the calibration sources (blue area) and the calibration data (black line).

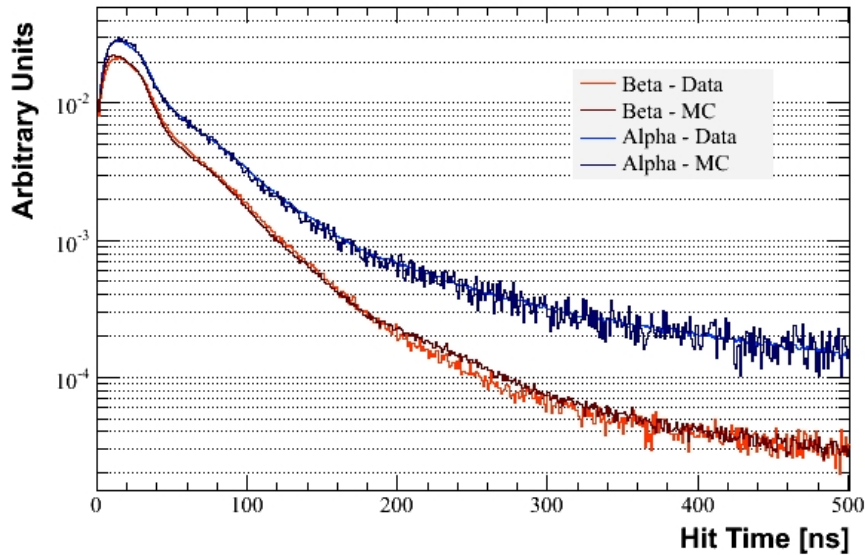


Figure 3.4: Time comparison between G4Bx simulations reproducing the α and β calibration sources at $z=+3\text{ m}$ and the calibration data.

The perfect energy and time reproduction of G4Bx with respect to calibration data, as a result of the Monte Carlo fine tuning, is shown in Figures 3.3 and 3.4.

Chapter 4

^8B Solar Neutrino Measurement above 3 MeV

In this section I report the analysis performed in Borexino for the ^8B neutrino measurement above 3 MeV. I have been deeply involved on this analysis, during all my first PhD year. Results have been published in [36], representing the ^8B solar neutrino observation with the lowest energy threshold ever reached in real time.

Considering the Inner Vessel of Borexino, the signal to background ratio above 3 MeV is about 1/100. The main difficulty for the accomplishment of this analysis has been the elaboration of background rejection techniques. Above 3 MeV the expected contaminations come from radioactive decays of residual ^{214}Bi and ^{208}Tl within the liquid scintillator, decays of cosmogenic isotopes, high energy γ -rays from neutron capture and cosmic muons. The dominant background in the energy range of interest for solar ^8B neutrinos originates from spallation processes of high energy cosmic muons (for details see Chapter 7). The development of coincidence based methods allowed the reduction of cosmogenic background below the rate of interaction of ^8B neutrinos, thus the measurement of neutrino rate.

4.1 Physical motivation

As already described, matter interaction effects can dramatically influence the pattern of neutrino oscillations in the Sun, since the neutrino matter interaction cross sections are flavor dependent and the matter distribution in the Sun contains only first generation particles (electrons). The oscillation theory in the MSW-LMA scenario predicts a peculiar behavior of survival probability (P_{ee}) as a function of neutrino energy (see Figure 4.1):

- at low energies ($E < 1 \text{ MeV}$) the oscillation mechanism is the same as in the vacuum and P_{ee} is about 60%;
- at high energies ($E > 5 \text{ MeV}$) the oscillations are dominated by matter effects during the travel through the Sun, and P_{ee} decreases down to 30%.

The real time experiments based on Čerenkov technique have a high energy threshold and could observe only the final part of ^8B neutrino spectrum. In 2008 the Borexino Collaboration published the measurement of ^7Be solar neutrino, investigating for the first time in real time the vacuum region [35]. Thus, in 2008 the situation for the P_{ee} mapping was the one showed in Figure 4.1. It is evident that the energy region between 1 and 4 MeV was

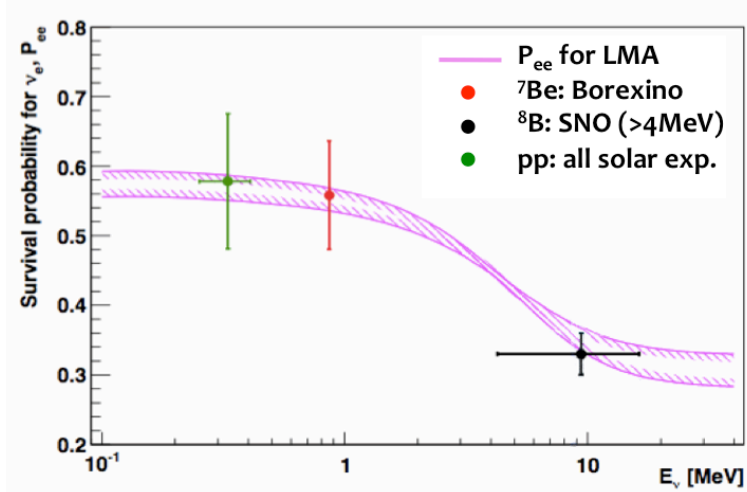


Figure 4.1: Electron neutrino survival probability as function of the neutrino energy, evaluated for the ${}^8\text{B}$ neutrino source assuming the BPS09(GS98) Standard Solar Model [38, 39] and the oscillation parameters from the MSW-LMA solution $\Delta m^2 = 7.69 \times 10^{-5} \text{ eV}^2$ and $\tan^2 \theta = 0.45$ [40]. Dots represent the experimental results: ${}^7\text{Be}$ by Borexino (red), ${}^8\text{B}$ from SNO (black) and pp from all the solar neutrino experiments (green).

totally unexplored¹. For this reason we decided to attempt a deeper exploration of the transition region, through the ${}^8\text{B}$ solar neutrino measurement above 3 MeV (electron scattering energy). We set the energy threshold at 3 MeV in order to avoid the contamination from external background coming from PMTs. We also performed the analysis above the threshold of 5 MeV, to facilitate the comparison with results reported by SNO [95] and SuperKamiokaNDE phase-I [94] at the same threshold. This energy range is unaffected by the scintillator intrinsic background, since the light quenching effect reduces the visible energy of ${}^{208}\text{Tl}$ ($Q=5.001 \text{ MeV}$, quenched to about 4.8 MeV) from ${}^{232}\text{Th}$ contamination in the scintillator below the energy threshold of 5 MeV.

4.2 The energy and the radial cuts

The reported analysis is based on 488 live days of data acquisition, between July 15th 2007 and August 23rd 2009, with a target mass of 100 t, defined by a FV cut of radius 3 m. In Figure 4.2 I show the original energy spectrum above 3 MeV in the whole Borexino vessel; the rate is about 30 cpd/100 t. The expected rate for ${}^8\text{B}$ solar neutrino, in the SSM+(MSW-LMA), is about 0.3 cpd/100 t above 3 MeV; this means that the signal to background ratio above is about 1/100. The first two cuts we decided to apply concern the energy threshold and the definition of the Fiducial Volume (FV). As deeper described in Section 4.3.3, the origin of these two cuts is due external background gamma penetration: 2.61 MeV gammas from ${}^{208}\text{Tl}$ contamination on the photomultipliers (PMTs) can reach the detector core and mimic the neutrino signals.

¹After the present ${}^8\text{B}$ analysis in Borexino, the lowest energy threshold in Čerenkov experiments, corresponding to 3.5 MeV, has been reached by the SNO experiment [37].

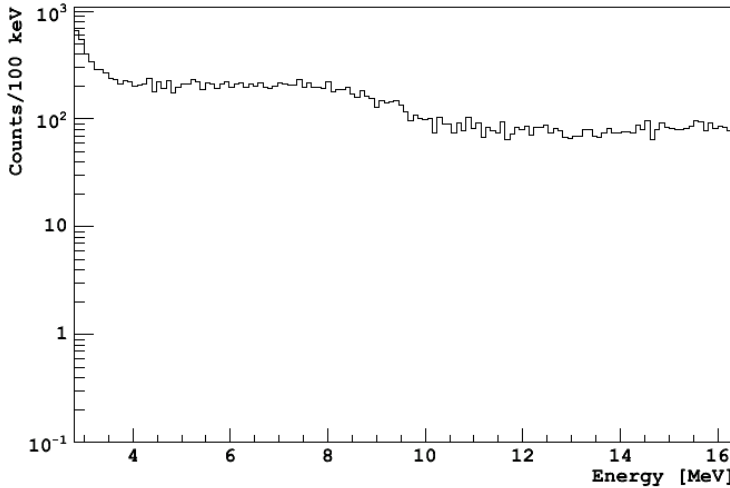


Figure 4.2: Energy spectrum of Borexino events above 3 MeV for the period between July 15th 2007 and August 23rd 2009.

4.2.1 Energy threshold determination

In Borexino distortions of the energy scale are due to different factors:

- physical effects, or in other words the quenching in the scintillator;
- geometrical effects, because of the light collection asymmetry in the detector²;
- the electronics design, which was thought for optimal performance in the low-energy range of ^{7}Be neutrinos, in a regime where a single photoelectron is expected for each PMT. At higher energies, the electronics response to multiple photoelectron hits on a single channel is not linear. For each triggered channel, the charge from photoelectrons in a 80 ns gate is integrated and recorded, but photoelectrons in the following 65 ns dead time window are lost. The resulting fraction of lost charge increases with energy and can reach $\sim 10\%$ at ~ 10 MeV. Moreover, the number of detected photoelectrons depends on the event position in the active volume, due to differences in PMT coverage.

Calibration of the energy scale allows to establish with high confidence the energy threshold for the ^{8}B neutrino analysis and the error in its determination. It also makes possible to calibrate the energy scale, allowing the determination of the energy spectrum of the electrons scattered by ^{8}B neutrinos.

As explained in Section 2.6.1, in Borexino a long and accurate calibration campaign has been performed in June-July 2009. To avoid contamination during calibration, we calibrated the response of the detector with encapsulated γ sources. The scintillation induced by γ -rays is due to the ionizing tracks of the secondary electrons, thus, the γ and β energy

²In Borexino the South hemisphere is affected by an inefficiency in the light collection due to the amount of dead PMTs that is larger than in the North hemisphere; in particular the ratio between the efficiencies is about $\epsilon_S/\epsilon_N=80\%$.

scales are closely related.

For an accurate determination of the energy scale for ^8B neutrino analysis, the dominant non-linearities have been reproduced with a Monte Carlo simulation and studied on calibration data. Actually, establishing a correlation between the β and γ energy scales required extensive simulations with the G4Bx Monte Carlo code. As deeply explained in Section 3.2, G4Bx is based on Geant4 [91] and simulates in detail all the detector components, and includes scintillation, Čerenkov photon production, absorption and scattering of light in the scintillator and in the buffer and the PMT response.

To calibrate the detector energy response to ^8B neutrinos, we used an $^{241}\text{Am}^9\text{Be}$ neutron source positioned at the center of the detector and at several positions at 3 m radius (see Table 2.3). Neutron capture on ^1H and on ^{12}C in the scintillator results in the emission of γ -rays from the 2.223 MeV and 4.945 MeV excited states, respectively. In addition, neutron capture on the stainless steel of the insertion system produces γ -rays from the 7.631 MeV (^{56}Fe) and 9.298 MeV (^{54}Fe) excited states. We validate the Monte Carlo code by simulating the four γ -rays in both positions. In left panel of Figure 4.3 I show the results of the calibration of the γ -equivalent energy scale in the detector center. Monte Carlo simulations reproduce γ peak positions and resolutions at $\sigma_1 = 1\%$ precision in the detector center (as shown in Figure 4.3), and at $\sigma_2 = 4\%$ precision at 3 m from the detector's center. Assuming the same accuracy for the β -equivalent energy scale, we extrapolate it by simulating electrons uniformly distributed in the scintillator, and then selecting those with reconstructed position within the fiducial volume. The error on the energy scale is obtained with a linear interpolation from σ_1 in the detector center to σ_2 at 3 m, along the radius. The β -equivalent energy scale, in the energy region above 2 MeV, can be parametrized as:

$$N = a \cdot E + b, \quad (4.1)$$

where N is the number of photoelectrons (p.e.) detected by the PMTs, $a = (459 \pm 11)$ p.e./MeV and $b = (115 \pm 38)$ p.e.. The non-zero intercept b is related to the fact that this description is valid only in this energy range and that the overall relation between N and E is non linear.

The conclusion of this study is that, within a 3 m radial distance from the center of the detector, the 3 MeV and 5 MeV energy thresholds for the ^8B analysis correspond to (1494 ± 51) p.e. and (2413 ± 68) p.e., respectively; the uncertainties have been calculated by propagating the errors of Eq. 4.1.

4.2.2 Fiducial volume definition

As described in Section 3.1.3, the positions of scintillation events are reconstructed with a photon time-of-flight method. The Borexino electronics records the time of each detected photoelectron introducing a dead time of 145 ns after each hit for each individual channel. Therefore, the timing distribution is biased at high energy, where multiple photoelectrons are detected by each channel, and the position reconstruction is energy dependent.

To measure this effect, we deployed during the calibration campaign the $^{241}\text{Am}^9\text{Be}$ neutron source at the six cardinal points of the sphere defining the fiducial volume, *i.e.* those points lying on axis through the center of the detector, with off-center coordinates from the set $x = \pm 3$ m, $y = \pm 3$ m, and $z = \pm 3$ m. The recoiled proton from neutron scattering allows us to study the reconstructed position as function of the collected charge up to ~ 5000 p.e..

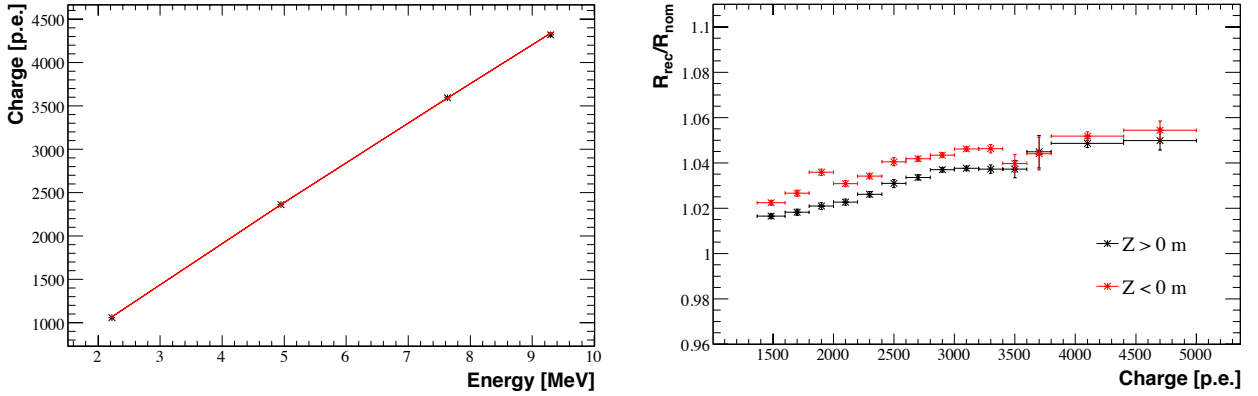


Figure 4.3: *Left:* Black crosses are the measured peak positions of γ radiation induced by neutron captures in ^1H (2.223 MeV), ^{12}C (4.945 MeV), ^{56}Fe (7.631 MeV) and ^{54}Fe (9.298 MeV) in the detector center. Red line is the Monte Carlo prediction for γ rays generated in the detector center. *Right:* Ratio of the reconstructed radial position of γ events from the $^{241}\text{Am}^9\text{Be}$ source in Borexino to the source radial position measured by the CCD camera system, as a function of the measured charge.

In right panel of Figure 4.3 I report the ratio of measured versus nominal position of the $^{241}\text{Am}^9\text{Be}$ source. Using this data we define the Fiducial Volume $R_{\text{nom}} < 3\text{ m}$. The non-homogeneous distribution of live PMTs, in particular the large deficit of live PMTs in the bottom hemisphere [85], is responsible for the different spatial response at mirrored positions about the x-y plane. Thus, as shown in Figure 4.3, two radial functions have been defined for positive and negative z positions.

After all post-calibration improvements to the event reconstruction algorithm, typical resolution in the event position reconstruction is $(13 \pm 2)\text{ cm}$ in x and y, and $(14 \pm 2)\text{ cm}$ in z at the relatively high ^{212}Bi energies. The spatial resolution is expected to scale as $1/\sqrt{N}$ where N is the number of triggered PMTs. Systematic deviations of reconstructed positions from the nominal source position are due to the 3.5 cm accuracy of the CCD cameras in the determination of the calibration source position, and in 1.6 cm introduced by the energy dependency. The overall systematics are within 3.8 cm throughout the 3 m-radius Fiducial Volume.

4.3 Background removal

Considering the Borexino FV, the event rate above 3 MeV is about 4 cpd. The expected rate for ^8B solar neutrino, in the SSM+(MSW-LMA) framework, is about 0.3 cpd/100 t above 3 MeV. This means that we have to face a signal to background ratio of about 0.07 in the FV.

The main background components above 3 MeV are:

1. cosmic muons and their interaction products;
2. penetration of external γ 's from photomultipliers (PMTs);
3. internal ^{214}Bi $\beta + \gamma$ decays ($Q=3.27\text{ MeV}$);

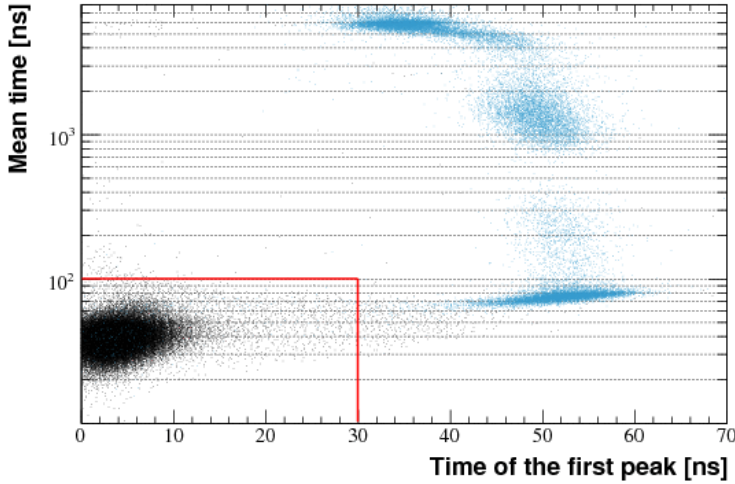


Figure 4.4: Distribution of the mean value of the reconstructed hits time (*mean time*) as a function of the peak of the reconstructed hits time (*peak time*) for scintillation events (black) and for muons (light blue); red lines represent the threshold values to distinguish muons and scintillation events.

4. internal ^{208}Tl $\beta + \gamma$ decays ($Q=5.001\text{ MeV}$).

As described below, each background component has been treated with a specific removal technique.

4.3.1 Muon rejection

The cosmic muon rate at LNGS is $(1.16 \pm 0.03)\text{ m}^{-2}\text{hr}^{-1}$ with an average energy of about 270 GeV (see Chapter 7). Each day, ~ 4300 muons deposit energy in Borexino inner detector. Depending on deposited energy and track length, there is a small but non-zero probability that a cosmic muon induces a number of photoelectrons comparable to the multi-MeV electron scatterings of interest for this analysis, and is mistaken for a point-like scintillation event. A measurement of the neutrino interaction rate in Borexino requires high performance rejection of muon events and an accurate estimate of the muon tagging efficiency. As described in 2.2.1, the Borexino WT is instrumented with 208 PMTs to serve as a muon veto. In addition, we perform pulse-shape discrimination on the hit time distribution of inner detector PMTs, since for track-like events, like muons, such distribution generally extends to longer times than for point-like events, like β -decays and $\nu\text{-e}$ scattering. We exclude muons from the event sample in the energy range of interest (3.0–16.3 MeV, or 1413–6743 p.e.) by imposing the following requirements (ID cuts, see Figure 4.4):

- The peak of the reconstructed hits time distribution, with respect to the first hit, is between 0 ns and 30 ns.
- The mean value of the reconstructed hits time distribution, with respect to the first hit, is between 0 ns and 100 ns.

Isotope	τ [s]	Q [MeV]	Decay	Expec. Rate [cpd/100 t]	Fraction >3 MeV	Expec. Rate >3 MeV [cpd/100 t]	Meas. Rate >3 MeV [cpd/100 t]
^{12}B	0.03	13.4	β^-	1.24 ± 0.04	0.886	1.10 ± 0.03	1.48 ± 0.06
^8He	0.17	10.6	β^-	0.023 ± 0.011	0.898		
^9C	0.19	16.5	β^+	0.084 ± 0.027	0.965	$(1.6 \pm 0.3) \times 10^{-1}$	$(1.7 \pm 0.5) \times 10^{-1}$
^9Li	0.26	13.6	β^-	0.062 ± 0.004	0.932		
^8B	1.11	18.0	β^+	0.240 ± 0.054	0.938		
^6He	1.17	3.5	β^-	NA	0.009	$(5.3 \pm 0.8) \times 10^{-1}$	$(5.1 \pm 0.7) \times 10^{-1}$
^8Li	1.21	16.0	β^-	0.35 ± 0.06	0.875		
^{11}Be	19.9	11.5	β^-	0.031 ± 0.005	0.902	$(2.8 \pm 0.5) \times 10^{-2}$	$(3.6 \pm 3.5) \times 10^{-2}$
^{10}C	27.8	3.6	β^+	0.47 ± 0.04	0.012	$(5.7 \pm 0.5) \times 10^{-3}$	$(6.6 \pm 1.8) \times 10^{-3}$

Table 4.1: Expected muon-induced contaminants with Q-value >3 MeV in Borexino. They are ordered by increasing mean life and the horizontal lines regroup isotopes with similar τ . The expected rate is obtained by extrapolating the data from KamLAND [96] in accordance with the empirical law defined in Eq 4.2.

The efficiency of the selection cuts was evaluated on a sample of 2170207 events, identified by the OD as muons. Only 22 of these events, a fraction of $(1.0 \pm 0.2) \times 10^{-5}$, survive the ID cuts in the energy and spatial region of interest, and are tagged as possible scintillation events.

At that time, we did not have an absolute value for the OD muon veto efficiency (now published in [80]), but we estimated it to be larger than 99%, from G4Bx simulations. The residual muon rate, due to the combined inefficiency of the two tagging systems, taking into account the fact that the two detectors are independent, is $(4.5 \pm 0.9) \times 10^{-4}$ muons/day/100 t above 3 MeV and $(3.5 \pm 0.8) \times 10^{-4}$ muons/day/100 t above 5 MeV.

4.3.2 Cosmogenic background study and rejection

As explained and studied in Chapter 7, surviving cosmic muons can interact with ^{12}C nuclei of the scintillator, through spallation interaction. The final state is usually composed by unstable nuclei and free neutrons. The first will β -decay and the latter, after thermalization, will be captured by ^1H or ^{12}C nuclei, emitting a 2.22 MeV or a 4.94 MeV gamma, respectively. Both the spallation final state products can thus mimic the neutrino events in liquid scintillator.

The rejection of cosmic muon products has been developed in different ways, depending on the cosmogenic nature: fast cosmogenic isotopes, slow cosmogenic isotopes or cosmogenic neutron captures.

Fast cosmogenic veto

In Table 4.1 I report a list of expected cosmogenic isotopes produced by muons in Borexino. The short-lived cosmogenics ($\tau < 2$ s), as well as the γ -ray capture on ^{12}C , are rejected by a 6.5 s cut after each muon. The associated Dead Time has been quoted applying the 6.5 s veto on a selected data sample formed by muons and ^{210}Po decay events; the sample of ^{210}Po has been chosen thanks to its uniform distribution in time, with respect to the muon sample. The corresponding evaluated Dead Time is 29.2%.

Figure 4.5 shows the time distribution of events following a muon. The data are well fit by

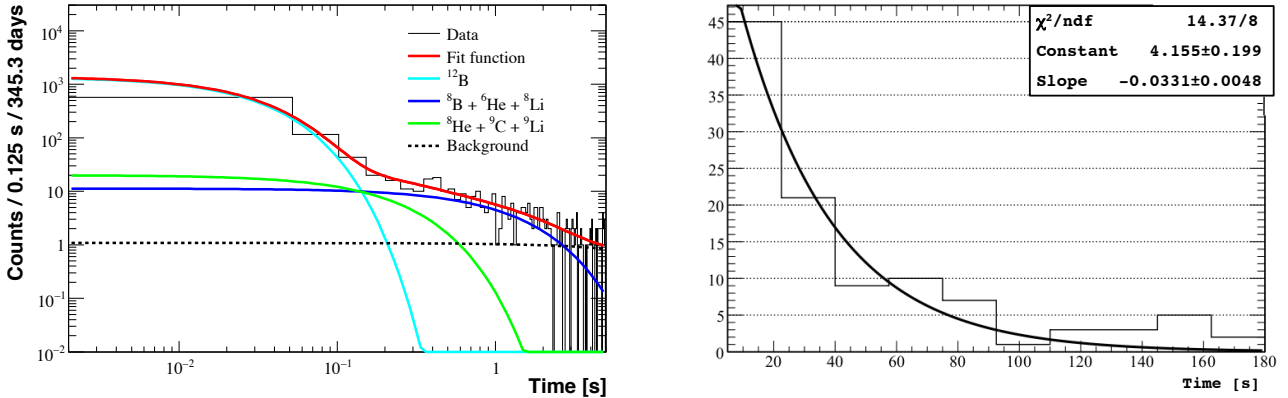


Figure 4.5: *Left:* Cumulative distribution of events with energy > 3 MeV within a 6.5 s window after a muon. The time distribution has been fit to three decay exponentials. The ensuing exponential lifetimes are $\tau = (0.031 \pm 0.002)$ s, (0.25 ± 0.21) s, (1.01 ± 0.36) s and corresponds to the contribution from ^{12}B , $^{8}\text{He} + ^9\text{C} + ^9\text{Li}$ and $^{8}\text{B} + ^6\text{He} + ^8\text{Li}$, respectively. *Right:* Fit of the time distribution of ^{10}C candidates selected through the TFC technique.

three exponentials with characteristic times of (0.031 ± 0.002) s (^{12}B), (0.25 ± 0.21) s (^{8}He , ^{9}C , ^{9}Li) and (1.01 ± 0.36) s (^{8}B , ^{6}He , ^{8}Li), in good agreement with the lifetimes of the short-lived isotopes (see Table 4.1). From the fit we estimate the production rates of these cosmogenic isotopes in Borexino. We conclude that rejection of events in a 6.5 s window following every muon crossing the SSS reduces the residual contamination of the short lived isotopes to $(1.7 \pm 0.2) \times 10^{-3}$ cpd/100 t above 3 MeV and $(1.3 \pm 0.2) \times 10^{-3}$ cpd/100 t above 5 MeV.

The expected rates (R) quoted in Table 4.1 are obtained by scaling the production rates (R^0) measured by KamLAND [96] with:

$$R = R^0 \left(\frac{E_\mu}{E_\mu^0} \right)^\alpha \frac{\Phi_\mu}{\Phi_\mu^0}, \quad (4.2)$$

where $E_\mu = (270 \pm 3_{\text{stat}} \pm 18_{\text{sys}})$ GeV [97] and $\Phi_\mu = (1.16 \pm 0.03) \text{ m}^{-2} \text{ hr}^{-1}$ [77] are the mean muon energy and flux used in the present analysis; $E_\mu^0 = (260 \pm 4)$ GeV and $\Phi_\mu^0 = (5.37 \pm 0.41) \text{ m}^{-2} \text{ hr}^{-1}$ are the corresponding KamLAND values. $\alpha = 0.77$ is a scaling parameter to relate cosmogenic production rate at different mean energies of the incoming muon flux; it is obtained in [96] by fitting the production yield of each isotope, simulated by FLUKA, as a function of muon beam energy. Overall, Borexino data results are in agreement with the values quoted in Table 4.1 within 15%.

Cosmogenic neutron rejection

Cosmogenic neutrons produced in the scintillator thermalize in few ns. After thermalization they interact through elastic scattering with nuclei until their capture on ^1H or ^{12}C , with the consequent emission of a 2.22 MeV or 4.94 MeV gamma respectively. We measured the capture time for neutrons in the Borexino scintillator using a neutron calibration source and we obtained (256.0 ± 0.4) μs . The energy of the dominant γ -rays from neutron capture on ^1H is below the analysis energy threshold (3 MeV). On the other

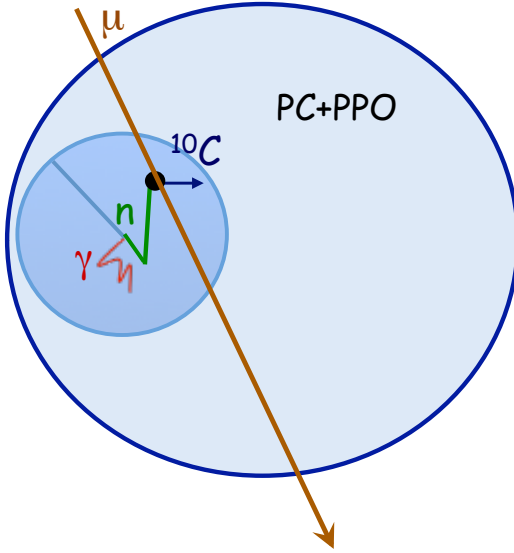


Figure 4.6: Representation of the three-fold coincidence technique: a muon (orange arrow) crossing the Borexino IV interacts with a ^{12}C nucleus (black dot) producing a ^{10}C isotope (blue arrow) and a neutron (green line). The neutron capture on ^1H or ^{12}C produces a gamma (red line). A radial cut (light blue sphere) around the emitted gamma is applied in order to individuate the ^{10}C .

hand, the 4.94 MeV γ -rays from neutron captures on ^{12}C is a potential background for this analysis. Using data from $^{241}\text{Am}^9\text{Be}$ neutron source, we evaluated the ratio between the number of captures on ^{12}C with respect to the total. Scaling the cosmogenic neutron capture rate on ^1H by this fraction we find a neutron capture rate on ^{12}C corresponding to $R_n = (0.86 \pm 0.01) \text{ cpd}/100 \text{ t}$. The fast cosmogenic veto, described in previous section, rejects neutrons produced in the scintillator or in the buffer by muon spallation with 99.99% efficiency. To reject neutrons produced in water, we applied a second 2 ms veto after each muon crossing the Water Tank only. The rejection efficiency for neutrons produced in water is 0.9996. The overall survival neutron rate in the energy range of interest and in the fiducial volume is $(8.6 \pm 0.1) \times 10^{-5} \text{ cpd}/100 \text{ t}$.

^{10}C identification and subtraction

Long-lived ($\tau > 2 \text{ s}$) cosmogenic isotopes cannot be rejected with the 6.5 s veto. The removal of these contaminants requires a separate treatment. Since ^7Be ($\tau = 76.9 \text{ d}$, Q-value=0.9 MeV) and ^{11}C ($\tau = 29.4 \text{ min}$, Q-value=2.0 MeV) are below the energy threshold, we only focused on ^{10}C and ^{11}Be . The fraction of the ^{10}C energy spectrum above 3 MeV, evaluated on Monte Carlo simulation data, is 1.2%. When ^{10}C is produced in association with a neutron, ^{10}C candidates are tagged by the three-fold coincidence (TFC) with the parent muon and subsequent neutron capture in the scintillator [32]. A representation of the TFC is shown in Figure 4.6. The efficiency of the Borexino electronics in detecting at least one neutron soon after a muon has been estimated to be 94% by two parallel (1-channel and 8-channel) DAQ systems that digitize data for 2 ms after every OD trigger at 500 MHz. The rate of muons associated with at least 1 neutron, measured by the Borexino electronics, is $\sim 67 \text{ cpd}$. Thus, to reject ^{10}C from the analysis we exclude all data within a 120 s window after a $\mu + n$ coincidence and within a 0.8 m distance from the neutron cap-

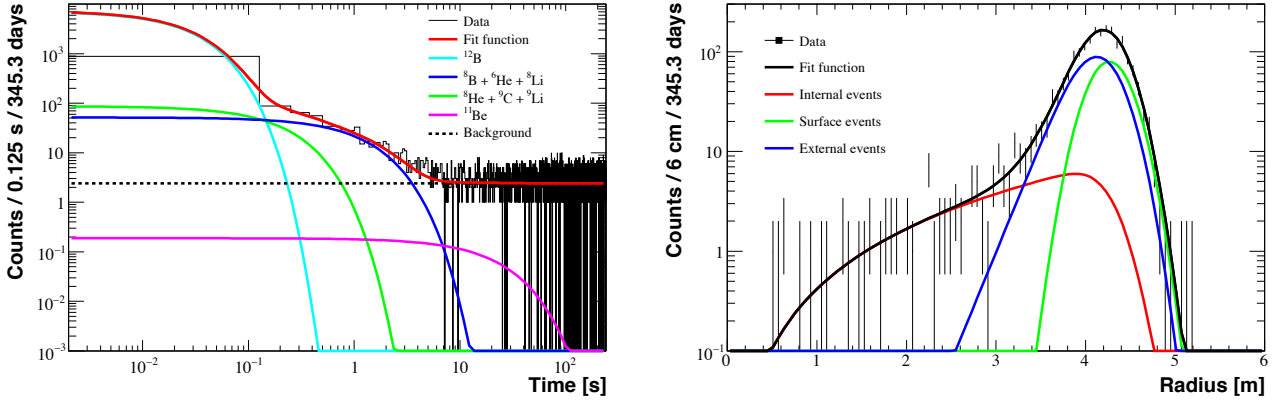


Figure 4.7: *Left:* Time profile of events with energy >3 MeV within 240 s after a muon and within 2 m from its track in the entire Borexino active volume (278 t). The distribution has been fit to the three decay exponentials as in Figure 4.5, plus the ^{11}Be component, with fixed mean-lives. *Right:* Fit of the radial distribution for events with $E > 3$ MeV. The red line represents the uniformly distributed event component in the active mass, the green line the surface contamination, and the blue line is external background.

ture point. The efficiency of this cut is 0.74 ± 0.11 , for a 0.16% dead time. A time profile analysis of events tagged by this veto above 3 MeV is shown in right panel of Figure 4.5. The exponential likelihood fit returns a characteristic time of (30 ± 4) s, consistent with the lifetime of ^{10}C . The total ^{10}C rate evaluated by the fit is (0.50 ± 0.13) cpd/100 t, in production channels with neutron emission. Thus, the residual ^{10}C contamination from neutron-producing channels above 3 MeV is $(6.0 \pm 0.2) \times 10^{-3}$ cpd/100 t. The dominant neutron-less ^{10}C production reaction is $^{12}\text{C}(\text{p},\text{t})^{10}\text{C}$. From [32] we know the $^{12}\text{C}(\text{p},\text{d})^{11}\text{C}$ production rate. Evaluating the ratio between the $^{12}\text{C}(\text{p},\text{d})^{11}\text{C}$ and $^{12}\text{C}(\text{p},\text{t})^{10}\text{C}$ cross sections [98], we could extrapolate the $^{12}\text{C}(\text{p},\text{t})^{10}\text{C}$ rate, corresponding to $(0.6 \pm 1.8) \times 10^{-3}$ cpd/100 t. The residual background above 3 MeV from ^{10}C is 2.2×10^{-3} cpd/100 t. The overall ^{10}C rate above 3 MeV, $(6.6 \pm 1.8) \times 10^{-3}$ cpd/100 t, agrees with the expected one, quoted in Table 4.1.

^{11}Be estimation

The other long-lived cosmogenic isotope we had to consider is ^{11}Be . In left panel of Figure 4.7 I show the time profile of events within 240 s after a muon and within a 2 m distance from its track in the entire active volume (278 t). The efficiency of the distance cut is assumed to be the same as the one measured for cosmogenic ^{12}B (84%) by performing fits to the time distribution of events after a muon before and after the track cut. The measured ^{11}Be rate above 3 MeV is $(3.6 \pm 3.5) \times 10^{-2}$ cpd/100 t, consistent with the $(2.8 \pm 0.5) \times 10^{-2}$ cpd/100 t rate extrapolated from the KamLAND measurements [96]. Since all measured rates deviated less than 18% from the extrapolated value, we adopt the latter as the residual rate of ^{11}Be in our sample.

4.3.3 External background rejection

The Borexino PMTs and concentrators are contaminated by ^{232}Th and ^{238}U (for details see Chapter 5). The dangerous contaminants from PMTs are thus represented by the γ -rays from the β -decay of ^{208}Tl (2.61 MeV) and ^{214}Bi (up to 3.27 MeV), that can reach the FV. We decided to set the energy threshold at 3 MeV in order to avoid this contamination. In addition the fiducial volume cut is very effective against the ^{208}Tl and ^{214}Bi background due to ^{222}Rn and ^{220}Rn emanated from the nylon vessel, as well as residual external γ -ray background. In right panel of Figure 4.7 the radial distribution of all scintillation events above 3 MeV has been fit to a model which takes into account the three sources of backgrounds: a uniform distribution in the detector for internal events, a delta-function centered on the vessel radius for the point-like radioactive background in the nylon, and an exponential for external γ -ray background. All the three components are convoluted with the detector response function. From this radial analysis we conclude that within the fiducial volume there is a small contribution of events from surface contamination and the exterior of $(6.4 \pm 0.2) \times 10^{-3} \text{ cpd}/100 \text{ t}$ for events above 3 MeV and $(3 \pm 11) \times 10^{-6} \text{ cpd}/100 \text{ t}$ for events above 5 MeV, thus compatible with zero.

4.3.4 Internal intrinsic contamination rejection

Intrinsic ^{238}U and ^{232}Th contamination in the Borexino scintillator contributes above 3 MeV through ^{214}Bi ($Q=3.27 \text{ MeV}$) and ^{208}Tl ($Q=5.001 \text{ MeV}$).

Internal ^{214}Bi rejection

^{214}Bi events can be detected by looking for β - α delayed coincidence ($\tau=237 \mu\text{s}$) between ^{214}Bi and ^{214}Po . In particular, we search of the coincidences selecting events falling in a time window between $20 \mu\text{s}$ and 1.4 ms with a spatial separation $<1.5 \text{ m}$ ($\epsilon = 1$). The ^{214}Po α -decays are selected in the $0.3\text{-}1.2 \text{ MeV}$ ($\epsilon = 1$) energy range. The remaining contribution of ^{214}Bi surviving in our sample is negligible: $(1.1 \pm 0.4) \times 10^{-4} \text{ cpd}/100 \text{ t}$.

Internal ^{208}Tl estimation

The parent of ^{208}Tl is ^{212}Bi that α -decays into ^{208}Tl with a branching ratio of 36% and a lifetime of $\tau = 4.47 \text{ min}$. In the second channel with branching ratio 64%, ^{212}Bi β -decays into ^{212}Po with a lifetime of $\tau = 431 \text{ ns}$. We estimate the ^{208}Tl rate from the fast ^{212}Bi - ^{212}Po coincidences. ^{212}Bi - ^{212}Po events are selected in a time window between 400 and 1300 ns, with an efficiency of 0.35, and requiring a maximum spatial distance between the two events of 1m ($\epsilon = 1$). ^{212}Bi and ^{212}Po are selected in $[20, 1200] \text{ p.e.}$ ($\epsilon = 1$) and $[420, 580] \text{ p.e.}$ ($\epsilon = 0.93$) energy regions, respectively. α 's from ^{212}Po are strongly quenched in the Borexino scintillator; we estimated the corresponding quenched energy from the ^{210}Po and ^{214}Po peaks. We found 21 ^{212}Bi - ^{212}Po coincidences in the entire data set, within the FV. Accounting for the efficiency of the selection cuts and the branching ratios of the ^{212}Bi decays, this corresponds to a ^{208}Tl contamination in our neutrino sample of $(8.4 \pm 2.0) \times 10^{-2} \text{ cpd}/100 \text{ t}$ rate (29 ± 7 events).

In Table 4.2 I report a summary of the cut sequence described above. The energy spectrum of the final sample, compared with simulated spectra of ^8B neutrinos and of each residual

Background	Rate [10^{-4} cpd/100 t] $> 3 \text{ MeV}$	Rate [10^{-4} cpd/100 t] $> 5 \text{ MeV}$
Muons	4.5 ± 0.9	3.5 ± 0.8
Neutrons	0.86 ± 0.01	0
Ext. background	64 ± 2	0.03 ± 0.11
Fast cosmogenic	17 ± 2	13 ± 2
^{10}C	22 ± 2	0
^{214}Bi	1.1 ± 0.4	0
^{208}Tl	840 ± 20	0
^{11}Be	320 ± 60	233 ± 44
Total	1270 ± 63	250 ± 44

Table 4.2: Residual rates of background components after the data selection cuts above 3 and 5 MeV.

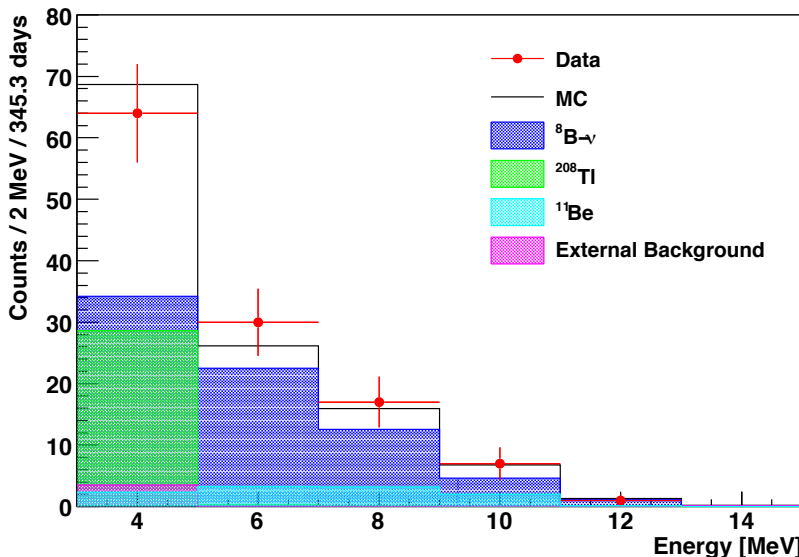


Figure 4.8: Comparison between the final spectrum after data selection (red dots) and Monte Carlo simulations (black line). The expected electron recoil spectrum from oscillated ^8B ν interactions (filled blue histogram), ^{208}Tl (green), ^{11}Be (cyan) and external background (violet), are equal to the measured values in Table 4.2.

background component listed in Table 4.2, is shown in Figure 4.8. The total exposure, after applying all the analysis cuts just listed, is 345.3 days.

4.4 ^8B solar neutrino rate above 3 MeV

After applying previous listed removal techniques, we found as mean value for ^8B neutrino events:

- $\text{Num}_\nu = 75 \pm 13$, above 3 MeV;

Source	$E > 3 \text{ MeV}$		$E > 5 \text{ MeV}$	
	σ_+	σ_-	σ_+	σ_-
Energy threshold	3.6%	3.2%	6.1%	4.8%
Fiducial mass	3.8%	3.8%	3.8%	3.8%
Energy resolution	0.0%	2.5%	0.0%	3.0%
Total	5.2%	5.6%	7.2%	6.8%

Table 4.3: Evaluated systematic errors on the ${}^8\text{B}-\nu$ count rates.

- $\text{Num}_\nu = 46 \pm 8$, above 5 MeV.

4.4.1 Evaluation of systematic errors

The dominant sources of systematic errors are the determinations of the energy threshold and of the fiducial mass, both already discussed in the previous sections. The first introduces a systematic uncertainty of $+3.6\% - 3.2\%$ above 3 MeV and $+6.1\% - 4.8\%$ above 5 MeV. The second systematic source is responsible for a $\pm 3.8\%$ uncertainty in the ${}^8\text{B}$ neutrino rate. A secondary source of systematics, related to the effect of the energy resolution on the threshold cuts, has been studied on a simulated ${}^8\text{B}$ neutrino spectrum and is responsible for a systematic uncertainty of $+0.0\% - 2.5\%$ above 3 MeV and $+0.0\% - 3.0\%$ above 5 MeV. The systematic errors are shown in Table 4.3.

4.4.2 Results on ${}^8\text{B}$ solar neutrino rates

Considering also systematic uncertainties, the resulting count ${}^8\text{B}$ solar neutrino rates are:

- $0.217 \pm 0.038(\text{stat}) {}^{+0.008}_{-0.008}(\text{syst}) \text{ cpd}/100 \text{ t}$, above 3 MeV;
- $0.134 \pm 0.022(\text{stat}) {}^{+0.008}_{-0.007}(\text{syst}) \text{ cpd}/100 \text{ t}$. above 5 MeV.

The final energy spectrum after all cuts and residual background removal is shown in Figure 4.9. It is in agreement with the scenario which combines the high metallicity Standard Solar Model, BPS09(GS98) [39] (see Section 1.6), and the prediction of the MSW-LMA solution.

4.5 The ${}^8\text{B}$ solar neutrino flux and the P_{ee}

From the measured rate it is possible to evaluate the corresponding solar neutrino flux. The equivalent ${}^8\text{B}$ neutrino flux from the electron scattering rate above 5 MeV (Table 4.4), is:

$$\Phi_{{}^8\text{B}} = (2.7 \pm 0.4_{\text{stat}} \pm 0.2_{\text{syst}}) \times 10^6 \text{ cm}^{-2}\text{s}^{-1},$$

in good agreement with the SuperKamiokaNDE-I and SNO D₂O measurements with the same threshold, as reported in Table 4.5.

The corresponding value above 3 MeV is:

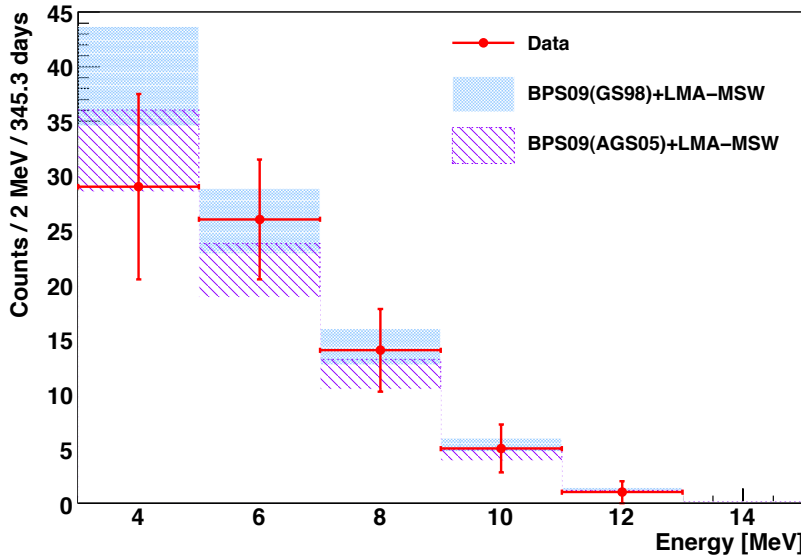


Figure 4.9: Comparison of the final spectrum after data selection and background subtraction (red dots) to Monte Carlo simulations (blue) of oscillated ${}^8\text{B}$ ν interactions, with amplitude from the Standard Solar Models BPS09(GS98) (high metallicity) and BPS09(AGS05) (low metallicity), and from the MSW-LMA neutrino oscillation model.

$$\Phi_{{}^8\text{B}} = (2.4 \pm 0.4_{\text{stat}} \pm 0.1_{\text{syst}}) \times 10^6 \text{ cm}^{-2}\text{s}^{-1}.$$

The expected value for the case of no neutrino oscillations, including the theoretical uncertainty on the ${}^8\text{B}$ flux from the Standard Solar Model [38, 39], is $(5.88 \pm 0.65) \times 10^6 \text{ cm}^{-2}\text{s}^{-1}$. This means that we confirm the solar ν_e disappearance at 4.2σ .

In Table 4.5 I report the comparison between ${}^8\text{B}$ - ν flux measured by Borexino and the other solar neutrino experiments, based on elastic scattering detection technique. Our result is in perfect agreement with previous ones.

To evaluate the survival probability corresponding to the measured rate, we have to take into account that ${}^8\text{B}$ neutrinos have a continuum spectrum. To define the neutrino electron survival probability \bar{P}_{ee} averaged in the energy range of interest, we define the measured recoiled electron rate R , through the following convolution:

$$R = \int_{T_e > T_0} dT_e \int_{-\infty}^{+\infty} dt \left(\frac{dr}{dt}(t) \cdot g(t - T_e) \right) \quad (4.3)$$

where:

- g is the detector energy response, assumed to be gaussian;
- the resolution depending on the energy;
- the differential rate is:

$$\frac{dr}{dT_e}(T_e) = \int_{E_\nu > E_0} dE_\nu (\bar{P}_{ee} \cdot \Psi_e + (1 - \bar{P}_{ee}) \cdot \Psi_{\mu-\tau}) \quad (4.4)$$

	[3.0, 16.3] MeV	[5.0, 16.3] MeV
Rate [cpd/100 t]	$0.22 \pm 0.04 \pm 0.01$	$0.13 \pm 0.02 \pm 0.01$
$\Phi_{\text{exp}}^{\text{ES}} [10^6 \text{ cm}^{-2} \text{s}^{-1}]$	$2.4 \pm 0.4 \pm 0.1$	$2.7 \pm 0.4 \pm 0.2$
$\Phi_{\text{exp}}^{\text{ES}} / \Phi_{\text{th}}^{\text{ES}}$	0.88 ± 0.19	1.08 ± 0.23

Table 4.4: Measured event rates in Borexino and comparison with the expected theoretical flux in the BPS09(GS98) MSW-LMA scenario [99].

Experiment	Threshold [MeV]	$\Phi_{sB}^{\text{ES}} [10^6 \text{ cm}^{-2} \text{s}^{-1}]$
SuperKamiokaNDE I [94]	5.0	$2.35 \pm 0.02 \pm 0.08$
SNO D ₂ O [95]	5.0	$2.39^{+0.24}_{-0.23} {}^{+0.12}_{-0.12}$
SNO Salt Phase [100]	5.5	$2.35 \pm 0.22 \pm 0.15$
SNO Prop. Counter [101]	6.0	$1.77^{+0.24}_{-0.21} {}^{+0.09}_{-0.10}$
Borexino	3.0	$2.4 \pm 0.4 \pm 0.1$
Borexino	5.0	$2.7 \pm 0.4 \pm 0.2$
Kamland [102]	5.5	$2.77 \pm 0.26 \pm 0.32$
SuperKamiokaNDE III [103]	5.0	$2.32 \pm 0.04 \pm 0.05$

Table 4.5: Results on ${}^8\text{B}$ solar neutrino flux from elastic scattering, normalized under the assumption of the no-oscillation scenario reported by SuperKamiokaNDE, SNO, and Borexino.

with:

$$\Psi_e = \frac{d\sigma_e}{dT_e}(E_\nu, T_e) \cdot N_e \cdot \frac{d\Phi_e}{dE_\nu}(E_\nu), \quad (4.5)$$

and:

$$\Psi_{\mu-\tau} = \frac{d\sigma_{\mu-\tau}}{dT_e}(E_\nu, T_e) \cdot N_e \cdot \frac{d\Phi_e}{dE_\nu}(E_\nu). \quad (4.6)$$

where T_e and E_ν are the electron and neutrino energies, and σ_x ($x=e,\mu-\tau$) are the cross sections for elastic scattering for different flavors. $T_0=3 \text{ MeV}$ is the energy threshold for scattered electrons, corresponding to a minimum neutrino energy of $E_0=3.2 \text{ MeV}$, N_e is the number of target electrons, and $d\Phi_e/dE_\nu$ is the differential ${}^8\text{B}$ solar neutrino flux [104].

Using the Equation 4.6, we obtain $\bar{P}_{ee}=0.29 \pm 0.10$ at the mean energy of 8.9 MeV for ${}^8\text{B}$ neutrinos. We could such add two new points in the mapping of the survival probability (see Figure 4.10).

4.6 Conclusions

The analysis I have just described represents an attempt to investigate for the first time the unexplored energy region for solar neutrinos between 1 and 3.5 MeV. We demonstrate

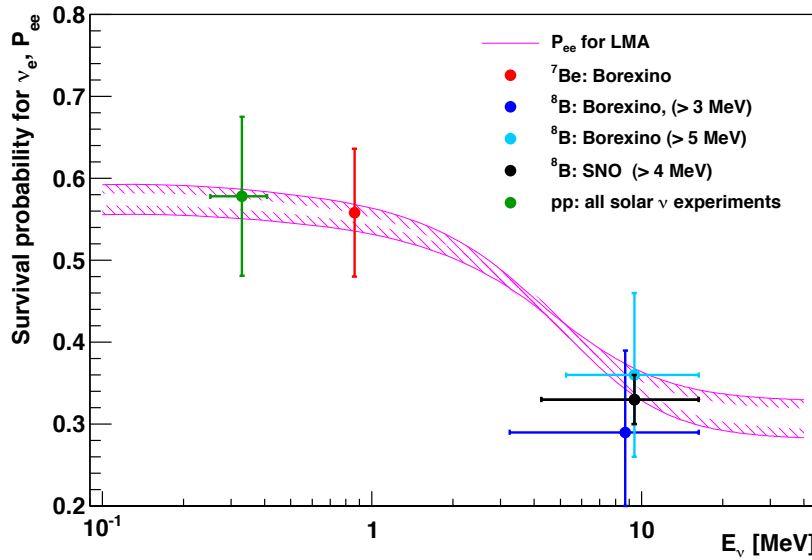


Figure 4.10: Electron neutrino survival probability as function of the neutrino energy, evaluated for the ^8B neutrino source assuming the BPS09(GS98) Standard Solar Model [38, 39] and the oscillation parameters from the MSW-LMA solution $\Delta m^2 = 7.69 \times 10^{-5} \text{ eV}^2$ and $\tan^2 \theta = 0.45$ [40]. Red, blue and light blue dots represent the Borexino results from ^7Be [35] and ^8B measurements. The error bars include also the theoretical uncertainty of the expected flux from the BPS09(GS98) SSM.

that, thanks to its excellent radiopurity and the developed analysis techniques, Borexino measures the ^8B solar neutrino with the lowest energy threshold ever reached in real time. Borexino is thus the first experiment able to detect in real time, and in the same target, neutrinos in the low energy, vacuum dominated- and in the high energy, matter enhanced-regions.

Considering the Borexino measurement of ^7Be neutrinos (0.862 MeV) and the associated probability $P_{ee}(^7\text{Be}) = 0.56 \pm 0.10$ [35], we can evaluate the distance between the two survival probabilities; this confirm the presence of a transition between the vacuum and the matter oscillation regimes at 1.9σ level.

As evident from Figure 4.10, the energy region between 1 and 3 MeV represents an unexplored ground where the ultimate validation of MSW-LMA solution can be present. In next chapters I will show the results of the attempt of decreasing the detection energy threshold for $^8\text{B}-\nu$ down to 2 MeV. In addition, in Borexino we recently reached the first pep solar neutrino measurement [31].

Chapter 5

Study of External Background Sources above 2 MeV

One of my main goal has been the measurement of ^8B solar neutrino flux above 2 MeV (see next Chapter). The attempt for this involved a big effort in studying, for the first time in Borexino, the energy region between 2 and 3 MeV. The main contaminants are the 2.61 MeV gammas coming from the ^{208}Tl produced on the PMTs (see Section 2.3.5). In the following pages I will show the study I performed on background sources above 2 MeV. The applied techniques involve:

- the use of the radial analysis on the whole Borexino vessel;
- the improvement and modification of the G4Bx performances;
- the comparison with previous estimates.

As explained in the text, the first attempt of the analysis have been performed above 5 MeV, the cleanest Borexino energy region (see previous Chapter), where the individuation of new background sources is easier. In some cases, results have been rescaled to the window above 2 MeV. Then the analysis has been extended down to 2 MeV.

5.1 Approaching the analysis

Many of the background source above 2 MeV also affect the energy region above 3 MeV. As explained in the previous Chapter, many rejection techniques have been developed to remove muons, cosmogenics, ^{208}Tl and ^{214}Bi from the data sample: all the listed techniques in Chapter 4 are also applied for the present analysis. The estimated residuals are listed in Table 5.1 for different energy ranges in the whole vessel.

The new contaminants I have to face above 2 MeV are represented by gammas coming from the PMTs, the buffer and the Inner Vessel surface. As mentioned in Section 2.3, possible γ 's are:

- 2.61 MeV γ 's of ^{208}Tl from PMTs and IV;
- γ 's up to 3.27 MeV of ^{214}Bi from PMTs and IV;
- 2.22 MeV γ 's from neutron capture on ^1H in the buffer.

Residual Rate (cpd)	2.14 - 4.89 MeV	2.14 - 16.3 MeV	4.89 - 16.3 MeV
^{214}Bi	0.020 ± 0.001	0.020 ± 0.001	0
^{208}Tl	0.11 ± 0.03	0.11 ± 0.03	0
^{10}C	0.07 ± 0.03	0.07 ± 0.03	0
^{11}Be	0.027 ± 0.005	0.095 ± 0.020	0.07 ± 0.01
Total Rate (cpd)	0.30 ± 0.04	0.23 ± 0.05	0.07 ± 0.01

Table 5.1: Estimated residuals of the contaminants in the Inner Vessel for the 3 energy windows [2.14, 4.89] MeV, [2.14, 16.3] MeV e [4.89, 16.3] MeV, after applying the removal techniques listed in Chapter 4.

The study of these contaminants is quite delicate, mostly due to their low statistics. For this reason I decided to study them using the whole volume of the IV (278 t). This decision obviously involves many inconveniences:

- the loss of light collection efficiency closing the vessel, affecting the energy threshold definition;
- the problem in the definition of the vessel shape, that is not exactly spheric and is changing in time.

The analysis I'm going to show is based on data taken in the period from January 2008 to December 2009, for a global livetime of 486.2 d, reduced to 336.4 d after the fast cosmogenic veto (see Section 4.3.2).

5.1.1 The energy threshold

The main problem in the definition of the energy threshold in the entire vessel is the loss of light collection efficiency, closing the vessel. In particular, we need at least to define:

- a threshold around 2 MeV in order to avoid the ^{11}C contamination ($Q \simeq 1.8 \text{ MeV}$);
- a threshold around 5 MeV in order to select the cleanest energy region (free from internal ^{208}Tl).

I decided to calibrate the efficiency loss directly on our calibration data, using the AmBe source that well satisfy the requirements on value of energies (see Section 2.6.1). As already mentioned, the AmBe source has been positioned in different positions in the Borexino IV (see Table 2.3). I selected gammas from neutron capture on proton (2.22 MeV) and on ^{12}C (4.94 MeV) for different positions of the source, constructing a function of nhits (see Section 3.1.2) depending on radius. In Figure 5.1, I report the energy threshold definition for 2.22 MeV and 4.94 MeV γ 's, respectively.

In order to know the effective values of visible energy, γ 's of 2.22 MeV and 4.94 MeV have been simulated in the center of Borexino: the corresponding values of visible energy are 2.10 MeV and 4.80 MeV, respectively. As neutrino interactions in Borexino involve electrons, that have a slightly different energy loss from γ 's in the scintillator, it is necessary to know the corresponding values of deposited energy by electrons. For this reason,

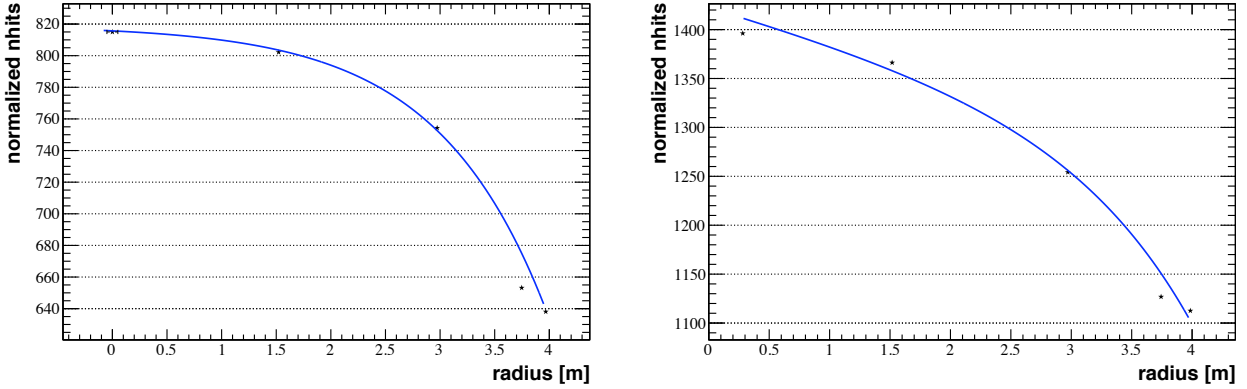


Figure 5.1: *Left:* behavior of the number of photoelectrons (p.e.) as a function of the radius for 2.22 MeV γ 's from AmBe source, fitted with a function: $f(r)=a-be^r$, with $a=819.10\pm 0.04$ and $b=3.398\pm 0.002$. *Right:* behavior of number of photoelectrons as a function of radius for 4.94 MeV γ 's from AmBe source, fitted with a function: $f(r)=a-br-ce^r$, with $a=1426\pm 1$, $b=34.4\pm 0.9$ and $c=3.47\pm 0.06$.

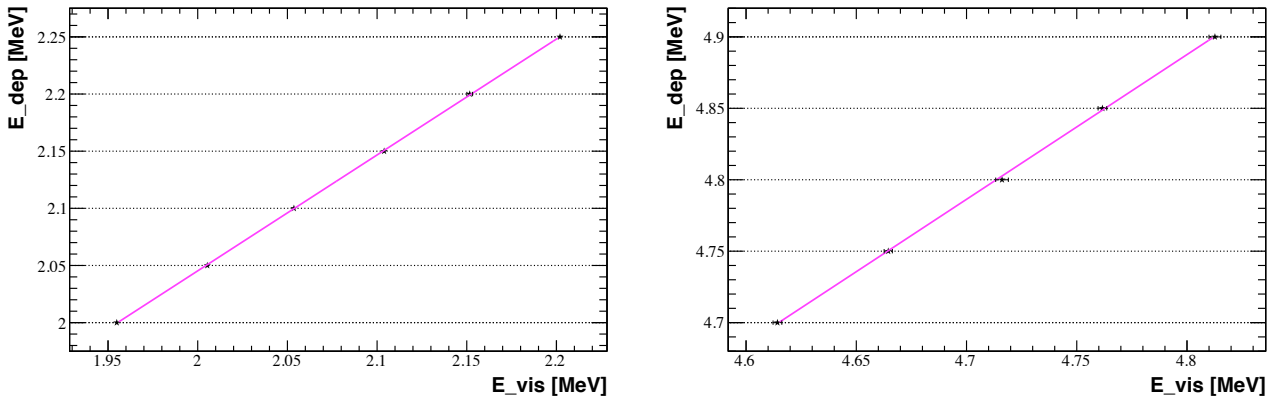


Figure 5.2: Behavior of the deposited energy as a function of the visible energy for simulated electrons with energy around 2 MeV (left panel) and 4.8 MeV (right panel) in the center of Borexino. The fit functions are of type: $E_{dep} = a+bE_{vis}$; for the first plot $a=0.025\pm 0.067$ and $b=1.014\pm 0.014$, for the second plot $a=0.017\pm 0.014$ and $b=1.014\pm 0.007$.

electrons with energy around 2.1 MeV and 4.8 MeV have been simulated in the center of Borexino, obtaining the trend of deposited energy as a function of the visible one for β -like events (see Figure 5.2). Fitting these distributions, I obtained, for visible energies of 2.10 MeV and 4.80 MeV:

- $T_e = 2.14$ MeV
- $T_e = 4.89$ MeV.

that represent the effective energy threshold values used for the external background analysis in the whole vessel. In future I will refer to energy threshold of 2 MeV and 5 MeV, meaning 2.14 MeV and 4.89 MeV, respectively.

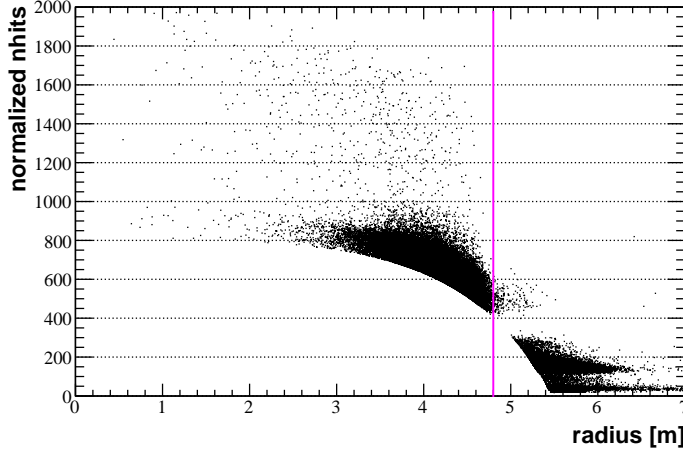


Figure 5.3: Distribution of the number of photoelectrons as a function of the radius for events above 2.14 MeV.

Studying the behavior of the number of photo-electrons with respect to the radius for events above the defined threshold at 2.14 MeV, I obtained the plot in Figure 5.3. It is evident that a radius of about 4.8 m sets the effective passage from the scintillator to the buffer¹. For this reason, in the present analysis a radial cut at 4.8 m is applied. This allows the study of the entire Borexino IV.

5.1.2 The radial analysis technique

In [106], the analytical description for the radial distribution of events in a perfect spherical vessel is reported. In particular, through a radial analysis it is possible to distinguish internal, external and surface events:

- Inner events are described by the *bulk distribution*, done by the convolution between the uniform spatial distribution of events with the detector resolution [105]:

$$V_d(r) = \frac{3}{R^3} \frac{r}{\sqrt{2\pi}\sigma} \int_{-R}^R r' \cdot e^{-\frac{(r-r')^2}{2\sigma^2}} dr' \quad (5.1)$$

where R is the vessel radius.

- Radial distribution of R_n emanated by the vessel can be described by a *Rayleigh distribution*, similar to a Gaussian centered in R , with a longer queue toward the center of the detector:

$$F(r) = \frac{r}{\sqrt{2\pi}\sigma R} \cdot e^{-\frac{(r-R)^2}{2\sigma^2}} \quad (5.2)$$

where R is the vessel radius.

- Finally, the distribution of external background events is represented by the convolution between the detector resolution and an exponential describing the penetration

¹This is due to the fact that the Borexino IV is deformed and the bigger radius reached in the period 2008-2009 corresponds to 4.8 m in the North hemisphere.

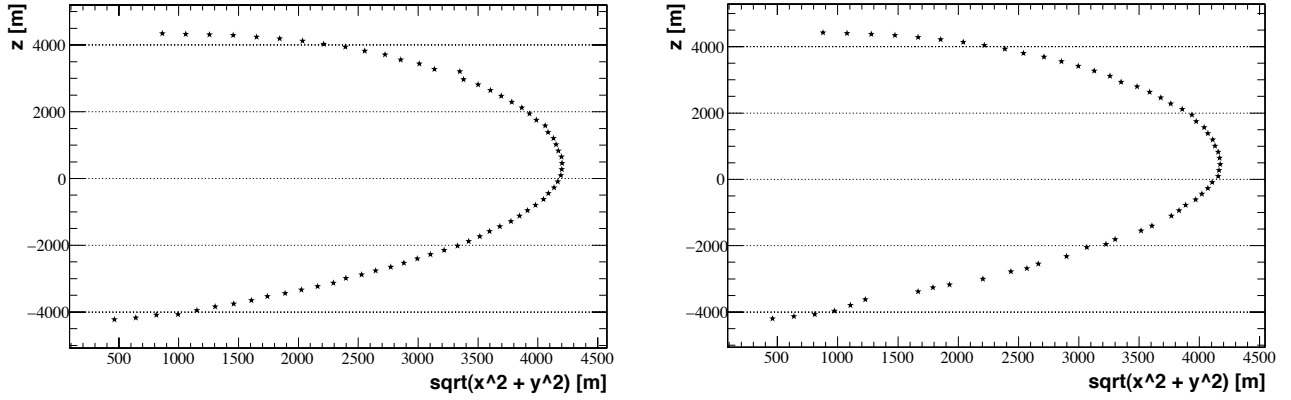


Figure 5.4: z coordinate versus $\rho = \sqrt{x^2 + y^2}$ for two different periods (beginning of November 2008 in the left panel and end of May 2009 in the right panel), based on data from CCD cameras.

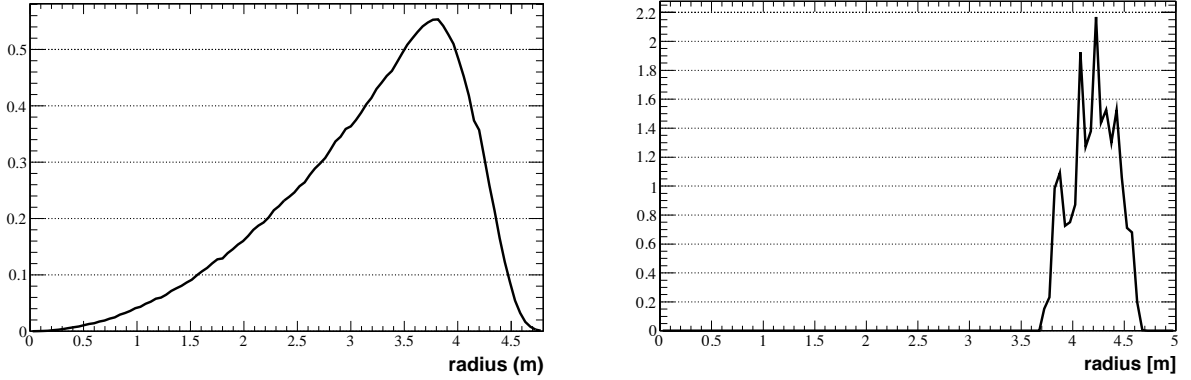


Figure 5.5: Total distributions of events in the bulk (left) and on the vessel surface (right), obtained by the sum of the distributions for simulated events in vessels with different shapes, known by the CCD camera data. The number of simulated events depends on the length of the period between two vessel pictures.

of γ 's:

$$F(r) = \left[\lambda(e^{R/\lambda} - 1) - R \right]^{-1} (e^{r/\lambda} - 1) \quad (5.3)$$

where λ the attenuation length of external γ 's.

Defining the three different radial distributions it is possible in principle to count, through a fit, the number of external, surface and internal events.

In fact, the Borexino vessel shape is slightly deformed from the theoretical sphere shape, due to the buoyancy between the buffer and the scintillator. Moreover the deformation changes in time, due for example to the refilling operations or to temperature changes. The use of the radial analysis in Borexino strongly requires to take into account the vessel deformation. The precise vessel shape is known from pictures taken by the CCD cameras. In Figure 5.4, I report the value of z coordinate versus $\rho = \sqrt{x^2 + y^2}$ for two different periods (beginning of November 2008 and end of May 2009), based on data from CCD cameras; the changing in the vessel deformation is evident.

In order to take into account the vessel deformation and its changing in time, I reproduce

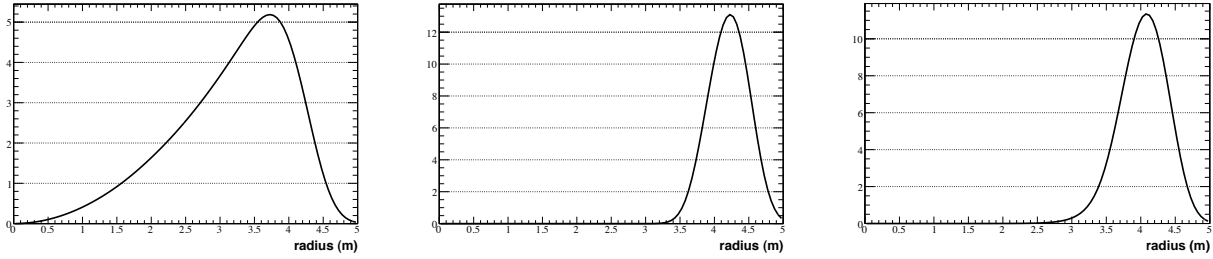


Figure 5.6: From left to right: radial distributions obtained for bulk, surface and external component respectively, by simulating events in deformed vessels. The external component is obtained by summing exponentials done in Eq. 5.3 for different values of R , basing the surface distribution in Figure 5.5 (right). The value of σ (Eq. 5.2) and λ is 20 cm (Eq. 5.3).

the distributions in the vessel and on the surface, through a specific Monte Carlo code that:

- constructs 23 different vessel shapes, corresponding to the series of 23 pictures of the vessel taken in the period considered for the present analysis: from January 2008 to December 2009;
- in every vessel generates a number of events weighted for the length of the considered period;
- sums all the weighted distributions to create the global one, for the period 2008-2009.

From the distributions of simulated events, I obtained two step functions, describing bulk and surface components for the deformed vessel (see Figure 5.5). Convoluting these functions with the detector resolution the final shapes reported in Figure 5.6 have been obtained. The external component is obtained by convolving with the detector resolution the sum of the exponentials, done in Eq. 5.3, each one having a different value of R (corresponding to the right panel of Figure 5.5).

In conclusion, to well reproduce the radial distribution of events in the Borexino IV it is necessary to take into account:

- the nominal distribution in a spheric vessel;
- the vessel deformation;
- the detector response.

A precise study of all the components (bulk, surface and external) also requires to consider the possible dependence of the radial distribution on the event energy. This involves the use of the Monte Carlo code perfectly reproducing the Borexino features. As explained in Section 3.2, G4Bx has been well developed and tuned to reproduce internal (bulk) events from many sources. In the following section I will describe my effort to make G4Bx able to well reproduce the external and surface events too.

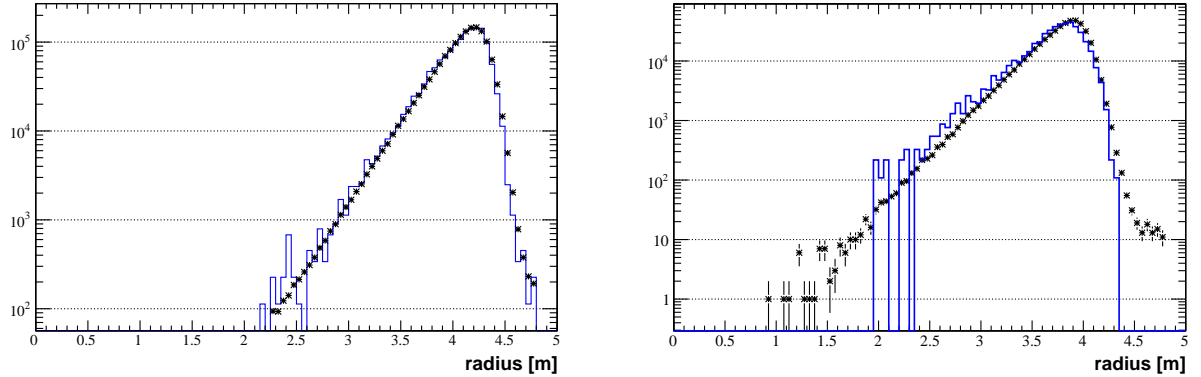


Figure 5.7: Comparison between calibration data (dots) and MC simulations (blue line) for the position in the North hemisphere (left) and the South hemisphere (right) above 2.14 MeV in the whole IV.

5.1.3 The external background simulator

In order to perform the analysis of the external backgrounds (and in fact also the neutrino analyses - see next Chapter and [31]), a precise reproduction of the radial and energy distributions of external events is necessary. During my PhD, I have been in charge of developing a tool in G4Bx (see Section 3.2) able to generate in the fastest and most precise way all the possible components from all the possible sources of external background. In Appendix A a detailed manual for the use of the external background generator is reported.

As described in [79], the SSS, the PMTs and the light concentrators are contaminated by non-negligible amounts of ²³²Th, ²³⁸U and ⁴⁰K. Mainly the long-ranged gamma-rays from the daughter nuclides ²⁰⁸Tl (2.61 MeV) and ²¹⁴Bi (up to 3.27 MeV) contribute to the external background observed in the inner part of the detector. The knowledge of the energy spectrum shape and the radial distribution of this external backgrounds is strongly required for the ⁸B neutrino analysis above 780 nhits (see next Chapter).

This challenging goal has been reached combining two different approach:

- the information from the external calibration of the detector (see Section 2.6.2);
- the development of a special Monte Carlo simulation procedure for the background coming from the PMTs and the concentrators.

In particular, I have been in charge for the second task.

Taking into account the attenuation length of about 24 cm estimated from the calibration data, the rate of external gamma rays is reduced by a factor of 10⁷ within a Fiducial Volume of 3 m radius. The spectral analysis requires the simulation of a sample of ~10⁴ γ -rays in the FV, thus approximately 10¹² primary events had to be generated. In order to speed up the time-consuming simulation, I developed several techniques in the simulation procedure:

1. Only primary events directed towards the IV are simulated. Depending on the source, the G4Bx generator (see Section 3.2.2) can be G4Gun (just for gammas) or

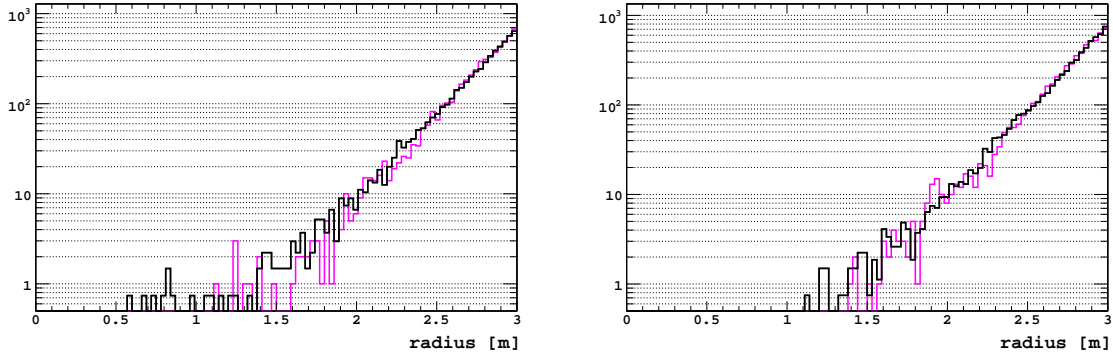


Figure 5.8: Comparison of the reconstructed position from the calibration data (black) and the 2.61 MeV simulated external gamma (pink), surviving in the Fiducial Volume above 400nhits, for the position in the upper (left) and the lower (right) hemisphere. The χ^2/ndf between the two histograms (MC and data) is around 0.8-0.9.

RDM (for nuclei). The direction is defined through angle limits, set in the Stacking; the access to the Stacking is easily reached by the user through a macro, I expressly wrote for the purpose.

2. Through the generator it is possible to define the origin for primary events as a sphere of 6.5 m radius. Through the Stacking it is also possible to define different source shapes and positions: deformed vessels, deformed buffers, etc.
3. In the first step, the optic processes are deactivated and all information concerning the energy deposition, the vertex position and the direction of the particle are written in a binary file.
4. For the second step, a specific generator called G4Bx was written: it reads the binary file from the first step and generates for each deposit an electron, propagating with the corresponding starting energy, position and direction. It is possible to set (easily by the user) a threshold for the energy and the deposit position: an electron is generated for each deposit only if for a done event the sum of the energy deposited exceeds a given threshold and lies within a given radius.
5. The first step simulation outputs are used as input for more second step simulations.

Finally, after the electronics chain simulation (exactly reproducing the run by run detector configuration, see Section 3.3), each simulation output from the second step is reconstructed through the Echidna reconstruction code (see Section 3.1).

In order to validate the external background simulations, a simulation of the point-like external 2.61 MeV gamma source has been performed and compared with the calibration data. During calibrations, the source was positioned in two positions:

- (4.26, -0.75, 5.31) m, for the North hemisphere;
- (2.56, -0.75, -6.31) m, for the South hemisphere.

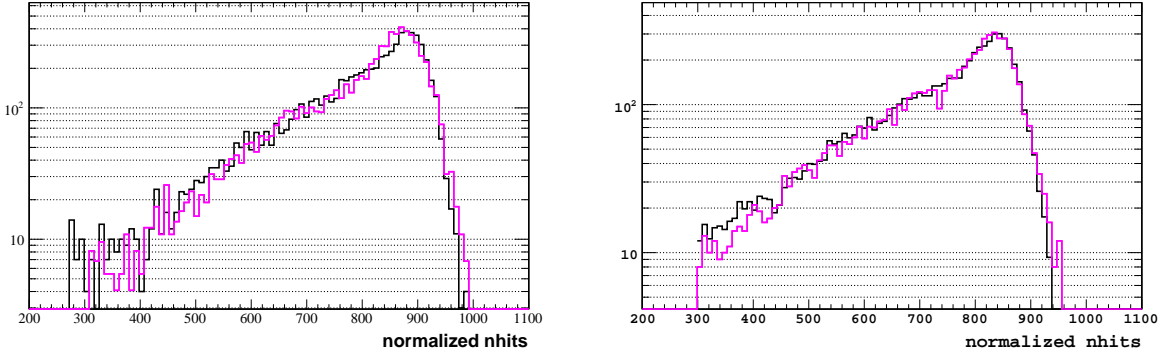


Figure 5.9: Comparison of the reconstructed nhits from the calibration data (black) and 2.61 MeV simulated external gammas (pink), surviving in the Fiducial Volume, for the North (left) and the South (right) position. The χ^2/ndf between the two histograms (MC and data) is around 1.3.

In order to check the agreement between the Monte Carlo and the data, I simulated 2.61 MeV γ 's in the two positions. Considering separately the North and the South and selecting the events above 2.14 MeV, I found a good agreement in the North hemisphere and a little less satisfactory in the South (see Figure 5.7): it seems that the global distribution is a little shifted toward the center.

For most the neutrino analyses, it is important to know the radial and energy distributions of events within the standard fiducial volume of 3 m radius. As shown in Figure 5.8 and 5.9, the agreement with data is greatly good. In particular, the accuracy of the energy and radial distribution of simulated events are at level of 0.5%. This results represent a great success and make me sure of the reliability of the simulated spectra of the external backgrounds.

5.2 Radial analysis above 5 MeV in the whole IV

As first attempt, I decided to start studying the energy region above the 4.89 MeV threshold, the cleanest one. Almost free from gamma contamination, the energy region above the 4.89 MeV threshold is the cleanest in Borexino: external and surface backgrounds are not expected. In fact, considering:

- the external background: the highest energy gamma is the 2.61 MeV from ^{208}Tl ;
- the surface background: the highest energy contaminant is ^{208}Tl with $Q=5.001 \text{ MeV}$, quenched at about 4.8 MeV.

On the contrary, a contamination of high energy gammas from the buffer (see Section 2.3.4) is expected.

In Figure 5.10 I report the radial distribution of data events above 4.89 MeV fitted with distributions *bulk+external* described in Section 5.1.2; the presence of a non-bulk component is evident.

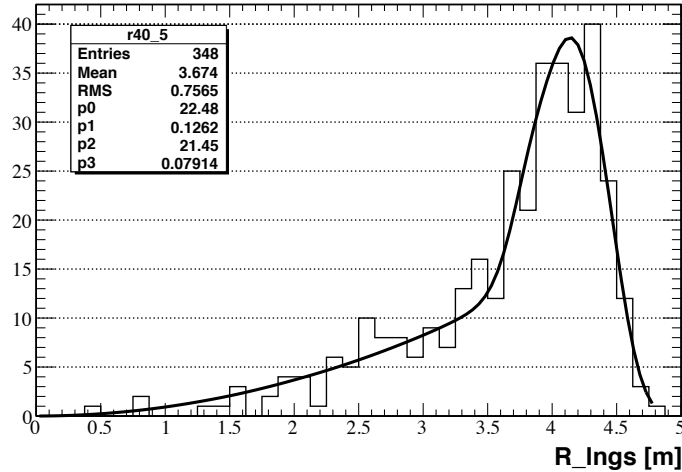


Figure 5.10: Radial distribution of events above 4.89 MeV after applying the removal techniques listed in Chapter 4, fitted with distributions *bulk+external* described in Section 5.1.2.

5.2.1 Study of high energy contaminants from the buffer

From the experience of the geoneutrino analysis performed in Borexino [14], we know that the Borexino buffer is more contaminated than the scintillator in the Inner Vessel. The main contaminants are ^{210}Po , ^{238}U and ^{232}Th , being roughly estimated as 100 times the ones in the scintillator. The presence of these contaminants can imply the production of high energy γ 's in the buffer, propagating within the vessel. In particular, from ^{210}Po we expect (α, n) reactions on ^{13}C producing both deexcitation γ 's and γ 's from neutron capture, basically on ^1H (2.223 MeV); from ^{232}Th we expect a contamination of ^{208}Tl ($\beta + \gamma$, $Q=5.001$ MeV).

Done this considerations, I performed a Monte Carlo study (through G4Bx) of the possible buffer contaminants.

Monte Carlo predictions of ^{16}O deexcitation γ 's rate

As published in [14], we measured a ^{210}Po contamination in the buffer of about 10^6 cpd/1 t, that means about 10^9 cpd in the whole buffer. ^{210}Po α -decays emitting an α of 5.4 MeV. As measured by the Borexino collaborators from Ferrara [107], the probability to have (α, n) reactions in our scintillator is $(4.6 \pm 0.3) \times 10^{-8}$. This means we expect about 50 (α, n) reactions per day in the whole buffer. The most probable (α, n) reaction is $^{13}\text{C}(\alpha, n)^{16}\text{O}$ (99.7%, see [108]); in 9.2% of cases ^{16}O is produced in an excited state, decaying with emission of 6.13 MeV γ (8%) or 6.04 MeV γ (1.2%). In summary, we expect about 5 cpd from ~ 6 MeV deexcitation γ 's in the buffer. They clearly fall above the energy threshold at 4.89 MeV and could represent the high energy contaminants penetrating with an external radial shape.

In order to evaluate the impact of these high energy contaminants from the buffer, I simulated, homogeneously in the whole buffer, 6.13 MeV γ 's, taking into account the vessel deformation and the consequent deformation of the buffer shell in different periods. I also took into account the different detector configurations (as live channels and live PMTs, see Section 3.3) during the data taking. Simulations were performed through the

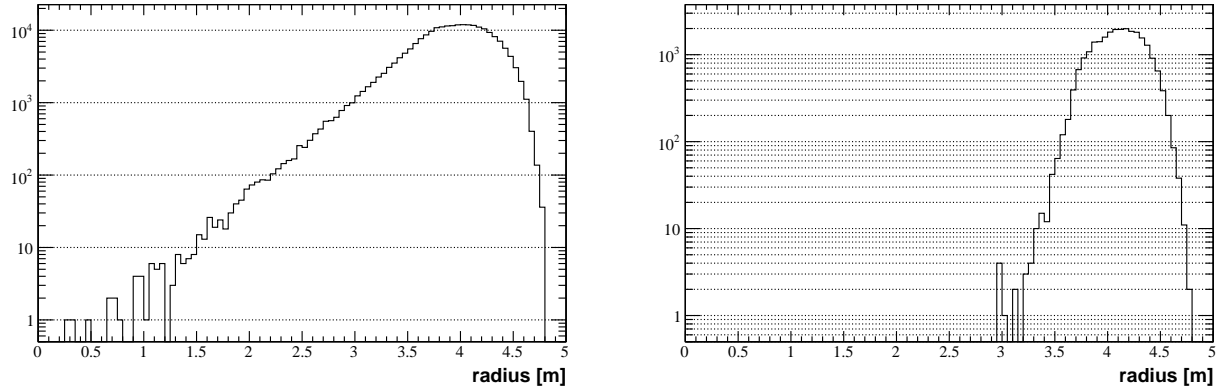


Figure 5.11: *Left:* radial distribution of 6.13 MeV γ 's generated in the buffer, taking into account the vessel deformation and its changing in time, surviving above 4.89 MeV. *Right:* radial distribution of ^{208}Tl events generated in the buffer, taking into account the vessel deformation and its changing in time, surviving above 4.89 MeV.

tools described in Section 5.1.3.

After reconstructing the simulated data with the Echidna code, I found that 2.2% of 6.14 MeV γ 's survive in 4.8 m above the 4.89 MeV threshold². For this reason I expect about 0.1 cpd of 6 MeV gammas in my data sample.

The radial shape I obtained from the simulation is shown in the left panel of Figure 5.11.

Monte Carlo predictions of buffer ^{208}Tl rate

As already mentioned, the Borexino buffer is about 100 times more contaminated by ^{232}Th than the scintillator. Knowing the contamination of internal ^{208}Tl in the scintillator of about 0.11 cpd/278 t, about 40 cpd of ^{208}Tl are expected in the buffer. In order to evaluate its impact on the data sample above 4.89 MeV I simulated, with the same procedure as in the previous Section, ^{208}Tl events homogeneously in the whole buffer taking into account the vessel deformation in time. 0.2% of them survive above 4.89 MeV in 4.8 m, that means about 0.2 cpd of ^{208}Tl from the buffer are expected.

The radial shape obtained for this contaminant is shown in the right panel of Figure 5.11.

5.2.2 Monte Carlo predictions of ^{208}Tl emanated by the vessel

As seen for the ^{208}Tl produced in the buffer, it is possible that also ^{208}Tl emanated by the vessel survive above 4.89 MeV. In particular, in [86] the measured ^{232}Th contamination of the vessel is 1.6 ppt, corresponding to 6.4×10^{-5} Bq/kg. Being our vessel 32 kg, about 177 cpd of ^{232}Th , corresponding to about 64 cpd of ^{208}Tl , are expected.

I used the tools I developed in G4Bx (see Section 5.1.3), in order to define deformed surfaces, corresponding to deformed vessels. ^{208}Tl on the vessel surface has been simulated taking into account its deformation in time and the detector configurations.

I found that 0.2% of ^{208}Tl survive above 4.89 MeV, that means about 0.11 cpd are expected

²These numbers represent the ratio between the reconstructed events above 4.89 MeV and in 4.8 m and all the simulated events.

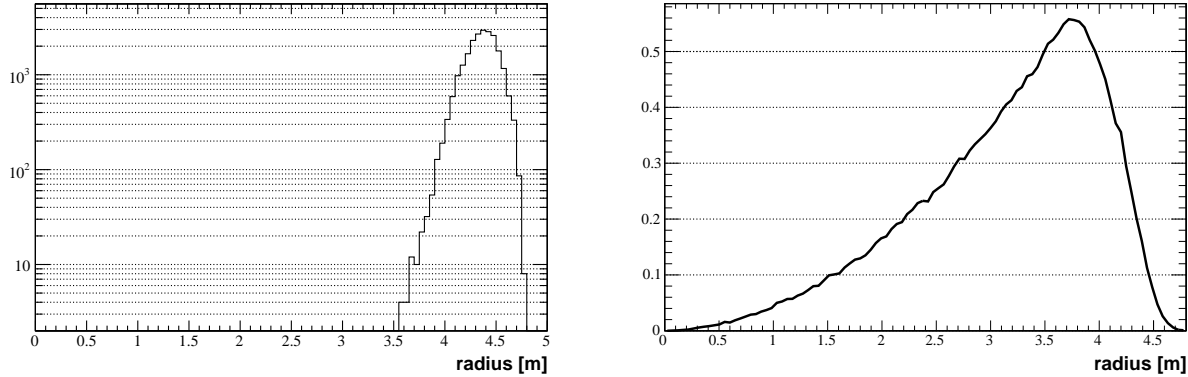


Figure 5.12: *Left:* Radial distribution of ^{208}Tl simulated events on vessels deforming in time. *Right:* Radial distribution of simulated bulk events above 4.89 MeV used for the fit.

in the data sample.

The obtained radial distribution is shown in left panel of Figure 5.12.

5.2.3 Monte Carlo simulation of bulk components

In order to complete the fit through the G4Bx simulations, also the bulk components have been simulated and reconstructed with the Echidna code: ^8B neutrinos and ^{11}Be cosmogenic have been produced uniformly in the Inner Vessel, taking into account its different shapes in time. The obtained radial distribution, containing both the contributions, is shown in right panel Figure 5.12.

5.2.4 Results for the energy region above 5 MeV

Finally, using the 4 fit components previously described:

- external from 6.13 MeV deexcitation γ 's from the buffer (Section 5.2.1);
- external from ^{208}Tl produced in the buffer (Section 5.2.1);
- surface from ^{208}Tl (Section 5.2.2);
- bulk from ^8B neutrinos and ^{11}Be cosmogenics (Section 5.2.3);

I obtained the fit shown in Figure 5.13. The fit results for the background components correspond to:

1. 6.13 MeV γ 's: $R_\gamma = (0.27 \pm 0.13) \text{ cpd}$; this number is roughly compatible with the expectation shown in Section 5.2.1. The corresponding count rate of (α, n) reactions in the whole buffer is estimated to be $(133 \pm 64) \text{ cpd}$ in the whole buffer.
2. ^{208}Tl from the buffer: $R_{\text{TL,buf}} = (0.15 \pm 0.11) \text{ cpd}$, roughly compatible with the expectation shown in Section 5.2.1.
3. Surface ^{208}Tl : $R_{\text{TL}} = (2.9 \pm 1.0) \times 10^{-5} \text{ Bq/kg}$; this value is compatible with the expectation, based on the measurements of the vessel contamination [86], of $\sim 2.3 \times 10^{-5} \text{ Bq/kg}$.

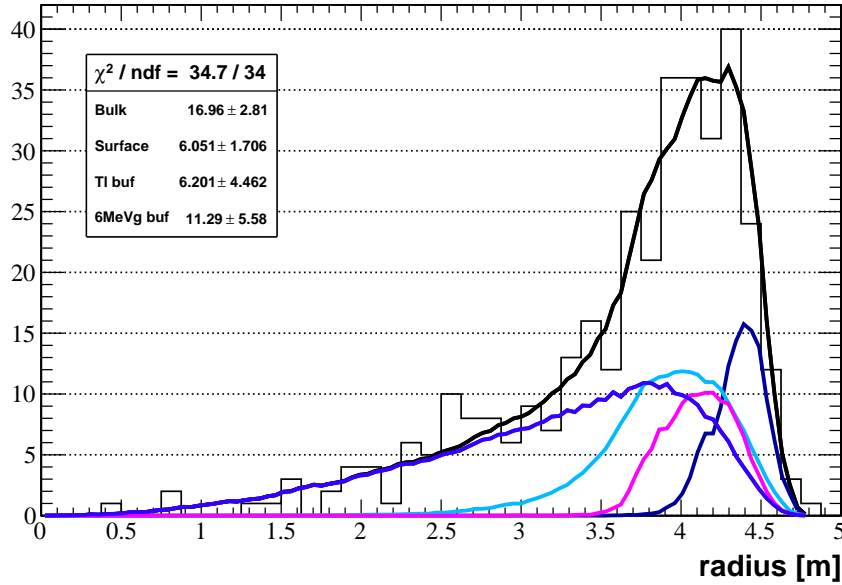


Figure 5.13: Radial fit of the four components: 6.13 MeV γ 's from the buffer (light blue), ^{208}Tl from the buffer (pink), surface ^{208}Tl (dark blue) and bulk (blue) of events above 4.89 MeV in 4.8 m.

$$4. \text{ Bulk: } R_{\text{bulk}} = (0.47 \pm 0.07) \text{ cpd}/278 \text{ t.}$$

Results from the fit are quite in agreement with expectations, thus showing the reliability of the radial analysis method. Using the measurements obtained above 4.89 MeV to fix some components in the radial fit, the energy region above 2.14 MeV has been considered.

5.3 Radial analysis between 2 and 5 MeV in the whole IV

The considered statistics is the same as used for the analysis above 4.89 MeV; the radial distribution of the event sample is shown in Figure 5.14. Since I am not applying a fiducial volume cut, both the external and the surface backgrounds must be considered. The background sources already treated above 4.89 MeV are:

- 6.13 MeV deexcitation γ 's from ^{16}O in the buffer;
- ^{208}Tl from the buffer;
- ^{208}Tl from the vessel.

The new background to consider is the one coming from the sphere, basically the ^{208}Tl emanated by the PMTs.

Finally there is the internal background, composed by the not removable ^{11}Be and ^{208}Tl and by the residuals of ^{10}C .

For this analysis the radial shapes obtained by simulations have been used, resorting to analytical functions just when needed.

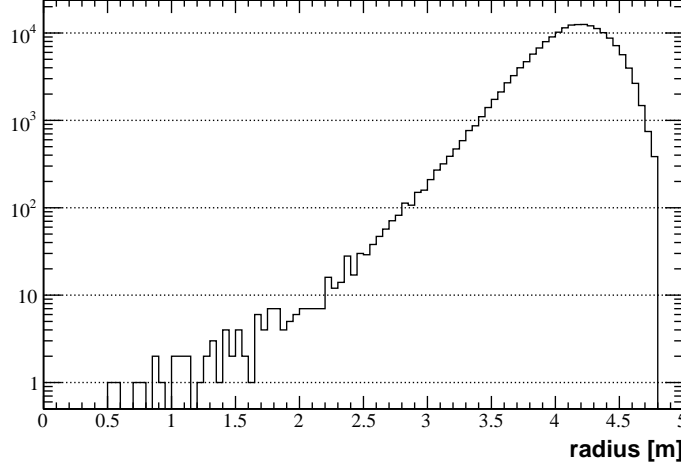


Figure 5.14: Radial distribution of event sample considered for the analysis between 2.14 and 4.89 MeV, within 4.8 m.

5.3.1 Monte Carlo predictions of γ 's rate from (α,n) reactions in the buffer

As already described in Section 5.2.1, in the Borexino buffer a ^{210}Po contamination is present. We expect, as measured in Section 5.2.4, about 133 (α,n) reactions per day in the whole buffer, corresponding to 133 neutrons per day in the buffer³.

As well known, neutron can be captured on ^1H or ^{12}C , with consequent emission of 2.22 MeV and 4.94 MeV, respectively. Thus, I simulated in the whole buffer 4.94 MeV and 2.22 MeV γ 's, taking into account the vessel deformation and the consequent deformation of the buffer shell in different periods. After reconstructing the simulated data with the Echidna code, I found that 0.5% of 2.22 MeV gammas and 1.1% of 4.94 MeV gammas survive in the energy region between 2.14 and 4.89 MeV. Moreover, considering that:

- for each molecule of pseudocumene we have 9 carbons and 12 hydrogens;
- the probability of neutron capture on ^{12}C is 1% of the ^1H one;

the ratio between the neutron captures on ^{12}C and on ^1H in the considered energy bin is:

$$\frac{N_\gamma(^{12}\text{C})}{N_\gamma(^1\text{H})} \simeq 1.7\% \quad (5.4)$$

It's clear that the main component is the one at 2.22 MeV. In particular about 0.67 cpd from this component are expected.

In addition, the penetration of 6.13 MeV γ 's from ^{16}O deexcitation has to be considered. I found that 1.1% of them survive between 2.14 and 4.89 MeV, that means:

$$\frac{N_\gamma(^{16}\text{O})}{N_\gamma(^1\text{H})} \simeq 20.2\% \quad (5.5)$$

³Note that (α,n) reactions could also happen in the Borexino vessel; the fact that in the IV we don't observe 2.22 MeV gammas, that are 100 times more probable than 4.89 MeV gammas, means that this type of contamination is negligible in the scintillator.

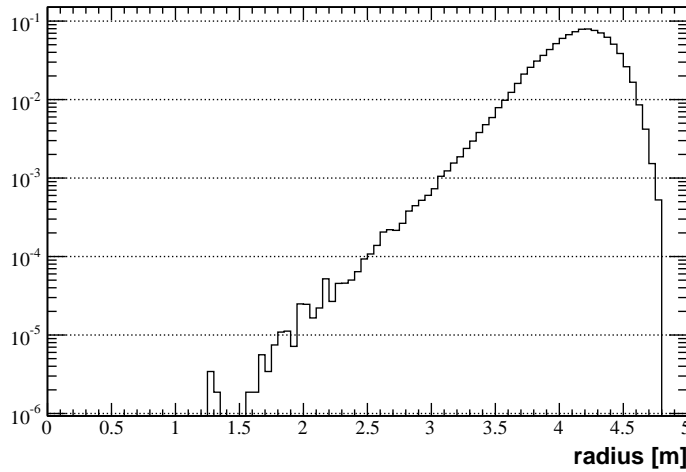


Figure 5.15: Radial distribution of gammas from neutron capture on ^1H (100%) and 6.13 MeV gammas (20.2%) simulated in buffers deforming in time, for the energy region between 2.14 and 4.89 MeV.

corresponding to about 0.13 cpd for 6.13 MeV γ 's.

The obtained radial distribution from G4Bx and after the Echidna reconstruction, including both the 2.22 and the 6.13 MeV gammas, is shown in Figure 5.15. For the following fit, this component is fixed to 0.8 cpd.

5.3.2 Monte Carlo predictions of buffer ^{208}Tl rate

Using the simulations already performed for the study of the energy region above 4.89 MeV, I found that 5.9% of surface ^{208}Tl falls between 2.14 and 4.89 MeV. Using the result for the region above 4.89 MeV, about 4.9 cpd are expected between 2.14 and 4.89 MeV. The obtained radial shape is shown in the left panel of Figure 5.16.

5.3.3 Monte Carlo predictions of surface ^{208}Tl rate

Using the simulations already performed for the study of the energy region above 4.89 MeV, I found that 45.5% of surface ^{208}Tl falls between 2.14 and 4.89 MeV. The obtained radial shape is shown in the right panel of Figure 5.16.

For the present analysis, the amplitude of the surface component, basing on the measurement performed in Section 5.2.2, is fixed at 2.9×10^{-5} Bq/kg.

5.3.4 Monte Carlo simulation of bulk components

In addition to the already simulated ^8B neutrinos and ^{11}Be cosmogenics, in the energy region between 2.14 and 4.89 MeV also the internal ^{208}Tl and the residuals of ^{10}C (see Table 5.1) must be simulated. After the Echidna reconstruction, the obtained radial distribution, containing all the contributions with the correct weight, is shown in Figure 5.17.

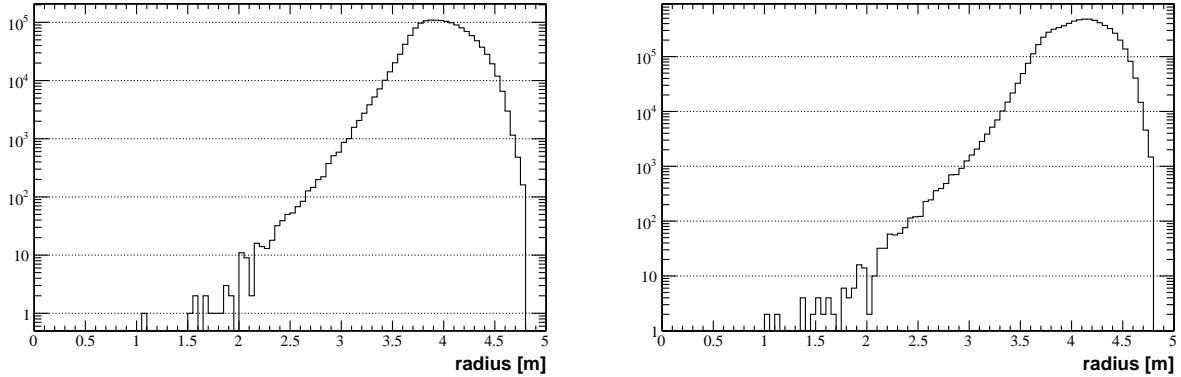


Figure 5.16: Radial distribution of ^{208}Tl simulated on in the buffers (left) and on the vessels (right) deforming in time, for the energy region between 2.14 and 4.89 MeV.

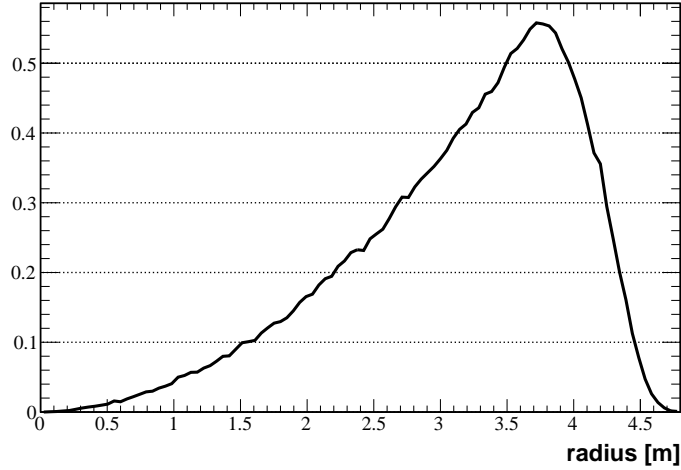


Figure 5.17: Function of the radial distribution of simulated bulk events between 2.14 and 4.89 MeV, for vessels deforming in time.

5.3.5 Monte Carlo study of external ^{208}Tl and ^{214}Bi

The new component to consider for the region [2.14,4.89] MeV is the external one. Basing on measurement on PMT and concentrator contamination [86], we expect about 2.1×10^3 Bq of ^{232}Th and $1.1 \cdot 10^4$ Bq of ^{238}U . The dangerous daughters for the energy region above ~ 2 MeV are ^{208}Tl (2.61 MeV) and ^{214}Bi (up to 3.27 MeV), respectively.

As described in Section 5.1.3, I wrote useful tools to simulate both these contaminants. Comparison of the radial distributions above 2.14 MeV of the two sources show that they are indistinguishable. For these reason, I used a common radial shape to describe the contaminants from the PMTs.

Approach trough G4Bx simulations

Through the G4Bx simulation, I found that 1.9×10^{-5} of 2.61 MeV γ 's and 3.6×10^{-7} of ^{214}Bi γ 's produced on PMTs (6.5 m radius sphere) survive in 4.8 m and above 2.14 MeV;

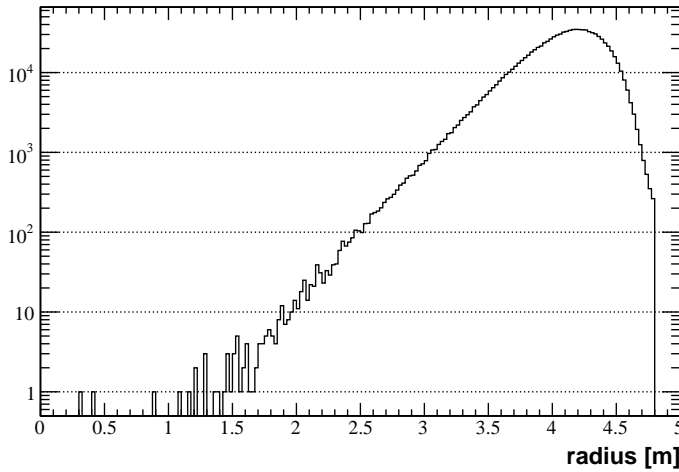


Figure 5.18: Radial distribution of 2.61 MeV γ 's simulated on a sphere of 6.5m radius, surviving above 2.14 MeV in 4.8 m.

this implies an expectation of about 1240 cpd for ^{208}Tl and 370 cpd for ^{214}Bi . Globally about 1600 cpd from PMT contamination are expected to survive within the IV.

The radial distribution of external 2.61 MeV gammas as obtained from G4Bx is shown in Figure 5.18. Using this distribution and the ones described in Sections 5.3.1, 5.3.2, 5.3.3, 5.3.4 and fixing the count rates as following:

- the surface component at $2.9 \times 10^{-5} \text{ Bq/kg}$ ($\sim 55 \text{ cpd}$);
- the (α, n) gammas from the buffer component at 0.8 cpd;
- the ^{208}Tl from the buffer component at 4.9 cpd;

as expected from the measurement above 4.89 MeV, the obtained fit result is not good. As shown in Figure 5.19, the penetration of the simulated external background doesn't well reproduce the radial distribution of the events: again, the global distribution seems to be shifted toward the Borexino center. The discrepancy in the radial shape of the external background is due to a lack of a fundamental simulation ingredient: the vessel shape. We know the precise vessel shape in a discontinue way, more or less once every one or two months. The precise knowledge of the vessel shape in a continue way is strongly demanded for a good reproduction of the external background radial shape in the whole IV. For this reason, another approach for the description of the external component is necessary.

By the way, it is important to note that the surface and buffer contaminants are almost not penetrating in the standard 3 m radius FV. This will be an important point for the next Chapter.

Semi-analytical approach

Done the discrepancy of the radial distribution for simulated external ^{208}Tl , we used an analytical shape in order to fit the external background.

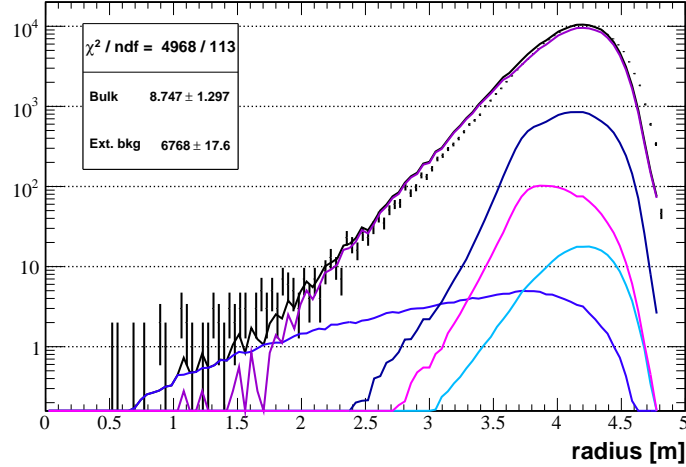


Figure 5.19: Fit of the radial distribution of events between 2.14 and 4.89 MeV using the five components: (α, n) gammas from the buffer (light blue) fixed at 0.8 cpd, buffer ^{208}Tl (pink) fixed at 4.9 cpd, surface ^{208}Tl (dark blue) fixed at 2.9×10^{-5} Bq/kg, external ^{208}Tl (violet) and bulk (blue).

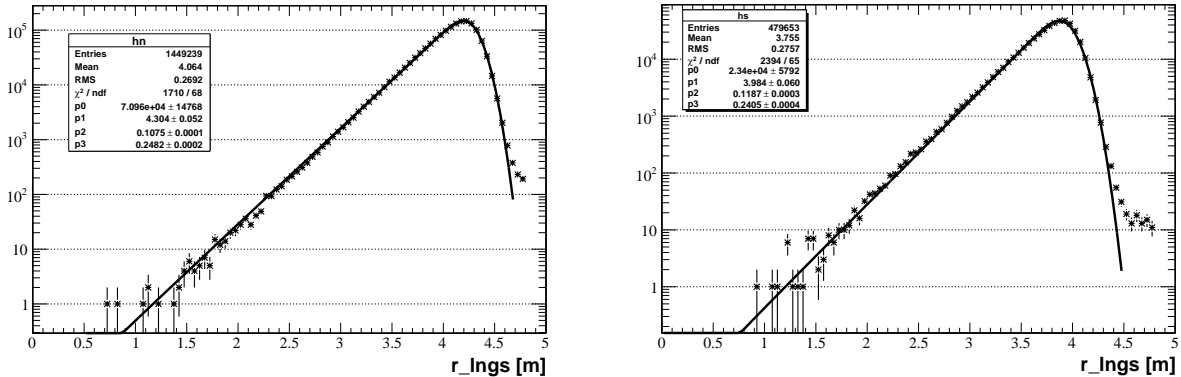


Figure 5.20: Radial distribution of external calibration data for the position in the North hemisphere (left) and the South hemisphere (right), fitted with an exponential.

We consider once again the external calibration data: since the gammas come from a fix point on the sphere, even if the vessel on July 2010 was slightly deformed, the geometry can be considered spherical. Fitting the radial distribution for the North and the South case with a simple exponential function:

$$f(r) = \frac{e^{r/\lambda} - 1}{(e^{R_{\text{ves}}/\lambda} - 1)\lambda - R_{\text{ves}}}; \quad (5.6)$$

convoluted with the resolution of the detector, the evaluated penetration λ is about 24-25 cm (see Figure 5.20). In order to use this results to construct a function describing the external background penetration in case of deformed vessels, we considered that:

- depending on z the distance travelled by the gamma before reaching the vessel is changing;

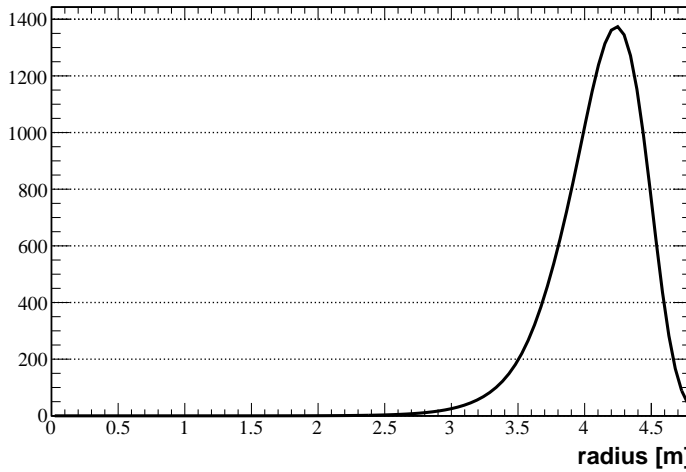


Figure 5.21: Function describing the penetration of the external background weighted for the distance between the sphere and the vessel with: $A=1000$, $\sigma=12\text{ cm}$, $\lambda=24.4\text{ cm}$ and $\lambda_w=30\text{ cm}$.

- consequently, the number of gammas reaching the vessel depends on z .

We wrote an analytical function $\phi(r)$, done by the exponential obtained by the *ad hoc* Monte Carlo (see Section 5.1.2), weighted for the distance between the sphere and the vessel:

$$F(r) = \sum_i W_{R_i} \int_0^{R_i} \phi(r) dr \quad (5.7)$$

with:

$$W_{R_i} = Ae^{(6.5m-R_i)/\lambda_w} \quad (5.8)$$

and where R_i is the vessel radius for a specific z_i and λ_w is the parameter describing the attenuation of the gamma flux, depending on $d_i = 6.5\text{ m} - R_i$. The shape of this function, after the convolution with the detector response, is shown in Figure 5.21.

Using this distribution and fixing the parameters already measured:

- the surface component at $2.9 \times 10^{-5}\text{ Bq/kg}$ ($\sim 55\text{ cpd}$);
- the (α,n) gammas from the buffer component at 0.8 cpd ;
- the ^{208}Tl from the buffer component at 4.9 cpd ;
- the penetration λ of the external ^{208}Tl at 24.4 cm ;

I obtain the fit shown in Figure 5.22. The description of the external distribution seems to very better fit the data. The fit results are:

- $\lambda_w = (27.7 \pm 0.2)\text{ cm}$;
- $\sigma = (11.64 \pm 0.09)\text{ cm}$;
- $R_{ext} = (490 \pm 1)\text{ cpd}$;

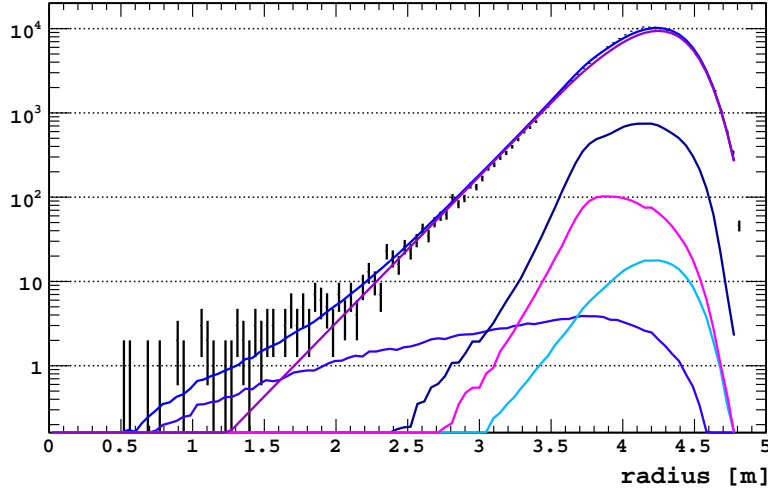


Figure 5.22: Data sample of events between 2.14 MeV and 4.89 MeV in 4.8 m fitted with the 4 components: external background (light blue), surface background (dark blue), neutron from the buffer (pink) and bulk (blue).

- $R_{\text{bulk}} = (0.7 \pm 0.1) \text{ cpd}$.

It is immediately evident that the σ value is in agreement with expectation. The measured rate of PMTs contaminants is about 30.6% of the quoted one ($\simeq 1600 \text{ cpd}$), based on values reported in [86] (see beginning of this Section).

5.4 Conclusions

The analysis here reported shows many interesting results, first of all the feasibility of an analysis based on the radial fit, that is a fundamental element for next Chapter. Other important points are:

1. the presence of a contamination from high energy γ 's from the buffer;
2. the importance of the precise knowledge of the vessel shape in case of analysis in the whole vessel;
3. the super-estimation of the PMTs contaminations based on measurement reported in [86].

It is also evident that the data sample above 2 MeV in the whole scintillator volume is strongly dominated by the PMT, surface and buffer background components. This implies that, in view of the isolation of the bulk component, a reduction of the external contamination is required. This can be reached applying the well known radial cut at 3 m, as applied in the analysis described in next Chapter. Actually, even if the G4Bx simulation of backgrounds coming from the PMTs does not perfectly reproduce the radial distribution in the whole vessel, the agreement MC/data within 3 m is very good (see Section 5.1.3). This allows a deep use of G4Bx simulations for the study of the energy region above 2 MeV in the standard FV.

Chapter 6

^8B Solar Neutrino Measurement above 2 MeV

As described in Chapter 4 and published in [36], we measured the ^8B solar neutrino flux above 3 MeV and we found results in agreement with the SSM+(MSW-LMA) expectations in both the considered energy regions: above 3 MeV and above 5 MeV (see Table 4.4). The curious thing is that both Borexino (with an energy threshold of 3 MeV) and SNO (with an energy threshold of 3.5 MeV [37]) report results in very good agreement with the SSM+(MSW-LMW) predictions above 5 MeV; instead, close to the threshold, they show a possible deficit in the measured fluxes (see Figure 6.1)¹. This aspect requires further examinations.

In addition, in the context of the survival probability mapping, the investigation of the transition region (1–4 MeV) is fundamental to definitely validate the MSW-LMA oscillation solution or to underline the presence of Non Standard Physics in neutrino interaction with matter, as Non Standard Interaction or sterile neutrinos (see Section 1.6.6).

For these reasons, and also to increase the sensitivity of the experiment, we decided to try to lower the energy threshold down to about 2 MeV, in order to approach the still unexplored energy region between 1 and 3 MeV. The Borexino collaboration has very recently measured the pep neutrinos ($E_\nu=1.44$ MeV) [31], which constitute a new data point between 1 and 3 MeV. We are also trying to approach this energy region, considering ^8B neutrinos above 2 MeV. In particular, I will show how two different and independent techniques, the spectral and the radial fits, give results perfectly compatible. The final rate result is obtained combining the two fits in a two-dimensional maximum likelihood fit. This result is in agreement, within the errors, with the SSM+(MSW-LMA) predictions.

6.1 The expected backgrounds above 2 MeV in the Borexino Fiducial Volume

As shown in Chapter 5, the dominant component above 2 MeV in the IV is represented by the external ^{208}Tl . The application of a radial cut at 3 m allows to exponentially reduce the penetration of this background. For this reason the considered Fiducial Volume in the present analysis corresponds to a sphere of 3 m radius.

¹Very recently a new and more precise analysis from SNO has been presented in [53], very close and fully compatible with the previous one.

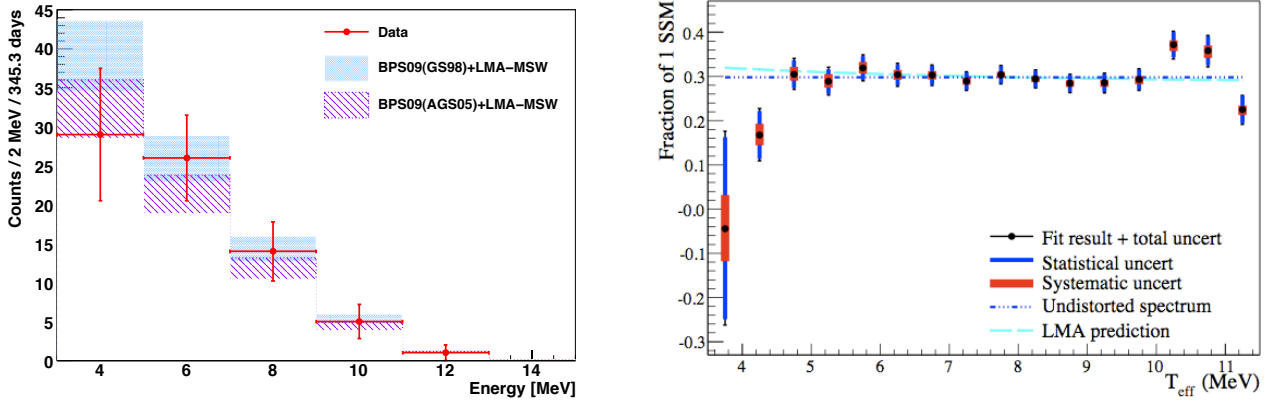


Figure 6.1: *Left:* ^8B solar neutrino spectrum measured by Borexino, compared to the expectations based on Standard Solar Model BPS09(GS98) (*high metallicity*) in MSW-LMA scenario. *Right:* comparison between the ^8B solar neutrino spectrum measured by SNO [37] and the expectations based on BPS09(GS98) in MSW-LMA scenario.

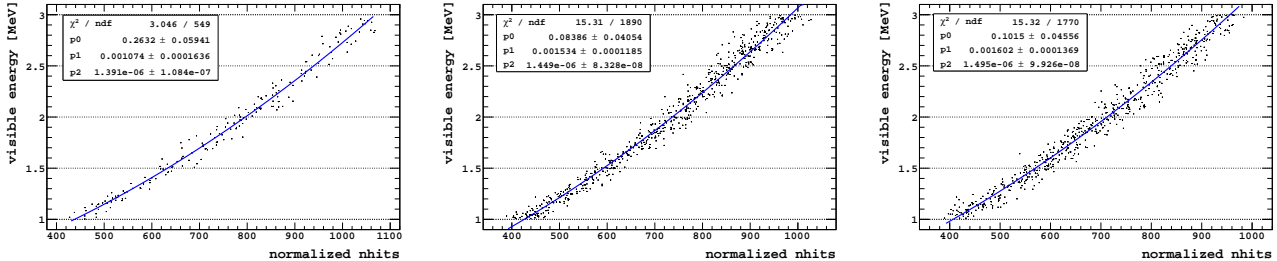


Figure 6.2: Visible energy as a function of the reconstructed nhits for simulated events within: a sphere of 0.5 m radius (left), a shell with minimum and maximum radii 2.7 m and 3 m in the North hemisphere (middle) and a shell with minimum and maximum radii 2.7 m and 3 m in the South hemisphere (right). Distributions have been fitted with an order 2 polynomial function.

6.1.1 The energy threshold

In order to avoid the contamination from ^{11}C ($Q = 1.982 \text{ MeV}$, $Q_{\text{quench}} \simeq 1.8 \text{ MeV}$) cosmogenic, the energy threshold for the analysis has been set at 780 nhits. Since the light collection efficiency decreases with radius, 780 nhits correspond to 1.95 MeV at Borexino center, to 2.16 MeV at 3 m in the North hemisphere and to 2.26 MeV at 3 m in the South hemisphere (see Figure 6.2).

The corresponding mean value for the energy threshold has been evaluated on the G4Bx simulations and corresponds to $E_{\text{thr}} = (2.07 \pm 0.01) \text{ MeV}$. The corresponding minimum neutrino energy is $E_0 = 2.33 \text{ MeV}$,

6.1.2 The expected contaminants

The expected contaminants in the FV above 780 nhits are:

- * internal, done by internal contaminants (^{214}Bi , ^{208}Tl , ^{10}C , ^{11}Be); they are listed in Table 6.1 and have been treated as in Chapter 4;

Contaminants	Residual rate [cpd]
^{214}Bi	$(8.00 \pm 0.03) \times 10^{-3}$
^{208}Tl	0.04 ± 0.01
^{10}C	0.03 ± 0.01
^{11}Be	0.034 ± 0.007
Total	0.11 ± 0.02

Table 6.1: Estimated residuals of internal contaminants in the Borexino Fiducial Volume above 780 nhits, after applying the removal techniques listed in Chapter 4.

Contaminant	Measured at source	Expected in ^8B region based on [79] [86]	Expected in ^8B region based on Chapter 5
^{208}Tl from PMTs	$\sim 6.5 \cdot 10^7$ cpd [79]	~ 8.5 cpd	~ 1.3 cpd
^{214}Bi from PMTs	$\sim 9.5 \cdot 10^8$ cpd [79]	~ 2.0 cpd	~ 0.3 cpd
^{208}Tl from Concentrators	$\sim 6.5 \cdot 10^7$ cpd [79]	~ 8.5 cpd	~ 1.3 cpd
^{214}Bi from Concentrators	$\sim 9.5 \cdot 10^8$ cpd [79]	~ 2.0 cpd	~ 0.3 cpd
^{208}Tl from Buffer	~ 40 cpd		$\sim 2 \cdot 10^{-3}$ cpd
^{16}O γ 's from Buffer	~ 5 cpd [107][108]		$\sim 4 \cdot 10^{-3}$ cpd
2.2 MeV γ 's from Buffer	~ 50 cpd [107]		$\sim 9 \cdot 10^{-4}$ cpd
^{208}Tl from IV	~ 64 cpd [86]	$\sim 7 \cdot 10^{-3}$ cpd	$\sim 9 \cdot 10^{-3}$ cpd
^{208}Tl from North End Regions	$\sim 3 \cdot 10^7$ cpd [86]	~ 0.60 cpd	
^{208}Tl from South End Regions	$\sim 3 \cdot 10^7$ cpd [86]	~ 0.37 cpd	

Table 6.2: Expected rates of the external, surface and buffer contaminants in the Borexino FV and above 780 nhits. Evaluations for the $^8\text{B}-\nu$ region were done both using measurements done in the past [79] [86] and using measurements reported in Chapter 5.

* **external**, mostly represented by 2.61 MeV and ^{214}Bi γ 's from PMTs and concentrators, but also from the End Regions (North and South poles of the IV) and from the vessel surface. In particular:

- the expected penetrating rate within 3 m of surface ^{208}Tl has been quoted using the simulations I performed on deformed vessels; it corresponds to about 9×10^{-3} cpd;
- the contribution from the ^{208}Tl from the End Regions has been evaluated combining informations from special MC simulations and measurements reported in [86]; it corresponds to about 6% of external ^{208}Tl expectations.

Table 6.2 shows the expected rates of all the external contaminants; it has been completed using also the measurements reported in Chapter 5. Comparing the third and the last column, it is evident that expectations based on [86] were overestimated. Summarizing, the expected rate is about 2.6 cpd for external ^{208}Tl and about 0.6 cpd for external ^{214}Bi .

It is evident that the main contribution comes from external 2.61 MeV gammas.

Backgrounds	Fixed rate [cpd]
Internal ^{214}Bi	$(8.00 \pm 0.03) \times 10^{-3}$
Internal ^{10}C	0.03 ± 0.01
Internal ^{11}Be	0.034 ± 0.007
^{208}Tl from IV	$(7 \pm 2) \cdot 10^{-3}$
^{208}Tl from End Regions	6% of ^{208}Tl from PMTs

Table 6.3: Background components fixed in the spectral fit above 780 nhits.

6.2 The binned likelihood spectral fit above 2 MeV in the Fiducial Volume

The standard approach for the Borexino analyses is the spectral fit. The idea is to fit the data sample, considering the energy spectrum of each component; spectra can be obtained through G4Bx. The only question concerns the $^8\text{B}-\nu$ spectrum. In principle, since ^8B neutrinos have a continuum spectrum, the spectral shape depends on the oscillation parameters, in other words, on the survival probability. By the way, as shown in Section 6.2.1, Borexino is not sensitive to the spectral distortion due to the neutrino oscillations; for this reason the problem related to the $^8\text{B}-\nu$ spectral shape is treated as a source of systematic.

Considering Tables 6.1 and 6.2, many background sources must be taken into account for a spectral fit. Most of them are particularly relevant between 2 and 3 MeV, the energy region dominated by the external ^{208}Tl peak. The known components, already studied in Chapters 4 and 5 and listed in Tables 6.1 and 6.2, have been fixed to their measured value, as shown in Table 6.3. Concerning the ^{208}Tl from the End Regions, the spectral shape is very similar to the external ^{208}Tl one; its value is forced to be 6% of the external one.

The data set considered for the present analysis involves 2008, 2009 and 2010 until June, for a total live time (LT) of 628 d. The 29.8% of dead time due to the cosmogenic veto (6.5 s after muons, see Section 4.3.2) reduces the effective LT to 441.4 d.

In order to check the goodness of the sample in the FV, the ^8B neutrino rate above 5 MeV has been first estimated. To evaluate the energy threshold corresponding to 5 MeV, the behavior of the nhits variable (see Section 3.1.2) as a function of the visible energy obtained by G4Bx simulations has been considered. As shown in Figure 6.3, the distribution can be fitted with a polynomial function $f(E_{\text{vis}}) = a + b \cdot E_{\text{vis}} + c \cdot E_{\text{vis}}^2$. The corresponding nhits value is 1399.4. After applying the removal techniques listed in Chapter 4 and the statistical subtraction of residual contaminants listed in Table 6.1, I found above 1399.4 nhits:

$$R_{^8\text{B}\nu} (E_e > 5 \text{ MeV}) = (0.09 \pm 0.01_{\text{stat}}) \text{ cpd}/100 \text{ t},$$

perfectly compatible with expectations based on SSM+(MSW-LMA), $(0.11 \pm 0.01) \text{ cpd}/100 \text{ t}$, and other previous measurements (see Chapter 4).

After applying the removal techniques listed in Chapter 4, I obtain a sample of 1243 events, above 780 nhits in the FV.

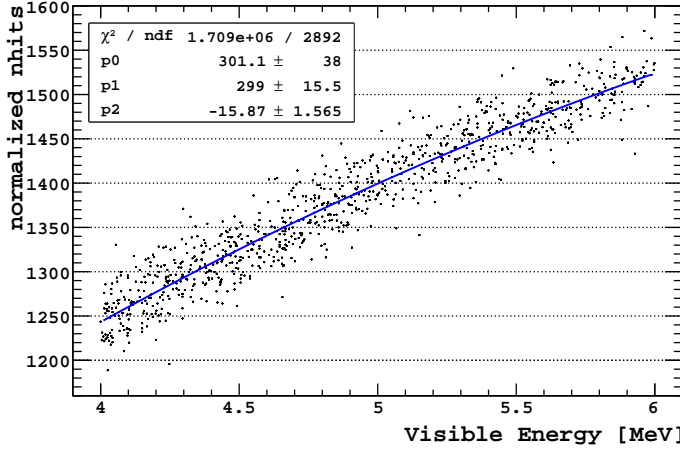


Figure 6.3: Number of normalized nhits as a function of the visible energy around 5 MeV obtained by G4Bx simulation, fitted with a polynomial function $f(E_{\text{vis}}) = a + b \cdot E_{\text{vis}} + c \cdot E_{\text{vis}}^2$.

I have chosen to use the likelihood as test statistic for two reasons:

- the small number of entries in some of the high energy bins of our final energy spectrum;
- the possibility to extend the likelihood in a multi-dimensional approach, in order to combine the spectral information and the radial distribution of the events (see Section 6.4) in the likelihood to maximize.

The results of the binned likelihood spectral fit are shown in Figure 6.4. In particular I obtained:

$$\begin{aligned}
 R_{^{8}\text{B}\nu} &= (0.31 \pm 0.04) \text{ cpd}/100 \text{ t} \\
 R_{\text{Int.Tl}} &= (0.04 \pm 0.02) \text{ cpd}/100 \text{ t} \\
 R_{\text{Ext.Tl}} &= (1.94 \pm 0.07) \text{ cpd}/100 \text{ t} \\
 R_{\text{Ext.Bi}} &= (0.39 \pm 0.23) \text{ cpd}/100 \text{ t}.
 \end{aligned} \tag{6.1}$$

Considering Table 6.2, the results for external ^{208}Tl and ^{214}Bi are slightly smaller than the expectations based on papers and are roughly in agreement with the expectations based on measurements shown in Chapter 5. Internal ^{208}Tl rate is perfectly in agreement with the measured value listed in Table 6.1.

6.2.1 Systematic errors for the spectral fit

The systematic error on the $^{8}\text{B}-\nu$ rate due to the uncertainties on the fixed components can be estimated by varying the fixed values in a range between -3σ and $+3\sigma$ and fitting the data for each combination of the fixed parameters. Varying the fixed values of internal ^{214}Bi , ^{10}C , ^{11}Be and of surface ^{208}Tl , I performed $7^4 = 2401$ fits. The distribution of obtained ^{8}B rates has mean equal to 0.31 cpd and RMS equal to 0.02 cpd; this last is assumed as

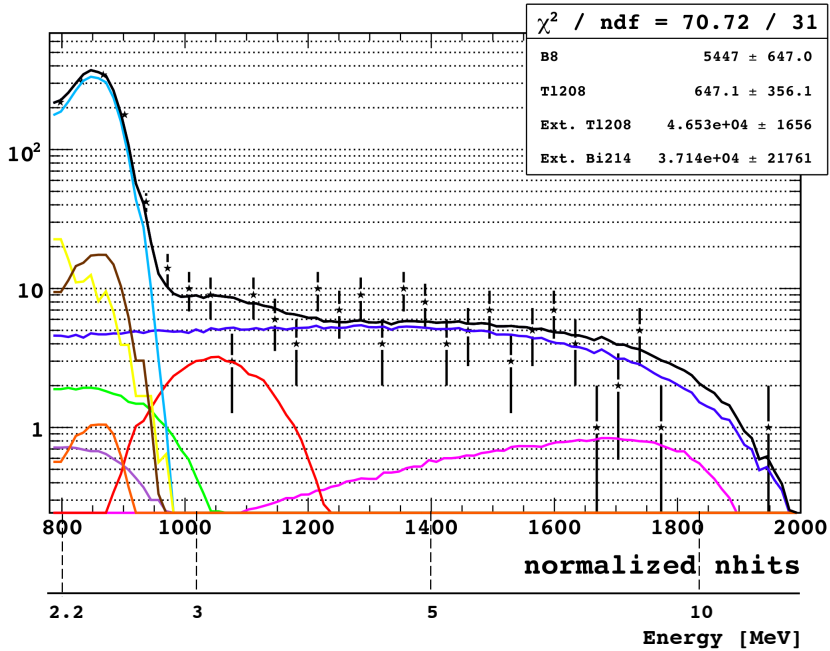


Figure 6.4: Spectral fit above 780 nhits in the FV obtained for an effective LT of 441.4 d using the spectral shapes obtained through G4Bx: ${}^8\text{B}$ -v (blue), external ${}^{208}\text{Tl}$ (light blue), internal ${}^{10}\text{C}$ (green) and internal ${}^{214}\text{Bi}$ (violet), external ${}^{214}\text{Bi}$ (yellow), ${}^{208}\text{Tl}$ from the End Regions (brown), surface ${}^{208}\text{Tl}$ (orange), internal ${}^{208}\text{Tl}$ (red) and internal ${}^{11}\text{Be}$ (pink). Many of these components are fixed to the values listed in Table 6.3.

systematic error due to the fixed components².

As already mentioned, a source of systematic can be the uncertainty on the ${}^8\text{B}$ spectral shape. In order to evaluate it, I repeated the spectral fit using 49 different spectral shapes obtained by varying the $\Delta m_{12}^2 = (7.6 \pm 0.2) \times 10^{-5} \text{ eV}^2$ and $\theta_{12} = 0.45 \pm 0.06$ [110] from the central value $\pm 1\sigma$, $\pm 2\sigma$, $\pm 3\sigma$. The resulting spectral shapes are almost indistinguishable. In Figure 6.5 the two extreme shapes obtained for $\Delta m_{12}^2 \pm 3\sigma$ and $\theta_{12} \pm 3\sigma$ are reported. The distribution of the ${}^8\text{B}$ rates has mean peaked at 0.31 cpd and RMS=0.01 cpd. The associated systematic error is $\pm 3.2\%$.

In order to estimate the systematic error linked to the method, I realized a Monte Carlo toy. 1000 samples of events poissonianly extracted by the final p.d.f. fitted on the data have been created; for each sample I performed the same fit as for the ${}^8\text{B}$ analysis estimating, as usual:

- the number of ${}^8\text{B}$ events, B_{meas} ;

²I obtained the same result also through a simpler and faster method: repeating the fit fixing all the internal background rates to the mean value \pm their statistical error. Calling $R_{{}^8\text{B}_v}^+$ and $R_{{}^8\text{B}_v}^-$ the obtained rate for $\text{Rates}^+ = \text{Rates}_{\text{mean}} + \sigma$ and $\text{Rates}^- = \text{Rates}_{\text{mean}} - \sigma$, respectively, I obtained:

- $R_{{}^8\text{B}_v}^+ = (0.29 \pm 0.04) \text{ cpd}/100 \text{ t};$
- $R_{{}^8\text{B}_v}^- = (0.33 \pm 0.04) \text{ cpd}/100 \text{ t}.$

The systematic error is evaluated as the distance between the central values and corresponds to $\pm 6.5\%$.

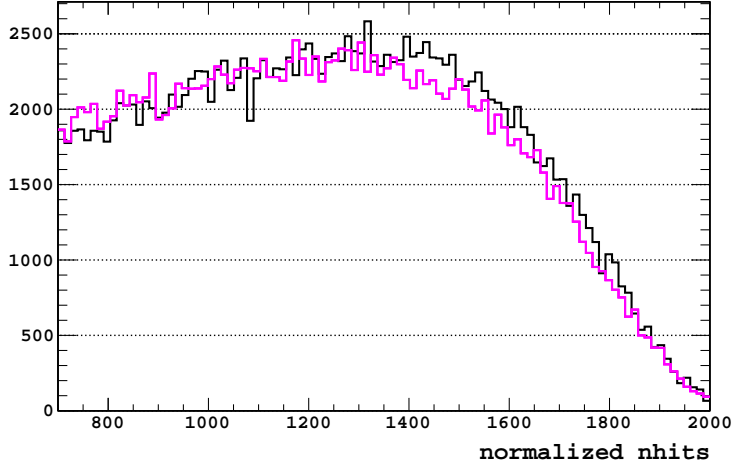


Figure 6.5: Spectral shapes for ${}^8\text{B}$ neutrinos in Borexino obtained for $\Delta m_{12}^2 \pm 3\sigma$ and $\theta_{12} \pm 3\sigma$, as quoted in [110]. The two spectra are almost indistinguishable.

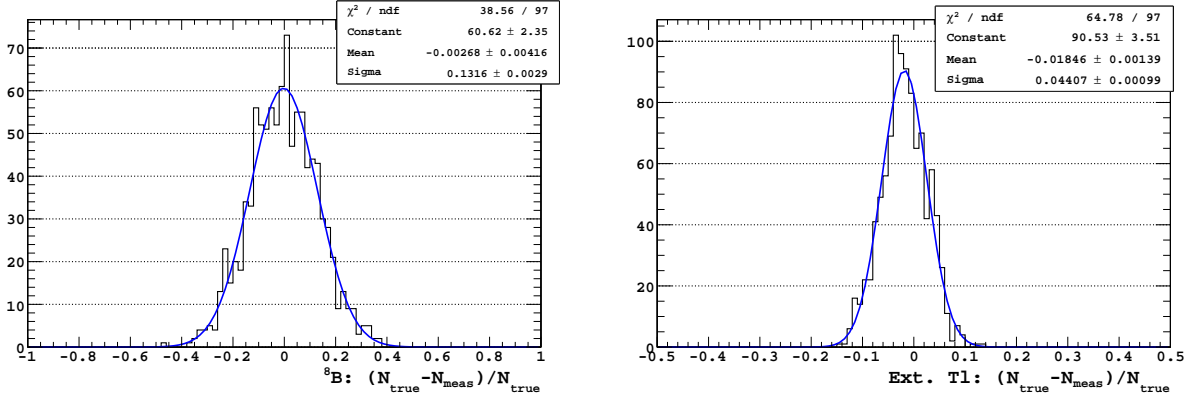


Figure 6.6: Discrepancies between $(B_{\text{real}} - B_{\text{meas}})/B_{\text{real}}$ (left) and $(E_{\text{real}} - E_{\text{meas}})/E_{\text{real}}$ (right) obtained through the MC toy applying the binned likelihood spectral fit.

- the number of external ${}^{208}\text{Tl}$ events, E_{meas} ;
- the number of external ${}^{214}\text{Bi}$ events;
- the number of internal ${}^{208}\text{Tl}$ events.

For the systematic error evaluation, I considered the discrepancies $(E_{\text{real}} - E_{\text{meas}})/E_{\text{real}}$ and $(B_{\text{real}} - B_{\text{meas}})/B_{\text{real}}$. Results are shown in Figure 6.6. The mean value of the bias is compatible with zero for the ${}^8\text{B}$ component; a little bias (+1.8%) is present for the external ${}^{208}\text{Tl}$. The systematic uncertainties are given by the error on the bias mean value and correspond to about 0.1% for the external rate and 0.4% for the bulk one.

Finally, I consider the systematic error due to the little uncertainty in the position reconstruction, affecting the Fiducial Volume definition. This has been studied by the Borexino

Systematic source	$+\sigma_R$	$-\sigma_R$
Fixed components	+6.4%	-6.4%
Spectral shape	+3.2%	-3.2%
Method	+0.4%	-0.4%
FV cut	+0.2%	-1.4%
Total	+7.1%	-7.3%

Table 6.4: Systematic errors on the 8B rate measurement through the radial fit above 780 nhits using an unbinned maximum likelihood fit.

Collaboration [109] and for energy above 2 MeV corresponds to +0.2% and -1.4%. Global systematic errors are listed in Table 6.4.

6.2.2 Final result

Taking into account the systematic errors, the result for the 8B rate obtained through the binned likelihood spectral fit above 780 nhits is:

$$R_{^8B-\nu} = (0.31 \pm 0.04_{\text{stat}} \pm 0.02_{\text{sys}}) \text{ cpd}/100 \text{ t}. \quad (6.2)$$

The global error on the measurement is about $\pm 14\%$.

6.3 The binned likelihood radial fit above 2 MeV in the Fiducial Volume

A new and independent method to study the energy region above 2 MeV is the radial fit. As anticipated in Chapter 5, the application of a radial fit above 2 MeV within 3 m reduces the external components and allows to reach a good sensitivity for the bulk one.

As demonstrated in Chapter 5, the study of the event radial distribution is a good method to distinguish surface, PMT, buffer and bulk components. I will show the results of the radial analysis I performed in the 3 m radius FV above 780 nhits.

6.3.1 The external and surface component in the FV

The most interesting and useful aspect in the FV is that the radial distributions of the external gammas does not depend on the vessel shape neither on the South or North hemisphere. In fact, considering data from external calibrations above 780 nhits, the radial distributions for the two positions of the source are perfectly superimposed within 3 m, as shown in the left panel of Figure 6.7. The radial distribution in the FV for the whole data sample of the external calibrations can be fitted with the simple exponential: $f(r) = e^{a+br}$; fit results are shown in the right panel of Figure 6.7. In particular, I found the penetration length:

$$\lambda_{\text{cal}} = (25.6 \pm 0.4) \text{ cm}, \quad (6.3)$$

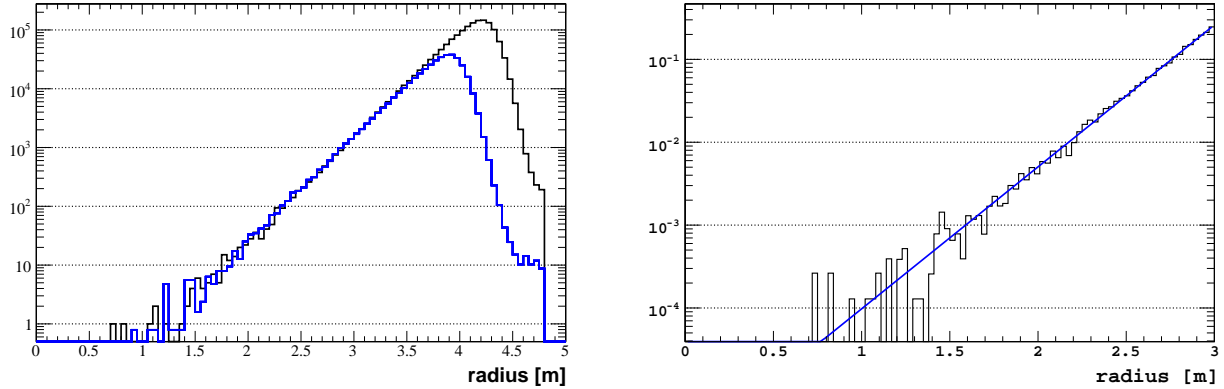


Figure 6.7: *Left:* superimposition of the radial distributions of external calibration data above 780 nhits, for the positions in the North hemisphere (black) and in the South hemisphere (blue). *Right:* global radial distribution of external calibration data in the FV above 780 nhits, fitted with an exponential: $f(r) = e^{a+br}$.

compatible with the ones obtained in Section 5.3.5.

For this reason, for the radial analysis in the FV, the external component is described using simply an exponential function. This makes the analysis of the external background independent from G4Bx simulations.

As checked on G4Bx simulations, the λ is the same for all the ^{208}Tl sources: PMTs and concentrators, IV and End Regions.

6.3.2 The bulk component in the FV

The use of the bulk distributions obtained from the Monte Carlo, separately for all the internal components (^{214}Bi , ^{208}Tl , ^{10}C , ^{11}Be and ^8B neutrinos), is redundant. Actually, as shown in Figure 6.8, within the FV, the radial distributions of internal events simulated in deformed vessels changing in time (blue lines) perfectly correspond to a simple volumetric distribution of events, obtained uniformly in a sphere of 3 m radius (black histograms). The only reason justifying the use of G4Bx distributions is the possibility of a dependence on the energy of internal events. Actually this could affect the event reconstruction only close to the vessel (border effect) and, as shown, this doesn't have influence in the FV. For this reason in the present analysis the bulk component is simply described through the distribution obtained by the uniform generation of events in a sphere of 3 m radius.

In conclusion, I decided to fit the data radial distribution using these two simple shapes for the radial fit (volumetric and exponential).

6.3.3 Radial fit in the energy region above 780 nhits in the FV

Summarizing, the energy region above 780 nhits in the FV has been studied through a radial fit composed by:

- * **bulk component**, obtained by the uniform generation of events in a sphere of 3 m radius, having only the amplitude as a parameter; the residual internal contamination (see Table 6.1) will be statistically subtracted;

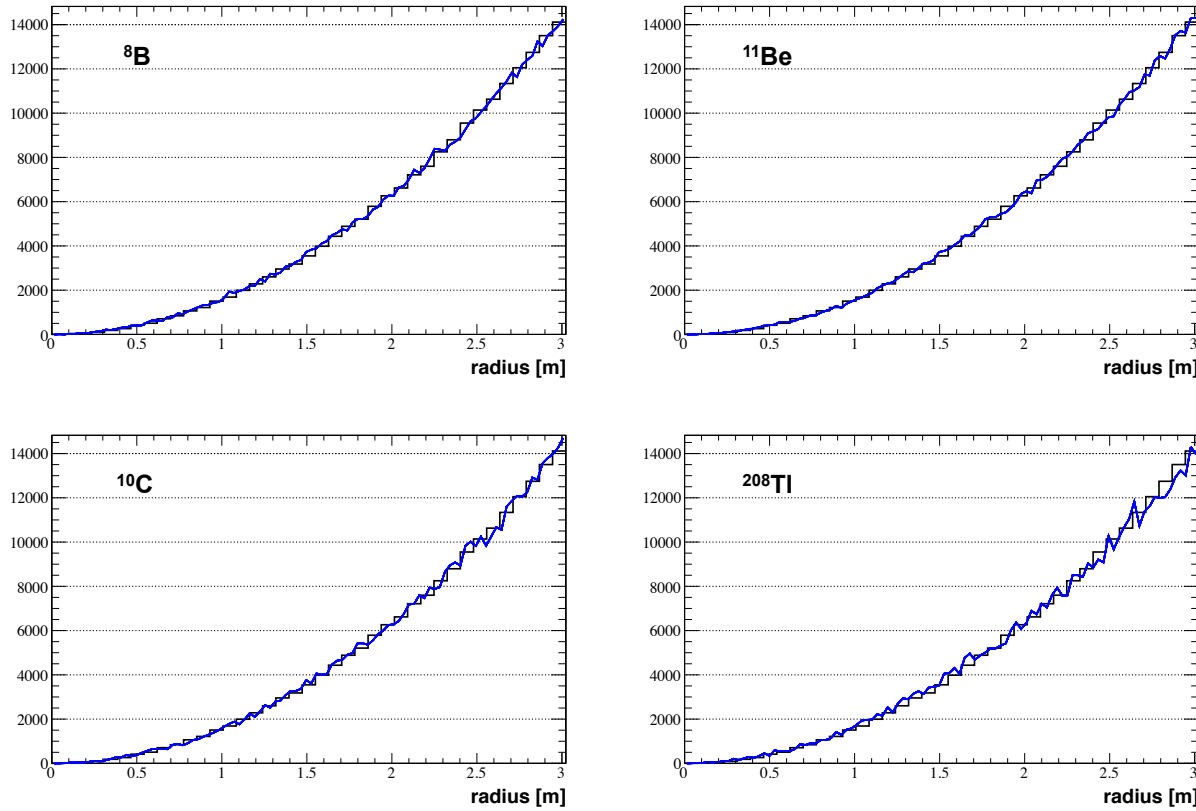


Figure 6.8: Superimposition of the radial distributions of internal ^8B neutrinos (top left), ^{11}Be (top right), ^{10}C (bottom left) and ^{208}Tl (bottom right) simulated with G4Bx (blue line) and a distribution of events obtained uniformly in a sphere of 3 m radius (black histogram).

* exponential function, representing the penetration of the external background; in particular the used the function is: $f(r) = A_{\text{E.B.}} e^{r/\lambda}$.

Before showing the results, some tests on the reliability of the method have been performed.

Testing the method

In order to show the reliability of the radial approach in the FV, in particular the sensitivity of the method in distinguishing the two components bulk and exponential, I considered the radial distributions obtained by other data samples, whose bulk and sample amplitude are known. The ratio between the bulk and the external events above 780 nhits is approximatively $0.4 \text{ cpd}/2.7 \text{ cpd} = 0.15$; this ratio has been reproduced on samples used for the tests.

The first considered sample is composed by:

- * a pure sample of ^{11}C events in the FV above 495 nhits for the bulk component ($N_{\text{bulk}} = 2168 \pm 47$);
- * the external calibration data in the FV above 720 nhits for the external component ($N_{\text{E.B.}} = 14300 \pm 120$); in this energy region, the penetration length measured from the external calibration data is $\lambda = (24.7 \pm 0.2) \text{ cm}$.

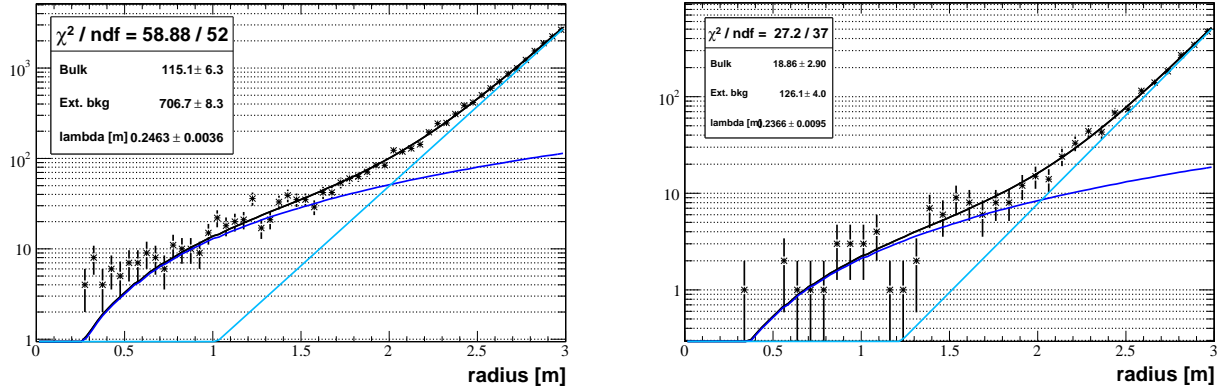


Figure 6.9: Left: radial distribution of the external calibration data above 720 nhits and of a pure sample of ¹¹C events above 495 nhits fitted with the bulk+exponential function described in 6.3.2.

Applying the bulk+exponential fit on the global radial distribution obtained from these ingredients, I got (see Figure 6.9):

$$\begin{aligned} N_{\text{bulk}} &= 2303 \pm 127 \\ N_{\text{E.B.}} &= 14133 \pm 167 \\ \lambda &= (24.6 \pm 0.4) \text{ cm} \end{aligned} \quad (6.4)$$

totally compatible with the real values listed above. This shows that the radial fit in 3 m is working properly.

Note that in the present test-sample I am considering a number of events about 12 times larger than the available one for the ⁸B analysis. For this reason the procedure has been repeated on a smaller event sample, reproducing the data one. It contains:

- * β -like events in the FV between 400 and 550 nhits for the bulk component ($N_{\text{bulk}} = 245 \pm 16$);
- * a subsample of the external calibration data in the FV above 720 nhits for the external component ($N_{\text{E.B.}} = 1680 \pm 41$); the penetration length obtained for this sample is $\lambda = (23.5 \pm 0.6)$ cm.

Fit results, shown in the right panel of Figure 6.9, are:

$$\begin{aligned} N_{\text{bulk}} &= 251 \pm 39 \\ N_{\text{E.B.}} &= 1681 \pm 54 \\ \lambda &= (23.7 \pm 0.9) \text{ cm} \end{aligned} \quad (6.5)$$

perfectly compatible with the known values listed above.

Heartened by this demonstration, I faced the radial fit above 780 nhits in the FV.

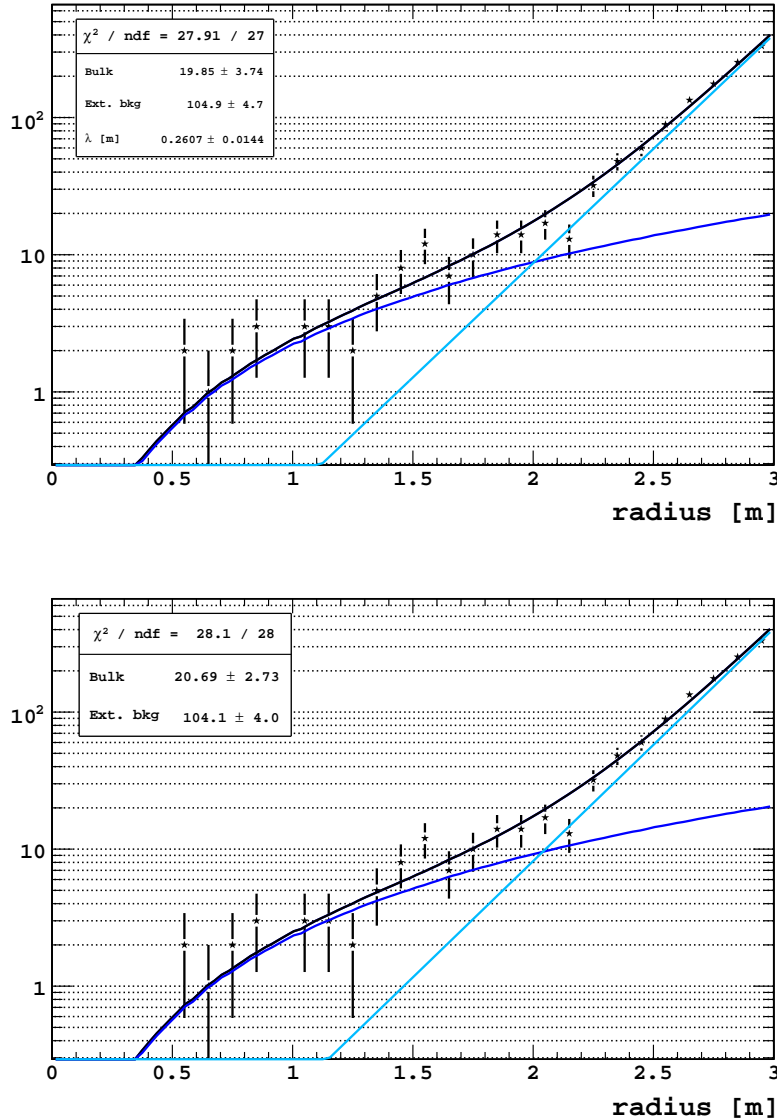


Figure 6.10: Top: radial fit above 780 nhits in the FV obtained for an effective LT of 441.4 d using the uniform volumetric distribution for the bulk (blue) and the exponential function: $f(r) = Ae^{r/\lambda}$ for the external and surface backgrounds (light blue). Bottom: radial fit above 2.14 MeV in the FV obtained for an effective LT of 441.4 d using the uniform volumetric distribution for the bulk (blue), the exponential function $f(r) = Ae^{r/\lambda}$ for the external and surface backgrounds (light blue) with $\lambda=25.6$ cm.

Results for the radial analysis above 780 nhits in the FV

The fit results are shown in the top panel of Figure 6.10. In particular, I obtain:

$$\begin{aligned} R_{{}^8B\nu} &= (0.34 \pm 0.09) \text{ cpd}/100 \text{ t} \\ R_{\text{Ext.Bkg}} &= (2.38 \pm 0.11) \text{ cpd}/100 \text{ t} \\ \lambda &= (26.1 \pm 1.4) \text{ cm} \end{aligned} \quad (6.6)$$

The $R_{{}^8B\nu}$ has been obtained by statistically subtracting the evaluated internal background rates (see Table 6.1) from the bulk component. On the other side, the $R_{\text{Ext.Bkg}}$ contains all

the external and surface background components. These results are perfectly compatible with the previous ones (see Eq. 6.1). The statistical error on the ^8B neutrino rate corresponds to 26%.

It is evident that the λ value from the fit is in principle compatible with the one found on calibration data (see Eq. 6.3), but seems a little higher in mean value.

Fixing the λ value to the one fitted on calibration data, 25.6 cm (Eq. 6.3), I found the results shown in the bottom panel of Figure 6.10, corresponding to:

$$\begin{aligned} R_{^8\text{B}\nu} &= (0.36 \pm 0.07) \text{ cpd}/100t \\ R_{\text{Ext.Bkg}} &= (2.37 \pm 0.09) \text{ cpd}/100t \\ \lambda &= 25.6 \text{ cm (fixed)} \end{aligned} \quad (6.7)$$

Again the $R_{^8\text{B}\nu}$ has been obtained by statistically subtracting the evaluated internal background rates (see Table 6.1) from the bulk component; the $R_{\text{Ext.Bkg}}$ contains all the external and surface background components. These results are perfectly compatible with the previous ones (see Eq. 6.1 and Eq. 6.6). Obviously, being the penetration length shorter, the external component decreases and the bulk one increases. Note that the statistical error on the ^8B neutrino rate is reduced to 19%.

Systematic errors for the radial fit

The systematic error on the $^8\text{B}\nu$ rate due to the little uncertainty on the penetration length of the external ^{208}Tl can be estimated from the fit results corresponding to $\lambda = (25.6 \pm 0.4) \text{ cm}$ (see Eq. 6.3). Calling $R_{^8\text{B}\nu}^+$ and $R_{^8\text{B}\nu}^-$ the obtained rate for $\lambda^+ = 26.0 \text{ cm}$ and $\lambda^- = 25.2 \text{ cm}$, respectively, I got:

$$\begin{aligned} - R_{^8\text{B}\nu}^+ &= (0.34 \pm 0.06) \text{ cpd}/100t; \\ - R_{^8\text{B}\nu}^- &= (0.38 \pm 0.07) \text{ cpd}/100t. \end{aligned}$$

The systematic error is evaluated as the distance between the central values and corresponds to $\pm 5.6\%$.

Once again, the systematic error related to the method can be evaluated by a Toy Monte Carlo. Using the bulk and exponential radial function used for the fit, I created 1000 samples of events reproducing the radial shape of the bulk component and the external component in the same bulk/external ratio as on the data sample. For each sample, the number of external and bulk events is randomly extract from the gaussian distribution having the expected rate $\times LT$ as mean and the squared root of it as σ . For each sample, the λ of the external component is uniformly extract between 0.24 cm and 0.28 cm. Calling S_b the sample of bulk events and S_e the sample of external events for each MC sample, for each sample $S_b + S_e$ I performed the same fit as for the ^8B analysis (bulk+exponential function) estimating, as usual:

- the number of bulk events B_{meas} ;
- the number of external events E_{meas} ;
- the penetration length (λ_{meas}).

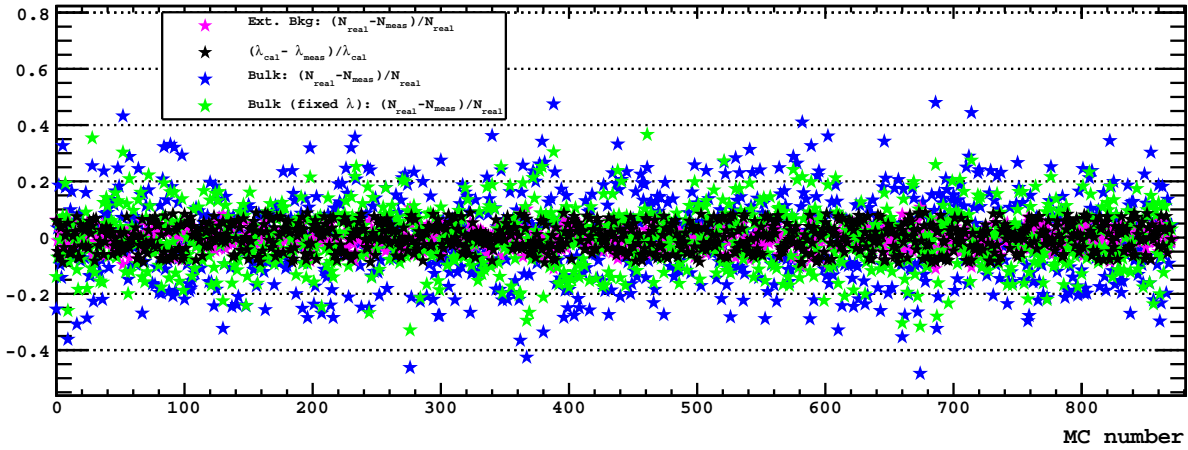


Figure 6.11: Discrepancies between $B_{\text{real}} - B_{\text{meas}}$ (blue for free λ and green for fixed λ), $E_{\text{real}} - E_{\text{meas}}$ (pink) and $\lambda_{\text{real}} - \lambda_{\text{meas}}$ (black) evaluated on 1000 samples of MC events reproducing the radial shape of the data sample for 8B analysis.

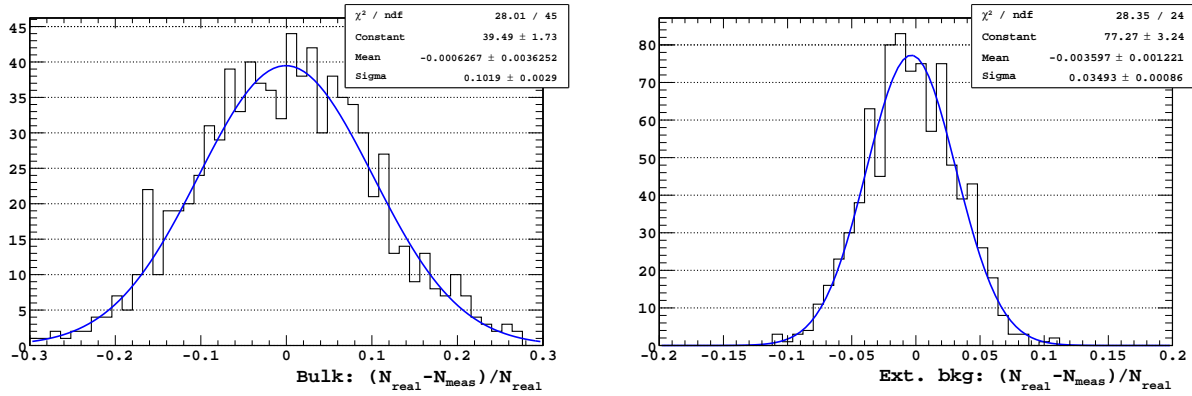


Figure 6.12: Discrepancies between $B_{\text{real}} - B_{\text{meas}}$ (left) and $E_{\text{real}} - E_{\text{meas}}$ (right) obtained through the MC toy for the radial fit. The $\lambda_{\text{real}} - \lambda_{\text{meas}}$ discrepancy is required to be less than 10%.

I repeated the fit also fixing the penetration length at the real value λ_{real} .

For the systematic error evaluation, I considered the discrepancies $(E_{\text{real}} - E_{\text{meas}})/E_{\text{real}}$ and $(\lambda_{\text{real}} - \lambda_{\text{meas}})/\lambda_{\text{real}}$ and $(B_{\text{real}} - B_{\text{meas}})/B_{\text{real}}$, both fixing and keeping free the λ . In Figure 6.11, the trend of the previous listed differences for each MC sample is reported. It is clear that the fixing of the penetration length improves the estimation of the bulk component (green dot distribution is closer to zero). The distributions of 8B and external rate discrepancy fixing the λ to the real value are shown in Figure 6.12. In both cases, the mean value of the bias is compatible with zero; the systematic uncertainty is given by the error on the bias mean value and corresponds to about 0.1% for the external rate and 0.4% for the bulk one.

Summarizing, considering also the systematic on the FV definition, the systematic errors for the binned radial fit are listed in Table 6.5.

Systematic source	$+\sigma_R$	$-\sigma_R$
λ_{cal}	+5.6%	-5.6%
Method	+0.4%	-0.4%
FV cut	+0.2%	-1.4%
Total	+5.6%	-5.8%

Table 6.5: Systematic errors on the ${}^8\text{B}$ rate measurement through the radial fit above 780 nhits.

Final result

Taking into account the systematic errors, result on ${}^8\text{B}$ rate through the binned likelihood radial fit analysis strategy above 780 nhits is:

$$R_{{}^8\text{B}-\nu} = (0.36 \pm 0.07_{\text{stat}} \pm 0.02_{\text{sys}}) \text{ cpd}/100 \text{ t}. \quad (6.8)$$

The global error on the measurement is about 20%.

This result is in agreement with the one obtained through the spectral fit (see Section 6.2.2). Result in Eq. 6.2 is more accurate: each background components has a precise spectral shape and the final error is smaller. The present analysis reinforces the spectral fit results with an independent method.

6.4 The multivariate binned likelihood fit above 2 MeV in the Fiducial Volume

In previous sections I have shown that the two fit procedures, based in spectral shapes and radial distributions respectively, gives ${}^8\text{B}$ rate values in reasonable agreement. The natural way to combine these results is the attempt of a two-dimensional fit, involving the two variables nhits and radius. For this reason, in this section I describe the last and conclusive fitting procedure performed in the present analysis: the binned multivariate likelihood fit. To perform this job, I used the fitting tool developed and used by the Borexino Collaboration for the pep analysis [31].

For a one-dimensional fit, the Poisson likelihood, L , of a hypothesis (i.e. the likelihood that our data fits a test spectrum with a set of parameters $\vec{\theta}$) is computed as:

$$L(\vec{\theta}) = \prod_{i=1}^n \frac{\lambda_i(\vec{\theta})^{k_i} e^{-\lambda_i(\vec{\theta})}}{k_i!} \quad (6.9)$$

where the product is over all bins and n is the total number of bins. $\lambda_i(\vec{\theta})$ is the expected number of entries in the i th bin given the fit parameters $(\vec{\theta})$ and k_i is the number of entries in the bin. As an example, k_i could be the number of entries in a particular energy bin, and $\lambda(\vec{\theta})$ the expected number of entries in that bin given the rates of each species described by the array of parameter θ .

In the present analysis, the likelihood is extended to two variables: the radial and the spectral distributions of the events. The probability density functions (p.d.f.'s) of these

variables are produced from MC simulations. The fitting tool starts from the 2D distribution (energy, radius) for simulated events, integrated over an energy range larger than the energy spectrum binning, then projects the radial variable to one-dimensional histograms and computes the corresponding likelihood. In this way, a correlation between the number of counts in the different histograms is introduced, as events that are in the energy spectrum will also be entries in the projections. To handle this issue, the p.d.f.'s of the hypothesis is normalized to the total number of entries in the projected data histograms. Consequently, the likelihood computed for the projections is defined as:

$$L_p(\vec{\theta}) = \prod_{j=1}^m \frac{a\lambda_j(\vec{\theta})^{k_j} e^{-a\lambda_j(\vec{\theta})}}{k_j!} \quad (6.10)$$

$$N = a \sum_{j=1}^m \lambda_j(\vec{\theta}) \quad (6.11)$$

where N is the total number of entries in the projected histogram and a is a scaling factor set to satisfy Eq. 6.11. Here $\lambda_j(\vec{\theta})$ represents the expected bin content of the projected histogram in the corresponding other variable, and k_j is the actual number of entries in that bin. The scaling does not affect the values of $\lambda(\vec{\theta})$ at the maximum likelihood but the uncertainties given by likelihood ratio tests may not be underestimated, as it is the case when the scaling is not done.

The total likelihood to maximize is then:

$$L_T(\vec{\theta}) = \prod_{i=1}^{m_E} L(\vec{\theta}) \times \prod_{j=1}^{m_p} L_p(\vec{\theta}) \quad (6.12)$$

where $L(\vec{\theta})$ and $L_p(\vec{\theta})$ are defined in Eq. 6.9 and 6.10, respectively. The first product is over the m_E independent energy spectra and the second is the product over all m_p projections to other dimensions (in the present case, the radial distribution) of regions of one of the energy spectra. This definition is included into the fitting code and is passed $-\ln L_T(\vec{\theta})$ to MINUIT as the test statistic to be minimized.

The used energy and radial distributions have already been described and used in previous sections. The only difference concerns radial distributions, that are directly obtained by the simulated events, instead of described as functions.

In Table 6.6, a list of all the used spectral shapes, the corresponding used radial distribution and the possible fixed value is reported for each fit component.

Fit results in the two variables radius and nhits are shown in Figure 6.13. In particular, I obtained:

$$\begin{aligned} R_{^8B\nu} &= (0.34 \pm 0.04) \text{ cpd}/100 \text{ t} \\ R_{\text{Int.}\Pi} &= (0.03 \pm 0.02) \text{ cpd}/100 \text{ t} \\ R_{\text{Ext.}\Pi} &= (2.11 \pm 0.07) \text{ cpd}/100 \text{ t} \end{aligned} \quad (6.13)$$

well compatible with results shown in Eq. 6.1 and 6.7. In particular, as expected, the 8B - ν rate is a compromise between the values obtained by the mono-dimensional fits.

Spectral shape	Radial shape	Fix value [cpd]
${}^8\text{B}-\nu$ ${}^{208}\text{Tl}$ from PMTs Internal ${}^{208}\text{Tl}$	bulk	free
	external	free
	bulk	free
Internal ${}^{214}\text{Bi}$ ${}^{10}\text{C}$ ${}^{11}\text{Be}$ ${}^{208}\text{Tl}$ from IV ${}^{208}\text{Tl}$ from E.R. ${}^{214}\text{Bi}$ from PMTs	bulk	$(8.00 \pm 0.03) \times 10^{-3}$
	bulk	0.03 ± 0.01
	bulk	0.034 ± 0.007
	external	$(7 \pm 2) \times 10^{-3}$
	external	6% of ${}^{208}\text{Tl}$ from PMTs
	external	0.39 ± 0.23

Table 6.6: Spectral shapes and corresponding radial shapes used for the multivariate likelihood fit above 780 nhits within 3 m. The external ${}^{214}\text{Bi}$ has been fixed to the value obtained in Eq. 6.1.

6.4.1 Systematic errors for the multivariate fit

The systematic error on the ${}^8\text{B}-\nu$ rate due to the uncertainties on the fixed components can be estimated from the fit results obtained varying the fixed values in a range between -3σ and $+3\sigma$ and fitting the data for each combination of the fixed parameters. Varying the fixed values of internal ${}^{10}\text{C}$, ${}^{11}\text{Be}$, surface ${}^{208}\text{Tl}$ and external ${}^{214}\text{Bi}$ between -3σ and $+3\sigma$, I performed $7^4 = 2401$ fits³. The distribution of obtained ${}^8\text{B}$ rates has mean equal to 0.35 cpd and RMS equal to 0.02 cpd. Since the central value for the ${}^8\text{B}$ rate obtained by the 2D fit is 0.34 cpd (see Eq. 6.13), the systematic error has been quoted as asymmetric and corresponds to -2.9% and $+8.8\%$.

The systematic due to the method is as usual evaluated through a Toy Monte Carlo: 1000 event samples have been simulated following the spectral and the corresponding radial distributions obtained by the fitting 2D p.d.f.. Each MC sample has been fitted in the same way as the data sample and the discrepancies $(E_{\text{real}} - E_{\text{meas}})/E_{\text{real}}$ and $(B_{\text{real}} - B_{\text{meas}})/B_{\text{real}}$ have been evaluated. As shown in Figure 6.14 a bias of $+3.6\%$ is present for the ${}^8\text{B}-\nu$ rate; this is treated as systematic error due to the method. Note that the bias related to the external ${}^{208}\text{Tl}$ is at level of 14% .

Considering also the already quoted systematics related to the FV cut and the uncertainty on the ${}^8\text{B}$ spectral shape, all the systematic sources are listed in Table 6.7.

Final result

Taking into account the systematic errors, result on ${}^8\text{B}$ rate through the multivariate binned likelihood fit above 780 nhits is:

$$R_{{}^8\text{B}-\nu} = (0.34 \pm 0.04^{+0.03}_{-0.02}) \text{ cpd}/100 \text{ t}. \quad (6.14)$$

The global error on the measurement is about $+15\%$ and -13% .

The expected rate in Borexino above 780 nhits within 3 m, based on SSM+(MSW-LMA)

³Due to the little error on internal ${}^{214}\text{Bi}$ (only 0.4%), this component has not been varied.

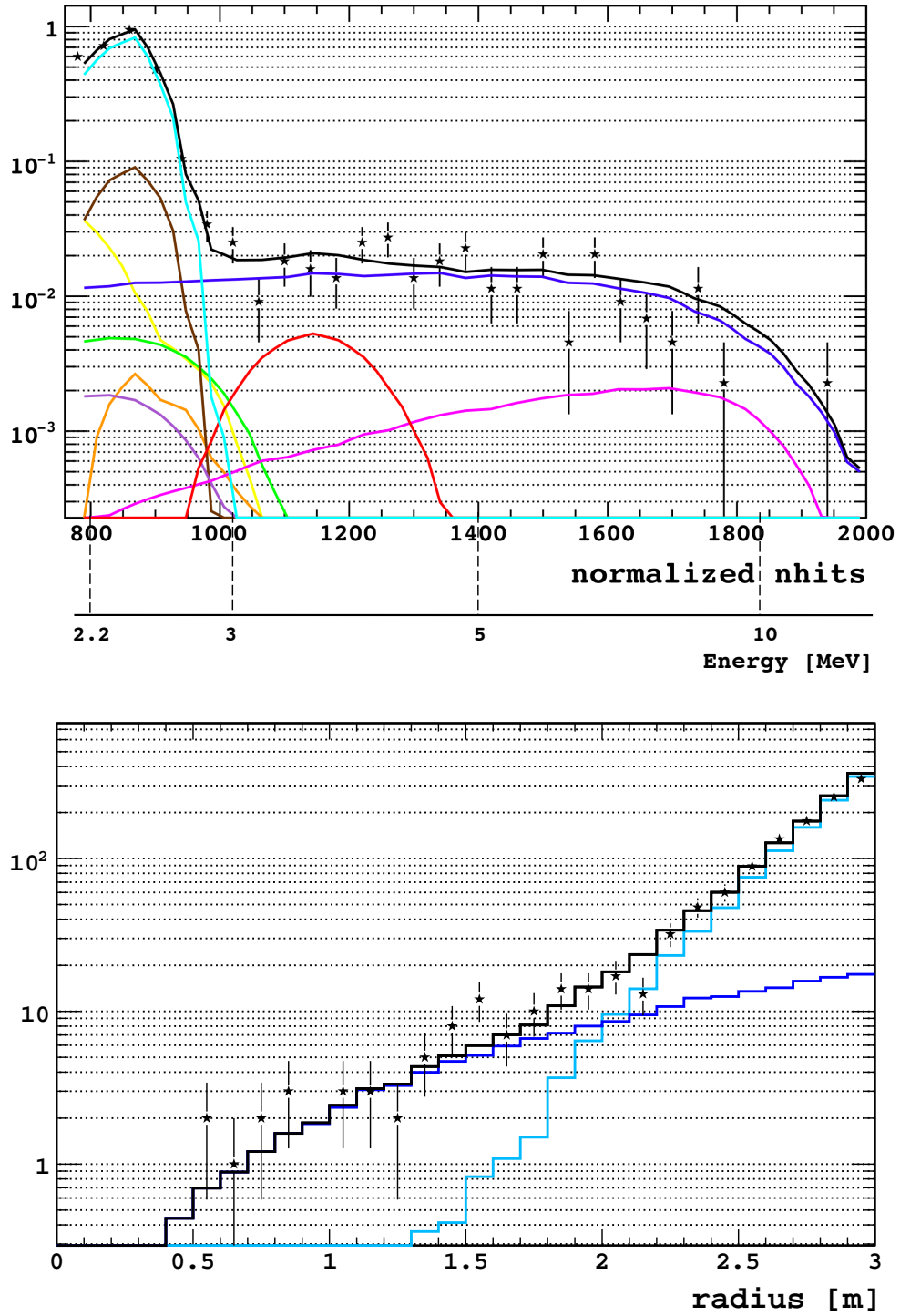


Figure 6.13: Result from the multivariate binned likelihood fit above 780 nhits within 3 m: the spectral (top) and the radial (bottom) part.

model for the oscillation parameters: $\Delta m^2 = (7.6 \pm 0.2) \times 10^{-5} \text{ eV}^2$ and $\sin^2 2\theta_{12} = 0.87 \pm 0.03$, is $(0.32 \pm 0.03) \text{ cpd}/100 \text{ t}$.

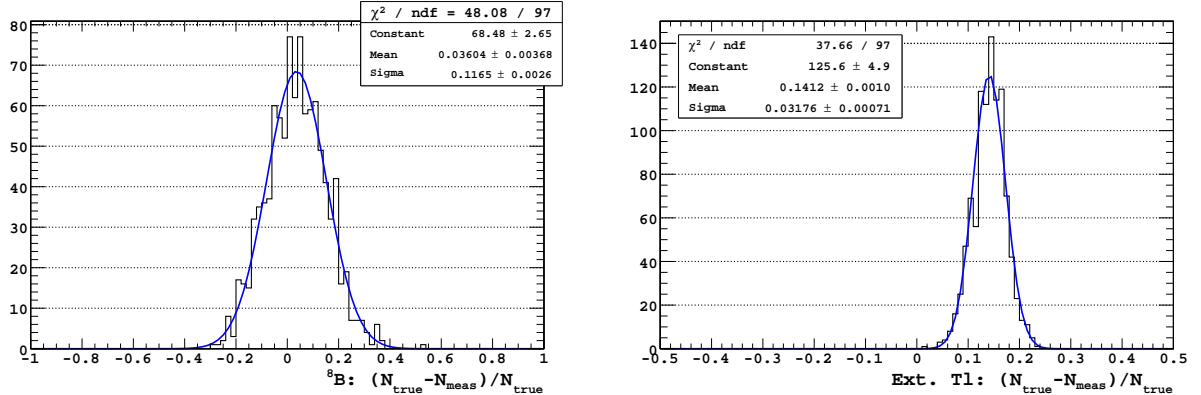


Figure 6.14: Discrepancies between $B_{\text{real}} - B_{\text{meas}}$ (left) and $E_{\text{real}} - E_{\text{meas}}$ (right) obtained through the MC toy for the multivariate fit.

Systematic source	$+\sigma_R$	$-\sigma_R$
Fixed components	+8.8%	-2.9%
Spectral shape	+3.2%	-3.2%
Method	+3.6%	-0%
FV cut	+0.2%	-1.4%
Total	+10.0%	-4.5%

Table 6.7: Systematic errors on the ${}^8\text{B}$ rate measurement through the radial fit above 780 nhits.

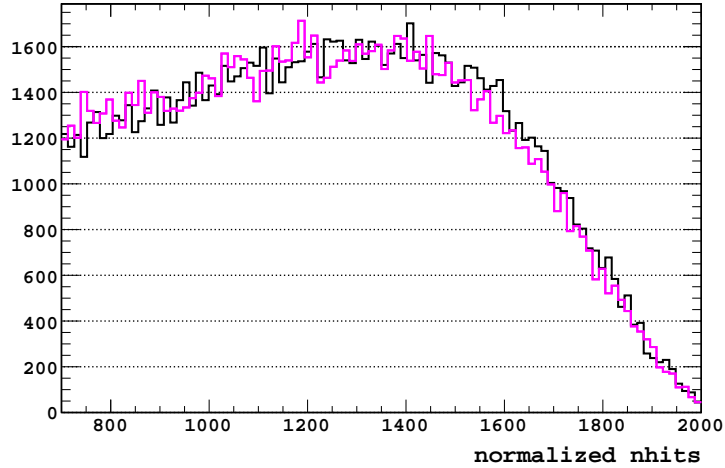


Figure 6.15: Spectral shapes for ${}^8\text{B}$ neutrinos in Borexino obtained for $\epsilon = -0.45$ (black) and $\epsilon = 0.45$ (pink). The two spectra are almost indistinguishable.

6.5 What about NSI?

As explained in Section 1.6.6 and in [45], Non Standard Interaction can play a crucial role in defining the neutrino interaction with matter and such new interactions may produce

ϵ	Expected 8B rate [cpd]	Expected 8B rate above 780 nhits [cpd]
-0.50	0.442	0.289
-0.45	0.438	0.286
-0.40	0.435	0.284
-0.35	0.434	0.284
-0.30	0.434	0.284
-0.25	0.436	0.286
-0.20	0.440	0.288
-0.15	0.445	0.291
-0.10	0.450	0.295
-0.05	0.456	0.299
0.00	0.463	0.303
+0.05	0.469	0.307
+0.10	0.475	0.310
+0.15	0.480	0.314
+0.20	0.485	0.317
+0.25	0.490	0.320
+0.30	0.494	0.323
+0.35	0.498	0.326
+0.40	0.501	0.328
+0.45	0.504	0.330
+0.50	0.507	0.332

Table 6.8: Expected 8B - ν rate in the Borexino FV, for the whole spectrum and above 780 nhits, depending on the NSI parameter ϵ . The values corresponding to $\epsilon=0$ are the ones expected in absence of NSI. The uncertainty on the rates is 10%.

appreciable deviations *only* in the intermediate energy region. The conversion of solar neutrinos is described by the mass-squared splitting $\Delta m^2 = m_2^2 - m_1^2$, the mixing angle θ_{12} , and the effective parameter ϵ . The P_{ee} can be written as usual:

$$P_{ee} = \frac{1}{2} + \frac{1}{2} \cos 2\theta_{12} \cos 2\theta_{\text{NSI}} \quad (6.15)$$

where θ_{NSI} is:

$$\theta_{\text{NSI}} = \frac{2\theta_{12} - \nu}{\sqrt{(\cos 2\theta_{12} - \nu)^2 + (\sin 2\theta_{12} + 2\epsilon\nu)^2}}. \quad (6.16)$$

The ν parameter depends on x_\odot , the solar radius unity:

$$\nu(x) = 1.53 \times 10^{-7} \left(\frac{\Delta m_{12}^2}{E} \frac{\text{MeV}}{\text{eV}^2} \right)^{-1} \left(\frac{N_e(x)}{\text{mol/cm}^3} \right), \quad (6.17)$$

where $N_e(x)$ is the electron density in the Sun. For 8B neutrinos, $x=0.04$, so:

$$\nu(x=0.04) = 0.18 \frac{E}{\text{MeV}}. \quad (6.18)$$

Using the new formula for the P_{ee} I could produce different energy spectra varying the ϵ parameter. Unluckily, once again, the little difference in the final spectra can not be

detected by Borexino (see Figure 6.15).

The other value that can be checked is the measured rate. In Table 6.8 the expected ${}^8\text{B}-\nu$ rate in the Borexino FV, for the whole spectrum and above 780 nhits, depending on the NSI parameter ϵ are reported. Unluckily the error on the measurement (see Eq. 6.1) and the 10% uncertainty on the expected rate are too big to discriminate between the presence or not of NSI.

6.6 The flux and the survival probability above 2 MeV

Considering result in Eq. 6.14, the corresponding unoscillated total flux of ${}^8\text{B}$ solar neutrinos is:

$$\Phi_{{}^8\text{B}} = (3.0 \pm 0.4^{+0.3}_{-0.2}) \times 10^6 \text{ s}^{-1} \text{ cm}^{-2} \quad (6.19)$$

perfectly compatible with results from other experiments listed in Table 4.5.

The survival probability has been evaluated defining the χ^2 function:

$$\chi^2 = \left(\frac{0.34 \text{ cpd}/100 \text{ t} - f(P_{ee}, f_{{}^8\text{B}})}{\sqrt{0.04^2 + 0.03^2}} \right)^2 + \left(\frac{1 - f_{{}^8\text{B}}}{0.14} \right)^2 \quad (6.20)$$

where:

- $f(P_{ee}, f_{{}^8\text{B}}) = P_{ee} \cdot f_{{}^8\text{B}} \cdot \sigma_{\nu_e} + (1 - P_{ee}) \cdot f_{{}^8\text{B}} \cdot \sigma_{\nu_\mu};$
- $f_{{}^8\text{B}}$ is the ratio between the measured flux and the value predicted by the SSM [34];
- σ_{ν_e} and σ_{ν_μ} are the cross sections folded on the ${}^8\text{B}$ energy spectrum above 2.07 MeV, for ν_e and ν_μ or ν_τ respectively.

Maximizing the χ^2 for the P_{ee} and $f_{{}^8\text{B}}$ parameters (see top panel of Figure 6.16), I obtain $\bar{P}_{ee} = 0.44^{+0.14}_{-0.11}$ at the mean energy of 8.3 MeV for ${}^8\text{B}$ neutrinos. This result is shown in the bottom panel of Figure 6.16, in addition to other experimental data mapping the survival probability. In particular the contribute from the Borexino experiment is evident in all the different energy regions: vacuum (pp and ${}^7\text{Be}$ neutrinos), transition (pep neutrinos) and transition/matter (${}^8\text{B}$ neutrinos).

It is also interesting to consider again the plot shown in left panel of Figure 6.1, concerning the spectral measurement above 3 MeV. Applying the multivariate fit technique in the energy bin [2,4] MeV it is possible to add a low energy point in the plot⁴, as shown in Figure 6.17. The agreement with the expectation is good, mostly considering the difficulty of treating the first bin, where the expected background/signal ratio is about 30.

6.7 Conclusions

In the present chapter the analysis of ${}^8\text{B}$ neutrinos with an energy threshold down to 2.07 MeV has been described. The deep study of the external backgrounds shown in Chapter 5 and the development of MC tools able to reproduce them have been fundamental in order to treat and distinguish the external components from the signal one.

⁴Note that this low energy bin is the most difficult to treat, given that the expected background/signal ratio is about 30 in the FV. Considering the whole spectrum above 2 MeV within 3 m, the background/signal ratio is a factor 3 lower.

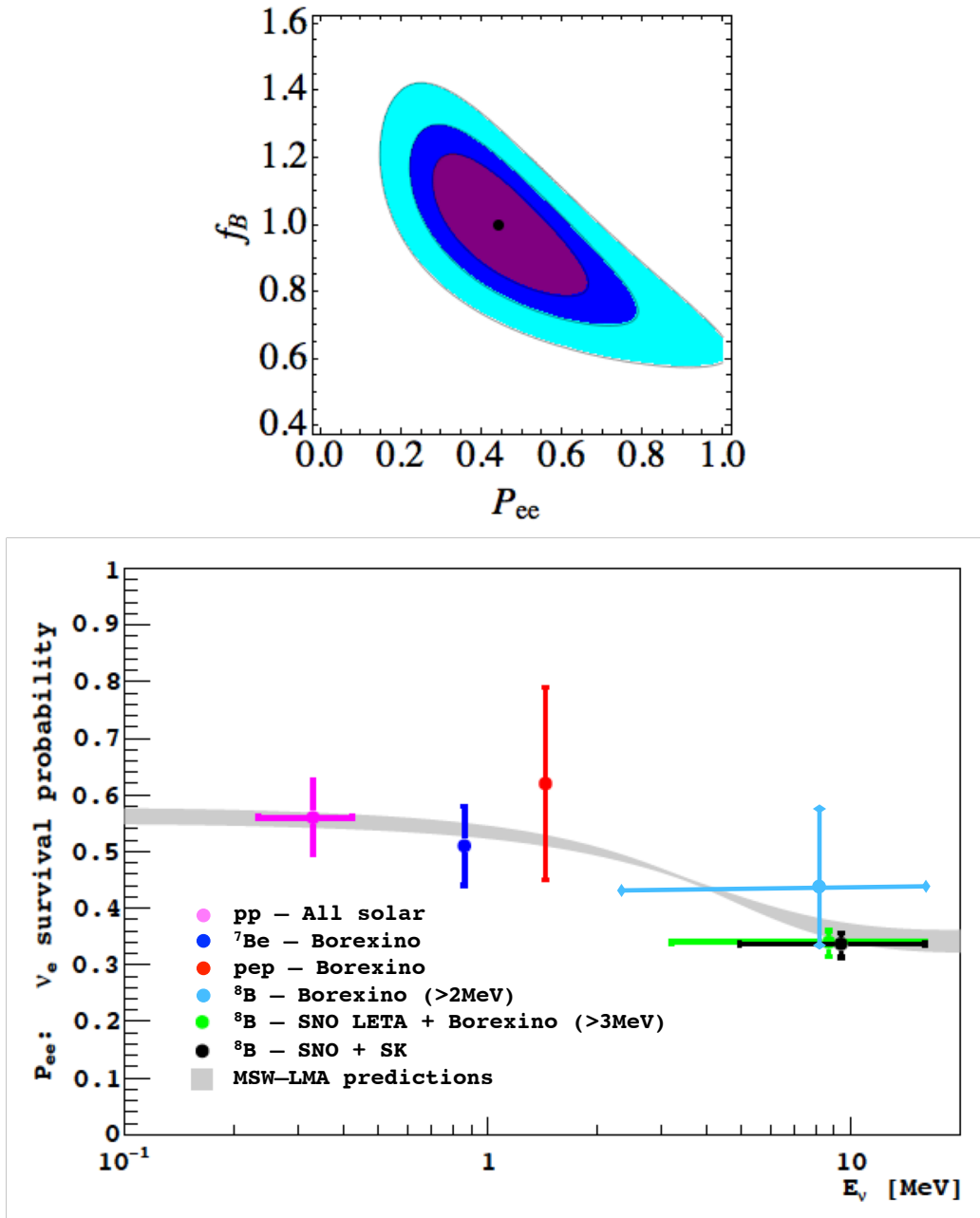


Figure 6.16: Top: Contour plot at 68%, 90% e 99% of CL for the χ^2 function defined in Eq. 6.20 varying the P_{ee} and f_B parameters. Bottom: Electron neutrino survival probability as a function of energy. The light blue point corresponds to the one measured through ^8B solar neutrinos above 2 MeV. The other experimental points correspond to: pp neutrino measurement given in [9] (pink); ^7Be neutrino measurement from Borexino [9] (blue); the pep neutrino measurement from Borexino [31] (red); the ^8B neutrino measurement from Borexino above 3 MeV [36] and SNO-LETA [37] (green) and the ^8B neutrino measurement from SNO-LETA and SuperKamiokande [111] (black). The MSW-LMA prediction band is the 1σ range of the mixing parameters given in [112].

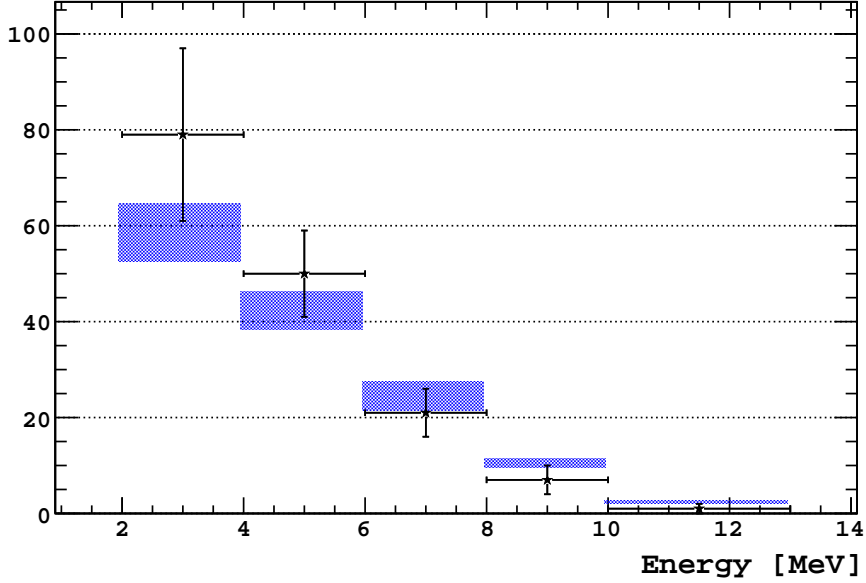


Figure 6.17: ^8B solar neutrino spectrum measured by Borexino above 2 MeV, compared to the expectations based on Standard Solar Model GS98 [34] in MSW-LMA scenario. The measure unit is events/441.4 d. Only statistical errors are shown.

The analysis has been performed through a multivariate fit, concerning the radial and the energy distribution of events, of all the components present above 2.07 MeV. The measured ^8B rate is $R_{^8\text{B}-\nu} = (0.34 \pm 0.04^{+0.03}_{-0.02}) \text{ cpd}/100 \text{ t}$, validating the SSM+(MSW-LMA) theory. This result has also been confirmed performing the one-dimensional fits in the radial and energy variables. Basing on the measurement obtained with the 2D fit, the survival probability for the mean neutrino energy of 8.3 MeV has been evaluated, that adds a new point in the mapping of the P_{ee} , involving the transition region.

The present measurement, added to the recent pep one, shows the feasibility of precise measurements, with liquid scintillator detector, of solar neutrino sources in the transition oscillation region. They also confirm the necessity of more accurate measurements of these solar neutrino sources, allowing a deeper knowledge of the transition region. This is now a fundamental point in order to confirm or exclude the presence of Non Standard Physics in neutrino propagation in matter, as Non Standard Interaction or Sterile Neutrino.

Chapter 7

Simulations of Muon Interaction Products in Borexino and Double Chooz

Cosmic ray muons and their spallation products are potential background contribution to low-energy underground experiments searching for and detecting rare events associated with neutrino interactions, double-beta decay and dark matter Weakly Interacting Massive Particles (WIMPs). In particular, cosmogenic isotopes contribute to the background through their decays (up to about 20 MeV, see Table 7.1) and neutrons can be captured on nuclei emitting a gamma [113]. The knowledge of cosmogenic neutron fluxes and the produced rates of radioisotopes in underground laboratories is thus crucial.

Underground neutron fluxes are difficult to measure since they are overwhelmed by gamma rays from local radioactivity. Also the cosmogenic isotope rates are hard to estimate because of the low production cross sections. Although these events may have a clear signature of an associated muon, large detectors are needed to study them with sufficient accuracy, especially to understand the neutron behavior at large distances from the muon track. In this context, many Monte Carlo (MC) codes have been developed to well describe muon interactions and subsequent hadronic cascades and neutron or isotope productions. This reliance on simulation must be accompanied by validation of the codes through experimental data and by comparison between different packages.

In these pages I will describe the work I performed in order to:

- * simulate underground muons and their products in Borexino through different MC codes;
- * compare different code results;
- * compare MC results with Borexino measurements;
- * taking advantage of the developed experience, perform the same simulations for Double Chooz, to be compared with future data.

7.1 Cosmic muons

Underground muons are the remnants of the air showers initiated by the collisions of primary cosmic rays with air nuclei (see Figure 7.1). In particular muons come from the decay of pions and kaons.

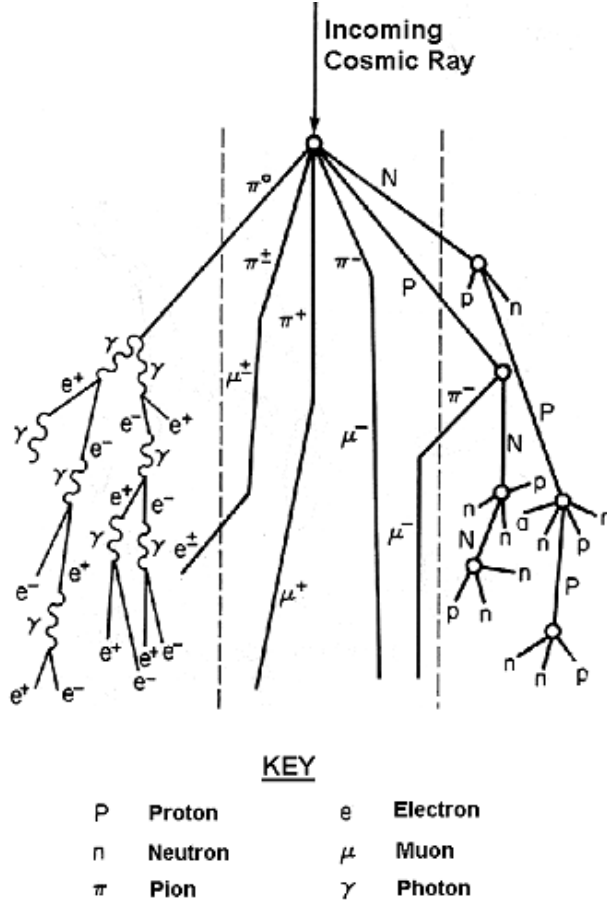


Figure 7.1: Picture representing the interactions of primary cosmic rays, producing secondary cosmic rays. In particular muons are produced by the pion and kaon decays.

The “all-particle” flux of the *primary* cosmic radiation can be described by an inverse power law energy spectrum [117], with differential flux given by:

$$\frac{dN}{dE} \propto E^{-(\gamma_p+1)} \quad (7.1)$$

where $\gamma_p \approx 1.7$ for $E \leq 10^3$ TeV, $\gamma_p \approx 2.0$ for $10^3 \text{ TeV} \leq E \leq 10^6 \text{ TeV}$ and $\gamma_p \approx 1.5$ for $E \geq 10^6$ TeV. From the primary spectrum, it is possible to evaluate the energy spectrum at the Earth surface of secondary uncorrelated muons, which is given, with good approximation, by [117]:

$$\frac{dN_\mu}{dE d\Omega} \approx \text{const} \cdot \mathcal{E}^{-(\gamma_p+1)} \cdot \left(\frac{1}{1 + a\mathcal{E} \cos \theta} + \frac{0.054}{1 + b\mathcal{E} \cos \theta} \right) \quad (7.2)$$

where E_μ is the muon energy at the surface, $a=1.1/115 \text{ GeV}$ and $b=1.1/850 \text{ GeV}$. The first and the second term in parenthesis of Eq. 7.2 represent the contributions of muons from π and K decays, respectively. In the limit of high energies, an approximate expression of the muon surface energy spectrum has the simple form:

$$\frac{dN_\mu}{dE} = \text{const} \cdot \mathcal{E}^{-\gamma} \quad (7.3)$$

where $\gamma = \gamma_p + 2 \approx 3.7$. The surface muon spectral index γ is therefore related to the primary cosmic ray spectral index.

The treatment of muon propagation through the matter has been deeply studied and investigated. The energy spectrum of underground muons can be derived taking into account the process of energy loss in the rock, which is assumed to have the form:

$$\frac{dE_\mu}{dh} = -(\lambda + \beta E_\mu) \quad (7.4)$$

where dh is a thin rock slab, usually in km water equivalent (km w.e.), λ is the contribution from the ionization energy loss and βE_μ is the contribution from radiative processes (bremsstrahlung, pair production and muon hadro-production). The parameters λ and β are functions of the muon energy, but for practical purposes can be assumed as constants [117]. The quantity $\epsilon = \lambda/\beta$ is called the critical energy and is defined as the energy value above which the radiative processes become dominant.

With the above assumptions, the general solution of Eq. 7.4 is:

$$E_\mu = (\mathcal{E} + \epsilon) e^{-\beta h} - \epsilon. \quad (7.5)$$

where E_μ is the muon energy after crossing the rock slant depth h . The underground muon energy spectrum can be thus obtained from Equations 7.3 and 7.5 using the following relation:

$$\frac{dN}{dE_\mu} = \left[\frac{dN}{d\mathcal{E}} \right]_{\mathcal{E}=\mathcal{E}(E_\mu)} \cdot \frac{d\mathcal{E}}{dE_\mu} \quad (7.6)$$

and is given by:

$$\frac{dN}{dE_\mu} = \text{const} \cdot [E_\mu + \epsilon(1 - e^{-\beta h})]^{-\gamma}. \quad (7.7)$$

This formula will be fundamental for the muon simulations in Borexino (see Section 7.5.1).

7.2 Neutron and isotope production by muon spallation

In muon spallation, an incoming muon interacts with a nucleus via an exchange of a virtual photon. The nucleus subsequently emits neutrons (or pions). It can also happen that a real photon undergoes photo-absorption and neutrons or pions are subsequently emitted. Thus, the results of a muon spallation are radioactive isotopes and neutrons. In Figure 7.2 two Feynman diagrams depicting muon spallation processes are shown. A detailed description of the theoretical models describing the muon spallation can be found in [114]. In organic liquid scintillator (LS), energetic muons and subsequent showers interact mostly with ^{12}C , the most abundant nucleus heavier than ^1H in the LS, generating neutrons and isotopes by electromagnetic or hadronic processes. A list of expected cosmogenic isotopes and their properties is shown in Table 7.1. For this reason, the muon-induced spallation of carbon targets is a matter of primary interest.

Most neutrons and radioactive isotopes do not come directly from muon-nucleus spallation reactions, but from the muon-initiated hadronic and electromagnetic cascades. These neutrons spread away from the primary muon track, thermalizing slowly, and finally get captured by protons or other nuclei (see for example [32] for ^{11}C production mechanisms). The radioactive decays of cosmogenic isotopes represent an annoying source of background

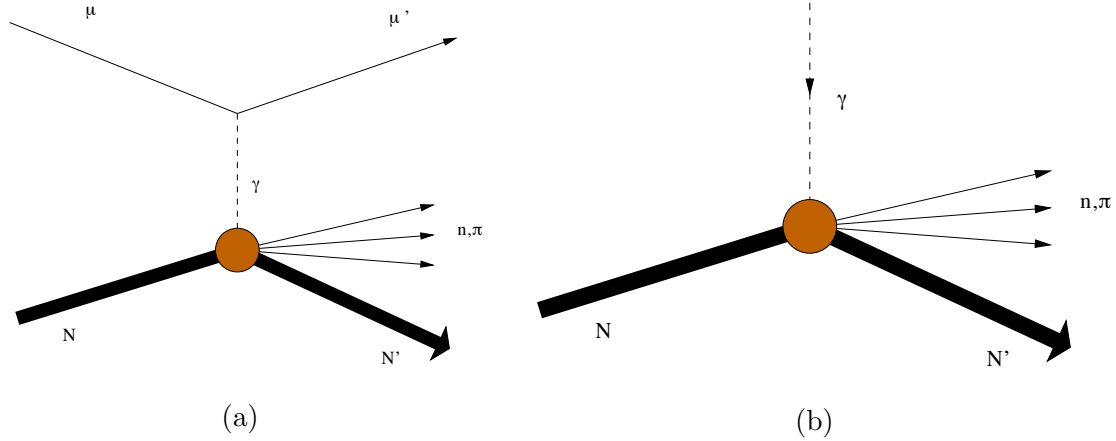


Figure 7.2: Feynman diagrams depicting muon spallation (a) and photo-absorption (b). In panel (a) an incoming muon exchanges a virtual photon with a nucleus. Panel (b) shows a real photon being absorbed by the nucleus. The nucleus subsequently emits neutrons or pions.

above 1 MeV.

In Borexino, cosmogenic isotopes are identified by looking for a coincidence with the parent muon, as already shown in ${}^8\text{B}$ [36] and pep neutrino analysis [31]. In order to tag cosmogenic neutrons, as well described in [80], every time a muon crosses the Stainless Steel Sphere (SSS), an especially long event (1.6 ms, 100 times longer than an ordinary event) is acquired after the main event, allowing to record and tag the γ 's from cosmogenic neutron capture.

7.3 Muon and neutron detection in Borexino

As already underlined, a key element for the underground Borexino experiment is the suppression of the background induced by the residual cosmic muons. A high-efficiency veto and geometrical reconstruction of these muons is mandatory for an identification of cosmogenic backgrounds based on time and space coincidences with the parent muon.

As mentioned before (see Chapter 2), the Borexino detector is formed by an inner detector (ID) which contains liquid scintillator, the central target volume surrounded by a buffer. It is also equipped with an outer detector (OD), a water tank, which serves both as an additional passive shielding against external radiation and as an active veto, identifying crossing muons via their Čerenkov light emission. The identification of muons is based on the complementarity between outer and inner detectors, as well discussed in [80]. In particular, different methods of muon identification have been studied concerning both the OD and the ID:

1. **OD Flags:** the OD muon tags search for an increase in OD PMT activity above usual dark noise fluctuations; they operate at two different stages of data processing:
 - **Muon Trigger Flag (MTF):** it is a hardware trigger of the OD, given by a significant increase in number of hits in a time span comparable to the transit

Isotope	$\tau_{1/2}$	Q [MeV]	Decay	σ [μ barn]
^{12}B	0.02 s	13.4	β^-	
^{11}Li	0.09 s	20.8	β^-	
^9Li	0.18 s	13.6	$\beta^-/\beta+\text{n}$	$<2.12 \pm 0.35$
^8Li	0.84 s	16.0	$\beta^-/\beta+\text{n}$	
^8He	0.12 s	10.6	β^-	$<2.12 \pm 0.35$
^6He	0.81 s	3.5	β^-	16.02 ± 1.6
^9C	0.13 s	16.5	β^+	4.83 ± 1.51
^8B	0.77 s	18.0	β^+	7.13 ± 1.46
^{11}Be	13.80 s	11.5	β^-	<2.34
^{11}C	20.38 min	2.0	β^+	905 ± 58
^{10}C	19.30 s	3.6	β^+	115.4 ± 14.6

Table 7.1: Expected cosmogenic isotopes in Liquid Scintillator detectors [69].

time of a muon. The threshold is set to 6 PMTs firing within a timegate of 150 ns;

- **Muon Clustering Flag (MCF):** it is an offline software trigger based on the acquired OD data. Its trigger condition is a slight refinement of the MTF: two subsets of PMTs are regarded separately, distinguishing between hits at PMTs mounted on the SSS and PMTs mounted on the floor. The trigger condition is met if 4 PMTs of either subset fired within 150 ns.
2. **ID Flags:** for the ID we observe that typical muon pulses feature longer rise and decay times than neutrino-like scintillation events of comparable energy, since a muon crossing the buffer needs up to 45 ns to deposit all its ionization energy. In addition, the number of detected photons is several orders of magnitude above the usual light output of point-like events, prolonging the signal substantially by generating large amounts of PMT after pulses. Pulse shape discrimination (PSD) can therefore be used to identify muons.

The efficiencies of the available muon tags were investigated using two approaches. First, samples of muon events were selected independently of any tagging flag and have been used to find directly the identification efficiencies. Second, each flag has been tested against a muon sample selected by either of the remaining two flags. The overall Borexino muon identification efficiency reaches 99.992%.

In Borexino several reconstruction algorithms for muon tracks do exist. The primary goal of muon tracking in Borexino is to enhance the veto of cosmogenic radioisotopes by the introduction of geometrical cuts. Muons produce unstable nuclei by spallation processes on their trajectory through the scintillator and the decay of such nuclei can mimic the expected signal. For short-lived radioisotopes, it is usually sufficient to veto all events in the wake of a muon for a duration corresponding to several half-lives of the given isotope, as well described and applied for the ^8B neutrino analysis [36]. However, when the mean life of the dangerous nuclei is longer, as for ^{11}C or ^{10}C isotopes ($\tau_{^{11}\text{C}}=29$ min, $\tau_{^{10}\text{C}}=27$ s), particularly annoying for the pep neutrino analysis, the induced dead time can

become very large. To overcome this problem, the veto of events can be applied only to a cylindrical region around the muon track instead of the whole detection volume. The ^{11}C background events can be identified by a threefold coincidence relying on spatial and time information of the muon, the neutron, and the decay signal of the radionuclide as described in more detail in [31].

Moreover, muon tracking allows an accurate investigation of both cosmogenic neutron background and other muon-induced production of radioisotopes occurring in Borexino. Two independent tracking algorithms have been developed:

1. the OD tracking, based on the entry and exit points generated by the Čerenkov cone of muons in water.
2. the ID tracking that relies on the distinctive photon arrival time pattern created by the conical scintillation light front emitted by the muon track.

The results of both ID and OD tracking algorithms are later combined in a best fit global tracking. The resolutions achieved are at the level of about $3.5^\circ\text{-}5^\circ$ angular and about 35-50 cm lateral [80].

Once the muon has been detected, also cosmogenic neutron captures can be identified in Borexino. The number of neutrons generated and captured in the active volume of the detector after a single muon event can extend up to 200, introducing further difficulty. The challenging task of recording the highest possible number of γ 's from neutron capture within a few hundreds of μs is met as follows: every time an ID event is flagged also by the OD (MTF flag), an especially long event (1.6 ms, 100 times longer than an ordinary event) is acquired after the main event. The time between the end of the muon event and the beginning of the neutron event in the gate has been measured and is (150-50) ns. Hits recorded in this long neutron event include the tail of the muon after-pulse hits distribution as well as the hits due to neutron captures if present. In fact, the difficulty for neutron detection arises from the muon after-pulse hits that are generated in the PMTs for several tens of μs after the muon has already left the detector. This is most annoying for muons crossing the IV.

Events not correlated with a muon may accidentally fall inside the long neutron gate and are identified by the clustering algorithm. Such events are generally due to ^{14}C decays corresponding to about 50-100 hits and can be confused with partially contained γ -rays from neutron captures. However, these events generally occur in single multiplicity events and are mostly rejected by a proper cut introducing a negligible loss of signal (see [80] for details).

7.4 The simulation codes: Geant4 and FLUKA

As already mentioned, in this work I compare Geant4 and FLUKA simulations of cosmogenic neutron and isotope production, and validate them against the Borexino experimental data. We decided to compare these two different codes because many efforts have been done by the MC developers of the two community in order to reproduce the muon interactions in the best way. It seems that both the codes are reliable in reproducing hadronic showers and muon interactions, but, as it will be evident from this Chapter, improvements are still necessary.

The Geant4 toolkit [91] can potentially be used for end-to-end simulations of experiments, from background calculations down to detailed detector characterization. Its object-oriented design and open-source nature make it rather flexible. Critically, it generates and tracks in a realistic way the recoiling nuclei from individual neutron elastic interactions.

FLUKA [115] is a well-established simulation tool in nuclear and particle physics, and has been used for neutron calculations in a variety of experiments.

Detailed description of the two toolkits are largely available. In this Section I just want to recall the main concepts differentiating the two codes.

7.4.1 Something about Geant4

Geant4 is a free software package composed of tools which can be used to accurately simulate the passage of particles through matter. The toolkit includes the following aspects:

- the geometry of the system;
- the materials involved;
- the fundamental particles of interest;
- the generation of primary events;
- the tracking of particles through materials and electromagnetic fields;
- the physics processes governing particle interactions;
- the response of sensitive detector components;

where the user can directly act. In addition, the toolkit provides tools for:

- the generation of event data;
- the storage of events and tracks;
- the visualization of the detector and particle trajectories;
- the selection and analysis of simulation data at different levels of detail and refinement.

Users may construct stand-alone applications or applications built upon another object-oriented framework. In either case the toolkit will support them from the initial problem definition to the production of results and graphics for publication. With this purpose, the toolkit includes also:

- * user interfaces;
- * built-in steering routines;
- * command interpreters;

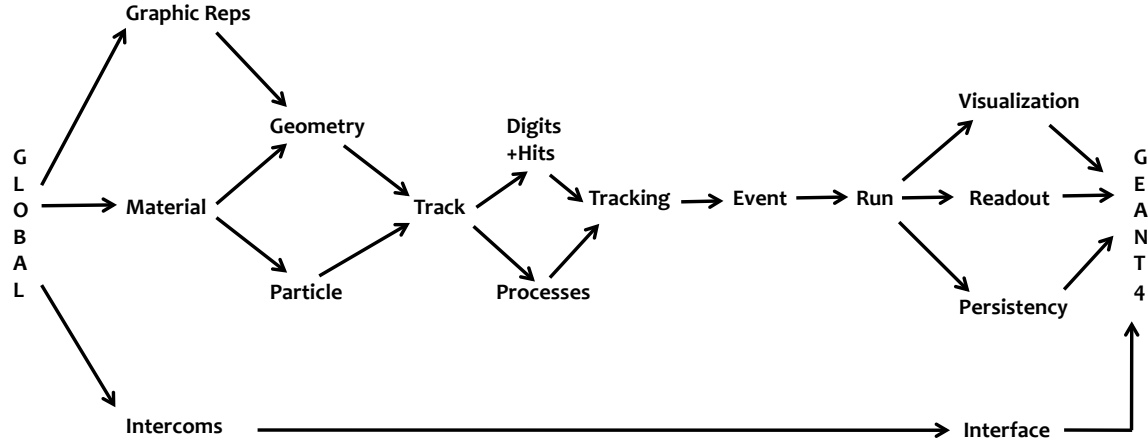


Figure 7.3: Geant4 class categories.

operating at every level of the simulation. At the heart of Geant4 is an abundant set of physics models to handle the interactions of particles with matter across a very wide energy range. Data and expertise have been drawn from many sources around the world and in this respect, Geant4 acts as a repository which incorporates a large part of all that is known about particle interactions. Depending on the purpose, it is possible to merge different physics models, treating different physics processes at different energy, defining a so called Physics List. Some ready-made Physics Lists are directly available in Geant4. The user can also prepare by him self his own Physics List.

Geant4 is written in C++ and exploits advanced software-engineering techniques and object-oriented technology to achieve transparency. For example, the way in which cross sections are input or computed is separated from the way in which they are used or accessed. Similarly, the computation of the final state can be divided into alternative or complementary models, according to the energy range, the particle type, and the material. To build a specific application the user-physicist chooses from among these options and implements code in user action classes supplied by the toolkit.

In contrast, object-oriented methods help manage complexity and limit dependencies by defining a uniform interface and common organizational principles for all physics models. Within this framework the functionality of models can be more easily recognized and understood, and the creation and addition of new models is a well-defined procedure that entails little or no modification to the existing code.

The Geant4 class category diagram is shown in Figure 7.3. Categories at the bottom of the diagram are used by virtually all higher categories and provide the foundation of the toolkit. The **global category** covers the system of units, constants, numerics and random number handling. The two categories **materials** and **particles** implement facilities necessary to describe the physical properties of particles and materials for the simulation of particle-matter interactions. The **geometry module** offers the ability to describe a geometrical structure and propagate particles efficiently through it.

Above these reside categories required to describe the tracking of particles and the physical processes they undergo. The **track category** contains classes for tracks and steps, used by the **processes category**, which contains implementations of models of physical interac-

tions: electromagnetic interactions of leptons, photons, hadrons and ions, and hadronic interactions.

All processes are invoked by the **tracking category**, which manages their contribution to the evolution of a track's state and provides information in sensitive volumes for hits and digitization.

Above these the **event category** manages events in terms of their tracks and the **run category** manages collections of events that share a common beam and detector implementation. A **readout category** allows the handling of pile-up.

Finally capabilities that use all of these categories and connect to facilities outside the toolkit through abstract interfaces, provide visualization, persistency and user interface capabilities.

7.4.2 Something about FLUKA

FLUKA is a general purpose tool for calculations of particle transport and interactions with matter, covering an extended range of applications spanning from proton and electron accelerator shielding to target design, calorimetry, detector design, Accelerator Driven Systems, cosmic rays, neutrino physics, radiotherapy etc.

Microscopic models are adopted whenever possible, consistency among all the reaction steps and/or reaction types is ensured, conservation laws are enforced at each step, results are checked against experimental data at single interaction level. As a result, final predictions are obtained with a minimal set of free parameters fixed for all energy/target/projectile combinations.

FLUKA can simulate with high accuracy the interaction and propagation in matter of about 60 different particles, including photons and electrons from 1 keV to thousands of TeV, neutrinos, muons of any energy, hadrons of energies up to 20 TeV and all the corresponding antiparticles, neutrons down to thermal energies and heavy ions. Time evolution and tracking of emitted radiation from unstable residual nuclei can be performed online. FLUKA can handle even very complex geometries, using an improved version of the well-known Combinatorial Geometry (CG) package. The FLUKA CG has been designed to track correctly also charged particles.

For most applications, no programming is required from the user. In particular, an user-friendly interface called Flair (FLUKA Advanced Interface) [116] has been recently developed, making the writing of the input file very intuitive and facilitating the execution of the code and visualization of the output files. The input file requires some standard informations, as the particle type and energy, the beam position, dimension and direction, the definition of the geometry and the materials of the detector, the physics processes to activate, the number of particles to simulate, the final state informations to save, etc. In Figure 7.4 an example of the Flair front-end is shown.

7.4.3 Choice of the Hadronic Physics Lists

An other preliminary study to perform concerns the choice of the hadronic physics models, describing hadronic showers produced by muon spallation in the rock. As already mentioned, after the muon spallation, primary neutrons, pions, and protons can all produce secondary neutrons and isotopes through hadronic interactions.

A simple cascade model [122] suggests that the number of nuclear cascade products such

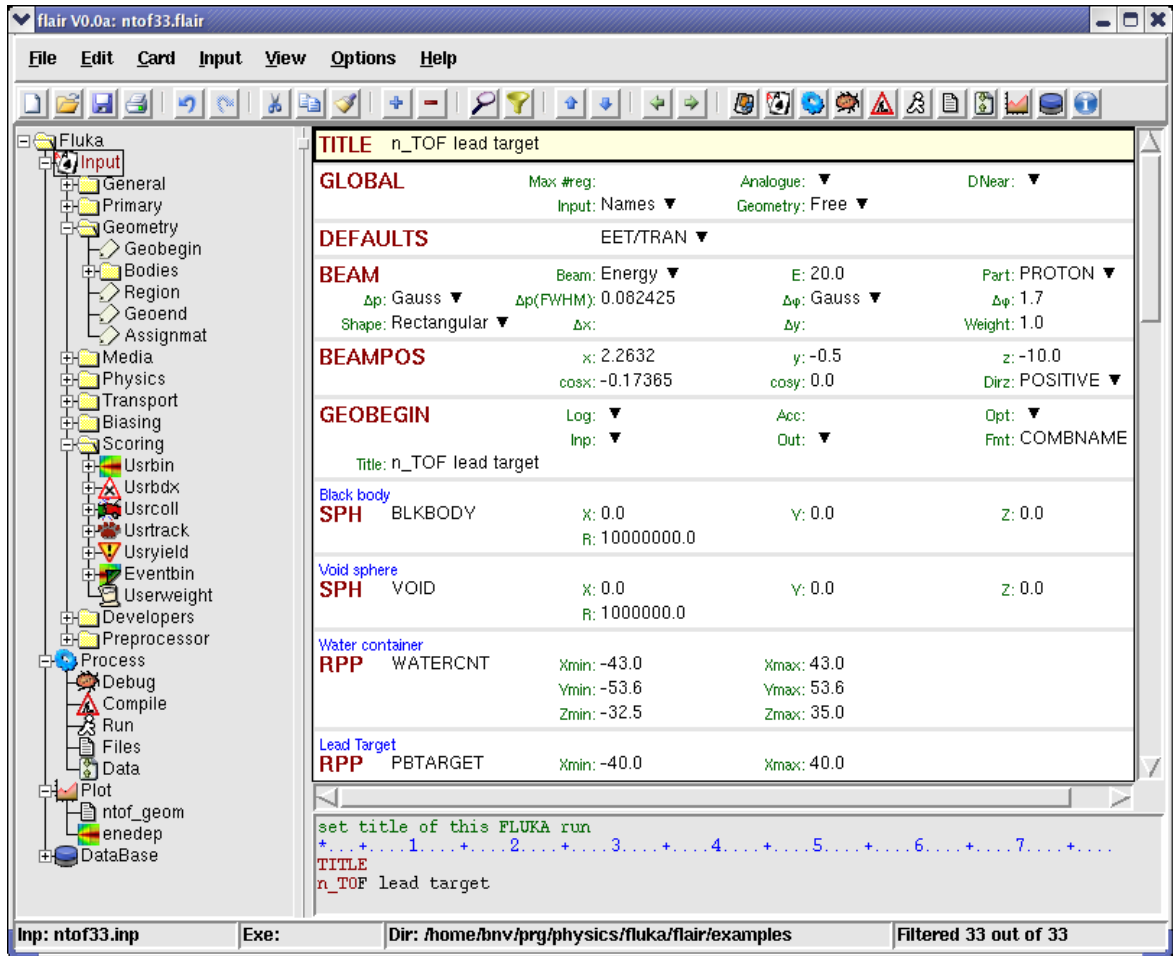


Figure 7.4: Flair front-end for the input file.

as neutrons, pions, and protons increases with the average muon energy approximately like $E_\mu^{0.7}$. This number has been confirmed through Monte Carlo simulations both with FLUKA [123] and Geant4 [124].

Geant4

In Figure 7.5 a summary of the hadronic physics models available in Geant4 is shown, as a function of the particle energy. A detailed description of each model can be found in [125]. For my purposes, I focused on:

- * Quark-Gluon String (QGS) model for proton, neutron, pion and kaon interactions with nuclei at kinetic energies above 12 GeV, interfaced to Precompound (P) model for the evaporation phase of the interaction;
- * Fritiof model (FTF) for the interaction of highly energetic protons, neutrons, pions and kaons starting from 4-5 GeV; it can also be interfaced to Precompound (P) model for the evaporation phase of the interaction (FTFP);
- * Low Energy Parameterized (LEP) model for proton, neutron, pion and kaon interactions with nuclei at kinetic energies between 9.5 GeV and 25 GeV;

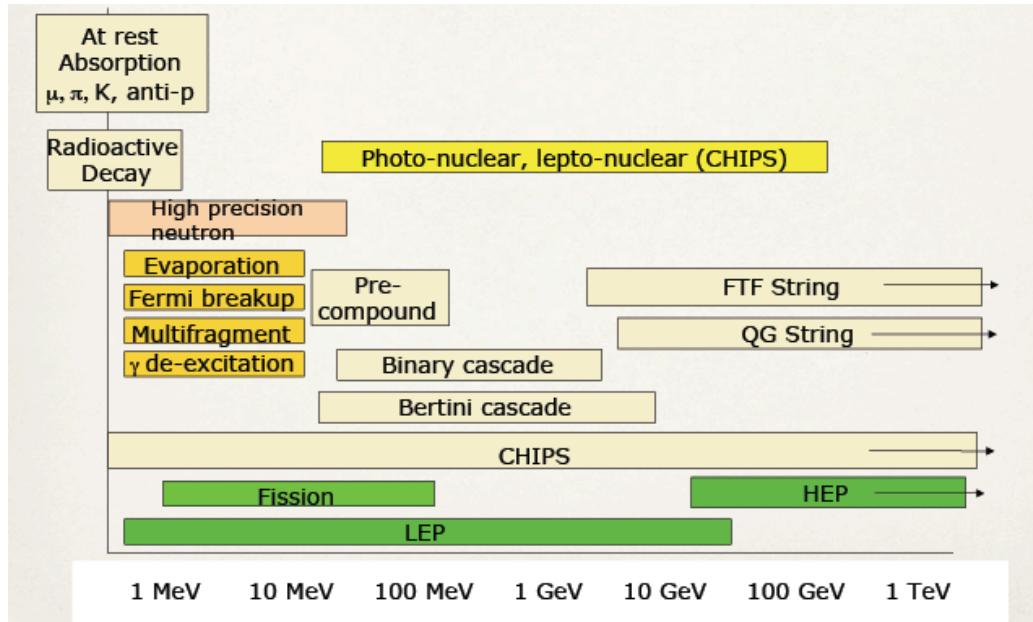


Figure 7.5: Available hadronic physics models in Geant4.

- * Bertini cascade (BERT) model, which includes intra-nuclear cascade, followed by precompound and evaporation phases of the residual nucleus, for proton, neutron, pion and kaon interactions with nuclei at kinetic energies below 9.9 GeV;
- * Binary cascade (BIC) model, that is a data driven intra-nuclear cascade model intended for energies below 5 GeV;
- * High Precision Neutron (HP) model, describing parameterized capture and fission for low-energy neutrons (below 20 MeV).

Many of these models were already present in G4Bx: Radioactive Decay, High Precision Neutron, Binary and Bertini Cascade and QG Strings. After some studies in the recent Geant4 documentation, I decided to include also the so called FTF String model.

As evident, it is possible to cover the entire muon energy spectrum expected at LNGS through a combination of different physics models. In particular, in Geant4 some "ready-made" Physics Lists merging different physics models are available; in particular I focused on: FTF_BIC, FTFP_BERT, QGSP_BIC_HP, QGSP_BERT_HP. In implementing them into G4Bx, the HP models has been added also in the first two physics lists. A summary of the physics models and energy ranges, for each physics list chosen to be tested, is shown in Table 7.2. The four Physics Lists have been tested with and without the activation of the Ion Physic List; this last defines the light ions likely to be produced by the hadronic interactions, like deuterons, tritons, ^3He , α 's and generic ions.

Summarizing, for the Geant4 side eight Hadronic Physics Lists are tested.

The other Physics Lists automatically activated for each simulation are:

- Electromagnetic Process for Leptons (G4eMultipleScattering, G4eIonisation, G4eBremsstrahlung, ...);
- Nuclear Decay Process (G4Decay, G4RadioactiveDecay);

FTF_BIC_HP*	HP	Binary	LEP	FTF
Protons		0 → 5 GeV		4 GeV → 100 TeV
Neutrons	0 → 20 MeV	19.9 MeV → 5 GeV		4 GeV → 100 TeV
π		0 → 5 GeV		4 GeV → 100 TeV
K			0 → 5 GeV	4 GeV → 100 TeV
FTFP_BERT_HP*	HP	Bertini		FTF
Protons		0 → 5 GeV		4 GeV → 100 TeV
Neutrons	0 → 20 MeV	19.9 MeV → 5 GeV		4 GeV → 100 TeV
π, K		0 → 5 GeV		4 GeV → 100 TeV
QGSP_BIC_HP	HP	Binary	LEP	QGSP
Protons		0 → 9.9 GeV	9.5 → 25 GeV	12 GeV → 100 TeV
Neutrons	0 → 20 MeV	19.9 MeV → 9.9 GeV	9.5 → 25 GeV	12 GeV → 100 TeV
π, K		0 → 9.9 GeV	9.5 → 25 GeV	12 GeV → 100 TeV
QGSP_BERT_HP	HP	Bertini	LEP	QGSP
Protons		0 → 9.9 GeV	9.5 → 25 GeV	12 GeV → 100 TeV
Neutrons	0 → 20 MeV	19.9 MeV → 9.9 GeV	9.5 → 25 GeV	12 GeV → 100 TeV
π, K		0 → 9.9 GeV	9.5 → 25 GeV	12 GeV → 100 TeV

Table 7.2: Summary of the Hadronic Physics Models used in the different Geant4 Physics Lists. The Physics Lists marked with * have been manually modified respect to the ones usually distributed by the Geant4 collaboration, in order to insert the HP Models for neutron already present in the other two lists.

- standard Elastic Scattering for hadrons (G4HadronElasticPhysics).

For Double Chooz muon simulations (see Section 7.7.2), also the process for μ^- capture will be activated (G4MuonMinusCaptureAtRest).

FLUKA

FLUKA has been often used to describe underground muon interactions and evaluate their products [123]. A description of physics models adopted in FLUKA can be found in [115] and [126]. About hadron interactions, FLUKA forecasts just one standard combination of models, covering a large energy range. In particular, different physical models, or event generators, are responsible for the various aspects of particle production at different energies. High-energy hadronic interactions are described based on the dual parton model followed by a preequilibrium-cascade model. In addition, models for nuclear evaporation, breakup of excited fragments, and γ deexcitation treat the disintegration of excited nuclei. Hadronic interactions of photons are simulated in detail from threshold up to TeV energies. For nuclei up to copper, measured photonuclear cross sections in the low-energy region are used. The implementation of hadronic interactions of muons has been shown to give reliable predictions for the MACRO experiment [127]. For neutrons with energy lower than 20 MeV, FLUKA uses its own neutron cross section libraries, containing more than 200 different materials, selected for their interest in physics, dosimetry and accelerator engineering and derived from the most recently evaluated data.

In the FLUKA input it is possible to set the defaults suitable for a specified kind of problems. For my purpose, I chose the PRECISION one, activating:

- ElectroMagnetic FLUKA: transport of electrons, positrons and photons;
- Rayleigh scattering and inelastic form factor corrections to Compton scattering;
- Detailed photoelectric edge treatment and fluorescence photons;
- Low-energy neutron transport on down to thermal energies (high energy neutron threshold at 20 MeV);
- Fully analogue absorption for low-energy neutrons;
- Particle transport threshold set at 100keV, except neutrons;
- Multiple scattering threshold at minimum allowed energy, for both primary and secondary charged particles;
- Delta ray production on with threshold 100keV;
- Restricted ionisation fluctuations on, for both hadrons/muons and EM particles;
- Heavy particle bremsstrahlung with explicit photon production above 300keV;
- Muon photonuclear interactions with explicit generation of secondaries;
- Heavy fragment transport activated.

In addition, the threshold for the electrons and δ -rays production and transportation is set at 8 MeV (nuclear reactions below this threshold are not possible) and for photons at 1 MeV; this allows to speed up the simulations, avoiding the tracking of the enormous amount of low energies gammas and electrons produced.

The two options MUPHOTON allowing muon photonuclear interactions and PHOTONUC allowing gamma interactions with nuclei are also activated. In order to achieve reasonable results for residual nuclei production the Evaporation and the Coalescence module must be activated. The Evaporation treatment accurately describes the production of residual nuclei. The Coalescence mechanism describes the emission of energetic light fragments.

7.5 Cosmogenic neutron and isotope simulations in Borexino

As already explained, we want to perform simulations by the two codes FLUKA and Geant4. As explained in Section 3.2, the Borexino Monte Carlo code, G4Bx, is based on Geant4 and has been implemented and developed through several years by many members of the Borexino Collaboration. Clearly, the modification and the implementation of necessary tools for cosmogenic simulations has been prompter for the Geant4 side than for the FLUKA side.

In order to compare the different MC codes and the data, we decided to consider as observables the following variables:

- * the cosmogenic isotope and the neutron capture rates;

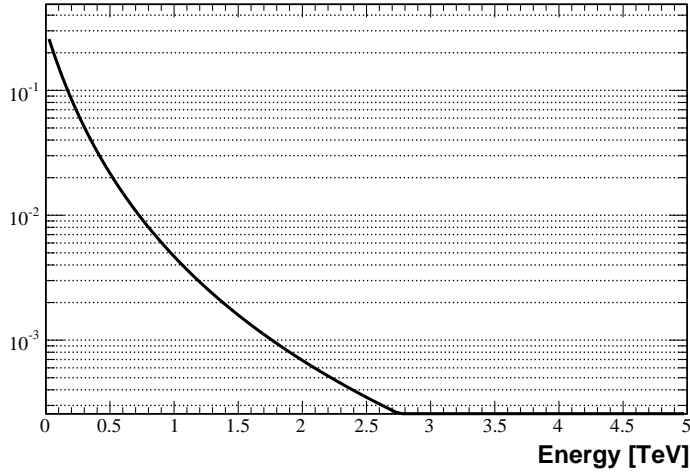


Figure 7.6: Energy spectrum of muons surviving underground obtained from Eq. 7.8 for $\gamma=3.7$, $\epsilon=0.618$, $\beta=0.383$ and $h=3.8$ km w.e..

- * the neutron capture time;
- * the neutron capture multiplicity for a muon;
- * the lateral distance between the neutron capture and the parent muon track.

Trying to minimize the complexity and to maximize the reliability of the simulations, two choices have been taken:

- * to simulate a cylindric muon beam with a vertical and downward direction on the top of Borexino;
- * to reproduce the quoted underground energy spectrum for cosmic muons.

7.5.1 The muon spectrum underground at LNGS

As shown in Section 7.1, the muon energy spectrum underground is done by:

$$\frac{dN}{dE_\mu} = \text{const} \cdot [E_\mu + \epsilon(1 - e^{-\beta h})]^{-\gamma}. \quad (7.8)$$

In particular, as calculated in [118], for $\gamma=3.7$: $\epsilon=0.618$ and $\beta=0.383$. At National Laboratories of Gran Sasso (LNGS), $h=3.8$ km w.e..

From Eq. 7.8, the average underground muon energy at depth h is:

$$\langle E_\mu \rangle = \frac{\epsilon(1 - e^{-\beta h})}{\gamma - 2} \quad (7.9)$$

and its asymptotic value is $\epsilon/(\gamma - 2)$. At great depths h , the underground muon energy spectrum given by Eq. 7.8 is almost flat for $E \ll \langle E_\mu \rangle$, and then decreases with energy.

In order to check the present knowledge of the spectral index and in general of the spectral shape of cosmic muons underground, some investigations in the literature about the two variables spectral index γ and mean muon energy $\langle E_\mu \rangle$ have been necessary.

Measurements of the spectral index

The spectral index of surviving underground muons has been measured by several experiments in last years. In particular, at LNGS we can profit of two measurements:

- * from the Large Volume detector (LVD) [119]: $\gamma_p + 1 = 2.77 \pm 0.05$ at sea level;
- * from the Monopole Astrophysics and Cosmic Ray Observatory (MACRO):
 - in [120]: $\gamma_p + 1 = 2.78 \pm 0.01$ at sea level;
 - in [97]: $\gamma = 3.79 \pm 0.02_{\text{stat}} \pm 0.11_{\text{sys}}$ underground;

The measurements are in agreement and seem to be well reproduced by the theoretical expectations.

Measurements of the mean muon energy at LNGS

Again, about the mean muon energy of surviving muons at LNGS we can profit of measurement done by MACRO experiment [97]: $\langle E_\mu \rangle = (270 \pm 3_{\text{stat}} \pm 18_{\text{sys}}) \text{ GeV}$.

In addition, in [121] through the Monte Carlo code called MUSUN, the muon mean energy is quoted as about 273 GeV at LNGS.

Finally, using the parametrization in Eq. 7.8 and the parameters from [118] for $\gamma = 3.7$, the evaluated $\langle E_\mu \rangle$ is 275 GeV. So this description has been chosen for generating muons (see Figure 7.6).

7.5.2 Simulation procedure

The main difference between Geant4 and FLUKA is the treatment of the output informations:

- * In Geant4 it is possible to follow a particle from its birth to its death. In particular, considering the present simulation planning, the simulated muon is tagged with an event_id being the same for all its products; each muon product will be also identified from the birth (vertex) to the death through the track_id.
- * In FLUKA is quite hard to follow a particle from the beginning to the end for two fundamental reasons:
 - the code has been written to produce global averaged informations about a particle beam and is not forecasting an internal user intervention or modification;
 - every time a particle undergoes an inelastic scattering, the track_id changes.

This required an effort in order to enter in the code and modify it, saving all the useful informations for the study to be performed (like neutron-muon distance or multiplicity).

Moreover considering the low cross sections for the cosmogenic isotopes production (about $\mu\text{barn}\text{-mbarn}$ [69]), it is necessary to simulate a big number of incident muons (some 10^7) for each MC code and for each Physics List. This implies the necessity to develop some tools speeding up the simulations. In particular, we decided to:

1. not to generate the optics;
2. not to create the PMTs in the simulations;
3. to save in the output file only the interesting products, radioactive isotopes and neutron.

This means that we will not have any information about the reconstructed energy and position of muon products.

Geant4

As discussed in Section 7.4.3, eight Physics Lists for the Geant4 side must be tested. For this purpose I used the Geant4 generator G4Gun, simulating μ^+ and μ^- in a ratio $R_\mu = \frac{N_{\mu^+}}{N_{\mu^-}} \simeq 1.38$, as measured by the OPERA experiment [128].

The simulation procedure is organized as following:

1. construction of the standard Borexino detector (see Section 3.2.1) without PMTs;
2. construction of the hall C with rock and concrete;
3. generation of muons on a circle of 7 m radius, positioned at (0,0,14) m respect to the Borexino vessel center, corresponding to about (0,0,22) m respect to the ground of the hall C. In this way the muon events born in the rock, allowing the hadronic showers;
4. activation of electromagnetic and nuclear decay Physics Lists;
5. activation of an hadronic Physic List;
6. recording of cosmogenic isotopes produced in the IV (the so called Zone I of the detector);
7. recording of cosmogenic neutron captures in the IV.

The output binary files are read by a macro allowing to extract useful informations and producing a root file containing all the recorded informations for each event¹.

FLUKA

The Borexino materials are described as in Geant4. The detector geometry is described in a simplified way, through concentric spheres:

- a $30 \times 30 \times 25$ m³ cube for the rock (composition from [129]);
- a $30 \times 30 \times 0.3$ m³ cube for the concrete layer (composition from [129]);
- a cube $25 \times 25 \times 24$ m³ for the hall C, containing air;
- a cylinder+hemisphere for the water tank;

¹Note that in Geant4 the event_id variable flags the parent muon and all its products, allowing for example to extract informations about neutron lateral distance or multiplicity.

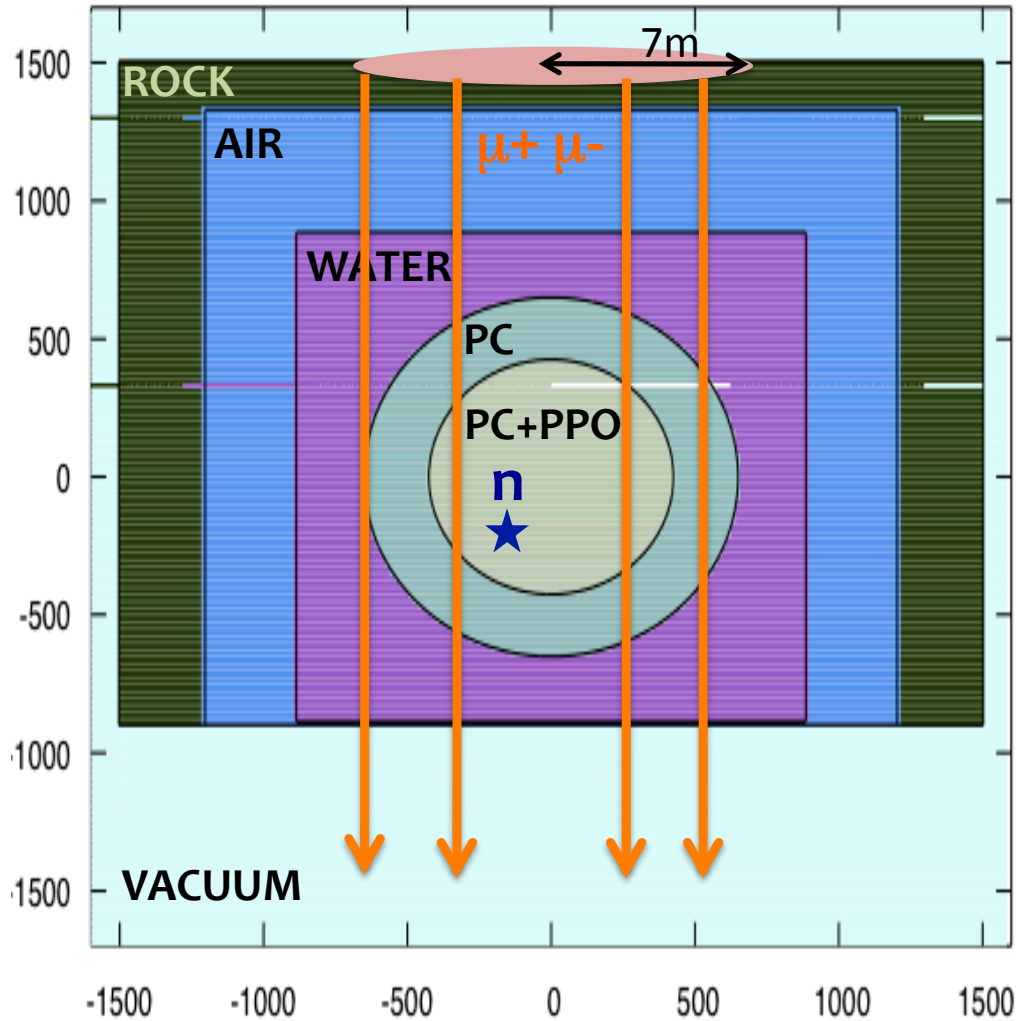


Figure 7.7: Borexino geometry as realized in FLUKA. Measure unit is cm. Colors correspond to different materials, from outside to inside: vacuum, rock, air, water, Pseudocumene, PC+PPO. A scheme of the muon beam position and direction is also shown. Neutron captures (blue star) are recorded only if they happen in the Inner Vessel.

- a sphere of 6.85 m radius for the SSS, containing the buffer liquid;
- a sphere of 4.25 m radius for the Inner Vessel, containing PC+PPO.

FLUKA gets its input mainly from a simple file. It offers a rich choice of options for scoring most quantities of possible interest and for applying different variance reduction techniques, without requiring the users to write a single line of code. For the present simulations it is necessary to manually introduce two descriptions:

1. the muon spectrum underground;
2. the source position on a circle centered in (0,0,22) m from the ground.

This has been possible using the user routine source.f, available for users and allowing to describe particular primary spectra, source distribution, beam direction and so on. The

command SOURCE in the FLUKA input allows to activate this user routine. A scheme of the realized Borexino geometry with the beam position and direction is shown in Figure 7.7.

In order to count:

1. the number of crossing muons;
2. the number of produced isotopes in the Inner Vessel;
3. the number of neutron captures in the Inner Vessel.

the two user routines mgdraw.f and usrrnc.f, available for users and allowing to directly access to the particle tracks, have been used. The commands USERDUMP and USERWEIG in the FLUKA input allow to activate these user routines. The output informations are recorded in an ASCII file and read by a perl macro, written for the purpose.

7.5.3 Geant4 and FLUKA simulation results and comparison with data

Based on the input described in previous sections, simulations in Geant4, testing eight Hadronic Physics Lists, and in FLUKA have been performed.

The cosmogenic rates

Rate results for cosmogenic products are summarized in Table 7.3. About Geant4, results obtained with and without the activation of the Light Ion (LI) Physics List are perfectly compatible; for this reason just the results with the activation of LI Physics List are shown in the table.

In the following, the results on the specific production rates are presented.

- * Results with and without the IonPhysics activated are very similar.
- * ^{11}C : regardless of the used hadronic model, the Geant4 rates are significantly smaller ($\sim 1/4$) than the measured one; FLUKA predicts a higher rate, but still far from the real one ($\sim 1/2$).
- * ^{10}C : a part from FTF_BIC_HP, the Geant4 and FLUKA rates are smaller than the real one ($\sim 70\%$).
- * ^{11}Be : the QGSP_BIC_HP well reproduces the measured rate; results are strongly dependent on the model.
- * ^{12}B : the Geant4 Physics Lists predict almost the same rate, corresponding to about 45% of the measured one; FLUKA prediction is closer to the real value (70%).
- * $^{8}\text{He} + ^{9}\text{C} + ^{9}\text{Li}$: QGSP_BIC_HP and FTF_BERT_HP predict the same rate; regardless of the used hadronic model, the Geant4 rates are significantly smaller ($\leq 1/2$) than the measured one; FLUKA prediction is about 90% of the real value.
- * $^{8}\text{B} + ^{6}\text{He} + ^{8}\text{Li}$: regardless of the used hadronic model, the Geant4 rates are significantly smaller ($\leq 1/2$) than the measured one; on the contrary, FLUKA prediction are more than twice the real value.

Cosmogenic [cpd/100 t]	QGSP_BIC (2593 d)	QGSP_BERT (3027 d)	FTF_BIC (2667 d)	FTFP_BERT (2816 d)	FLUKA (1913.9 d)	Data
^{11}C	4.44 ± 0.03	6.21 ± 0.03	6.9 ± 0.03	6.12 ± 0.03	12.76 ± 0.05	28 ± 1
^{10}C	0.201 ± 0.005	0.384 ± 0.007	0.490 ± 0.009	0.373 ± 0.006	0.384 ± 0.008	0.55 ± 0.15
^{11}Be	0.035 ± 0.002	$(3.8 \pm 0.7) \cdot 10^{-3}$	0.052 ± 0.003	$(1.3 \pm 0.4) \cdot 10^{-3}$	0.018 ± 0.001	0.035 ± 0.006
^{12}B	0.475 ± 0.008	0.520 ± 0.008	0.521 ± 0.008	0.468 ± 0.007	0.79 ± 0.01	1.29 ± 0.06
$^{8}\text{He} + ^{9}\text{C} + ^{9}\text{Li}$	0.018 ± 0.008	0.035 ± 0.008	0.062 ± 0.009	0.035 ± 0.008	0.108 ± 0.001	0.19 ± 0.05
$^{8}\text{B} + ^{6}\text{He} + ^{8}\text{Li}$	0.130 ± 0.004	0.108 ± 0.004	0.217 ± 0.005	0.101 ± 0.003	1.389 ± 0.001	0.57 ± 0.07
Neutrons [cpd/278 t] sim/data	157.3 ± 0.2	177.4 ± 0.2	131.6 ± 0.2	168.8 ± 0.2	186.8 ± 0.3	$246.4 \pm 5.5_{\text{sta}} \pm 4.4_{\text{sys}}$

Table 7.3: Rate results for cosmogenic products in Borexino obtained by G4Bx with different hadronic Physics Lists and by FLUKA. For each of the Geant4 Physics List, the HP model and Light Ion Physics List are activated. Last line represent the ratio between the neutrons rate obtained from the simulation and the real one. The period in days indicated in the second line corresponds to the simulated data taking time.

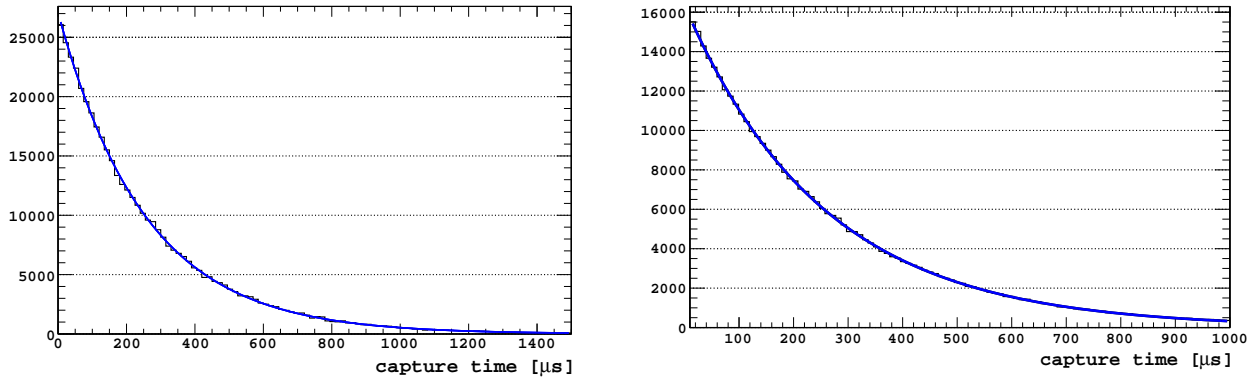


Figure 7.8: Neutron capture time in the Borexino scintillator for the QGSP_BIC_HP_LI Physics List (left) and FLUKA (right), fitted with an exponential function. The constant value returned are $\tau_{\text{G4}} = (254.9 \pm 0.4) \mu\text{s}$ and $\tau_{\text{FL}} = (253.9 \pm 0.5) \mu\text{s}$, respectively.

* **Neutrons:** regardless of the used Geant4 hadronic model, the predicted neutron rate is smaller ($\leq 70\%$) than the measured one; Physics Lists using Bertini Cascade predict a bigger rate than the Binary Cascade; FLUKA predicts a slightly higher rate, still far from the real value (77%).

Summarizing, the five MC tested models (4 for Geant4 and 1 for FLUKA) predict neutron rates significantly lower than the measured one (see last line in Table 7.3).

The observables:

- neutron capture time;
- neutron lateral distance, evaluating the distance between the neutron capture point and the muon track;
- neutron multiplicity, evaluating the number of produced neutrons per parent muon.

have been also considered.

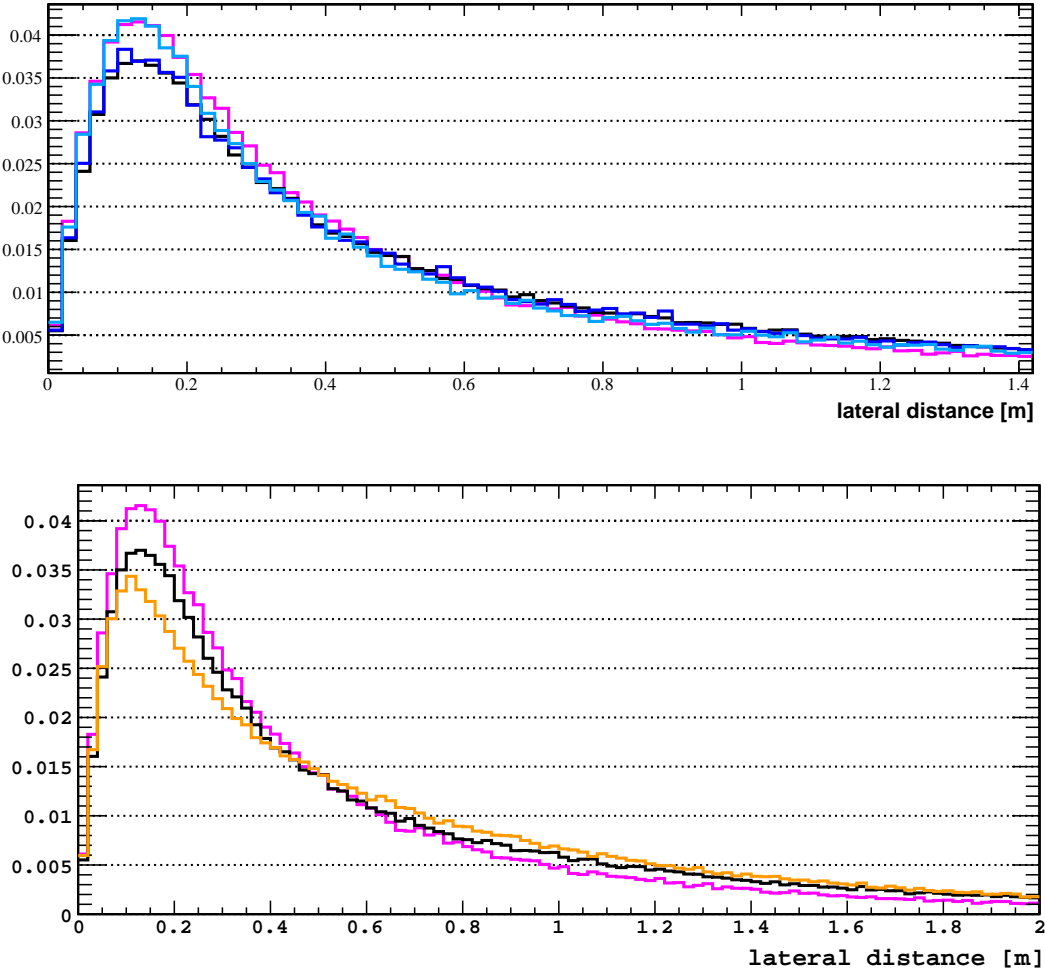


Figure 7.9: Top: Neutron lateral distance for the Physics Lists: QGSP_BIC_HP (pink), QGSP_BERT_HP (black), FTF_BIC_HP (light blue), FTFP_BERT_HP (blue). Bottom: Comparison of the neutron lateral distance obtained through FLUKA (orange), Geant4-QGSP_BIC_HP (pink) and Geant4-QGSP_BERT_HP (black).

The neutron capture time

The neutron capture time has been estimated for the QGSP_BIC_HP_LI Physics List (see Figure 7.8) and for FLUKA and correspond to $\tau_{\text{G4}} = (254.9 \pm 0.4) \mu\text{s}$ and $\tau_{\text{FL}} = (253.9 \pm 0.5) \mu\text{s}$, respectively. These values are in good agreement with the measured one: $\tau = (257.4 \pm 2.4) \mu\text{s}$ [80].

The neutron lateral distance

First, the lateral distance for the four Hadronic Physics Lists and FLUKA have been compared. As shown in the top panel of Figure 7.9, the 4 Physics Lists predict slightly different lateral distance. In particular, the dependence on Bertini or Binary Cascade is evident. For all the Physics Lists the distribution peak is around 13 cm. The mean distance values are listed in Table 7.4. Once again the dependence on Bertini or Binary

Cosmogenic	QGSP_BIC	QGSP_BERT	FTF_BIC	FTFP_BERT	FLUKA
Lat. distance [m]	0.460±0.001	0.527±0.001	0.491±0.001	0.524±0.001	0.567±0.001
Neut. multiplicity	4.04 ± 0.03	4.38 ± 0.03	3.58 ± 0.03	4.37 ± 0.03	4.15 ± 0.07

Table 7.4: Mean values of multiplicity and lateral distance for cosmogenic neutrons in the Borexino IV, obtained through FLUKA and Geant4 with different Hadronic Physics Lists (for each of them the HP model and Light Ion Physics List are activated).

Cascade model is evident: the Bertini model predicts a slightly bigger mean lateral distance. The FLUKA lateral distance distribution is shown in the bottom panel of Figure 7.9, compared with two Geant4 Physics Lists. A slight difference is evident. The FLUKA mean distance value is listed in Table 7.4.

The comparison with the measured distance distortion is not trivial. This is due to the resolution and systematic effects of the spatial reconstruction in Borexino. The position reconstruction algorithm works well for neutron clusters belonging to muon events that are not showering and generate normally only a low number of neutrons in the detector. In general, only a slight systematic shift of the reconstructed neutron positions to the center of the detector is observed. On the contrary, showering muon events that generate a large number of neutrons, produce also a large amount of scintillation light. This leads to two effects, which deteriorate the efficiency of the position reconstruction algorithm:

1. large after-pulses: the neutron capture peaks are superimposed on the tail of the after-pulse hits, affecting the position reconstruction algorithm as there is no way to discriminate γ -ray hits from after-pulse hits.
2. a fraction of the ID electronics boards, preferentially located on the half detector closer to the muon track, can be saturated and become unavailable for neutron detection. This decrease of detector uniformity aggravates the effect of after-pulse hits on the position reconstruction.

As well described in [80], the measured lateral distance is affected by different effects:

1. the muon lateral resolution σ_μ ;
2. the neutron mean free path λ ;
3. the uncertainty in the reconstruction of the light barycenter of the 2.22 MeV γ -rays from neutron capture (σ_n).

The muon lateral resolution function is composed of a Gaussian uncertainty σ and a constant asymmetric offset μ that can be associated with radial shifts of the reconstructed tracks. For the neutron, σ_n is dominated by the reconstruction uncertainty, the mean free path of the γ -ray ($\sigma_\gamma \simeq 23$ cm) and the diffusion of the thermalized neutron before capture ($\sigma_{\text{diff}} \simeq 4$ cm [130]). In order to compare the simulation results with the data, I applied the following techniques:

- only neutrons within 3.7 m and muons with impact parameter less than 5 m are considered in the data and simulations samples;

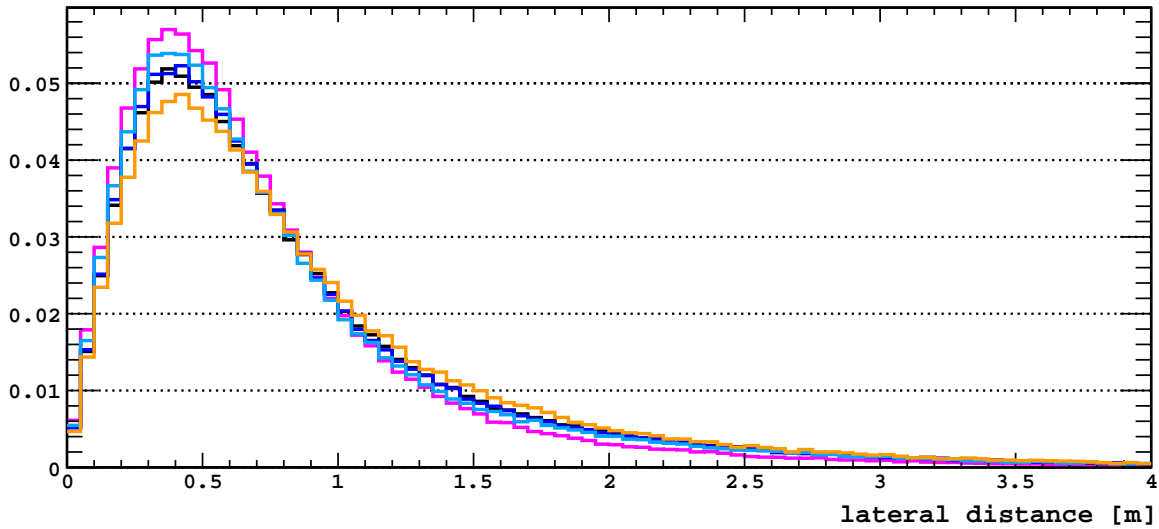


Figure 7.10: Neutron lateral distance for the Geant4 Physics Lists QGSP_BERT_HP_LI (black), QGSP_BIC_HP_LI (pink), FTF_BIC_HP_LI (light blue) and FTFP_BERT_HP (blue) and FLUKA (orange). Neutrons are selected within 3.7 m and muons with impact parameter within 5 m. The lateral distance is smeared as explained in the text.

- the neutron capture positions and the muon impact parameter have been smeared in order to reproduce data. In particular, the simulated neutron radial position has been smeared by a quantity gaussianly distributed, with a $\sigma=36$ cm; the muon impact parameter is modified by a constant inward offset of 24 cm and smeared by a quantity gaussianly distributed, with a $\sigma=35$ cm.

The resulting distributions for each simulation model are shown in Figure 7.10. The comparisons with data are shown in the top panel of Figure 7.11. About Geant4 models, the agreement data/BERT is perfect at low distance (< 2.5 m); a clean sample of neutrons with lateral distance longer than 2.5 m is not available for the comparison. About FLUKA the agreement with data is slightly worse (see bottom panel of Figure 7.11).

In Table 7.5 the mean values of the neutron lateral distance is shown for the subsample of data and Monte Carlo events used for the comparison.

Cosmogenic	QGSP_BIC	QGSP_BERT	FTF_BIC	FTFP_BERT	FLUKA	Data
Lat. dist. [m]	0.748 ± 0.001	0.856 ± 0.001	0.824 ± 0.001	0.848 ± 0.001	0.850 ± 0.002	0.789 ± 0.006
Neut. mult.	2.66 ± 0.04	2.78 ± 0.04	2.33 ± 0.03	2.81 ± 0.04	2.71 ± 0.09	2.49 ± 0.06

Table 7.5: Comparison between the mean values of multiplicity and lateral distance for cosmogenic neutrons selected in the Borexino FV with particular cuts (see text for details) for FLUKA, Geant4 with different Hadronic Physic Lists and Borexino data.

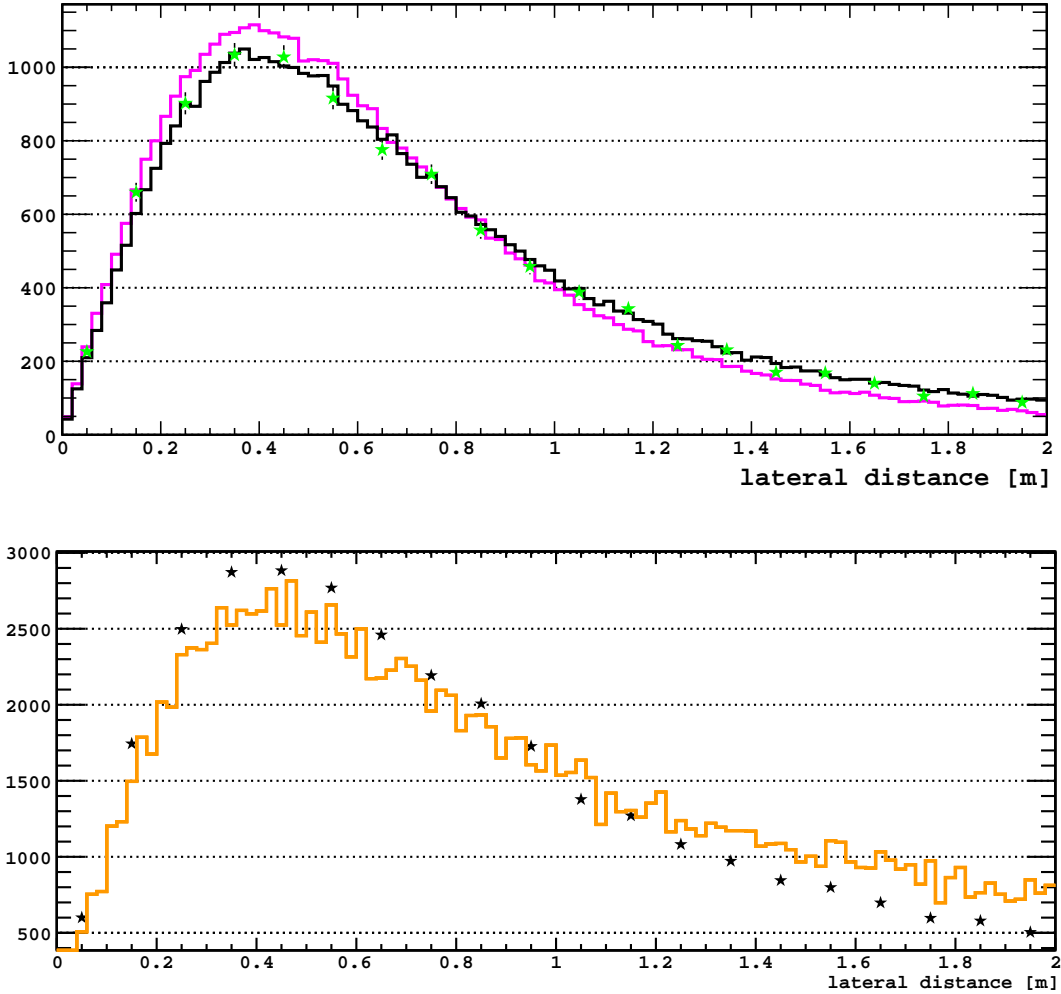


Figure 7.11: Top: Comparison of the lateral distance for the Physics Lists QGSP_BERT_HP_LI (black line) and QGSP_BIC_HP_LI (pink line) with data (green dots). Bottom: Comparison of the lateral distance for FLUKA results (orange line) and with data (dots).

The neutron multiplicity

The different Geant4 Physics Lists and FLUKA give very similar results for the neutron multiplicity (see Figure 7.12). In particular, the mean value of the multiplicity is between 3.6 and 4.4 (see Table 7.4 for details).

In order to compare the multiplicity with the measured one, I chose the Geant4-QGSP_BERT_HP_LI Physics List and FLUKA. On the data, neutrons multiplicities are affected by the uncorrelated background, rejected applying an energy-cut², that also erases neutrons near the vessel. For this reason the multiplicity spectrum on the data is obtained selecting just neutron events detected in the FV (radius < 3 m), with a 200 μ s delay after the neutron gate start and with at least one cluster. Since the neutron gate starts about 16 μ s after the muon, the global delay of selected neutrons respect to the parent muon is

²Neutrons have to be in an area limited by two straight lines in the (nhits,empty_boards) plane. The first line is defined by the two intersection points with the axes: nhits=500 and empty_boards=100. The second line is defined by the two intersection points with the axes: nhits=900 and empty_boards0=270.

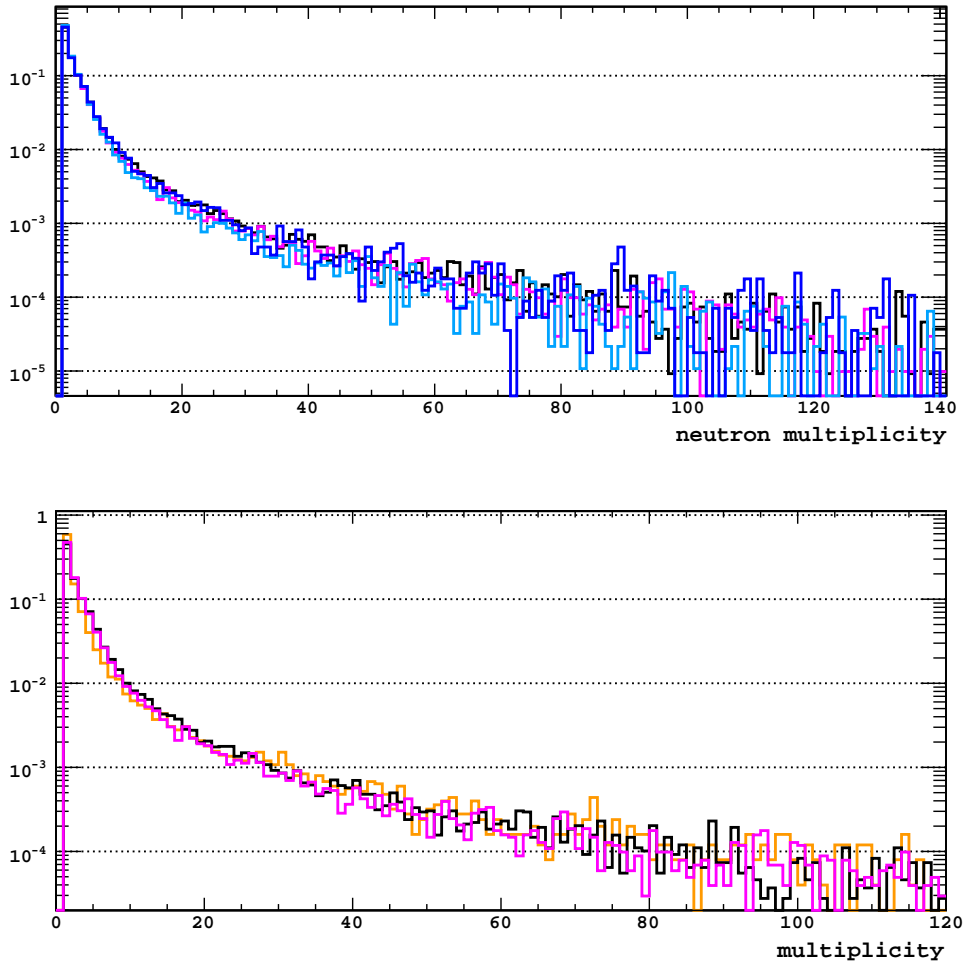


Figure 7.12: Top: Neutron multiplicity for the Physics Lists: QGSP_BIC_HP (pink), QGSP_BERT_HP (black), FTF_BIC_HP (light blue), FTFP_BERT_HP (blue). Bottom: Comparison of the neutron multiplicity obtained through FLUKA (orange), Geant4-QGSP_BIC_HP (pink) and Geant4-QGSP_BERT_HP (black).

about $216\text{ }\mu\text{s}$. Simulated neutrons are selected with the same criteria. In Figure 7.13 the comparisons data/Geant4 and data/FLUKA are shown. The agreement is nice. In particular, the mean multiplicity is 2.49 ± 0.06 for data, 2.78 ± 0.04 for QGSP_BERT_HP_LI and 2.71 ± 0.09 for FLUKA (see Table 7.5).

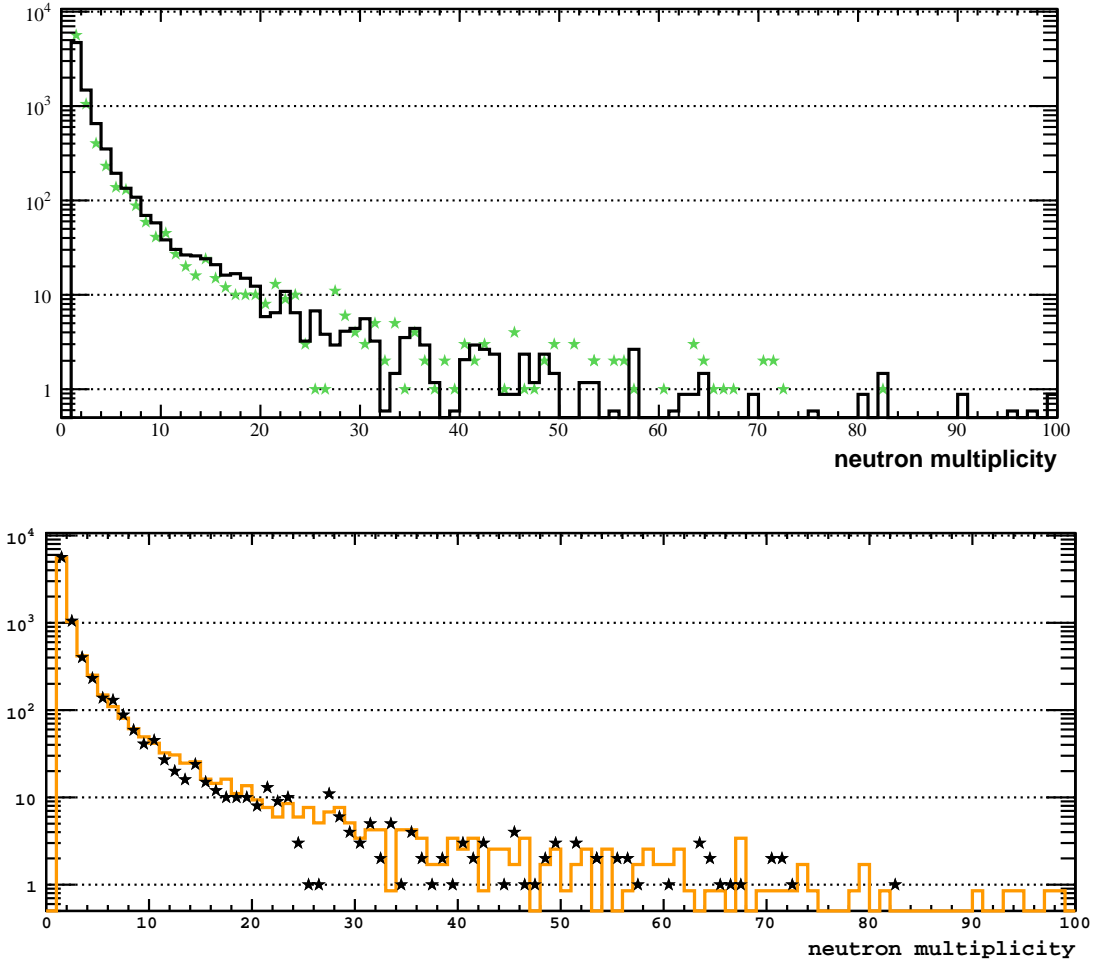


Figure 7.13: Top: Comparison of the neutron multiplicity for the Physics Lists QGSP_BERT_HP_LI (black line) and data (green dots) in the Borexino Fiducial Volume. Bottom: Comparison of the neutron multiplicity obtained with FLUKA (orange line) and data (black dots) in the Borexino Fiducial Volume.

7.6 Simulations of the CNGS muon beam in Borexino

The CERN Neutrinos to Gran Sasso (CNGS) facility in collaboration with the OPERA detector aims at directly detecting ν_μ to ν_τ oscillations [131]. An intense muon-neutrino beam ($10^{17} \nu_\mu/d$) is generated at CERN and directed over 732 km towards the OPERA detector (see Figure 7.14), located in the Hall C at LNGS (see Figure 2.2). The CNGS neutrino beam produces muons in the rock upstream of Borexino via charged current interactions of ν_μ [80]. Further charged and neutral current ν_μ interactions occur inside the detector. These events are a background to neutrino analysis and must be removed from the data set. At the same time they constitute a sample of muons of known direction and we use them to determine Borexino muon tagging efficiency. In addition, since Borexino is just in front of the OPERA detector, we exploited the on-time events common to the two experiments to test the Borexino tracking algorithms for horizontal tracks.

The mean neutrino energy is about 18 GeV and the mean energy of the induced muons is about 16 GeV, much smaller than the cosmic muon one. The energy spectrum of CNGS



Figure 7.14: Picture of the OPERA detector situated at LNGS in the first part of the Hall C; the second part of the Hall C hosts CTF and Borexino.

muons is shown in Figure 7.15. The expected number of muons per charged current neutrino interaction is one, with only 0.3% of the interactions producing more than one muon. At the LNGS, the neutrino beam arrives with an incline of 3.5° below the horizon, corresponding to a zenith angle of 93.5° ; its width is more than one kilometer.

In order to try a validation of the Monte Carlo codes for lower energy muons through a comparison with Borexino data, I simulated the CNGS muon beam with FLUKA and Geant4, recording the produced isotopes and neutrons. The procedures and the detector descriptions for the two simulation codes are identical to those used for cosmic muons. The only different things are:

- the muon energy spectrum;
- the muon beam start position: circle of 7 m radius, positioned at (15,0,0) m respect to the Borexino vessel center (muon events born in the rock, allowing the hadronic showers);
- the muon beam direction: in the Borexino coordinates, $\theta=93.5^\circ$.

Results on isotope and neutron rates per crossing muon are shown in Table 7.6. As for cosmic muon simulations:

- * the ^{11}C rate predicted by FLUKA is about twice the one predicted by Geant4 (regardless from the Hadronic Physics List);
- * the neutron rate predicted by FLUKA is about 1.2 times the one predicted by Geant4 (regardless from the Hadronic Physics List).

On the contrary, a part from $^8\text{B}+^6\text{He}+^8\text{Li}$ and $^8\text{He}+^9\text{C}+^9\text{Li}$ rates, the predictions for the other isotopes rates show a better agreement between FLUKA and Geant4. This can be

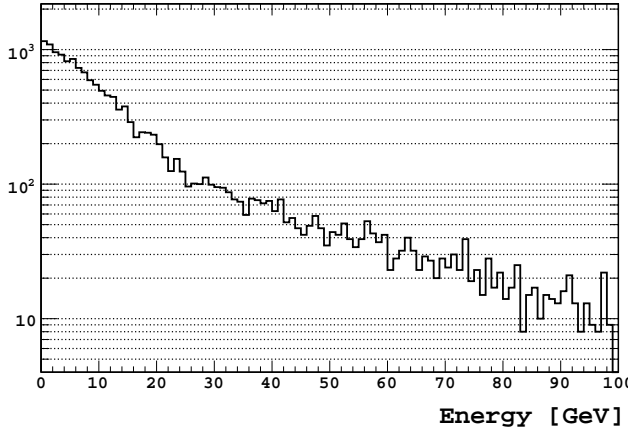


Figure 7.15: Energy spectrum of CNGS muons in Hall C at LNGS, from Monte Carlo simulations [132].

Cosmogenic [cpμ/100 t]	QGSP_BIC 10980272 μ _{cross}	QGSP_BERT 23120269 μ _{cross}	FTF_BIC 18492083 μ _{cross}	FTFP_BERT 24773391 μ _{cross}	FLUKA 64545 μ _{cross}
¹¹ C	$(1.75 \pm 0.02) \cdot 10^{-4}$	$(1.90 \pm 0.02) \cdot 10^{-4}$	$(2.21 \pm 0.02) \cdot 10^{-4}$	$(2.11 \pm 0.02) \cdot 10^{-4}$	$(4.75 \pm 0.06) \cdot 10^{-4}$
¹⁰ C	$(4.9 \pm 0.4) \cdot 10^{-6}$	$(8.6 \pm 0.4) \cdot 10^{-6}$	$(1.14 \pm 0.05) \cdot 10^{-5}$	$(0.99 \pm 0.04) \cdot 10^{-5}$	$(1.08 \pm 0.05) \cdot 10^{-5}$
¹¹ Be	$(1.4 \pm 0.2) \cdot 10^{-6}$	$(0.7 \pm 0.2) \cdot 10^{-6}$	$(1.5 \pm 0.2) \cdot 10^{-6}$	$(6 \pm 1) \cdot 10^{-7}$	$(1.9 \pm 0.2) \cdot 10^{-6}$
¹² B	$(2.00 \pm 0.02) \cdot 10^{-4}$	$(2.20 \pm 0.02) \cdot 10^{-4}$	$(2.10 \pm 0.02) \cdot 10^{-4}$	$(2.04 \pm 0.02) \cdot 10^{-4}$	$(1.35 \pm 0.02) \cdot 10^{-4}$
⁸ He + ⁹ C + ⁹ Li	$(2.9 \pm 0.3) \cdot 10^{-6}$	$(1 \pm 1) \cdot 10^{-6}$	$(1.3 \pm 2) \cdot 10^{-6}$	$(1 \pm 2) \cdot 10^{-6}$	$(0.7 \pm 0.6) \cdot 10^{-4}$
⁸ B + ⁶ He + ⁸ Li	$(1.4 \pm 0.2) \cdot 10^{-5}$	$(3.55 \pm 0.07) \cdot 10^{-5}$	$(3.79 \pm 0.09) \cdot 10^{-5}$	$(3.79 \pm 0.09) \cdot 10^{-5}$	$(0.7 \pm 0.6) \cdot 10^{-5}$
Neutrons [cpμ/278 t]	$(6.93 \pm 0.03) \cdot 10^{-3}$	$(6.98 \pm 0.02) \cdot 10^{-3}$	$(6.34 \pm 0.02) \cdot 10^{-3}$	$(6.34 \pm 0.02) \cdot 10^{-3}$	$(7.84 \pm 0.02) \cdot 10^{-3}$

Table 7.6: Rate results for CNGS muon interaction products obtained by FLUKA and G4Bx with different hadronic Physics Lists. For each of Geant4 Physics List, the HP model and Light Ion Physics List are activated. The numbers in the second line indicate the number of simulated CNGS muons, crossing the SSS.

CNGS	QGSP_BIC	QGSP_BERT	FTF_BIC	FTFP_BERT	FLUKA
Lat. distance [m]	0.438 ± 0.001	0.468 ± 0.001	0.451 ± 0.001	0.468 ± 0.001	0.453 ± 0.002
Neut. multiplicity	1.89 ± 0.01	1.89 ± 0.01	1.73 ± 0.01	1.97 ± 0.01	1.59 ± 0.02

Table 7.7: Mean values of multiplicity and lateral distance for neutrons from CNGS muons in the Borexino IV, obtained through FLUKA and Geant4 with different Hadronic Physics Lists.

related to the lower energy of the muon beam and to the consequent easier description of muon interactions.

In Figure 7.16, the neutron lateral distance and multiplicity are shown. Mean value for lateral distance and multiplicity are listed in Table 7.7. FLUKA predicts a slightly lower (15%) neutron multiplicity with respect to Geant4 Physics List, even if global distributions are quite in agreement. About lateral distance, as evident from top panel in Figure 7.16, Geant4 Physics Lists are perfect in agreement, instead FLUKA distribution is a little different. The mean values are in any case well compatible and they are reported

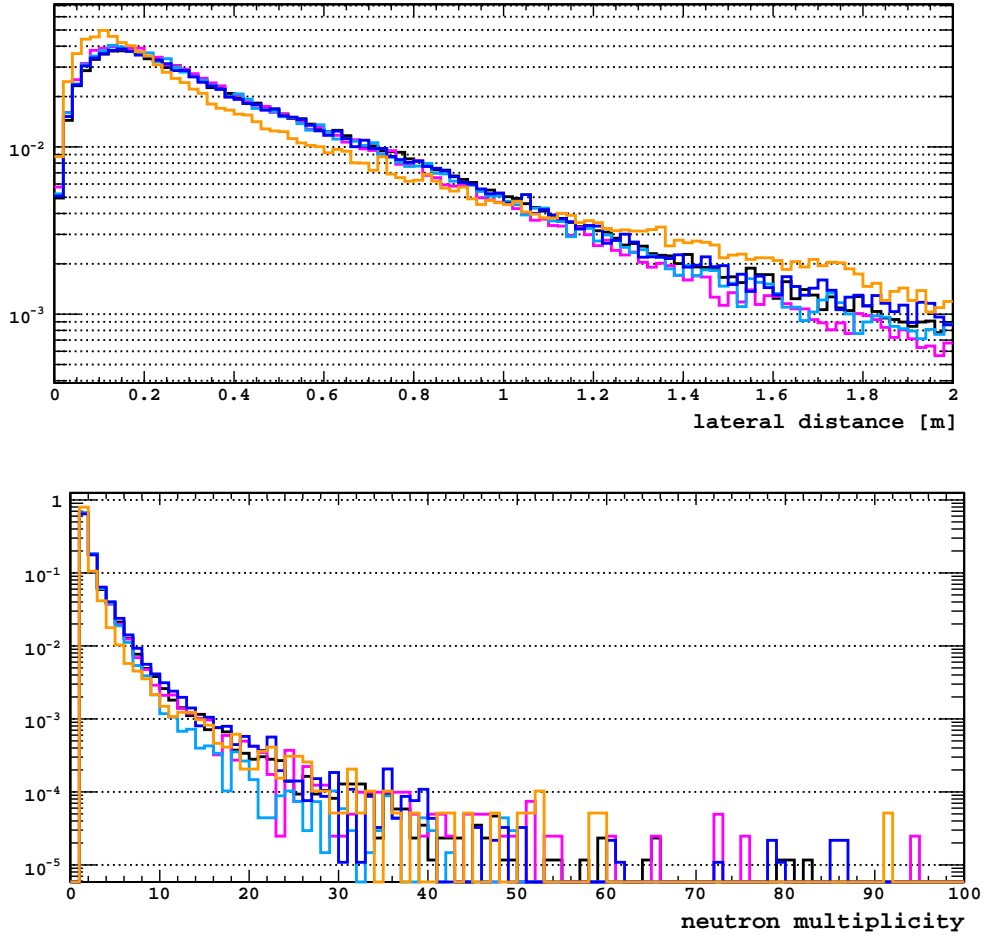
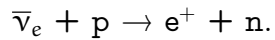


Figure 7.16: Top: Comparison of the neutron lateral distance for FLUKA (orange) and the Geant4 Physics Lists: GSP_BIC_HP (pink), QGSP_BERT_HP (black), FTF_BIC_HP (light blue), FTFP_BERT_HP (blue) in the Borexino IV. Bottom: Comparison of the neutron multiplicity obtained with FLUKA (orange), Geant4-QGSP_BIC_HP (pink) and Geant4-QGSP_BERT_HP (black), Geant4-FTF_BIC_HP (light blue), Geant4-FTFP_BERT_HP (blue) in the Borexino IV.

in Table 7.7. It is evident that the neutron multiplicity, due to the lower muon energy ($\langle E_{\mu, \text{CNGS}} \rangle \approx 16 \text{ GeV}$), is smaller (less than 50%) than the one for cosmic muons (see Table 7.4); instead, as expected, the lateral distance is very similar to the one related to cosmic muons.

7.7 Cosmogenic neutron and isotope simulations in Double Chooz

As described in Section 1.7, the signature for $\bar{\nu}_e$ detection in Double Chooz (DC) is done by the event coincidence following the inverse β -decay:



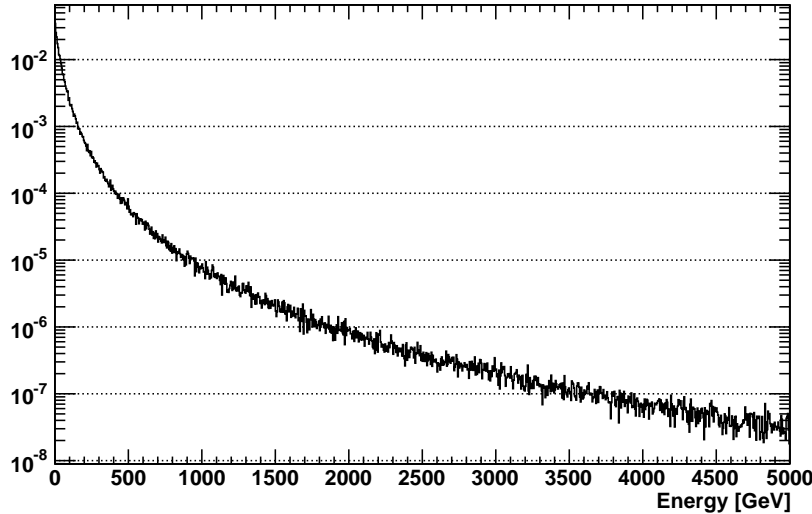


Figure 7.17: Energy spectrum of cosmic muons surviving underground at DC-Far site, obtained through MUSIC simulations [134].

The prompt event is represented by the e^+ annihilation and the delayed event by the neutron capture on Gadolinium ($\tau \simeq 30 \mu s$). Thanks to this strong signature, the detector does not need a huge cosmic rays protection: the DC far detector is located underground at 300 m w.e.. This implies a lower muon energy spectrum ($\langle E_\mu \rangle \simeq 60 \text{ GeV}$) and a higher cosmic muon flux ($\sim 10 \text{ Hz}$ of muons crossing the Gamma Catcher Vessel) with respect to deep underground experiments. This second aspect has two main consequences:

1. the expected cosmogenic rates are larger than in Borexino;
2. it is not possible (for evident Live Time exigences) the application of an after muon veto.

For $\bar{\nu}_e$ experiments, the only dangerous cosmogenic isotopes are ${}^9\text{Li}$ and ${}^8\text{He}$, since they can $\beta + n$ decay ($\text{BR}_{{}^9\text{Li}} \simeq 50\%$, $\text{BR}_{{}^8\text{He}} \simeq 16\%$) and mimic a signal coincidence. For this reason it is extremely important to determine the cosmogenic contamination in Double Chooz.

On the strength of my experience developed for the cosmogenic simulations in Borexino, I could apply the same procedure for DC.

In order to adapt the Geant4 and FLUKA scripts to the Double Chooz configuration, the main changes to perform involve:

- the muon spectrum underground;
- the detector geometry;
- the definition of materials.

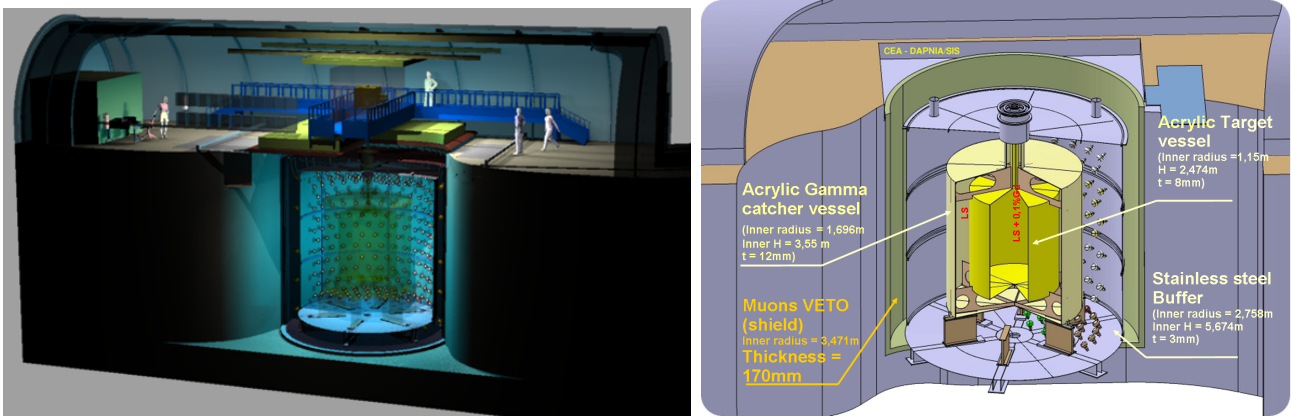


Figure 7.18: *Left:* Design of the Far Double Chooz detector site. *Right:* Double Chooz detector design.

7.7.1 The muon spectrum underground at DC-Far site

The energy spectrum of surviving muons at DC-Far site well known, thanks to accurate MUSIC simulations performed in the past [134]. Simulation results are shown in Figure 7.17. The mean energy is $\langle E_\mu \rangle \simeq 64$ GeV. I used this spectrum for producing primary particles in FLUKA and Geant4 codes. The used muon charge ratio is the sea level one:

$$R_\mu = \frac{N_{\mu^+}}{N_{\mu^-}} = 1.261 \pm 0.009 \quad [135].$$

7.7.2 Simulation procedure

As described in Section 1.7.1, the Double Chooz (DC) detector has a geometry concept very similar to the Borexino one, formed by concentric cylinders instead of spheres (see Figure 7.18). For my purpose I do not need to describe photomultipliers and optical properties of materials.

Geant4

The DC detector has been described using the standard solid volume G4Tub available in the Geant4 package. The cavern and the pit where the detector is located have been constructed too, using a combination of rotated half a tub for the cavern and a tub for the pit. The structure pit+cavern is contained in a G4Box of rock. The origin of the coordinate system is in the center of the Target. For details about dimensions and materials, see Table 7.8.

The muon beam origin (horizontal 4 m radius disk) is placed in the cavern rock, at $z=15$ m with respect to the Target center. The beam direction is vertical and downward.

As for Borexino simulations, the Electromagnetic, the Nuclear Decay Physics Lists and one of the Hadronic Physic Lists are activated. Cosmogenic isotopes and neutron captures are recorded only if generated in the Target. The output binary files are read by a dedicated macro allowing to extract useful informations concerning rates, neutron capture times, neutron lateral distance and so on.

Component	G4 Volume	Dimensions	Material
Rock	G4Box	12.3 m × 23 m × 12.3 m	Rock: $\rho=2.7 \text{ g/cm}^3$, SiO_2
Cavern	G4Tub (+rotation)	R=4.645m, H=20.0m	Air: $\rho=1.29 \cdot 10^{-3} \text{ g/cm}^3$, N(70%)+O(30%)
Pit	G4Tub	R=3.450 m, H=7.0 m	Air: $\rho=1.29 \cdot 10^{-3} \text{ g/cm}^3$, N(70%)+O(30%)
Tank	G4Tub	R=3.250 m, H=6.830 m	Stainless Steel: $\rho=7.87 \text{ g/cm}^3$, Fe(71%)+Cr(19%)+Ni(10%)
Muon veto	G4Tub	R=3.240 m, H=6.810 m	Mineral Oil + PPO(6 g/l): $\rho=0.821 \text{ g/cm}^3$
Stainless Steel Tank	G4Tub	R=2.758 m, H=5.675 m	Stainless Steel: $\rho=7.87 \text{ g/cm}^3$, Fe(71%)+Cr(19%)+Ni(10%)
Buffer	G4Tub	R=2.755 m, H=5.669 m	Mineral Oil: $\rho=0.820 \text{ g/cm}^3$
γ Catcher Vessel	G4Tub	R=1.696 m, H=3.562 m	Acrylic: $\rho=1.14 \text{ g/cm}^3$, polymer
Liquid Scintillator (LS)	G4Tub	R=1.684 m, H=3.538 m	PXE+PPO: $\rho=0.798 \text{ g/cm}^3$, $\text{C}_{16}\text{H}_{18}$ (20%)+ $\text{C}_{12}\text{H}_{24}$ (80%)+PPO(6 g/l)
Target Vessel	G4Tub	R=1.150 m, H=2.474 m	Acrylic: $\rho=1.14 \text{ g/cm}^3$, polymer
Target	G4Tub	R=1.142 m, H=2.458 m	Same as LS + Gd(1 g/l)

Table 7.8: Details of solid volumes, dimensions and material I used to describe the DC far detector through Geant4. In the second columns, R is the radius and H the height of the tub.

FLUKA

As for Geant4, the geometry description has been simplified, constructing:

- a parallelepiped for the Word;
- a series of concentric cylinder for the Cavern+Pit, the Tank, the Muon Veto, the Stainless Steel Tank, the Buffer, the GCV and the Target.

Material description is the same as for Geant4 (see Table 7.8). A scheme of the realized Double Chooz geometry is shown in Figure 7.19.

As for the Borexino case, the user routines source.f is used, in order to implement the muon energy spectrum and the original position (horizontal 4 m radius disk at (0,0,15) m from the Target center); the routines mgdraw.f and usrrnc.f are also used in order to count the number of crossing muons, produced isotopes and neutron captures in the Target.

7.7.3 Geant4 and FLUKA simulation results

Rate results for cosmogenic products in Double Chooz are summarized in Table 7.9, both for Geant4 and FLUKA.

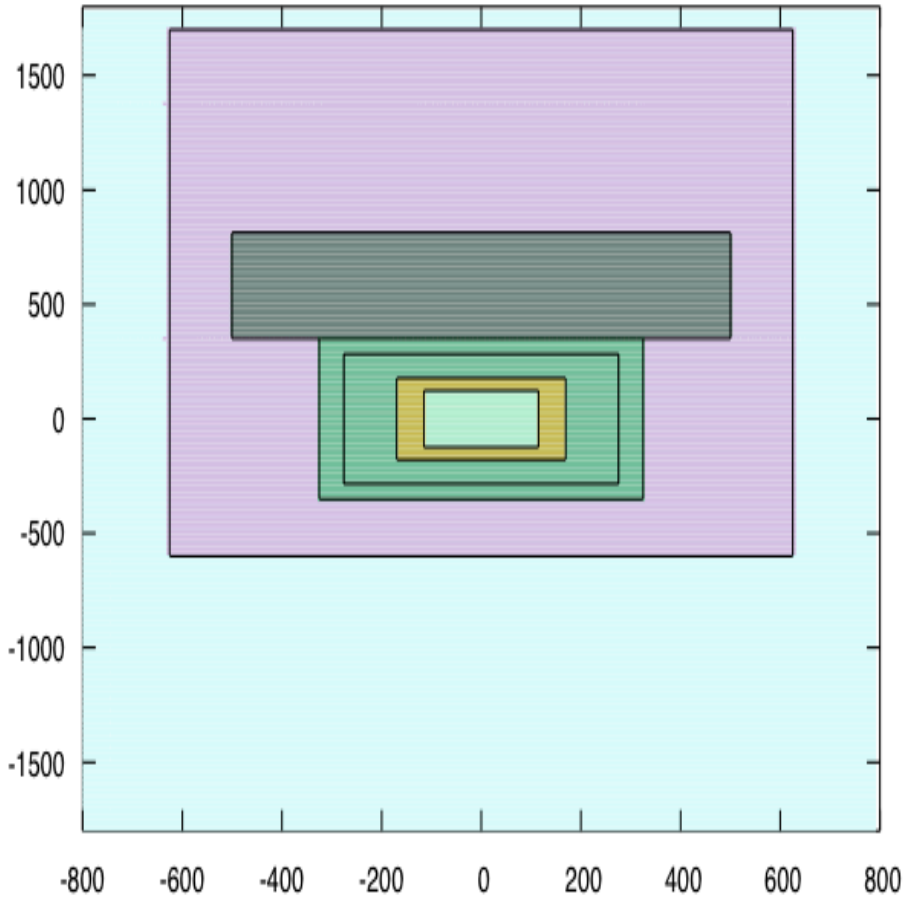


Figure 7.19: Frontal view of the Double Chooz geometry as described in FLUKA. Measure unit is cm. Colors correspond to different materials, from outside to inside: vacuum, rock, air, mineral oil, PXE+PPO and PXE+PPO+Gd.

Experimental results are not yet available for a comparison.

General considerations about estimated rates are:

- * ^{11}C : as already seen for Borexino simulations, FLUKA predicts a double rate with respect to Geant4 Physics Lists. Geant4 rates are quite in agreement, regardless from the Hadronic Physics Lists; in particular, the QGSP_BERT and FTF_BERT predict the same rate.
- * ^{10}C : as already noticed, the Geant4-QGSP_BIC predicts a 50% rate with respect to all the other models.
- * ^{11}Be : depending on the model, results are quite variable.
- * ^9C : the Geant4-QGSP_BIC predicts a 10% rate with respect to all the other models.
- * ^8B : results are strongly dependent on the model.
- * ^6He : the Geant4-QGSP_BIC predicts a 50% rate with respect to the other Geant4 models; FLUKA prediction is about 10 times the Geant4 ones.

Cosmogenic [cpd/Target]	QGSP_BIC (10.9 d)	QGSP_BERT (8.0 d)	FTF_BIC (5.3 d)	FTFP_BERT (13.7 d)	FLUKA (8.1 d)	Measured
^{11}C	299 ± 5	356 ± 7	423 ± 9	352 ± 5	755 ± 10	
^{10}C	8.3 ± 0.9	21 ± 2	22 ± 2	17 ± 1	19 ± 2	
^{11}Be	2.4 ± 0.5	0.1 ± 0.1	0.6 ± 0.3	0.1 ± 0.1	1.2 ± 0.4	
^9C	0.09 ± 0.09	0.7 ± 0.3	1.1 ± 0.5	1.3 ± 0.3	1.1 ± 0.4	
^8B	1.8 ± 0.4	0.2 ± 0.2	2.6 ± 0.7	0.07 ± 0.07	11 ± 1	
^6He	1.8 ± 0.4	3.4 ± 0.6	2.4 ± 0.7	3.3 ± 0.5	27 ± 2	
^8Li	13 ± 1	6.9 ± 0.9	14 ± 2	5.9 ± 0.7	43 ± 2	
^8He	/	/	0.6 ± 0.3	/	0.4 ± 0.2	
^9Li	0.6 ± 0.2	1.1 ± 0.4	2.6 ± 0.7	1.3 ± 0.3	4.8 ± 0.8	2.3 ± 1.2
^{12}B	59 ± 2	53 ± 3	60 ± 3	45 ± 2	57 ± 3	
Neutrons from μ^- -capture capture on H	3839 ± 19 121 ± 3 344 ± 6	4075 ± 23 84 ± 3 523 ± 8	3360 ± 25 116 ± 5 397 ± 9	3902 ± 17 78 ± 2 505 ± 6	4200 ± 23 n.a. $<(927 \pm 11)$	

Table 7.9: Rate results for cosmogenic products in the Double Chooz Target obtained by Geant4 with different Hadronic Physic Lists and with FLUKA. For each of them the HP model is activated. Light Ion Physics List is activated. Results are in cpd/Target. The period in days indicated in the second line corresponds to the simulated data taking time.

- * ^8Li : BIC model predicts a rate about twice the BERT one; FLUKA rate is about 3 times the BIC one.
 - * ^8He : only FTF_BIC and FLUKA predict a detectable rate in about a week of data taking.
 - * ^9Li : depending on the model, results are quite dependent on the model and seem to underestimate preliminary data results.
 - * ^{12}Bi : rates are quite in agreement, regardless from the model.
 - * Neutrons: results are quite in agreement, regardless from the model; FLUKA rate (as seen also for Borexino) are slightly (3%) higher than the highest Geant4 one. Because of their lower energy (~ 64 GeV), cosmic μ^- can be captured at rest and produce a neutron, following the reaction: $\mu^- + p \rightarrow \nu_\mu + n$. In Geant4 it is possible to activate the process called G4MuonMinusCaptureAtRest. BIC model predicts about 50% more μ^- captures than BERT model.
- Basing on the emitted γ energy, the rate of neutron capture on ^1H has been evaluated. In Geant4 the gamma following neutron capture on ^1H is monocromatic at 2.2246 MeV. In FLUKA, the gamma generation by low-energy neutrons is treated in the frame of a *multigroup scheme*. A downscattering matrix provides the probability, for a neutron in a given energy group, to generate a photon in each of a number of gamma energy groups, covering the range 1 keV to 20 MeV. With the exception of a few important gamma lines, the actual energy of the generated photon is sampled randomly in the energy interval corresponding to its gamma group (see [115] for details). This means that the gammas from neutron capture on ^1H are not monoenergetic in FLUKA; they correspond to the gamma group 18, including γ 's in the energy range between 2 and 2.5 MeV. Selecting just gammas from neutron

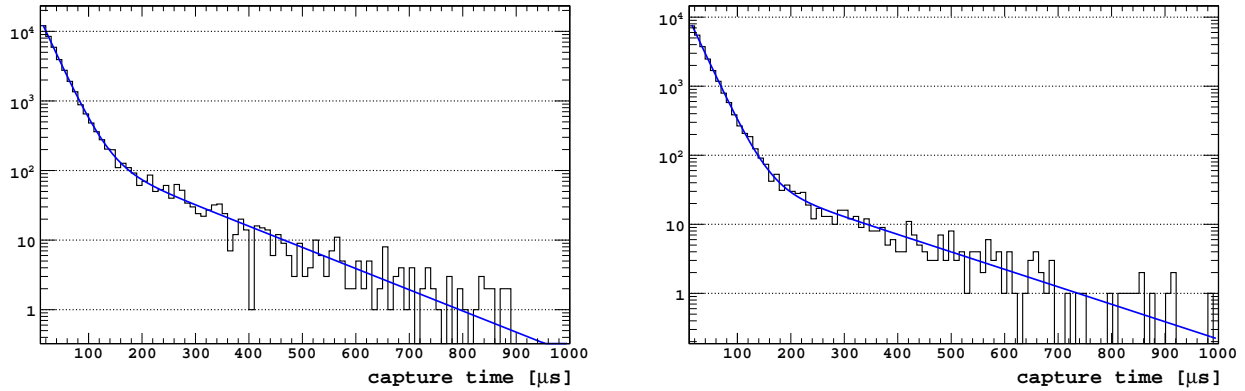


Figure 7.20: Distribution of neutron capture time for the Geant4-FTF_BERT (left) and the FLUKA (right) models fitted with the sum of two exponentials.

capture in this energy range I found a rate that is almost double the one predicted by Geant4. Since the neutron captures on Gd mixture produce different γ lines up to ~ 8 MeV, the application of a cut between 2 and 2.5 MeV returns just an upper limit on the neutron capture rate on ^1H .

As already seen for the Borexino simulations, the rate predictions of cosmogenic isotopes are quite variable and strongly depend on the used model. Situation is better for neutron rate: the agreement between the different model is within 10%.

The neutron capture time

The neutron capture time in DC depends on two exponential components representing the capture time on ^1H and on Gd. In Figure 7.20 the neutron capture time obtained for the Geant4-FTF_BERT Physics List and for FLUKA is shown. Distributions are fitted with the sum of two exponentials, returning characteristic times:

- Geant4: $\tau_{^1\text{H}} = (143 \pm 4)$ μs , $\tau_{\text{Gd}} = (25.8 \pm 0.2)$ μs ;
- FLUKA: $\tau_{^1\text{H}} = (172 \pm 9)$ μs , $\tau_{\text{Gd}} = (26.1 \pm 0.2)$ μs .

Results for τ_{Gd} are in very good agreement, on the contrary the FLUKA $\tau_{^1\text{H}}$ is 20% longer than the Geant4 one.

Observable	QGSP_BIC	QGSP_BERT	FTF_BIC	FTFP_BERT	FLUKA
Lateral dist. [m]	0.406 ± 0.002	0.455 ± 0.002	0.444 ± 0.003	0.454 ± 0.002	0.408 ± 0.003
Neutron mult.	2.17 ± 0.03	2.16 ± 0.03	2.01 ± 0.04	2.09 ± 0.02	2.06 ± 0.05

Table 7.10: Mean multiplicity and lateral distance for cosmogenic neutrons in the Target of Double Chooz obtained by FLUKA and Geant4, with different Hadronic Physics Lists (for each of them the HP model and Light Ion Physics List are activated).

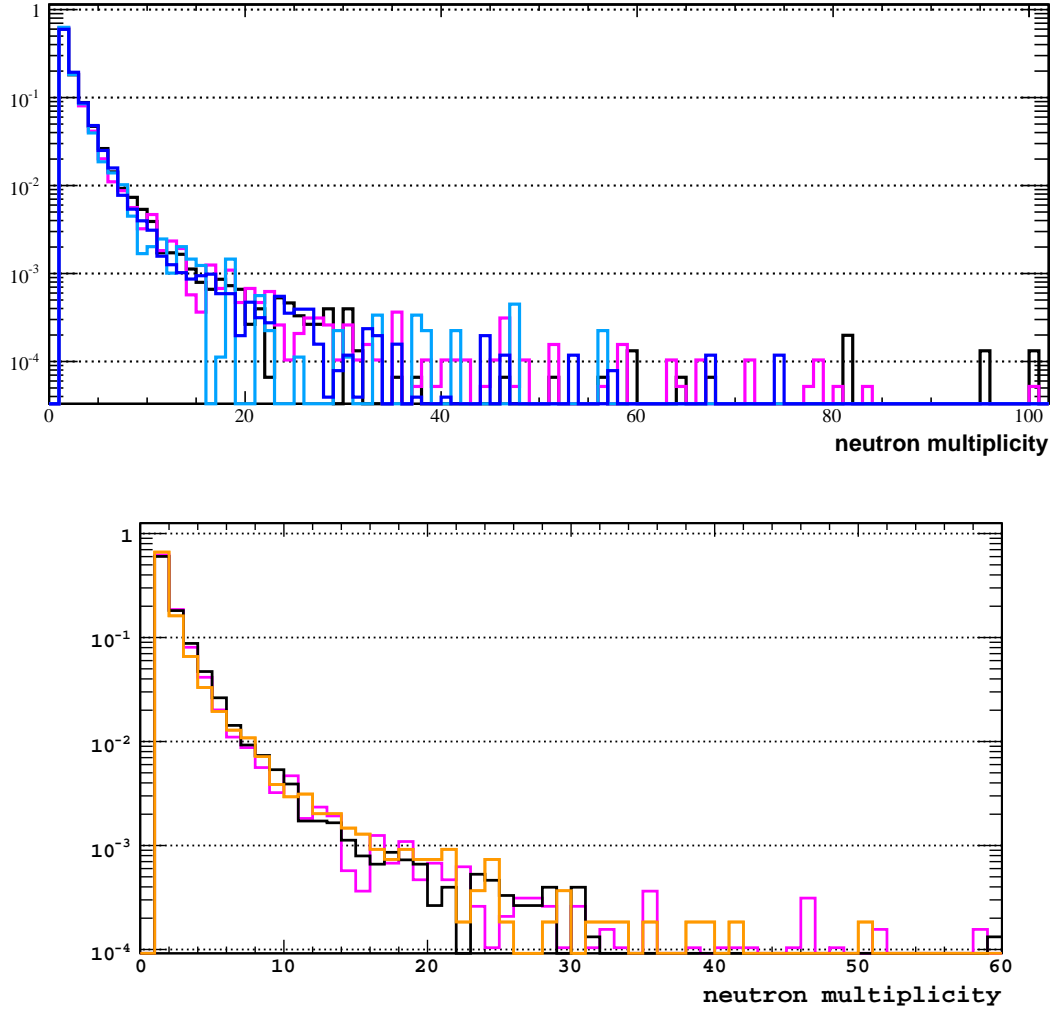


Figure 7.21: Top: Neutron multiplicity in the Double Chooz Target for the Physics Lists without Light Ion activation: QGSP_BIC_HP (pink), QGSP_BERT_HP (black), FTF_BIC_HP (light blue), FTFP_BERT_HP (blue). Bottom: Comparison of the neutron multiplicity obtained with FLUKA (orange line) and Geant4 (black for QGSP_BERT_HP and pink for QGSP_BIC_HP) in the Double Chooz Target.

The neutron multiplicity and lateral distance

Concerning the neutron multiplicity and the neutron lateral distance with the respect to the muon track, resulting distributions are shown in Figure 7.21 and 7.22, respectively. Comparison between different models shows a very good agreement. In Table 7.10 a summary of the mean values is reported. It is easy to remark that the neutron multiplicity in DC is quite smaller (about half) of the Borexino one (see Table 7.4); this is due to the lower muon energy in DC ($\langle E_{\mu,DC} \rangle \simeq 64 \text{ GeV}$) than in Borexino ($\langle E_{\mu,BX} \rangle \simeq 270 \text{ GeV}$), making the interaction of muons in DC weaker. In the same way the lateral distance in DC is slightly bigger than the one due to CNGS muons (see Table 7.7), having $\langle E_{\mu,CNGS} \rangle \simeq 16 \text{ GeV}$. On the other side, the neutron lateral distance is always of the order of 0.5 m.

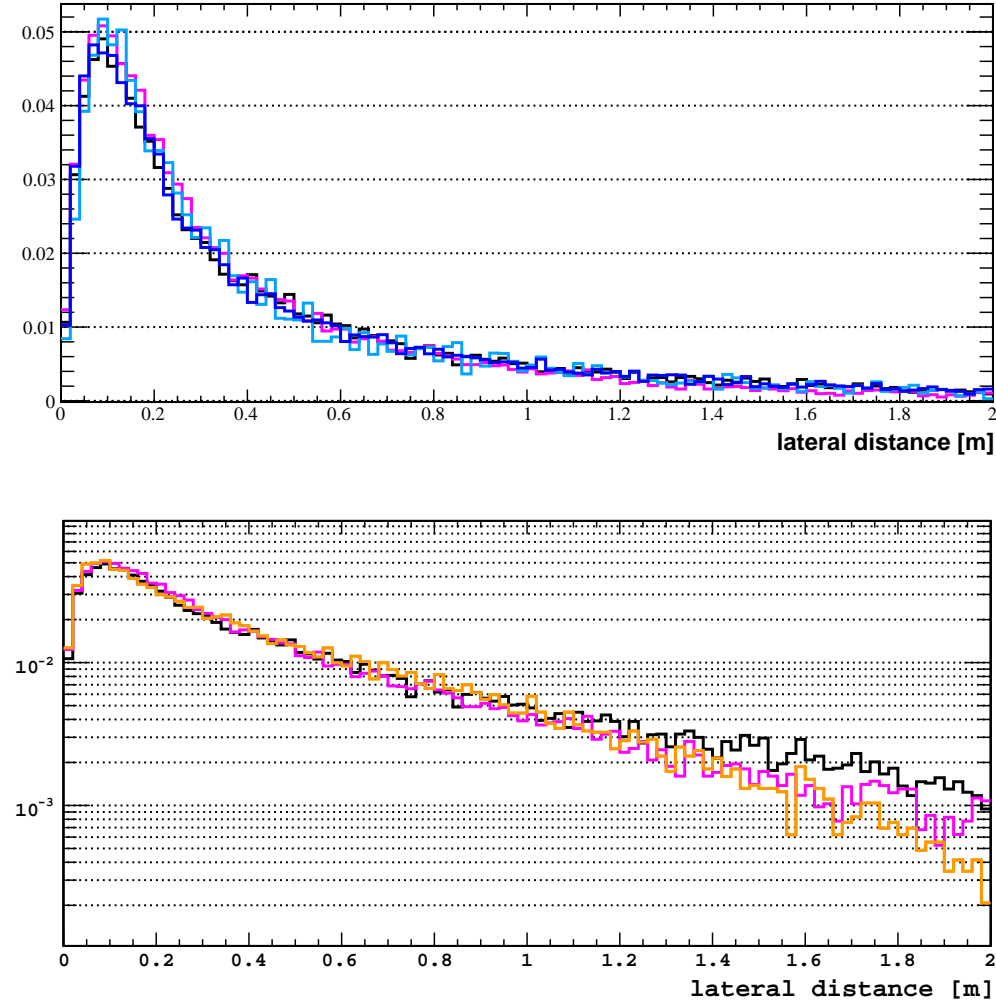


Figure 7.22: Top: Neutron lateral distance in the Double Chooz Target for the Physics Lists without Light Ion activation: QGSP_BIC_HP (pink), QGSP_BERT_HP (black), FTF_BIC_HP (light blue), FTFP_BERT_HP (blue). Bottom: Comparison of the neutron lateral distance obtained through FLUKA (orange), Geant4-QGSP_BIC_HP (pink) and Geant4-QGSP_BERT_HP (black) in the DC Target.

7.8 Conclusions

Study of cosmogenic products seems to have always been source of disagreement between different experiments and between data and Monte Carlo simulations. T. Hagner et al. published measured cosmogenic isotope rates, obtained through an experiment expressly constructed for estimating cosmogenic contamination in Liquid Scintillator detectors [69]. Their results are in disagreement with the measured values in Borexino [36] and Kamland [96]. A significant example is ^{11}C : both Borexino and Kamland measure a ^{11}C rate that is twice the predictions from Hagner et al. experiment.

In the same way, estimated cosmogenic isotope rates from Monte Carlo simulations result to be in disagreement with the measured data. Citing once more the Kamland experiment, they measure a ^{11}C rate that is twice the FLUKA prediction. I see the same disagreement for Borexino (see Table 7.3). Geant4 results (only available for Borexino)

are worse, predicting only ~25% of the real rate.

About cosmogenic neutron rate, the FLUKA rate I found is 77% of the real one. The Kamland Collaboration found a very similar discrepancy (75%). Again, Geant4 predictions for Borexino are a little worse, expecting less than 70% of the measured neutron rate. In addition, rates are often very different based on the used Physics Lists.

Problems in cosmogenic rate predictions for Geant4 and FLUKA have already been noticed [136] [124]. Production of secondary neutrons or long-lived unstable nuclei rely on the ability of simulation codes to model high-energy hadronic and electromagnetic showers initiated by muon interactions. In addition, in [124] some neutron interactions problems are reported; in particular, as I could notice performing simulations, the 2.2230 MeV peak from $H(n,\gamma)D$ appears at 2.2246 MeV in Geant4.

On the other side, the other studied observables (neutron lateral distance w.r.t. the muon track and neutron multiplicity per muon) show a good agreement between MC codes and data.

Done this considerations, it is clear that the neutron interactions are well reproduced by Geant4 and FLUKA; the problem seems to be originated in the upper step: the muon interactions, or in other words, the description of the hadronic shower development (maybe related to some cross section values?). As explained in [136], the observed inconsistency between measured and simulated neutron yields makes the predictions of muon-induced neutron rate in various detectors uncertain by about a factor of two.

Conclusions

The work just presented involves two subjects: the ^8B solar neutrino analysis in Borexino, with an energy threshold first of 3 MeV and finally of 2 MeV; and the Monte Carlo study of cosmic muon interaction products both in Borexino and in Double Chooz.

The evidence of neutrino flavor oscillations comes from several experiments on solar, atmospheric, reactor and accelerator neutrinos. The importance of matter interaction effects in the phenomenon of the oscillations plays a crucial role in the case of solar neutrinos. The oscillation theory in the Standard Solar Model (SSM) with (MSW-LMA) scenario predicts a peculiar behavior of electron neutrino survival probability (P_{ee}) as a function of neutrino energy. The high energy region ($>4\text{-}5$ MeV), so called *matter region*, has been explored by the solar neutrino experiment SNO and SuperKamiokande through the measurement of high energy ^8B solar neutrinos.

In the Borexino experiment, the ^8B solar neutrino analysis has been performed with the lowest energy thresholds ever reached: 3 and 2 MeV. Depending on the set energy threshold, the analysis has been approached through two different methods. The setting of the energy threshold at 3 MeV demanded the study and the development of removal techniques for cosmogenic isotopes and internal ^{208}Tl surviving above the threshold. The measured rate above 3 MeV is $R_{^8\text{B}} = (0.22 \pm 0.04_{\text{stat}} \pm 0.01_{\text{syst}}) \text{ cpd}/100\text{ t}$; the corresponding value for the survival probability is $\bar{P}_{ee} = (0.29 \pm 0.10)$ at the mean energy of 8.9 MeV for ^8B neutrinos. These results have been published in 2010.

Decreasing the energy threshold down to 2 MeV required a deep and accurate study of the external backgrounds affecting the Borexino core and the development of precise Monte Carlo tools able to reproduce their radial and energy distributions. The analysis has been performed fitting the energy and the radial distributions of events, allowing to distinguish the signal from the backgrounds. This shows the ability of Borexino of measuring the ^8B neutrino flux with this incredibly low energy threshold. The measured rate above 2 MeV is $R_{^8\text{B}-\nu} = (0.34 \pm 0.04^{+0.03}_{-0.02}) \text{ cpd}/100\text{ t}$; the corresponding value for the survival probability is $\bar{P}_{ee} = 0.44^{+0.14}_{-0.11}$ at the mean energy of 8.3 MeV for ^8B neutrinos.

The results on the ^8B solar ν total flux obtained through both the measures above 3 and 2 MeV are compatible with the results from other solar neutrino experiments studying the $\nu_e\text{-e}$ scattering and investigating higher energy region above about 4 MeV. Solar neutrino measurements validate the Standard Solar Model in the oscillation framework of the MSW-LMA solution. In the context of the survival probability mapping, the contribute from the Borexino experiment is multiple. Through the measurement of ^7Be neutrino flux (0.86 MeV), Borexino first investigated the low energy oscillation region, corresponding to oscillation in vacuum. The ^8B solar neutrino measurement with low energy threshold allowed a first approach to the intermediate energy region (so called *transition region*). Recently, Borexino has also published the first measurement of pep neutrinos (1.44 MeV),

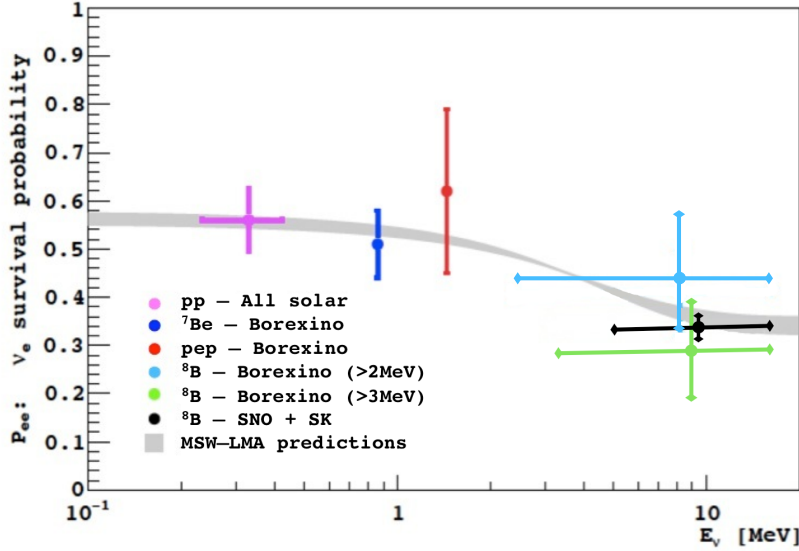


Figure 7.23: Electron neutrino survival probability as a function of energy. The light blue and the green points correspond to the ones measured by Borexino through ${}^8\text{B}$ solar neutrinos above 2 and 3 MeV respectively. The blue and red points correspond to the recent ${}^7\text{Be}$ and pep publication by Borexino [9] and [31]. The other experimental points correspond to: pp neutrino measurement given in [9] (pink) and the ${}^8\text{B}$ neutrino measurement from SNO-LETA [37] and SuperKamiokande [111] (black). The MSW-LMA prediction band is the 1σ range of the mixing parameters given in [112].

adding the P_{ee} experimental point in the transition region. A summary of the present P_{ee} mapping is shown in Figure 7.23.

Borexino results on ${}^8\text{B}$ and pep neutrino show the feasibility of measurements, with liquid scintillator detector, of solar neutrino sources in the transition oscillation region. They also confirm the necessity of more accurate measurements of these solar neutrino sources, allowing a deeper knowledge of the transition region. This is now a fundamental point in order to confirm or exclude the presence of Non Standard Physics in neutrino propagation in matter, as Non Standard Interaction or Sterile Neutrino. Next Borexino measurements, expected to be more accurate after the re-purification of the scintillator that is in progress at the moment, will be fundamental. In addition, a new experiment (SNO+) and a new project (LAGUNA) are already at work to realize solar neutrino measurements, clarifying this point.

Neutrino experiments often use underground liquid scintillator detectors. This is the case of Borexino, Kamland and Double Chooz. Liquid scintillators are affected by the cosmogenic contaminations: muons surviving underground can interact with ${}^{12}\text{C}$ nuclei, producing neutrons and unstable isotopes. This kind of background is particularly dangerous for experiments looking for rare events. Many Monte Carlo (MC) codes have been developed to describe muon interactions and subsequent hadronic cascade and neutron or isotope productions. The simulation must be accompanied by validation of the codes through experimental data and by comparison between different packages. In the present Thesis I showed the procedure and the results of simulations performed through Geant4 and FLUKA for Borexino and Double Chooz. The comparison with the Borexino data

shows two important results for muon beam with mean energy around 270 GeV. First, the neutron interactions are well reproduced by Geant4 and FLUKA, as testified by the agreement MC/data about the neutron lateral distance and multiplicity with respect to the parent muon and about the neutron capture time. On the contrary, the disagreement on the cosmogenic isotope and neutron rates shows an underestimation at level of the hadronic shower development. This problem has been already noticed in other contexts (different materials, different detector depths,...). Double Chooz data on cosmogenics rates will be available soon. This will allow a comparison MC/data also for another muon beam energy range, of about 64 GeV.

Appendix A

Manual for the External Background Simulation in G4Bx

by Margherita Buizza Avanzini, margherita.buizza@mi.infn.it

In these pages I will resume the procedure for the external background simulation in G4Bx. Present indications refer to the G4Bx version bxmc_2-beta. The updated version of BxStackingEB.cc is also needed (in /g4bx/src type *cvs update BxStackingEB*.cc* and in /g4bx/include type *cvs update BxStackingEB*.hh*).

I will show some examples of the useful macfile for the external events simulation. I will also attach some useful perl codes, allowing to launch a big production of external background on the Lione cluster: ccalisl.in2p3.fr.

I would like to thank Davide Franco, who wrote the first version of the G4Bx codes for the external background simulations, and Stefano Davini, for the help in the comprehension of the Lione grid.

Concept of the simulation procedure

External background comes mainly from the catodes of photomultipliers (PMTs). A good approximation to describe the original position of this backgrounds is the definition of a 6.5 m radius sphere. Most of the Borexino analyses are interested in the contamination surviving within 3m. The attenuation factor in this case is about 10^7 . The idea to speed up the simulations is to split them into two steps:

- * primary events are simulated on a sphere of 6.5 m radius (corresponding to the PMT photocathode surface);
- * only primary gamma-rays directed towards the IV (emission angle limits: $-33^\circ < \theta < 33^\circ$) are simulated;
- * in the first step, the optic processes are deactivated and all information concerning the energy deposition, the vertex position and the direction of the particle are written in a binary file;
- * in the second step, if for a done event the sum of the energy deposited exceeds a given threshold and lies within a given radius, an electron is generated for each deposit. Then, the electron is propagated with the corresponding starting energy, position and direction;

First step: writing the deposits

The first step is the fundamental one, setting the primary particles and the original position. In particular, you have to set:

- particles to simulate, including the generator. For example, for gammas the needed generator is G4Gun, for isotopes the needed generator is RDM (Radioactive Decay Modules);
- the original position of primary events. For example, for PMTs background a sphere of 6.5 m, for surface background the deformed vessel, ...;
- turn off the light production and the PMTs construction.

In particular, the following commands are necessary:

1. /run/writeeb 1 : allows the writing of deposit informations in a binary file;
2. /bx/detector/nopmts 1, /event/npethreshold -1, /bx/physics/cherenkov 0, /bx/physics/optical 0, /bx/physics/lightyield 0 : turning off of the optic processes;
3. /bx/stack/select EB : selecting the stacking processes expressly written for the External Background simulations.

A general suggestion is to set the /event/eventreport at a high number (10^6 - 10^7), in order to avoid cpu time loss needed to write informations about event.

In the following you can find some examples of first step mac files.

2.6MeV γ 's from PMTs

Here an example of the macfile to generate 2.6MeV γ 's from PMTs.

```
# Macfile to generate 2.6MeV gammas from PMTs /bxlog trace
/event/eventreport 10000000
/event/verbosity 0

/run/writeeb 1
/run/filename ttext
/run/heprandomseed 123456789

/bx/detector/configuration inScint
/bx/detector/PMTconfiguration simplePMT

/bx/physics/decay 1
/bx/detector/nopmts 1
/event/npethreshold -1
/bx/physics/cherenkov 0
/bx/physics/optical 0
/bx/physics/lightyield 0

/run/initialize
```

```

/bx/generator/select G4Gun
/bx/stack/select EB
/bx/stack/eb/kill -12
/bx/stack/eb/kill 12
/bx/stack/eb/killAngle 33 deg
/bx/generator/g4gun/particle gamma
/bx/generator/g4gun/energy 2.6 MeV
/bx/generator/g4gun/surface_radius 6.5 m
/bx/generator/g4gun/sphere_origin 0. 0. 0. m

/run/beamOn 100000000

```

^{214}Bi from PMTs

Here an example of the macfile to generate ^{214}Bi (nucleus) from PMTs. With respect to the previous macro, the generator is different.

```

# Macfile to generate 214Bi from PMTs /bxlog trace
/event/eventreport 10000000
/event/verbosity 0

/run/writeeb 1
/run/filename biext
/run/heprandomseed 123456789

/bx/detector/configuration inScint
/bx/detector/PMTconfiguration simplePMT

/bx/physics/decay 1
/bx/detector/nopmts 1
/event/npethreshold -1
/bx/physics/cherenkov 0
/bx/physics/optical 0
/bx/physics/lightyield 0

/run/initialize

/bx/generator/select RDM
/bx/stack/select EB
/bx/stack/rdm/kill -12
/bx/stack/rdm/kill 12
/bx/stack/rdm/killAngle 33 deg
/bx/stack/rdm/killLE 22 400
/bx/generator/rdm/ion 214 83 0
/bx/generator/rdm/surface_radius 6.5 m
/bx/generator/rdm/sphere_origin 0. 0. 0. m

/run/beamOn 100000000

```

In this macfile the option:

```
/bx/stack/rdm/killLE 22 400
killing gammas below 400keV has been added.
```

^{208}Tl from a deformed buffer

Here an example of the macfile to generate ^{208}Tl (nucleus) from a deformed buffer.

```
# Macfile to generate 208Tl in deformed buffer /bxlog trace
/event/eventreport 10000000
/event/verbosity 0

/run/writeeb 1
/run/filename tlbuffer
/run/heprandomseed 123456789

/bx/detector/configuration inScint
/bx/detector/PMTconfiguration simplePMT

/bx/physics/decay 1
/bx/detector/nopmts 1
/event/npethreshold -1
/bx/physics/cherenkov 0
/bx/physics/optical 0
/bx/physics/lightyield 0

/run/initialize

/bx/generator/select RDM
/bx/stack/select EB
/bx/stack/eb/BufferDef 2008_10_10_vessel_shape.dat /bx/stack/eb/kill -12
/bx/stack/eb/kill 12
/bx/generator/rdm/ion 208 81 0
/bx/generator/rdm/sphere_radius_min 3.7 m
/bx/generator/rdm/sphere_radius 6.5 m
/bx/generator/rdm/sphere_origin 0. 0. 0. m

/run/beamOn 100000000
```

Note that the two command:

```
/bx/generator/rdm/sphere_radius_min 3.7 m
/bx/generator/rdm/sphere_radius 6.5 m
```

are necessary to simulate a deformed buffer as the original volume for primary particles.

^{208}Tl from a deformed vessel

Here an example of the macfile to generate ^{208}Tl (nucleus) from a deformed vessel.

```

# Macfile to generate 208T1 on deformed vessel /bxlog trace
/event/eventreport 10000000
/event/verbosity 0

/run/writeeb 1
/run/filename tlsp
/run/heprandomseed 123456789

/bx/detector/configuration inScint
/bx/detector/PMTconfiguration simplePMT

/bx/physics/decay 1
/bx/detector/nopmts 1
/event/npethreshold -1
/bx/physics/cherenkov 0
/bx/physics/optical 0
/bx/physics/lightyield 0

/run/initialize

/bx/generator/select RDM
/bx/stack/select EB
/bx/stack/eb/VesselSupDef 2008_10_10_vessel_shape.dat /bx/stack/eb/kill -12
/bx/stack/eb/kill 12
/bx/generator/rdm/ion 208 81 0
/bx/generator/rdm/sphere_radius_min 3.7 m
/bx/generator/rdm/sphere_radius 4.8 m
/bx/generator/rdm/sphere_origin 0. 0. 0. m

/run/beamOn 100000000

```

Note that the two command:

```

/bx/generator/rdm/sphere_radius_min 3.7 m
/bx/generator/rdm/sphere_radius 4.8 m

```

are necessary to simulate a deformed vessel as the original volume for primary particles.

Second step: activating the optics

The second step, concerning the activation of the optic processes for each event depositing more than a settable energy (E^*) within a settable radius (R^*), is the same for each input binary file. The only things you need to set are E^* , R^* and the name of the deformed vessel you want to reproduce.

Here an example of the second step macfile, were $E^*=200\text{keV}$ and $R^*=3.1\text{m}$.

```

/bxlog trace
/event/eventreport 10000000

/run/filename tlbufferopt
/run/g4bx tlbuffer

```

```

/run/heprandomseed 123456788

/bx/detector/configuration inScint
/bx/detector/PMTconfiguration simplePMT
/bx/physics/ecut 10 mm
/bx/physics/gammacut 0.1 mm
/bx/physics/maxparentid 10000000

/bx/detector/deformedvessel 1
/bx/detector/vesselfilename 2008_10_10_vessel_shape.dat

/run/initialize

/bx/generator/select G4Bx
/bx/generator/G4Bx/emin 0.2 MeV
/bx/generator/G4Bx/radius 3.1 m
/run/beamOn 100000000

```

Pay attention to following comments:

- the activation of the vessel deformation MUST be set BEFORE the /run/initialize, responsible of the detector construction;
- the number of events to generate must be set at the same value as the first step.

Once obtained the second step binary file, you can run bx_elec, setting the run to a reasonable number, depending on the vessel deformation period. After this, you can run Echidna.

Huge production of external background

If you need to produce a huge number of external background reproducing the data taking condition, it is useful to automatize the process. In addition, it is recommended to work on a powerful cluster, as the Lione one. You can find all informations about this cluster and how to manage jobs on it at the following address: <http://cc.in2p3.fr/Calcul-au-CC>. In the following, I will attach a typical perl script I wrote and used for the production of all the external background for ${}^8\text{B}$ and pep analyses in Borexino. In particular, the script is structured in this way:

- * it reads from an ASCII file the list of runs to reproduce;
- * it reads from an ASCII file the list of deformed vessel shapes corresponding to the used run;
- * it reads from an ASCII file the list number of events to generate, corresponding to the used run;
- * it writes a settable number (not more than 5 at the same times) of a bash file launching the production of 20 runs (i.e. 20 jobs); it is recommended not to launch more than 100 jobs at the same time;

- * the first step simulation outputs are used as input for more second step simulations (20 in the following example);
- * second step macfile needs the command /event/64bit 1 allowing the conversion from 32bit to 64bit for the event writing;
- * all second step binary files are passed through the electronic chain simulator, bx_elec;
- * all the bx_elec output files are reconstructed through the official Borexino reconstruction code, Echidna;
- * the entire production process is run on the user temporary directory \\${TMPBATCH};
- * jobs are submitted using values for each submission parameters available on Lione grid (see <http://cc.in2p3.fr/docenligne/969>), expressly tuned for a huge production (10000 surviving events of external ^{214}Bi , for the detector configuration in the period 2008-2010);
- * only final rootfile are copied in the sps storage, available for Solar Neutrino Group (<http://cc.in2p3.fr/SPS>).

Pay attention because the Lione cluster is switching from the QBS grid system to the GE one; submission commands will be to modify (<http://cc.in2p3.fr/docenligne/972>).

```
#!/usr/bin/perl

$echidna_path = "/afs/in2p3.fr/home/b/uname/throng/MCproduction/offline/Echidna_c14";
$bxmlc_path = "/afs/in2p3.fr/home/b/uname/throng/MCproduction/offline/bxmlc_c14";
$storage = "/sps/nusol/MC_ext";
$tmpdir = "/scratch";
$scr = "\$TMPBATCH";

$darknoise = "true";
$darkrate = 1200;
$maxevents = 1E6;
$btb = 20;

# reading lists of runs, number of events and vessel deformation files
$filerun = "list_run.dat";
$filedef = "list_def.dat";
$filenev = "list_nev.dat";

open(FF, "<$filerun");
@run = <FF>;
close(FF);

open(GG, "<$filedef");
@def_file = <GG>;
close(GG);

open(EE, "<$filenev");
@pesi = <EE>;
```

```

close(EE);

$isotope = "214 83 0";
$enename = "bi_ext";

# for each $j, 20 jobs, corresponding to 20 different runs, are launched
for($j=0;$j<5;$j++){ # no more than 5 by 5      $K=int(rand(50));
    $L=int(rand(50));
    $ffile="launcher_.$j.sh";
    open(OO,>$ffile");
    print OO "#!/bin/sh \n";
    $Ni = 20*$j;
    $Nf = 20*($j+1);

    for($i=$Ni;$i<$Nf;$i++) {
        chomp(${run[$i]});
        $seednum1 = 123456789 - 2*($i+1) + $i*($j+1)*$K+$L;
        $peso= int(${pesi[$i]}/4.5);

        $outname1 = "{$enename}_${run[$i]}_$i";
        $filename1 = "bie_${run[$i]}_$i.mac";
        $runname = "{$enename}_${run[$i]}_$i.sh";

        open(OOUT,>"$storage/$runname");
        print OOUT«EOF;
        #!/bin/sh
        cd $bxmc_path/g4bx/
        source please_source_me

        # writing of first step macfile
        cat > $scr/$filename1 << ENDMAC;
        /bxlog trace
        /event/eventreport 10000000
        /event/verbosity 0
        /run/writeeb 1
        /run/filename biext
        /run/heprandomseed 123456789
        /bx/detector/configuration inScint
        /bx/detector/PMTconfiguration simplePMT
        /bx/physics/decay 1
        /bx/detector/nopmts 1
        /event/npethreshold -1
        /bx/physics/cherenkov 0
        /bx/physics/optical 0
        /bx/physics/lightyield 0
        /run/initialize
        /bx/generator/select RDM
        /bx/stack/select EB
        /bx/stack/rdm/kill -12
        /bx/stack/rdm/kill 12
    }
}

```

```

/bx/stack/rdm/killAngle 33 deg
/bx/stack/rdm/killLE 22 400
/bx/generator/rdm/ion 214 83 0
/bx/generator/rdm/surface_radius 6.5 m
/bx/generator/rdm/sphere_origin 0. 0. 0. m

/run/beamOn 100000000
ENDMAC

export ORI_LD=".:$LD_LIBRARY_PATH"
export ROOTSYS=/afs/in2p3.fr/system/amd64_sl5/usr/local/root/root_v5.20.00/root/
source /afs/in2p3.fr/system/amd64_sl5/usr/local/shared/bin/root_env.sh

# running of the first step macfile
cd $bxmc_path/g4bx/
source please_source_me
cd $bxmc_path/g4bx/Linux-g++
./g4bx $scr/$filename1

# loop generating 20 second step macfiles for each first step
n=0;
for ((ij=0;ij<20;ij+=1)); do
    rad=3.5;
    seednum2=\$((123456789 + \$RANDOM));
    seednum3=\$((12345678 - \$RANDOM));
    outname2=dep_${outname1}_\$n;
    filename2=G4Bx_bie_${run[$i]}_${i}_\$n.mac;
    outdat=tle_${j}_${i}_\$n;

    cat > $scr/\$filename2 << ENDMAC\$n; /bxlog trace
    /event/eventreport 10000000
    /run/filename $scr/\$outname2
    /run/g4bx $scr/$outname1.fil
    /run/heprandomseed \$seednum2
    /bx/detector/configuration inScint
    /bx/detector/PMTconfiguration simplePMT
    /bx/physics/ecut 10 mm
    /bx/physics/gammacut 0.1 mm
    /bx/physics/maxparentid 10000000
    /bx/detector/deformedvessel 1
    /bx/detector/vesselfilename ${def_file[$i]}
    /event/64bit 1
    /run/initialize
    /bx/generator/select G4Bx
    /bx/generator/G4Bx/emin 0.2 MeV
    /bx/generator/G4Bx/radius \$rad m
    /run/beamOn $peso
ENDMAC\$n

```

```

# writing input files for bx_elec
cat > $scr/InputFileList_${j}_${i}_$n.txt << ENDINP\$n;
BinaryFile: $scr/\$outname2.fil
MaxVertexes: $maxevents
VertexRate: 1E1
OverrideVertexTime: true
EndOfBlock
ENDINP\$n

cat > $scr/\$outdat.dat << ENDDAT\$ij;
Run: ${run[$i]}
MaxEvents: $maxevents
MaxTime: 8.64E4
StartTime: 1/9/3/16/5
BTBThreshold: $btb
PmtDarkNoise: $darknoise
DefLabenDarkRate: $darkrate
RandomSeed: \$seednum3
OutputFile: $scr/\$outname2.out.gz
InputFileList: $scr/InputFileList_${j}_${i}_$n.txt
DbSettings: bx_elec/data/bx_dbconfig.inp
UseRealEfficiencies: false
ForceEfficienciesToOne: true
PmtAfterpulses: true
ChargeSpectraType: 1
ENDDAT\$ij

# launching second step macfile
cd $bxmc_path/g4bx/
source please_source_me
cd Linux-g++
./g4bx $scr/\$filename2
sleep 1

unset ROOT_ENV_SET
export LD_LIBRARY_PATH="$ORI_LD":/afs/in2p3.fr/system/ia32_sl4/usr/local/pgsql/8.1/lib/
export LD_LIBRARY_PATH="$LD_LIBRARY_PATH":/afs/in2p3.fr/system/ia32_sl4/usr/local/lib/
export ROOTSYS=/afs/in2p3.fr/system/ia32_sl4/usr/local/root/root_v5.20.00/root/
source /afs/in2p3.fr/system/ia32_sl4/usr/local/shared/bin/root_env.sh

# launching bx_elec for each second step binary file
cd $bxmc_path/g4bx/
source please_source_me
cd $bxmc_path
./go_bx_elec.sh $scr/\$outdat
sleep 2

# launching echidna
cd $echidna_path
./echidna -f $scr/\${outname2}.out.gz -c $echidna_path/user.cfg -o \${outname2}_rec.root -l

```

```
$scr/\${outname1}_rec.log -p bx_writer.directory $scr -e 1000000000 simulation
sleep 1
done

mv $scr/*_rec.root $storage

EOF

close(OOUT);

system("ln -s $storage/$runname $runname");
sleep 2;
system("chmod +x $storage/$runname");

# defining the QSB parameters for running jobs
print OO "qsub -l platform=LINUX,T=4280000,scratch=30GB,spool=50MB,M=2GB -l
u_sps_nusol -e $storage/$runname.err -o $storage/$runname.out ./$runname \n";
sleep 1;
}
close(OO);
sleep 1;
system("chmod +x $ffile");
sleep 1;
system("nohup ./$ffile &");
print("fattoooo $j \n");
sleep 3;
}
```


Bibliography

- [1] S.T. Petcov, *Neutrino mixing, leptonic CP violation, the seesaw mechanism and beyond*", Int. J. Mod. Phys. A25 (2010).
- [2] L. Wolfenstein, *Neutrino oscillations in matter*, Phys. Rev. D17, 9 (1978).
- [3] S.P. Mikheev and A.Yu. Smirnov, *Resonance enhancement of oscillations in matter and solar neutrino spectroscopy*, Sov. J. Nucl. Phys. 42, 1441-1448 (1985).
- [4] S.P. Mikheev and A.Yu. Smirnov, *Resonant amplification of neutrino oscillations in matter and solar neutrino spectroscopy*, Nuovo Cim. C9, 17-26 (1986).
- [5] S.J. Parke, *Nonadiabatic Level Crossing in Resonant Neutrino Oscillations*, Phys. Rev. Lett. 57 (1986).
- [6] D. Notzold, *Exact Analytic Solutions For Mikheev-Smirnov-Wolfenstein Level Crossings*, Phys. Rev. D36, 1625 (1987).
- [7] T.K. Kuo and J. Pantaleone, *Neutrino oscillations in matter*, Rev. Mod. Phys. 61, 937-979 (1989).
- [8] J.N. Bahcall, *The luminosity constraint on solar neutrino fluxes*, Phys. Rev. C65, 025801 (2002).
- [9] G. Bellini *et al.* (The Borexino Collaboration), *Precision measurement of the ^7Be solar neutrino interaction rate in Borexino*, Phys. Rev. Lett. 107, 141302 (2011).
- [10] H. A. Bethe, *Energy production in stars*, Phys. Rev. 55, 434-456 (1939).
- [11] <http://www.sns.ias.edu/jnb/>.
- [12] T. Araki *et al.* (The KamLAND Collaboration), *Experimental investigation of geologically produced antineutrinos with KamLAND*, Nature 436, 499-503 (2005).
- [13] A. Gando *et al.* (The KamLAND Collaboration), *Partial radiogenic heat model for Earth revealed by geoneutrino measurements*, Nature Geoscience 4, 647-651 (2011).
- [14] G. Bellini *et al.* (The Borexino Collaboration), *Observation of Geo-Neutrinos*, Phys. Lett. B687, 299-304 (2010).
- [15] S. Abe *et al.* (The KamLAND Collaboration), *Precision Measurement of Neutrino Oscillation Parameters with KamLAND*, Phys. Rev. Lett. 100, 221803 (2008).

- [16] A. Strumia and F. Vissani, *Neutrino masses and mixings and...*, arXiv.org/abs/hep-ph/0606054v3 (2010).
- [17] Y. Fukuda et al. (The SuperKamiokande collaboration), *Evidence for oscillation of atmospheric neutrinos*, Phys. Rev. Lett. 81, 1562-1567 (1998).
- [18] M. Ambrosio et al. (The MACRO collaboration), *Atmospheric neutrino flux measurements using upgoing muons MACRO Collaboration*, Phys. Lett. B357, 481-486 (1995).
- [19] M.H. Ahn et al. (The K2K collaboration), *Measurement of Neutrino Oscillation by the K2K Experiment*, Phys. Rev. D74, 072003 (2006).
- [20] R. Davis *Solar neutrinos. II: Experimental*, Phys. Rev. Lett. 12, 303-305 (1964);
 R. Davis et al., *Search for neutrinos from the Sun*, Phys. Rev. Lett. 20, 1205-1209 (1968);
 B.T. Cleveland et al. (The Homestake Collaboration), *Measurement of the solar electron neutrino flux with the Homestake chlorine detector*, Astrophys. J. 496, 505-526 (1998).
- [21] W. Hampel et al. (The Gallex Collaboration), *GALLEX solar neutrino observations: Results for GALLEX IV*, Phys. Lett. B447, 127-133 (1999);
 J. N. Abdurashitov et al. (The SAGE Collaboration), *Measurement of the solar neutrino capture rate with gallium metal*, Phys. Lett. C60, 055801 (1999);
 M. Altmann et al. (The GNO Collaboration), *Complete results for five years of GNO solar neutrino observations*, Phys. Lett. B616, 174 (2005).
- [22] J. Hosaka et al. (The Super-Kamiokande Collaboration), *Solar neutrino measurements in Super-Kamiokande-I*, Phys. Rev. D73, 112001 (2006).
- [23] Q.R. Ahmad et al. (The SNO Collaboration), *Measurement of the rate of $\nu_e + d \rightarrow p + p + e^-$ interactions produced by 8B solar neutrinos at the Sudbury Neutrino Observatory*, Phys. Rev. Lett. 87, 071301 (2001);
 Q.R. Ahmad et al. (The SNO Collaboration), *Direct Evidence for Neutrino Flavor Transformation from Neutral-Current Interactions in the Sudbury Neutrino Observatory*, Phys. Rev. Lett. 89, 011301 (2002);
- [24] K. Eguchi et al. (The KamLAND collaboration), *First Results from KamLAND: Evidence for Reactor Anti-Neutrino Disappearance*, Phys. Rev. Lett. 90, 021802 (2003);
 T. Araki et al. (The KamLAND collaboration), *Measurement of Neutrino Oscillation with KamLAND: Evidence of Spectral Distortion*, Phys. Rev. Lett. 94, 081801 (2005).
- [25] C. Athanassopoulos et al. (The LSND collaboration), *Evidence for $\nu_\mu \rightarrow \nu_e$ Neutrino Oscillations from LSND*, Phys. Rev. Lett. 81, 1774 (1998);
 A. Aguilar et al. (The LSND collaboration), *Evidence for Neutrino Oscillations from the Observation of Electron Anti-neutrinos in a Muon Anti-Neutrino Beam*, Phys. Rev. D64, 112007 (2001).

- [26] A.A. Aguilar-Arevalo *et al.* (The MiniBoone Collaboration), *Unexplained Excess of Electron-Like Events From a 1 GeV Neutrino Beam*, Phys. Rev. Lett. 102, 101802 (2009).
- [27] G.P. Zeller *et al.* (The NuTeV Collaboration), *A Precise Determination of Electroweak Parameters in Neutrino-Nucleon Scattering*, Phys. Rev. Lett. 88, 091802 (2002).
- [28] H.V. Klapdor-Kleingrothaus *et al.*, *Evidence for Neutrinoless Double Beta Decay*, Mod. Phys. Lett. A16, 2409 (2001).
- [29] E. Fiorini *et al.*, *A search for lepton non-conservation in double beta decay with a germanium detector*, Phys. Lett. B25, 602 (1967);
H.V. Klapdor-Kleingrothaus *et al.* (The Heidelberg–Moscow Collaboration), *Latest Results from the Heidelberg–Moscow Double Beta Decay Experiment*, Eur. Phys. J. A12, 147 (2001).
- [30] T. Adam *et al.* (The OPERA Collaboration), *Measurement of the neutrino velocity with the OPERA detector in the CNGS beam*, arXiv:1109.4897v1 [hep-ex] (2011).
- [31] G. Bellini *et al.* (The Borexino Collaboration), *First evidence of pep solar neutrinos by direct detection in Borexino*, arXiv:1110.3230 (2011).
- [32] C. Galbiati *et al.*, *Cosmogenic ^{11}C production and sensitivity of organic scintillator detectors to pep and CNO neutrinos*, Phys. Rev. C71, 055805 (2005).
- [33] http://www.mpa-garching.mpg.de/aldos/solar_main.html.
- [34] A. Serenelli *et al.*, *Solar models with accretion. I. Application to the solar abundance problem*, arxiv.org/pdf/1104.1639v1 [astro-ph.SR] (2011).
- [35] C. Arpesella *et al.* (The Borexino Collaboration), *Direct Measurement of the 7Be Solar Neutrino Flux with 192 Days of Borexino*, Phys. Rev. Lett. 101, 091302 (2008).
- [36] G. Bellini *et al.* (The Borexino Collaboration), *Measurement of the solar 8B neutrino rate with a liquid scintillator target and 3 MeV energy threshold in the Borexino detector*, Phys. Rev. D82, 033006 (2010).
- [37] B. Aharmim *et al.* (The SNO Collaboration), *Low Energy Threshold Analysis of the Phase I and Phase II Data Sets of the Sudbury Neutrino Observatory*, Phys. Rev. C 81, 055504 (2010).
- [38] C. Pena-Garay and A.M. Serenelli, *Solar neutrinos and the solar composition problem*, arXiv:0811.2424 (2008).
- [39] A. Serenelli, *New Results on Standard Solar Models*, arXiv:0910.3690 (2009).
- [40] G.L. Fogli *et al.*, *Hints of $\theta_{13} > 0$ from global neutrino data analysis*, arXiv:0806.2649 (2008).
- [41] J.W.F. Valle, *Resonant oscillations of massless neutrinos in matter*, Phys. Lett. B199, 432 (1987).

- [42] M.M. Guzzo, A. Masiero and S.T. Petcov, *On the MSW effect with massless neutrinos and no mixing in the vacuum*, Phys. Lett. B260, 154 (1991).
- [43] E. Roulet, *Mikheyev-Smirnov-Wolfenstein effect with flavor-changing neutrino interactions*, Phys. Rev. D44, R935 (1991).
- [44] A. Friedland, C. Lunardini and C. Pena-Garay, *Solar neutrinos as probes of neutrino-matter interactions*, Phys. Lett. B594, 347 (2004).
- [45] A. Palazzo, *Hint of non-standard dynamics in solar neutrino conversion*, Phys. Rev. D83, 101701 (2011).
- [46] A. Palazzo, *Testing the very-short-baseline neutrino anomalies at the solar sector*, Phys. Rev. D83, 113013 (2011).
- [47] C. Giunti and M. Laveder, *Statistical Significance of the Gallium Anomaly*, arXiv:1006.3244 [hep-ph] (2006).
- [48] G. Mention *et al.*, *The Reactor Antineutrino Anomaly*, arXiv:1101.2755 [hep-ex] (2011).
- [49] J. Hamann *et al.*, *Cosmology seeking friendship with sterile neutrinos*, Phys. Rev. Lett. 105, 181301 (2010).
- [50] B. Baibussinov *et al.*, *A new search for anomalous neutrino oscillations at the CERN-PS*, arXiv:0909.0355v3 [hep-ex] (2009).
- [51] M. Cribier *et al.*, *A proposed search for a fourth neutrino with a PBq antineutrino source*, arXiv:1107.2335v2 [hep-ex] (2011).
- [52] M. Pallavicini, *Borexino Search for Sterile Neutrinos*, Slides for Short-Baseline Neutrino Workshop (SBNW11), Fermilab (2011).
- [53] B.Aharmim *et al.* (The SNO Collaboration), *Combined Analysis of all Three Phases of Solar Neutrino Data from the Sudbury Neutrino Observatory*, arXiv:1109.0763v1 [nucl-ex] (2011).
- [54] <http://snoplus.phy.queensu.ca/Home.html>.
- [55] C. Krauss for the SNO+ Collaboration, *SNO with Liquid Scintillator: SNO+*, Prog. Part. Nucl. Phys. 57 1, 150-152 (2006).
- [56] <http://www.laguna-science.eu/>.
- [57] G.L. Fogli *et al.*, *What we (would like to) know about the neutrino mass*, Proceeding of NO-VE 2008, IV International Workshop on Neutrino Oscillations in Venice (Venice, Italy, April 15-18, 2008).
- [58] G.L. Fogli *et al.*, *Hints of $\theta_{13} > 0$ from global neutrino data analysis*, Phys. Rev. Lett. 101, 141801 (2008).

- [59] G.L. Fogli *et al.*, *Overview of Neutrino Physics Phenomenology*, in *NEUTEL 2011*, Proceeding of the 14th International Workshop on Neutrino Telescopes (Venice, Italy, 2011).
- [60] K. Abe *et al.* (The T2K Collaboration), *Indication of Electron Neutrino Appearance from an Accelerator-produced off-axis Muon Neutrino Beam*, arXiv:1106.2822 [hep-ex] (2011).
- [61] L. Whitehead *et al.* (The MINOS Collaboration), *Recent results from MINOS*, Joint Experimental-Theoretical Seminar (24 June 2011, Fermilab, USA).
- [62] P. Adamson *et al.* (The MINOS Collaboration), *Improved search for muon-neutrino to electron-neutrino oscillations in MINOS*, arXiv:1108.0015 [hep-ex] (2011).
- [63] G.L. Fogli *et al.*, *Evidence of $\theta_{13} > 0$ from global neutrino data analysis*, arXiv:1106.6028v2 [hep-ph] (2011).
- [64] T.A. Mueller *et al.*, *Improved Predictions of Reactor Antineutrino Spectra*, Phys. Rev. C83, 054615 (2011).
- [65] M. Mezzetto and T. Schwetz, θ_{13} : *phenomenology, present status and prospect*, J. Phys. G37, 103001 (2010).
- [66] M. Apollonio *et al.* (The CHOOZ Collaboration), *Search for neutrino oscillations on a long base-line at the CHOOZ nuclear power station*, Eur. Phys. J. C27, 331 (2003).
- [67] F.X. Hartmann, *Low Level Scintillators and Gadolinium*, Presentation at the Workshop on Future Low Energy Neutrino Experiments, TU Munich, Munich, 9-11 October (2003).
- [68] P. Huber, M. Lindner, T. Schwetz, and W. Winter, *Reactor Neutrino Experiments Compared to Superbeams*, Nucl. Phys. B665, 487 (2003).
- [69] T. Hagner *et al.*, *Muon induced Production of Radioactive Isotopes in Scintillation Detectors*, Astropar. Phys. 14, 33-47 (2000).
- [70] J. K. Ahn *et al.* (The RENO Collaboration), *RENO: An Experiment for Neutrino Oscillation Parameter θ_{13} Using Reactor Neutrinos at Yonggwang*, arXiv:1003.1391v1 [hep-ex] (2010).
- [71] G. Mention, T. Lasserre and D. Motta, *A unified analysis of the reactor neutrino program towards the measurement of the θ_{13} mixing angle*, arXiv:0704.0498v2 [hep-ex] (2007).
- [72] F. Ardellier *et al.* (The Double Chooz Collaboration), *Double Chooz: A search for the neutrino mixing angle θ_{13}* , hep-ex/0606025 (2006).
- [73] X. Guo *et al.* (The Daya-Bay Collaboration), *A precision measurement of the neutrino mixing angle θ_{13} using reactor antineutrinos at Daya Bay*, hep-ex/0701029 (2007).
- [74] C. Arpesella *et al.* (The Borexino Collaboration), *Borexino at Gran Sasso. Proposal for a real time detector for low energy solar neutrinos* ed. By I.N.F.N. (1991).

- [75] J.N. Bahcall, *Why Do Solar Neutrino Experiments Below 1 MeV*, arXiv:hep-ex/0106086v1 (2001).
- [76] G. Bellini et al. (The Borexino Collaboration), *Absence of day-night asymmetry of 862 keV ^7Be solar neutrino rate in Borexino and MSW oscillation parameters*, arXiv:1104.2150v1 (2011).
- [77] S.P. Ahlen et al. (The MACRO Collaboration), *Study of penetrating cosmic ray muons and search for large scale anisotropies at the Gran Sasso Laboratory*, Phys. Lett. B249, 149-156 (1990).
- [78] E. Bellotti et al., *New measurement of rock contaminations and neutron activity in the Gran Sasso tunnel*, INFN/TC-85/19.
- [79] C. Arpesella et al. (Borexino Collaboration), *Measurements of extremely low radioactivity levels in BOREXINO*, Astrop. Phys. 18, 1-25 (2002).
- [80] G. Bellini et al. (The Borexino Collaboration), *Muon and Cosmogenic Neutron Detection in Borexino*, JINST 6:P05005 (2011).
- [81] K.B. McCarty, *The Borexino Nylon Film and the Third Counting Test Facility*, Ph.D. Thesis, Princeton University (2006).
- [82] G. Alimonti et al. (The Borexino Collaboration), *Light propagation in a large volume liquid scintillator*, NIMS A440, 360 (2000).
- [83] V.I. Tretyak, *Semi-empirical calculation of quenching factors for ions in scintillators*, Astropart. Phys. 33, 40-53 (2010).
- [84] J. Benziger et al., *A Scintillator Purification System for the Borexino Solar Neutrino Detector*, Nucl. Instrum. Meth. A587, 277-291 (2008).
- [85] G. Alimonti et al. (The Borexino Collaboration), *The Borexino detector at the Laboratori Nazionali del Gran Sasso*, Nucl. Instr. and Meth. in Phys. Res. A600, 568-593 (2009).
- [86] J. Benziger et al., *The nylon scintillator containment vessels for the Borexino solar neutrino experiment*, Nucl. Instrum. Meth. A582, 509 (2007).
- [87] S.E. Hardy, *Measuring the ^7Be Neutrino Flux From the Sun: Calibration of the Borexino Solar Neutrino Detector*, Ph.D. Thesis, Virginia Polytechnic Institute and State University (2010).
- [88] W. Maneschg et al., *Production and characterization of a custom-made ^{228}Th source with reduced neutron source strength for the Borexino experiment*, arXiv:1110.1217v1 [physics.ins-det] (2011).
- [89] O. SMirnov, *Report on the Borexino data analysis*, Borexino Internal Report (2007).
- [90] Y.Koshio, B.Caccianiga et al. *Position reconstruction and determination of the Fiducial Volume*, Borexino Internal Report (2010).
- [91] <http://www.geant4.org/geant4/results/publications.shtml>.

- [92] [http://root.cern.ch/.](http://root.cern.ch/)
- [93] S. Perasso, *Monte Carlo Based Measurement of ^7Be Solar Neutrino Flux in Borexino*, Ph.D. Thesis, Università di Genova (2010).
- [94] J. Hosaka *et al.* (The SuperKamiokaNDE Collaboration), *Solar neutrino measurements in SuperKamiokande-I*, Phys. Rev. D73, 112001 (2006).
- [95] B. Aharmim *et al.* (The SNO Collaboration), *Measurement of electron neutrino and total ^8B solar neutrino fluxes with the Sudbury Observatory Phase I Data Set*, Phys. Rev. C75, 045502 (2007).
- [96] S. Abe *et al.* (The KamLAND Collaboration), *Production of Radioactive Isotopes through Cosmic Muon Spallation in KamLAND*, Phys. Rev. C81, 025807 (2010).
- [97] M. Ambrosio *et al.* (The MACRO Collaboration), *Measurement of the residual energy of muons in the Gran Sasso underground Laboratories*, Astropart. Phys. 19, 313-328 (2003).
- [98] M. Yasue *et al.*, $^{12}\text{C}(p,t)^{10}\text{C}$ and $^{12}\text{C}(p,^3\text{He})^{10}\text{B}$ Reactions at $E_p=51.9\text{ MeV}$, J. Phys. Soc. Japan 42, 367 (1977).
- [99] S.P. Mikheev and A.Yu. Smirnov, *Resonance Amplification of Oscillations in Matter and Spectroscopy of Solar Neutrinos*, Sov. J. Nucl. Phys. 42, 913 (1985);
L. Wolfenstein, *Neutrino Oscillations in Matter*, Phys. Rev. D17, 2369 (1978);
P.C. de Holanda and A.Yu. Smirnov, *LMA MSW solution of the solar neutrino problem and first KamLAND results*, JCAP 0302, 001 (2003).
- [100] B. Aharmim *et al.* (The SNO Collaboration), *Electron Energy Spectra, Fluxes, and Day-Night Asymmetries of ^8B Solar Neutrinos from the 391-Day Salt Phase SNO Data Set*, Phys. Rev. C72, 055502 (2005).
- [101] B. Aharmim *et al.* (The SNO Collaboration), *Independent Measurement of the Total Active ^8B Solar Neutrino Flux Using an Array of ^3He Proportional Counters at the Sudbury Neutrino Observatory*, Phys. Rev. Lett. 101, 111301 (2008).
- [102] S. Abe *et al.* (The KamLAND Collaboration), *Measurement of the ^8B solar neutrino flux with the KamLAND liquid scintillator detector*, Phys. Rev. C84, 035804 (2011).
- [103] K. Abe *et al.* (The SuperKamiokaNDE Collaboration), *Solar neutrino results in Super-Kamiokande?III*, Phys. Rev. D83, 052010 (2011).
- [104] J. Bahcall *et al.*, *Standard Neutrino Spectrum from ^8B Decay*, Phys. Rev. C54, 411 (1996).
- [105] D. Franco, *The Borexino experiment: test of the purification system and data analysis in the Counting Test Facility*, Ph.D. Thesis, Università degli Studi di Milano (2005).
- [106] P. Lombardi and G. Ranucci, *Time and position distributions in large volume spherical scintillation detectors*, Nucl. Instrum. Meth. A574, 65-82 (2007).

- [107] Ferrara group of the Borexino Collaboration, *How many fake geo-neutrinos from ^{210}Po in Borexino?*, Borexino internal report, 2009.
- [108] E. Sanshiro, *Neutrino Geophysics and Observation of Geo-Neutrinos at KamLAND*, Ph.D. Thesis, Tohoku University (2005).
- [109] Y. Koshio, *The study of the fiducial volume systematic error for solar neutrino analysis*, Borexino Internal Report (2011).
- [110] T. Schwetz et al., *Global neutrino data and recent reactor fluxes: status of three-flavour oscillation parameters*, arXiv:1103.0734v2 [hep-ph] (2011).
- [111] J.P. Cravens et al. (The SuperKamiokaNDE Collaboration), *Solar neutrino measurements in Super-Kamiokande-II*, Phys. Rev. D78, 032002 (2008).
- [112] K. Nakamura and Particle Data Group 2010, *Review of Particle Physics*, J. Phys. G: Nucl. Part. Phys. 37, 075021 (2010).
- [113] <http://www.nndc.bnl.gov/capgam/>.
- [114] T. Luu and C. Hagmann, *Neutron Production by Muon Spallation I: Theory*, <https://e-reports-ext.llnl.gov/pdf/340911.pdf> (2006).
- [115] *FLUKA Online manual*, http://www.fluka.org/fluka.php?id=man_onl.
- [116] *Flair for FLUKA*, <http://www.fluka.org/flair/index.html>.
- [117] T. K. Gaisser, *Cosmic Rays and Particle Physics*, Cambridge University Press (1990).
- [118] P. Lipari & T. Stanev, *Propagation of multi-TeV muons*, Phys. Rev. D44, 3543-3554 (1991).
- [119] M. Aglietta et al. (The LVD Collaboration), *Upper Limit on the Prompt Muon Flux Derived from the LVD Underground Experiment*, Phys. Rev. D60, 112001 (1999).
- [120] M. Ambrosio et al. (The MACRO Collaboration), *Vertical muon intensity measured with MACRO at the Gran Sasso laboratory*, Phys. Rev. D52, 3793-3802 (1995).
- [121] V.A. Kudryavtsev, *Muon simulation codes MUSIC and MUSUN for underground physics*, arXiv:0810.4635v1 [physics.comp-ph] (2008).
- [122] O.G. Ryazhskaya and G.T. Zatsepin, Proceedings of the IX International Conference on Cosmic Rays, Vol. 21, p. 987, London (1965).
- [123] Y-F. Wang et al., *Predicting neutron production from cosmic-ray muons* Phys. Rev. D64, 013012 (2001).
- [124] M. Boswell et al., *MAGE - a GEANT4-based Monte Carlo Application Framework for Low-background Germanium Experiments*, arXiv:1011.3827v1[nucl-ex] (2010).
- [125] <http://geant4.web.cern.ch/geant4/UserDocumentation/UsersGuides/PhysicsReferenceManual/fo/PhysicsReferenceManual.pdf>.

- [126] A. Fassò *et al.*, *The physics models of FLUKA: status and recent development*, arXiv:hep-ph/0306267v1 (2003).
- [127] G. Battistoni *et al.* (The MACRO Collaboration), *Study of photonuclear interactions of muons in rock with the MACRO experiment*, arXiv:hep-ex/9809006v1 (1998).
- [128] N. Agafonova *et al.* (The OPERA Collaboration), *Measurement of the atmospheric muon charge ratio with the OPERA detector*, arXiv:1003.1907v1[hep-ex] (2010).
- [129] H. Wulandari *et al.*, *Neutron Flux at the Gran Sasso Underground Laboratory Revisited*, Astropart. Phys. 22, 313 (2004).
- [130] K. A. Hochmuth *et al.*, *Probing the Earth's interior with the LENA detector*, Earth Moon Planets 99, 253-264 (2006).
- [131] E. Gschwendtner *et al.*, *Performance and Operational Experience of the CNGS Facility*, Contribution to IPAC10, Kyoto (Japan), CERN-ATS-2010-153, (2010).
- [132] A. Ferrari *et al.*, *An updated Monte Carlo calculation of the CNGS neutrino beam*, CERN-AB-Note-2006-038 (2006).
- [133] P. Antonioli *et al.*, *A Three-Dimensional Code for Muon Propagation through the Rock: MUSIC*, Astropart. Phys. 7, 357-368 (1997).
- [134] A. Tang *et al.*, *Muon simulations for Super-Kamiokande, KamLAND and CHOOZ*, Phys. Rev. D74, 053007 (2006)
- [135] T.H. Burnett *et al.*, *Measurement of Cosmic-Ray Muon Charge Ratio at Sea Level between Energies of 10 and 1500 GeV*, Phys. Rev. Lett. 30, 937-940 (1973).
- [136] V. A. Kudryavtsev *et al.*, *Neutron- and muon-induced background in underground physics experiments*, The European Physical Journal A36, 171-180 (2008).

Acknowledges

Dottorato, tre anni. Devo dire che di strada ne ho fatta. E certo non solo dal punto di vista lavorativo, ma anche dal punto di vista personale. Credo che i due aspetti si siano intrecciati ed alimentati a vicenda, in quello che potrei definire un circolo virtuoso.

In primo luogo vorrei ringraziare il Prof. Bellini, che mi ha permesso di continuare il lavoro sui neutrini solari, di partecipare a conferenze e scuole di dottorato e che ha sempre avuto tempo per me. Allo stesso modo ringrazio Alessandra Tonazzo, per avermi così ben accolta nel gruppo dell'APC, per avermi dato fiducia e per avermi sempre aiutata e consigliata.

Ne approfitto per ringraziare anche il gruppo di Milano: Gioacchino, Emanuela, Livia, Barbara, Alessandra. Un grazie particolare va a Paolo L.. E uno ancora più speciale a Davide D., più come amico che come collega. E grazie anche ad Andrea che, nonostante le continue lamentele, c'è sempre stato quando avevo bisogno.

Puis je voudrais remercier le groupe de l'APC: Daniel Vignaud, pour m'avoir toujours conseillé et pour avoir lu presque tout ce que j'ai écrit à propos des neutrinos; Didier et Jamie, qui ont partagé leur bureau avec moi pour presque cinq mois. Merci beaucoup à Michel pour tout l'aide avec le cluster de Lyon, fondamental en certains moments. E grazie a Davide F., per avermi affidato molti dei suoi lavori e per i continui consigli. E a questo punto ringrazio anche il gruppo degli italiani espatriati a Parigi! Un pensiero particolare va a Silvia e Paolo e alle soirées parisiennes ;)

Cambiando area geografica mi sposterei al Gran Sasso... dove in primo luogo ringrazio George per la musica, le chiacchierate notturne ai Laboratori esterni e la splendida gita nel fiume. Poi ringrazio tantissimo Chiara G. che resta la mia preferita. E tutte le persone con cui ho condiviso tutti i periodi in trasferta e che, oltre all'aiuto sul lavoro, sono sempre riuscite a farmi sentire a casa: Chiara V., Massimo O., Andrea e Aldo I., Yura, Robbè, Andrej, Ana, Paolo S., Oleg, Igor, Francesco L., Vincenzo, Francesco Vissani e sicuramente ho dimenticato qualcuno. Riguardo alla fisica, un grazie particolare va ad Alessandro, che innumerevoli volte mi ha "sbloccato" da problemi, e Rino, senza il quale sarei ancora a chiedermi perché i miei neutroni non fanno scattering elastico!

Risalendo a Genova, mille grazie vanno a Gemma, sempre guida ispiratrice. Molti grazie anche a Marco e Sandra. E ovviamente a Stefano D., per le utilissime discussioni sia in ambito lavorativo che no. E anche se ormai è espatriato a Filadelfia, un carissimo grazie a Stefano P.; credo non ci sia nemmeno bisogno dirlo, ma nonostante la distanza in km sei una delle persone che sento in assoluto più vicine... grazie, sei speciale!

And obviously, considering the USA, I want to greatly thank all the guys from Princeton and Virginia Tech: first of all, as obvious, my sweet Richie; and then Alvaro, Pablito, Amanda, Szyszy and Steve. Thanks to you all for having shared with me many days of strong work or of light vacation, for having hosted me many times in different apartments, for having appreciated Pocoyo and Hello Kitty, for dinners together and all the relaxing and nice memories you left me in these years.

Thanks also to Frank and Cristian for their always delicious hospitality during the periods I spent in Princeton. E nel gruppo di Princeton nominerei anche Luca Grandi ("chi c***o è Luca Grandi?!").

And obviously I need to thank Spiderman and Donald Duck for their constant participation and fundamental help in each Borexino Working group!!

E passando alle amicizie di sempre, o anche recenti ma che sembrano di sempre, un carissimo grazie alla Ele e alla Vale, con le quali ho fatto i primi passi nel mondo della fisica e con le quali anche adesso, nonostante la dislocazione geografica sfavorevole, sento un legame profondo. Un grazie anche alle amiche del Faro, in particolare Chiara, perché anche gli svaghi dal lavoro sono importanti! E a Paola... da quel seminario con Marco le somiglianze che ci legano non hanno fatto che crescere... e ora poi?! Se ci fossimo messe d'accordo non ci saremmo riuscite! :-D E un grande grazie alla mia cara amica Elena... perché nonostante le disavventure teniamo sempre duro!

Vorrei ringraziare, forse un po' fuori contesto, anche Paola Pattini... per i preziosi, no che dico, fondamentali insegnamenti di questi ultimi anni. Decisamente la mia vita è cambiata da quando l'ho conosciuta!

E passando all'ambito familiare... un primo grandissimo grazie va ai nonni: Nando, Rosanna e Amelia. Perché sono tanto orgogliosi dei miei studi ("Allora come stanno i tuoi neutrini? E i tuoi BoXeRini") e credono che io sia chissà quale "scienziata". Un grazione alla zia Dadi, perché anche se non approfitto della vicinanza di abitazione per andarla a trovare, so che mi è sempre vicina.

E infine grazie a mio fratello 'mbo, che nonostante sia svampito come pochi, c'è sempre se ho bisogno. E ai miei genitori Angelo e Paola. Perché... mah come si fa a spiegarlo? Perché senza di voi non sarei arrivata fino qui e perché nei momenti di bisogno (come quest'ultimo) vi fate in quattro-otto-dodici per aiutarmi. E non sapete quanto questo mi dia e mi abbia dato forza.

Et enfin merci à JJ. Je crois on a eu de la chance à se rencontrer... et bien ça c'est un mérite à toi! Merci pour m'écouter, merci pour me conseiller, merci pour m'aimer. Je sais et je sens on a encore plein de choses à faire, à régler, à comprendre, à expérimenter. Mais je crois que si l'on se fait force et l'on reste ensemble... on va gagner toutes les batailles! Premièrement celle qui va nous arriver dans quelques mois... il s'agit d'une défi et d'une pari, parmi les plus grandes de toute une vie. Et j'ai décidé de les jouer avec toi... merci d'être à côté de moi.